Optimizing Steel Connections in Spatial Structures:

Prototyping Joinery with a Focus on Wire Arc Additive Manufacturing for Structural Efficiency and Fabrication

by
Mahirah Rohail

A thesis
presented to the University Of Waterloo
in fulfilment of the
thesis requirement for the degree of
Master of Architecture

Waterloo, Ontario, Canada, 2025
© Mahirah Rohail 2025

Author's Declaration

This thesis consists of material all of which I authored or co-authored: see Statement of Contributions included in the thesis. This is a true copy of the thesis, including any required final revisions, as accepted by my examiners.

I understand that my thesis may be made electronically available to the public.

Statement of Contributions

This thesis is the original work of Mahirah Rohail, who was the sole author of all sections of this research. While the majority of the work was conducted independently, certain aspects of the research involved external contributions, as outlined below:

- The metalwork processes were conducted at the Conestoga College, Fountain Street campus – Cambridge. The Wire Arc Additive Manufacturing processes were performed by Professor C. Tam Nguyen and Professor Jim Galloway, while the Plasma cutting was done by Jackson Macor, an alumnus of Conestoga.

- The digital stress analysis study was established and conducted by Abigail Lusabia, an undergraduate student in Civil and Environmental Engineering (CEE) at the University of Waterloo, under the supervision of Dr. Scott Walbridge. This includes all associated images as part of the analysis.

Abstract

Structural steel joints are a critical component in design that can determine the success of any architectural project. Steel connections are fundamental to architectural design, impacting structural integrity, safety, and aesthetic quality. While typical joints at a smaller scale have been mastered in the construction industry, developing unique structures in a larger context with custom joinery often creates challenges with accuracy, efficiency, and manufacturing cost. An alternative to conventional techniques is Additive Manufacturing (3D printing), which can efficiently develop optimized and intricate structural components while adhering to time and budget constraints. In particular, additively manufactured steel nodes are the prime focus of this research, which looks into developing joint designs derived from topology optimization to answer the question of whether the structural integrity can be maintained while focusing on the aesthetic appeal of the connection design. Currently, some experimentation is underway utilizing 3D-printed steel structures on a large scale. However, this stream is still relatively undeveloped and requires further exploration for efficiency and sustainability in the construction industry. The research focuses on developing small-scale prototypes of design iterations to eliminate ambiguities, selecting the more efficient design in terms of aesthetics, structure, and fabrication ability with the available technology. For this, ten experiments were done, which included six topology optimized joints and two simplified final joints, in addition to two sectional parts. The selected joint design was further tested for its key features using the Wire Arc Additive Manufacturing (WAAM) with a six-axis robotic arm in two experiments that involved approximately twelve hours of total weld time. These tests specifically explored the impact of process parameters and the main features of the joint, including achieving curvature and examining the impact of gravity on the weld pool during the deposition process. The presented research provides critical insights into how curvature can be effectively achieved, while ensuring adequate integrity and structural performance. The findings from the presented experiments contribute to new possibilities of structural design to understand how different typologies of joints impact structural performance while not limiting design possibilities.

Acknowledgements

Completing this thesis has been both a challenging and rewarding experience. As I reflect on the journey that led to this thesis, I am filled with gratitude for the many people who have supported me along the way, whose guidance and contributions have made this journey possible.

My deepest gratitude goes to my supervisor, Dr. Mohamad T. Araji, who, not only gave me the opportunity to pursue this research but also believed in my ability to take on this task. His guidance, patience, and support have shaped both this thesis and my growth as a researcher. I feel incredibly fortunate to have had the opportunity to learn under his mentorship, which has been instrumental in helping me produce meaningful work. I am also sincerely grateful to Dr. Scott Walbridge, my committee member, whose research in Additive Manufacturing provided me with the opportunity to contribute to this field. I am thankful for his constant guidance, support, and the connections he facilitated, all of which played a significant role in shaping my work.

I would also like to extend my profound thanks to the Conestoga team - Professor Jim Galloway, Professor Tam Nguyen, and Jackson Macor - for their support, for patiently answering my numerous questions, and for producing the Wire Arc Additive Manufacturing samples that were crucial to this research. Their time, knowledge, and generosity are deeply appreciated. I am also grateful to Abigail Lusabia for her invaluable help with digital simulations, and the MSAM Lab team at UWaterloo for providing insights on 3D printing.

Finally, I want to express my heartfelt thanks to my friends and family, who were always by my side. To my best friends, Marium and Mahnoor, for always listening to me, believing in me, and providing me moral support. To my peers, Adham and Waqas, with whom I spent my M.Arch journey - they became like a family, always there to listen, share a laugh, and support me through it all. And to my parents and siblings, whose constant encouragement, sacrifices, and love have been the foundation of my journey. I feel incredibly fortunate for such a caring and supportive family - without them I would not be here.

Dedication

To my parents, Rohail Majeed and Lalarukh, whose steadfast support and love have shaped my path, and to my brother, Danial, whose constant encouragement and belief in me inspired me to pursue this degree.

Table of Contents

Author's Declaration ii
Statement of Contributions iii
Abstract v
Acknowledgements vii
Dedication ix
List of figures xiv
List of tables xxiii

1 Introduction 1
1.1 Background 3
1.2 Problem Statement 6
1.3 Research Objectives 7
1.4 Scope and Limitations 9

2 Literature Review 11
2.1 Evolution of metal structures 13
2.2 Biomimicry in structures 19
2.2.1 Application in building design 21
2.2.2 Relationship to lattices 29
2.3 Digital tools 38
2.3.1 3D modelling tools 38
2.3.2 Structural optimization tools 39
2.4 Metal fabrication techniques 49
2.4.1 Conventional fabrication techniques 49

2.4.2 Additive Manufacturing processes 53
2.4.2.1 Role of Additive Manufacturing in prototyping 60
2.4.2.2 Environmental and economic sustainability 62
2.5 Wire Arc Additive Manufacturing (WAAM) 65
2.5.1 WAAM layer building and parameters 68
2.5.2 Geometric variability of WAAM deposited layers 70
2.5.3 Mechanical anisotropy in WAAM 74
2.5.4 Current trends and applications 78

3 Methodology 85
3.1 Joint design procedures 89
3.1.1 Application of biomimicry in design 89
3.1.2 Operative design strategies 94
3.1.3 Digital tools 99
3.1.4 Final joint design 99
3.2 Joint optimization 100
3.2.1 Digital stress analysis 100
3.2.2 Topology optimization studies 102
3.3 PLA prototyping 107
3.4 WAAM application and learning techniques 111
3.4.1 Lab and equipment 111
3.4.2 Expert opinions 114
3.4.3 Form considerations in relation to WAAM 117
3.4.4 WAAM anisotropy and weld paths 123
3.4.5 Experiment 1 – WAAM plate 125
3.4.5.1 Plasma Arc Cutting 129

3.4.6 Experiment 2 – WAAM hemisphere 131
3.4.7 Limitations in WAAM procedures 133

4 Results and Discussion 135
4.1 Digital stress analysis 137
4.2 Topology optimization 143
4.3 PLA prototyping 148
4.4 WAAM procedures 165
4.4.1 WAAM plate 165
4.4.2 WAAM hemisphere 170
4.4.2.1 Ring form 170
4.4.2.2 Surface curvature 172
4.4.3 Comparison of WAAM with PBF for joint fabrication 180

5 Conclusion 187
5.1 Summary 189
5.2 Conclusion based on results 191
5.3 Limitations 193
5.4 Future extension and application 195

Letters of Copyright Permission 199
Bibliography 210

List of Figures

Figure 1.1 Research objectives
Illustration by Author

Figure 2.1 Three-hinged arch – Galerie des Machine
[17] Public domain

Figure 2.2 John Hancock Center, Chicago
[20] Photograph by Ezra Stoller, Courtesy Yossi Milo Gallery, Licensed under *CC BY-SA 3.0*

Figure 2.3 Farnsworth House, Chicago
[25] Public domain - Image donated by Carol Highsmith to the library of Congress

Figure 2.4 The Pompidou Centre, Paris
[26] Photograph © Flickr user dalbera, licensed under *CC BY 2.0*

Figure 2.5 Tree structure at the Stuttgart Airport, Germany
[28] Photograph by CatalpaSpirit via Wikimedia commons, licensed under *CC BY-SA 4.0*

Figure 2.6 NVIDIA Voyager Building, California
[31] Reproduced by permission from Clarissa Eyu in Corporate Communications, NVIDIA

Figure 2.7 Biomimicry spiral: How nature's adaptation inspire architecture
Illustration by Author

Figure 2.8 Beijing National Stadium, China
[46] Photograph by CEphoto, Uwe Aranas, licensed under *CC BY-SA 3.0*

Figure 2.9 Left to Center - University of Namibia, Hydrology Center; Right: Namibian beetle
[48] Photographs © Matthew Parkes
[62] Photograph © Flickr user Harry and Rowena Kennedy, licensed under *CC BY-NC-ND 2.0*

Figure 2.10 California Academy of Sciences
[50] Photograph by WolfmanSF via Wikimedia commons, licensed under *CC BY-SA 3.0*

Figure 2.11 World Trade Center concept generation by SOM, using bamboo as an inspiration
[41] Photograph © SOM, reproduced by permission

Figure 2.12 The New Beijing Poly Plaza glass system
[53] Reproduced by permission from Terri Meyer Boake

Figure 2.13 Tabiat bridge, Tehran
[58] Reproduced by permission from Mohammad Hassan Ettefagh

Figure 2.14 Significance of biomimetic structures
Illustration by Author

Figure 2.15 Naturally occurring cellular structures
[61] Honey comb structure: Photograph by Gavin Mackintosh via Wikimedia commons, licensed under *CC BY 2.0*
[62] Paper Wasp Nest: Photograph by Reinhold Möller via Wikimedia commons, licensed under *CC BY-SA 4.0*
[63] Bubble structure: Photograph by Valeria Danilova via Pexels, free to use
[64] Leaf structure: Photograph by ClickerHappy, licensed under *CC 0*
[65] Giraffe pattern: Photograph by Lauren Bryant via Wikimedia commons, licensed under *CC BY 3.0*

Figure 2.16 Lattice Structures Classification
Illustration by Author

Figure 2.17 Strut-based lattice formed through a combination of unit cells
Illustration by Author

Figure 2.18 Voronoi pattern derived from Delaunay Triangulation
Illustration by Author

Figure 2.19 Above: plastic 3D printed joints; Below: SLM 3D printed joints
[55] Used with permission of American Society of Civil Engineers, from "Topology Optimization and 3D Printing of Three-Branch Joints in Treelike Structures", Wang, Longxuan; Du, Wenfeng; He, Pengfei; Yang, Mijia, 146, 2025; permission conveyed through Copyright Clearance Center, Inc.

Figure 2.20 Generative design three-branch tree joints
[117] Used with permission of Elsevier Science & Technology Journals, from "Joints for treelike column structures based on generative design and additive manufacturing", Wang, Hui; Du, Wenfeng; Zhao, Yannan; Wang, Yingqi; Hao, Runqi; Yang, Mijia, 184, 2025; permission conveyed through Copyright Clearance Center, Inc.

Figure 2.21 Cross-joint generative design based on machine-learning algorithm
[108] Reproduced by permission from author – Mijia Yang

Figure 2.22 Bionic tower structural design based on topology optimization
[119] Image by author - Konstantinos Daniel Tsavdaridis, licensed under *CC BY 4.0*

Figure 2.23 Top: Topology optimized beam, bottom: Cellular web beam
[119] Image by author - Konstantinos Daniel Tsavdaridis, licensed under *CC BY 4.0*

Figure 2.24 Shape optimization simulation results using static stress
Reprinted from [122], with the permission of AIP Publishing.

Figure 2.25 Comparison of topology optimization results generated by three Grasshopper plugins
[120] Image by authors - Mariam Selmi, Zeynep Yeşim ilerisoy, licensed under *CC BY-NC-ND 4.0*

Figure 2.26 Casting defects
Illustration by Author

Figure 2.27 Material extrusion system
Illustration by Author (based on [164])

Figure 2.28 Binder jetting system
Illustration by Author (based on [170])

Figure 2.29 Powder bed fusion system
Illustration by Author (based on [170])

Figure 2.30 Sheet lamination system
Illustration by Author (based on [170])

Figure 2.31 Direct energy deposition system
Illustration by Author (based on [170])

Figure 2.32 Wire Arc Additive Manufacturing system
Illustration by Author (based on [210])

Figure 2.33 Comparison between FDM and GMAAM process
Illustration by Author (based on [208] - courtesy of Jim Galloway)

Figure 2.34 Geometric variability of the weld pool
Image by Author

Figure 2.35 Steel node design by Arup – Left: Conventional design, Right: 3D printed design
[244] Photograph © ARUP

Figure 2.36 3D printed pedestrian bridge by MX3D
[245] Reproduced by permission from photographer – Adrian de Groot, and from company - MX3D

Figure 2.37 Topology optimized joint concept by MX3D
[248] Reproduced by permission from photographer – Leonard Faustle, and from company - MX3D

Figure 2.38 AM offers the advantage of cast nodes but with added benefit of eliminating the need to segment the chord
[150] Reproduced by permission from Tarana Haque, Technical Sales Manager, North America at Cast Connex

Figure 2.39 An AM saddle component printed directly onto a round HSS member
[150] Reproduced by permission from D Mark Douglass, Business Development Manager at Lincoln Electric Additive Solutions

Figure 3.1 Schematic workflow of methodology
Figure by Author

Figure 3.2 Left: Vintile Latticing, Middle: Octet Latticing, Right: Voronoi Latticing – showing multi-branch connection points
Illustration by Author

Figure 3.3 Voronoi latticing patterns – Left to right: Dense to light voids
Illustration by Author

Figure 3.4 Base form – Study connection
Illustration by Author

Figure 3.5 Subtractive and additive design operations
Illustration by Author

Figure 3.6 Subtraction – Carving: Create voids in the mass
Illustration by Author

Figure 3.7 Subtraction – Taper: Gradual narrowing of the sides at the top
Illustration by Author

Figure 3.8 Addition – Expand: Stretch the top surface to create a convex surface topography
Illustration by Author

Figure 3.9 Subtraction – Shear: Push down the upper surface to create a concave topography
Illustration by Author

Figure 3.10 Addition – Inflate: Stretch both top and bottom surfaces outwards
Illustration by Author

Figure 3.11 Subtraction – Pinch: Compress both the top and bottom surfaces inwards
Illustration by Author

Figure 3.12 Model set-up in Fusion 360
Illustration by Author

Figure 3.13 PLA prototyping – Work flow
Illustration by Author

Figure 3.14 FANUC ARC Mate 100iD Arc Welding Robot
Image by Author

Figure 3.15 FANUC standard Teach Pendant
Image by Author

Figure 3.16 Unsupported (Cantilevered) regions occurring when printing the joints vertically on the substrate
Illustration by Author

Figure 3.17 Horizontal print orientation creating minimal unsupported regions
Illustration by Author

Figure 3.18 Left: Vertical print with thin cross-section; Right: horizontal print with wide cross-section
Illustration by Author

Figure 3.19 WAAM printing process for the inflated joint
Illustration by Author

Figure 3.20 WAAM fabrication in x-y plane
Illustration by Author

Figure 3.21 In process plate printing
Image by Author

Figure 3.22 WAAM plate
Image by Author

Figure 3.23 Plasma Arc Cutting
Image by Author

Figure 3.24 Plasma cut plate being transferred using a G-clamp
Image by Author

Figure 3.25 Hemisphere print progress day 1 to day 5 - Above: Ring form, Below: Surface curvature
Images by Prof. C. Tam Nguyen

Figure 4.1 Case I: (a) Loading conditions, (b) and (c) Stress results
Images by Abigail Lusabia

Figure 4.2 Case II: (a) Loading conditions, (b) and (c) Stress results
Images by Abigail Lusabia

Figure 4.3 Case III: (a) Loading conditions, (b) and (c) Stress results
Images by Abigail Lusabia

Figure 4.4 Case IV: (a) Loading conditions, (b) and (c) Stress results
Images by Abigail Lusabia

Figure 4.5 Case V: (a) Loading conditions, (b) and (c) Stress results
Images by Abigail Lusabia

Figure 4.6 Case VI: (a) Loading conditions, (b) and (c) Stress results
Images by Abigail Lusabia

Figure 4.7 Case VII: (a) Loading conditions, (b) and (c) Stress results
Images by Abigail Lusabia

Figure 4.8 Topology optimization results – 2% mesh size
Illustration by Author

Figure 4.9 Topology optimization results – 1% mesh size
Illustration by Author

Figure 4.10 Progression of topology optimized joints as the target mass increased
Illustration by Author

Figure 4.11 8% infill density in Topology Optimized joints
Image by Author

Figure 4.12 65% target mass prototypes at scale 1:6 – Left: 2% mass, Right: 1% mass
Image by Author

Figure 4.13 45% target mass prototypes at scale 1:6 – Left: 2% mass, Right: 1% mass
Image by Author

Figure 4.14 25% target mass prototypes at scale 1:6 – Left: 2% mass, Right: 1% mass
Image by Author

Figure 4.15 PLA prototypes print support structures of topology optimized Joints Images and Diagram by Author

Figure 4.16 Surface texture of 25% target mass prints – Left: 2% mesh size, Right: 1% mesh size
Images and Diagram by Author

Figure 4.17 Comparison between unsmoothed and smoothed surface for 2% and 1% mesh sizes
Images and Diagram by Author

Figure 4.18 Operative design joints at scale 1:6 – Left: pinched joint, Right: inflated joint
Image by Author

Figure 4.19 25% infill density in operative design joints
Image by Author

Figure 4.20 Left: Concave joint (top) with supports (bottom), Right: Convex joint (top) with supports (bottom)
Image by Author

Figure 4.21 Front view of the hollow inflated joint section printed in PLA at a scale 1:4 – Left: support structure, Right: form
Image by Author

Figure 4.22 Top view of the hollow inflated joint section printed in PLA at a scale 1:4 – Left: support structure, Right: form
Image by Author

Figure 4.23 Double sided PLA printed section of an inflated joint branch at a scale 1:3 – Left: support structure, Right: form
Image by Author

Figure 4.24 Inflated joint branch sections indicating the unbuildable regions for a six-axis robot
Illustration by Author

Figure 4.25 Inflated joint proposed branch sections to show how a six-axis robot can manufacture the form
Illustration by Author

Figure 4.26 Inflated joint branch sections showcasing the joint form that can be fabricated using an eight-axis robot
Illustration by Author

Figure 4.27 WAAM plate – Edge finishes
Image by Author

Figure 4.28 Plasma cut joint form – 50% mass
Image by Author

Figure 4.29 Hemisphere – Left: Surface curvature, Right: Hollow interior
Image by Author

Figure 4.30 WAAM hemisphere – Surface study
Illustration by Author

Figure 4.31 WAAM sectional profiles over a curvature – conceptual study
Illustration by Author

Figure 4.32 Hemisphere – Top view comparison between tool paths, 3D model, and WAAM fabrication
Illustration by Author

Figure 4.33 Possible curvature angles with WAAM without the need for a support structure
Illustration by Author

Figure 4.34 The MSAM Lab, UWaterloo – Kitchener, Ontario
Image by Author

Figure 4.35 Powder Bed Fusion – Preview of horizontal print
Image and data by MSAM Lab, Diagram by author

Figure 4.36 Powder Bed Fusion – Preview of vertical print
Image and data by MSAM Lab, Diagram by author

Figure 5.1 Application instance of the designed joint
Illustration by Author

List of Tables

Table 2.1 Lattice definitions from literature
Table by Author

Table 3.1 Abaqus modules and parameters
Table by Author

Table 3.2 Topology optimization mesh parameters in Fusion 360
Table by Author

Table 3.3 PLA process parameters
Table by Author

Table 3.4 Expert opinions in relation to the optimized forms
Table by Author

Table 3.5 Void-to-Surface width ratios as per the target mass
Table by Author

Table 4.1 Results data of topology optimized PLA prototypes
Table by Author

Table 4.2 Results data of simplified joints PLA prototypes
Table by Author

Table 4.3 WAAM Parameters comparison
Table by Author

Table 4.4 Comparison of deposition time per layer
Table by Author

Table 4.5 MSAM Lab - Discussion overview with expert Francis Dibia
Table by Author

Table 4.6 Inflated joint estimated print costs in WAAM
Table by Author

Table 4.7 Comparison between PBF and WAAM functionality
Table by Author

Chapter 1

Introduction

This chapter serves as a background to the research area, forming a narrative about the topic significance and why it is essential to carry forward. It highlights the need for material innovation and the key role of steel in the construction industry, with a focus on steel structural connections. It also discusses innovation in connection joints through the amalgamation of biomimicry, digital optimization techniques, and additive manufacturing.

1.1 Background

Materials form the foundation of our inhabited environment, playing a fundamental role in shaping our world, ranging from large-scale infrastructure to minute technological products. Recent advancements in material innovation have contributed to a deeper understanding of material structures and their properties [1]. Key aspects of this innovation include developing materials that are lighter, stronger, and more durable [2], [3], and reducing costs and environmental impact while promoting sustainability [2].

In the construction industry, selecting appropriate building material is cardinal to functionality, structural integrity, and cost-effectiveness. Steel gained prominence after the Industrial Revolution due to its ductility, durability, strength, and recyclability [4], [5], [6]. These properties enable innovative designs and efficient manufacturing techniques, including off-site fabrication. Steel's flexibility allows for the construction of revolutionary structures such as space frames and bridges, capable of withstanding heavy loads and seismic forces [5], [7]. Additionally, pre-engineered steel components support rapid, cost-effective construction [8].

Steel connection joints play a pivotal role in structural performance, as most structural failures originate from connection issues [9]. Properly designed joints contribute significantly to structural efficiency by ensuring effective load transfer and maintaining the overall integrity of the framework [10].

Connections such as bolted, welded, and riveted joints influence the ductility, stiffness, and load-bearing capacity of steel structures [10]. Contemporary architectural trends highlight exposed steel connections as design features, reflecting material authenticity. However, unique structures with non-repetitive elements demand advanced fabrication methods, increasing costs and complexity [9].

Technological advancements have led to refined connection designs inspired by the need for better seismic performance, aesthetic integration, and reduced fabrication time. Tools like computational optimization and finite element analysis (FEA) are essential in developing efficient joint configurations that balance aesthetic appeal with structural resilience [9]. Improved fabrication techniques, including robotic welding and high-precision laser cutting, have further refined the manufacturing process, enhancing the reliability and performance of steel connections [9].

To further facilitate innovation, the building sector has taken a step towards 3D printing, commonly referred to as Additive Manufacturing (AM). AM is rapidly advancing and taking over multiple industries simply due to the versatility it provides in design and the ease of fabricating geometries that are otherwise impossible [11]. It builds an object layer by layer under computer control using robot technology [12], opening the possibilities of rapid prototyping, allowing the designers to quickly iterate and test their designs before committing to full-scale production. Quick prototypes can be made with cheaper materials to investigate design concepts. This creative freedom allows for the optimization of designs to meet specific performance criteria while reducing material waste and production time [10].

The use of additive manufacturing in the steel industry has significantly opened the possibilities of developing detailed and complex structural connections, with better precision, that were traditionally impractical [11]. This includes the creation of biomimetic forms and topologically optimized connections

with more ease, without the involvement of multi-step complex conventional processes. Biomimetic structures are naturally equipped with exhibiting strong mechanical properties, having the ability to withstand external forces through their unique structural patterns. Their integration in the structural joints can be vital due to their ability to channel loads more effectively.

AM of steel has the potential to play a key role in the circular economy as well because it can enable fabrication of exceptional quality components from recycled powdered residues [13]. In contrast, since conventional steel fabrication processes are subtractive, they generate significant material waste from cutting, shaping, and machining steel, contributing to higher embodied carbon [14]. These impacts are further accelerated when the steel components get transported to the construction site for assembly. If the components are large or heavy, they add to the transportation time, consuming more energy resources. Apart from these complexities, there are challenges when integrating additional functionalities into a steel structure because they can further introduce inadequacies in the structure, making it weak. In contrast to this, AM facilitates the integration of functionalities into building components, seamlessly incorporating them during printing, without the need for additional processes [15].

Despite technological developments, joint systems are not yet fully utilizing the capabilities of optimization tools to enable biomimetic structures through additive manufacturing, due to limited research in this area. Since ensuring steel joint efficiency is a critical component of structural design, this research offers a step towards achieving the potential of unconventional joint forms employing the concepts of biomimicry. It will do so while exploring the potential of additive manufacturing, in particular Wire Arc Additive Manufacturing (WAAM), to design a planar three-branch steel connection joint. The aim is to understand WAAM's potential in developing bio-inspired and computationally optimized joinery systems for balancing structural performance.

1.2 Problem statement

In contemporary architecture, conventional steel joint fabrication methods for unique forms are costly and limiting complexity [15]. While additive manufacturing has emerged as a promising solution for overcoming these limitations, its application in steel joint fabrication remains underexplored. The lack of research on integrating WAAM into steel joint design restricts the potential of computationally enhanced structural connections, reinforcing the industry's dependence on standardized, repetitive, and often inefficient joint configurations. This gap restricts the development of intricate and efficient structural connections, curbing opportunities for creativity in architectural design.

This research bridges this gap through a four-part investigative framework that systematically rethinks steel joint fabrication using WAAM-based additive manufacturing. The research begins with joint design, exploring non-traditional geometries to develop joint connections. Next, it advances into optimization, applying digital simulations and topology optimization to refine the joint configurations for load distribution. The third phase involves prototyping, where the optimized designs are physically realized and evaluated for printability, and geometric feasibility. Lastly, WAAM experiments are conducted to test the fabrication process, and process parameters and their impacts on manufactured pieces, assessing how AM can be practically integrated into architectural structures.

To measure the success of this research, structural stability and gravity performance will be assessed by evaluating the ability of WAAM fabricated joints to withstand gravitational impacts when achieving unsupported curvatures. Precision will be analyzed by considering the dimensional accuracy of the WAAM prints. Additionally, impacts of process parameters on heat accumulation in the layers will be examined to understand how thermal effects influence layer adhesion, distortion, and overall form

retention. This will be assessed by analyzing the form structure to observe how well the components maintain the desired shape, identifying any surface deformations caused by excessive heat buildup. These evaluation criteria will provide a comprehensive understanding of WAAM's viability for fabricating optimized steel joints, ensuring that they meet both structural and fabrication performance standards.

By amalgamating digital design, computational simulations, prototyping, and experimental validation, this study aims to enhance the role of steel joints in contemporary architecture, offering a new paradigm for structural connections that align with the evolving demands of digital fabrication and real-world implementation.

1.3 Research objectives

The primary goal of this research is to understand and utilize the capabilities of WAAM in designing steel connections for spatial structures to achieve unconventional forms. The study highlights the importance of advancing material innovation in the construction industry, recognizing the challenges in traditional steel fabrication methods. The specific goals of this study are as follows (Figure 1.1):

1. Develop joint forms through an iterative process based on biomimicry and supplemented through the application of operative design strategies.
2. Apply topology optimization and digital simulations to enhance the joints for better structural integrity.
3. Develop PLA (Polylactic Acid) filament prototypes to formally analyze the developed connection forms physically.
4. Analyze the impact of gravitational forces on weld bead formation and potential deformations during the WAAM process. The objective is to understand how gravity influences curvature formation and structural stability in three-dimensional joint configurations.

The research objectives are based on the need to bridge the gap between digital fabrication and real-world construction applications. By investigating the potential of WAAM in developing and optimizing structural connections, this study aims to provide insights into its feasibility, challenges, and practical applications of WAAM within the construction industry. The findings are intended to support further exploration and refinement in steel construction, laying a foundation for future experiments on joint design and AM techniques.

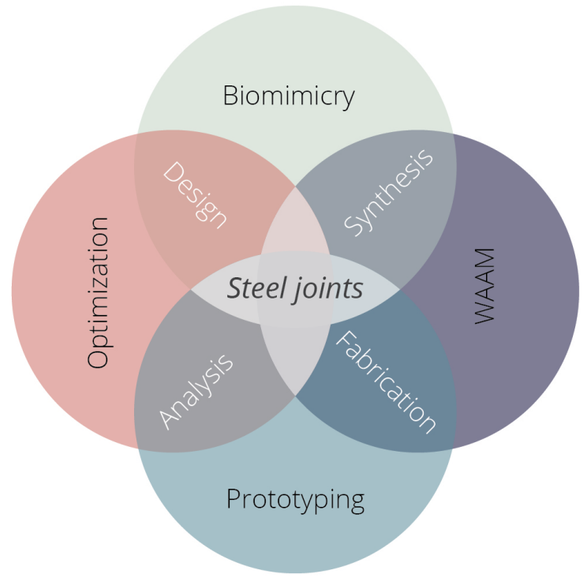


Figure 1.1 Research Objectives

1.4 Scope and limitations

This study investigates the application of WAAM in steel joint fabrication, focusing on design optimization, prototyping, and fabrication feasibility. The research will analyze the structural performance of WAAM-printed joints through computational simulations and experimental testing. However, the scope of this study is confined to the availability of a single WAAM robotic tool, available at the Conestoga College in Cambridge - Ontario, which restricts the study to abide by the available technology and its six-axis rotation capabilities. Being bound by the rotations of the robotic arm, the complexity of the joint designs is restricted. This constraint may also impact the ability to achieve desired geometries or configurations for the joints, particularly in cases where specific angles are crucial for structural integrity or aesthetic appeal. Access to usage is controlled by the Conestoga Robotics Lab team, who are responsible for preparing and performing the fabrication process, limiting the flexibility for direct experimentation and iterative modifications.

While this study seeks to expand knowledge in WAAM applications, it is subject to limitations of not having experimental data of performance testing on the joint designs with WAAM. The research is restricted to digital simulations only, which do not fully capture the layer-by-layer build characteristics of the WAAM process, such as interlayer bonding, thermal effects, residual stresses, or potential fabrication-induced distortions.

Despite these constraints, the study aims to explore innovative approaches to steel joint design and fabrication within the defined limitations, ultimately contributing to advancements in construction technology and architectural design. The core of this research is the creation of unique joints that can be produced rapidly without compromising structural integrity. It also promotes the integration of digital tools and optimization processes to facilitate the development of visually enhanced and structurally sound designs.

2.

Chapter 2

Literature Review

This section summarizes concepts and ideas from the literature review that culminate to form the basis of this research. The chapter is divided into six sections, beginning with an insight into steel structures, focusing on their evolution and fabrication. The subsequent sections delve into biomimicry, including the concept of lattices, and its influence of structural design, and the digital tools and optimization techniques that are used to conduct 3D modelling. Further, the discussion progresses towards conventional techniques vs Additive Manufacturing processes for the fabrication of such structures, including Wire Arc Additive Manufacturing which is the prime focus in this research.

2.1 Evolution of metal structures

Steel and its constituent parts have long been used in construction, evolving considerably due to technological advancements since the industrial revolution. A significant structure built during this time was the Galerie des Machines by architect Ferdinand Dutert in 1889, an early example of adapting joint designs to make them functional while reducing material usage. The notable structure has three-hinged arches (Figure 2.1), representing a significant advancement in structural design during the 19th century. The design made it possible to create slimmer and elegant arches that adapt well to movement and temperature changes while still maintaining their strength to cover wide spaces [16]. Since then, there has been substantial progress in structures, with an attempt to divert from bulkiness to a lightweight approach that adds to the aesthetic value of the design.

The modernist era exemplified structures where steel was celebrated as a structural component and highlighted in design rather than merely being used as a hidden support. Structural steel transformed modern architecture due to its superior strength and adaptability. It revolutionized building design and enabled the construction of iconic structures like skyscrapers and

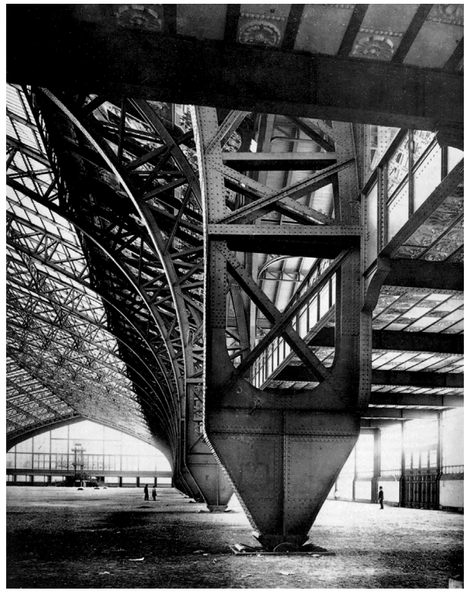


Figure 2.1 Three-hinged arch - Galerie des Machine [17]

bridges while replacing materials like wood and stone [18]. Technological advancements, including the Bessemer process and computer-aided design, significantly enhanced steel production and application. These innovations made steel more efficient, versatile, and central to architectural progress [18].

A conspicuous example of the structural expressionist style is the John Hancock Center in Chicago, Illinois (Figure 2.2) designed by Skidmore, Owings & Merril (SOM) and famous for its exposed X-bracing façade. Being one of the tallest buildings of that period and consisting of a load-bearing façade, its structural system allows for a sleek design, minimizing material use and hence promoting flexibility in the interior spaces while becoming an icon in modern architecture [19], [20], [21].



Figure 2.2 John Hancock Center – Chicago [20]

From modernism to high-tech architecture, there was a wave to push the boundaries of steel structures, exposing it as a key design feature. While architects like Mies Van Der Rohe built minimal structures like the Farnsworth house (Figure 2.3) [22], celebrating the simplicity of exposed structures during the modernist era, contrary to that, architects like Norman Foster, Richard Rogers, and Renzo Piano focused on a more high-tech approach, creating buildings that displayed these structures as the key feature. A prime example is the Centre Pompidou in Paris (Figure 2.4) by Richard Rogers and Renzo Piano, known for its inside-out design that exposes structural elements and mechanical systems. The structural capabilities of the material are highlighted by using exposed steel as the central feature on the façade, creating large open indoor spaces. The innovative design of the Pompidou Center influenced future works in how the visual expression of materials and structures adds to the aesthetic of space [22], [23], [24].



Figure 2.3 Farnsworth House – Chicago [25]

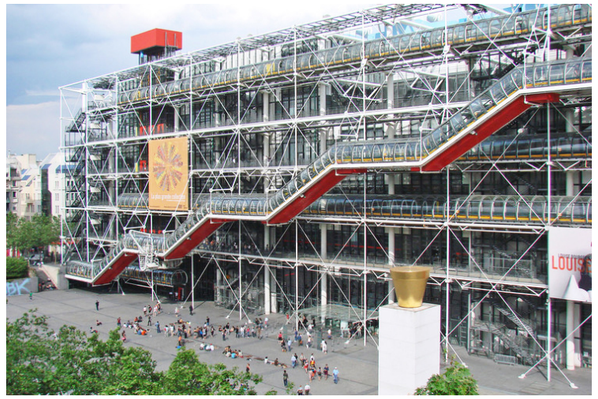


Figure 2.4 The Pompidou Centre – Paris [26]

In recent decades, steel construction has continued to evolve to create innovative structures. The tree structure supporting the roof of terminal 3 at the Stuttgart airport in Germany (Figure 2.5), designed by Gerkan, Mag, and Partners (GMP), showcases the dynamism that steel possesses. The structure takes inspiration from nature, with the steel columns consisting of four tubular poles forming a trunk that splits into branches at different levels to transfer the weight of the roof. The design allows for a lightweight construction that maintains its strength while drastically changing the typical aesthetics of a space [27].



Figure 2.5 Tree structure at the Stuttgart Airport – Germany [28]

A more recent example of steel wonders is the NVIDIA II Voyager building in Santa Clara – California by Gensler (Figure 2.6) [29]. The headquarters design showcases futuristic architecture, featuring a sculptural roof, a shaded trellis with integrated solar panels, and elevated workspace valleys, all designed using intricate and slender steel details. The lightweight steel canopy with a complex geometry makes it an exemplary structure, making the building

stand out for integrating innovative design elements with functional features [30], [31].



Figure 2.6 NVIDIA Voyager Building – California [31]

From the early days of the Eiffel Tower and Galerie des Machines to recent structures like the NVIDIA headquarters, steel has led to architectural innovation. With the development of better material properties and processes, achieving structures that are both more complex and more delicate has become a possibility. Modern design tools and recent technological advancements are pushing the limits of what steel can achieve even further, paving the way for significant innovation.

Designing with Structural Steel: A Guide for Architects [32], an AISC publication, explores joint design as a crucial aspect of integrating structural steel into architectural projects, highlighting the necessity of connections not only in structure but also as a means of enhancing the visual quality of a space. The book elaborates on the dual role of connections – balancing functionality with

aesthetics to transfer loads while celebrating the material qualities. In essence, the thoughtful design of steel connections not only enhances the visual and functional attributes of a place but also contributes to the usability of a space, impacting the mental well-being of its occupants [33].

2.2 Biomimicry in structures

Nature has perfected itself over thousands of years to adapt to changing external conditions, acting as an inspiration for design solutions that balance strength and flexibility in human-made structures to exhibit superior performance [34] - a concept known as biomimicry. Biomimicry is a term coined by Janine Benyus [35], derived from the Greek words bios (life) and mimesis (imitation). The International Organization for Standardization (ISO) [36] defines biomimicry as a design philosophy that draws inspiration from nature to develop sustainable solutions for social, environmental, and economic challenges.

The concept has gained significant attention in architecture and structural engineering, imitating natural processes, structures, and materials to create more efficient and resilient buildings and infrastructures [37]. The application of biomimicry in the built environment offers solutions that are sustainable, provide innovative design inspiration, enhance efficiency, improve resilience for adaptability to climate conditions, and incorporates biodiversity to support natural ecosystems (Figure 2.7) [38].

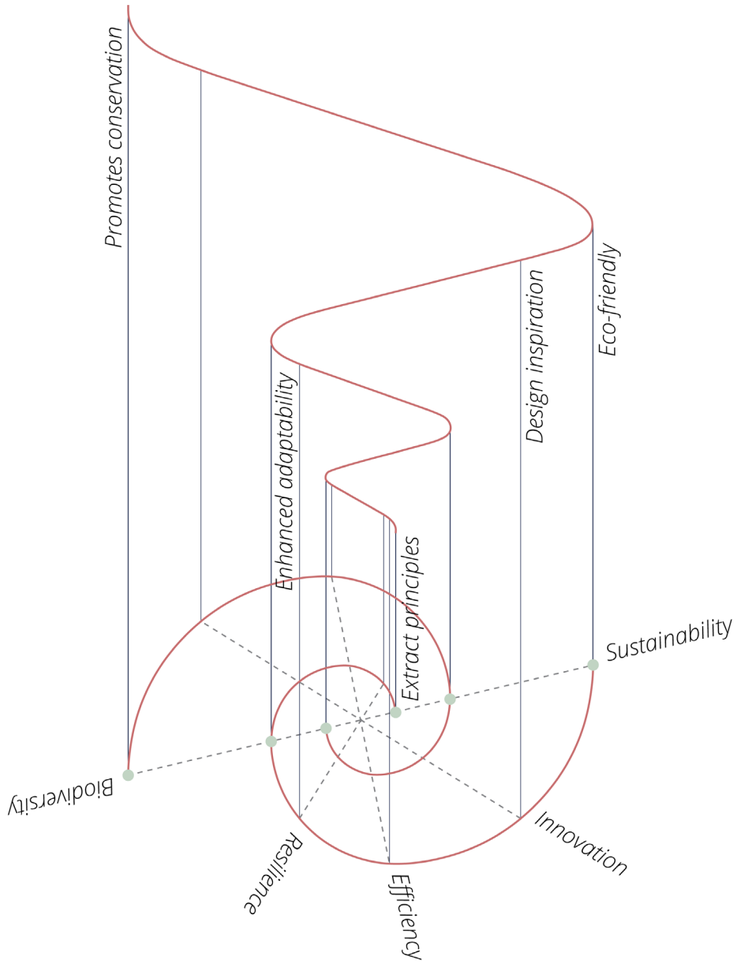


Figure 2.7 Biomimicry spiral - How nature's adaptation inspire architecture

2.2.1 Application in building design

In structural applications, biomimicry extends beyond aesthetics, incorporating functional principles from nature into engineering frameworks, enhancing resilience, load-bearing capacity, and material efficiency [39], [40]. As highlighted in Skidmore, Owings & Merrill LLP's research on nature-inspired structures [41], organic geometries offer unparalleled structural efficiency by optimizing material use while enhancing durability and adaptability.

As explained by Oguntona et al. [42], biomimicry is structured around three interconnected strategies: inspiration, imitation, and emulation, each aligning with different levels of architectural design: form, behaviour, and ecosystem [34], [43], [44]. At the form level, inspiration is taken from natural patterns and forms that influence design, such as honeycomb structures and the aerodynamic forms of birds, which optimize structural performance and energy efficiency. A built example of this is the Beijing National Stadium (Figure 2.8) that was inspired by a bird's nest [44], exhibiting a lattice like reciprocating (self-supporting) structure [45].



Figure 2.8 Beijing National Stadium - China [46]

At the behaviour level, imitation of biological features of how an organism does something [44]. The university of Namibia Hydrology Center imitated the behaviour of a Namibian desert beetle (Figure 2.9) that thrives in arid environments with minimal rainfall by efficiently collecting moisture from fog through body tilting against the wind. The building is similarly designed to capture and channel moisture from the air, providing a sustainable solution for water harvesting [43], [44], [47].

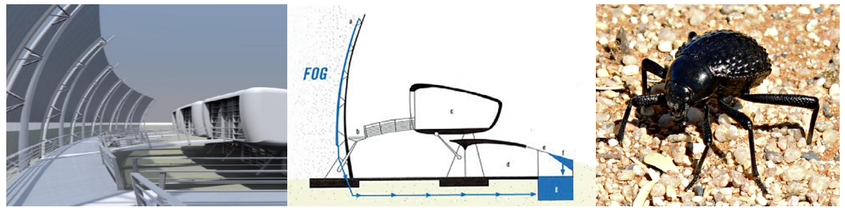


Figure 2.9 Left to Center - University of Namibia, Hydrology Center [48]; Right: Namibian beetle [49]

At the ecosystem level, the emulation strategy is applied where functional principles are abstracted and applied to holistic, sustainable architectural solutions [34], [42] e.g. the California Academy of Sciences, designed by Renzo Piano (Figure 2.10). The building applies biomimicry through the living roof system, featuring undulating mounds covered in native plants that provide insulation, facilitate natural ventilation and rainwater collection [50].

Biomimicry offers several advantages that contribute to the efficiency and resilience in built structures. Natural forms optimize material use, reducing waste while enhancing strength-to-weight ratios [38]. Nature's ability to withstand dynamic environmental forces inspires structural designs that enhance longevity and reduce vulnerability to earthquakes and extreme weather events [41]. Biomimicry fosters harmony between form and function, enabling the development of visually appealing structures that also serve

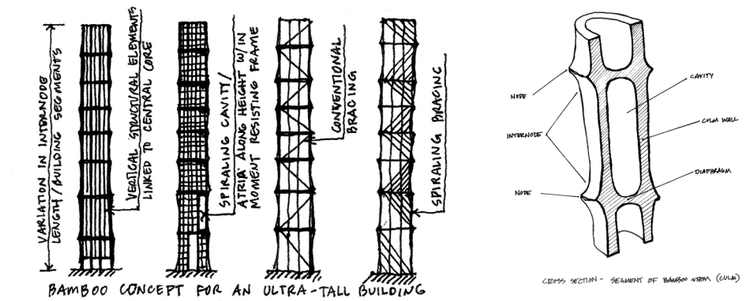


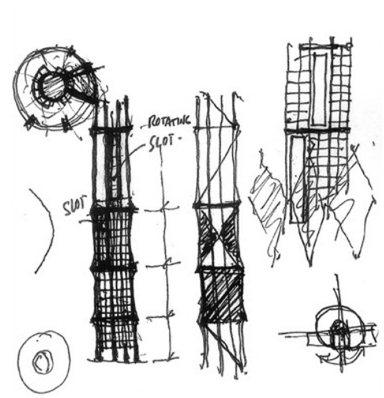
Figure 2.10 California Academy of Sciences [51]

practical purposes. From the structural segmentation of bamboo to the intricate networks of spider webs, biological precedents have informed the development of high-rise buildings, adaptive façades, and lightweight yet robust materials [41]. Designs inspired by natural structures such as seashells, honeycombs, and bird skeletons enhance both architectural beauty and structural performance [52].

Several architectural and structural innovations have been developed based on biomimetic principles. An example of this is the diagrid structural system that has been inspired by organic cell structures and is used to minimize the need for excess material while maintaining stability [40]. Similarly, Pin-fuse joints inspired by human shoulder joints allow structures to dissipate seismic energy, minimizing damage [41]. One of the most notable applications of biomimicry in high-rise buildings is the use of natural growth patterns to enhance stability [41]. The design for China World Trade Center Competition by SOM drew inspiration from bamboo (Figure 2.11), whose segmented structure was visioned to prevent buckling under extreme forces [41]. This principle

was applied to the tower's design, where internal cores and perimeter bracing mimicked the nodal reinforcements of bamboo culms. Further elaboration on the structure of bamboo was provided by Jamei et al. [37], explaining that bamboo's structural design is highly efficient in preventing buckling due to its hollow form. These internal nodes significantly enhance stability by reinforcing the structure against deformation and stopping the propagation of longitudinal cracks. In architecture, this natural optimization inspires lightweight yet strong structural designs, improving load-bearing capacity





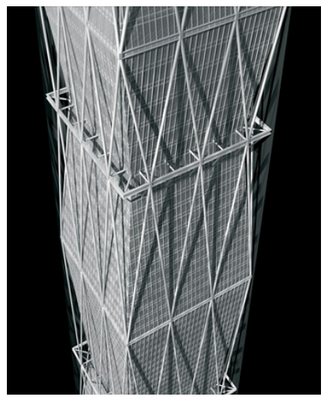


Figure 2.11World Trade Center concept generation by SOM, using bamboo as an inspiration [41]

and resilience while minimizing material use. Further, taking inspiration from a spider web and its working mechanism of stretching and absorbing force, SOM designed the Beijing Poly Plaza. It features a cable-net supported glass wall, inspired by the elasticity and resilience of spider webs (Figure 2.12). Just as spider silk stretches and absorbs force without breaking, the façade of this building moves with wind loads, reducing the risk of fractures and improving overall durability [41].

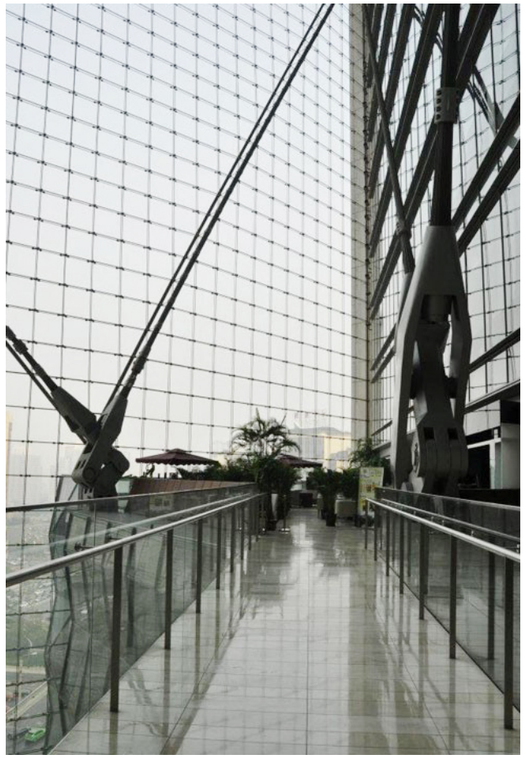


Figure 2.12 The New Beijing Poly Plaza glass system [53]

As highlighted by Jamei et al. [37], perhaps the most stable example of living structures are trees, that have evolved to distribute loads efficiently while maintaining structural integrity. Trees consist of a branching system to gradually distribute loads, reducing stress concentrations. Grigorian [54] elaborated that trees have optimized their structural design through evolutionary processes, distributing mechanical stresses efficiently and self-repairing minor damages - characteristics that have inspired novel construction techniques. Tree structures offer significant advantages in architecture and civil engineering, exhibiting fractal-like branching patterns that optimize load distribution, structural integrity, and material efficiency. In architecture, these principles translate into dendriform structures that enhance mechanical stability while maintaining aesthetic appeal [55].

In the construction industry, tree structures were popularized after its application at a terminal of the Stuttgart Airport in Germany as a form of spatial structure [56]. By mimicking the load bearing properties of trees, the design allows to create lightweight and high strength structures that minimize material usage. Additionally, tree-inspired designs contribute to dynamic load resistance, such as wind and seismic forces, through their branching mechanisms that distribute stresses evenly across multiple points [55]. Similarly, tree-inspired bridge designs also enable the distribution of loads through multiple pathways, ensuring stability while minimizing material use [57], e.g. The Tabiat bridge in Tehran that mimics a tree structure for its support system (Figure 2.13) [58].



Figure 2.13 Tabiat bridge, Tehran [59]

A significant advantage of biomimicry in architecture is resource optimization and waste reduction. By mimicking nature's structural hierarchies, architects and engineers can design lightweight yet durable materials that require fewer raw materials without compromising strength [37]. Jamei et al. [37] further elaborated by explaining that beyond performance enhancements, biomimetic architecture helps overcome conventional design limitations by providing holistic solutions to functional requirements. Figure 2.14 highlights these significant features of biomimetic structures and their advantages in structural design. Biomimicry promotes the development of sustainable solutions by drawing from nature's efficient design systems and biomimetic structures use those principles to become more resilient than regular structures, being able to adapt to circumstances that typical structures are not designed for. This adds innovation in existing structure models, brining about unconventional solutions to complex problems that can not be solved through conventional means.

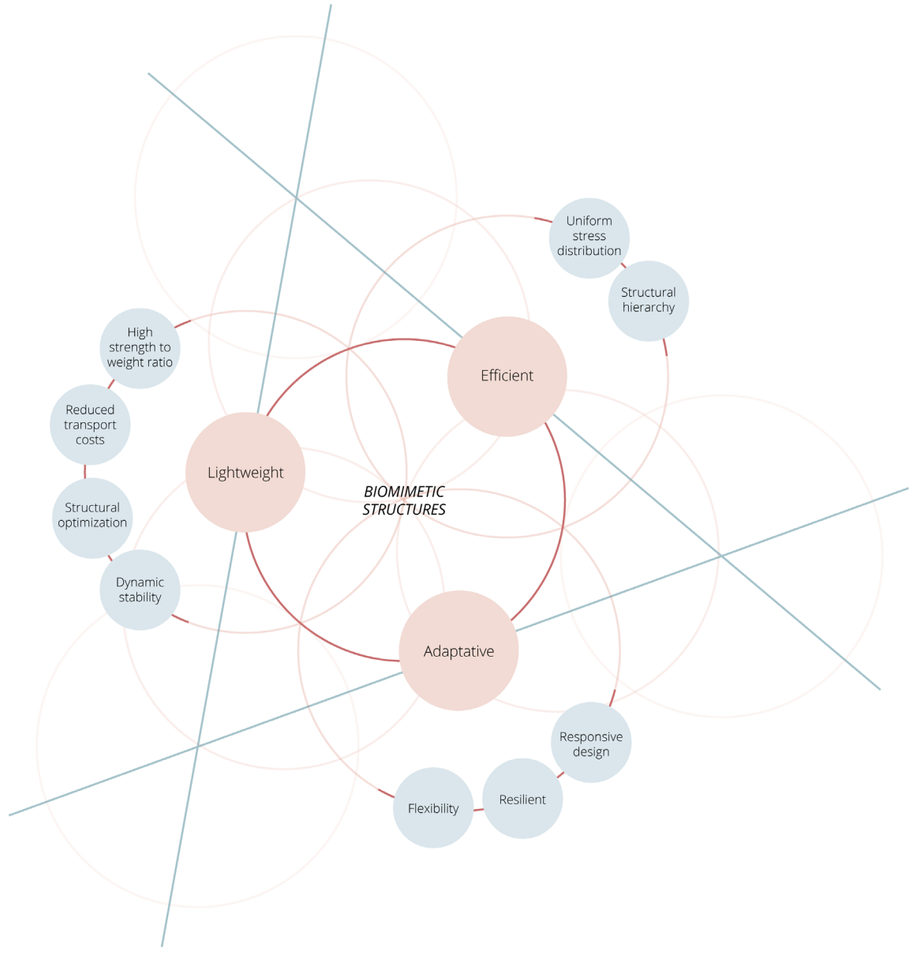


Figure 2.14 Significance of biomimetic structures

However, despite significant advancements and integration of biomimicry in architecture, its widespread adoption is limited due to advanced computational modelling and material science innovations [38]. Although biomimetic materials and structural systems have been extensively studied, the application of nature-inspired joints remains underexplored [60]. Therefore, gaps remain in the application of biomimicry at a micro structural level, especially due to the lack of standardized frameworks and building codes for implementing biomimicry in engineering and construction [42]. Further, large-scale implementation of biomimicry also remains a challenge due to cost constraints and manufacturing limitations [40], limiting it to highly budgeted projects.

2.2.2 Relationship to lattices

A specific category of biomimicry includes the cellular structures that commonly occur in the natural environment, such as bones, cork, leaves, bubbles, butterfly wings, and honeycombs (Figure 2.15) [61]. Naturally occurring cellular structures have been widely mimicked to create artificial cellular structures – lattice structures, due to their incredible properties.

Literature defines lattice structures in various ways, classifying them through multiple characteristic forms. The earliest definitions of lattice structures were introduced by Gibson and Ashby [67], who simply mentioned them as 3D cellular structures in which the cell walls have random orientations. Numerous scholars have developed definitions of lattice structures based on the Gibson and Ashby model, but a single cohesive definition doesn't exist. Pan et al. [68] discussed various definitions from the literature, providing a good view of scholars who attempted to define this term. For their research, Pan et al. [68] concluded that lattice structures are 3-dimensional porous structures formed by the tessellations of unit cells. Tao and Leu [69] defined a lattice structure as an architecture that has been formed by an array of spatial periodic unit cells



Figure 2.15 Naturally occurring cellular structures [62] [63] [64] [65] [66]

with edges and faces. Ahmed et al. [70], from the perspective of engineering applications, define lattice structures as patterns of unit cells designed to make a larger functional structure. However, this definition doesn't investigate the details of the structural typology. Ataollahi [71] defines lattice structures as interconnected porous unit cells arranged periodically and regularly. Syam et al. [72] simply defined the structure as consisting of nodes (the joinery points of struts) and struts (the linking member), whereas Tyagi and M [73] defined lattice structures as an interconnected network of struts and plates. Table 2.1 highlights the various definitions surrounding lattices.

Reference	Definition
Gibson and Ashby [67]	3D cellular structures in which the cell walls have random orientations
Pan et al. [68]	3-dimensional porous structures formed by the tessellations of unit cells
Tao and Leu [69]	An architecture that has been formed by an array of spatial periodic unit cells with edges and faces
Ahmed et al. [70]	Patterns of unit cells designed to make a larger functional structure
Ataollahi [71]	Interconnected porous unit cells arranged periodically and regularly
Syam et al. [72]	Structures consisting of nodes (the joinery points of struts) and struts (the linking member)
Tyagi and M [73]	An interconnected network of plates (linking surfaces) and struts (the linking member)

Table 2.1 Lattice definitions from literature

While many more definitions exist aside from the former, the purpose of stating these definitions is to identify that lattice structures have a series of meanings based on the research perspective of each scholar. It further leads to the idea that lattice structures can be classified into various types and have multiple forms and organizations, creating a difference in the definitions. Regardless of what classifications they have, lattice structures are considered an attraction in various industrial applications simply due to their properties of being lightweight, with high strength and stiffness, while providing a geometric design freedom [74].

The design of lattice structures is characterized by a balance between mechanical performance and material efficiency. They are engineered to

maximize strength with minimal material use, making them strong and efficient [75]. It is particularly beneficial in modern architecture, where the demand for innovative design solutions is increasing. These structures are defined by their cellular nature, where the geometry of the unit cells plays a crucial role in determining their overall properties [76]. Lattice structures are classified into several types based on mechanical response, morphology, and geometrical distribution [73]. They are further categorized according to the arrangement and typology of the unit cells, dividing the lattices into a series of geometries.

Figure 2.16 demonstrates the different categories of these lattice structures. The morphological and geometrical lattice structures are the most commonly occurring lattices. Morphological lattices are mostly porous structures, from which the strut-based lattices (also known as lattice-frame materials) [77] consist of nodes and struts arranged in a prismatic structure, formed with repeating unit cell (Figure 2.17) [74]. Surface-based lattices, also known as Triply Periodic Minimal Surfaces (TPMS), are mathematically explained as curved surfaces with a mean curvature of zero [74], [78]. However, TPMS lattices are considered unsuitable for load-bearing structures [79].

Plate-based structures are solid structures with plates between trusses and are a variation of strut lattices. Although all these lattices are 3-dimensional, the frequently occurring honeycomb structures in nature are 2-dimensional. Artificially, they are constructed with hexagonal, square, and triangular unit cells [80], having high porosity and low mass density, creating structures with high strength, while being ultra-light [81]. Porous strut lattices have an advantage over stochastic lattices because they can provide more strength while maintaining a lightweight structure, and their shock-absorbing properties make them a favoured a structure in architecture [82], [83].

Strut-based lattices are frequently selected due to their design simplicity over solid material structures, which are thought to have defects such as material wastage, inflexibility in design, greater volume, and difficulty of manufacturing

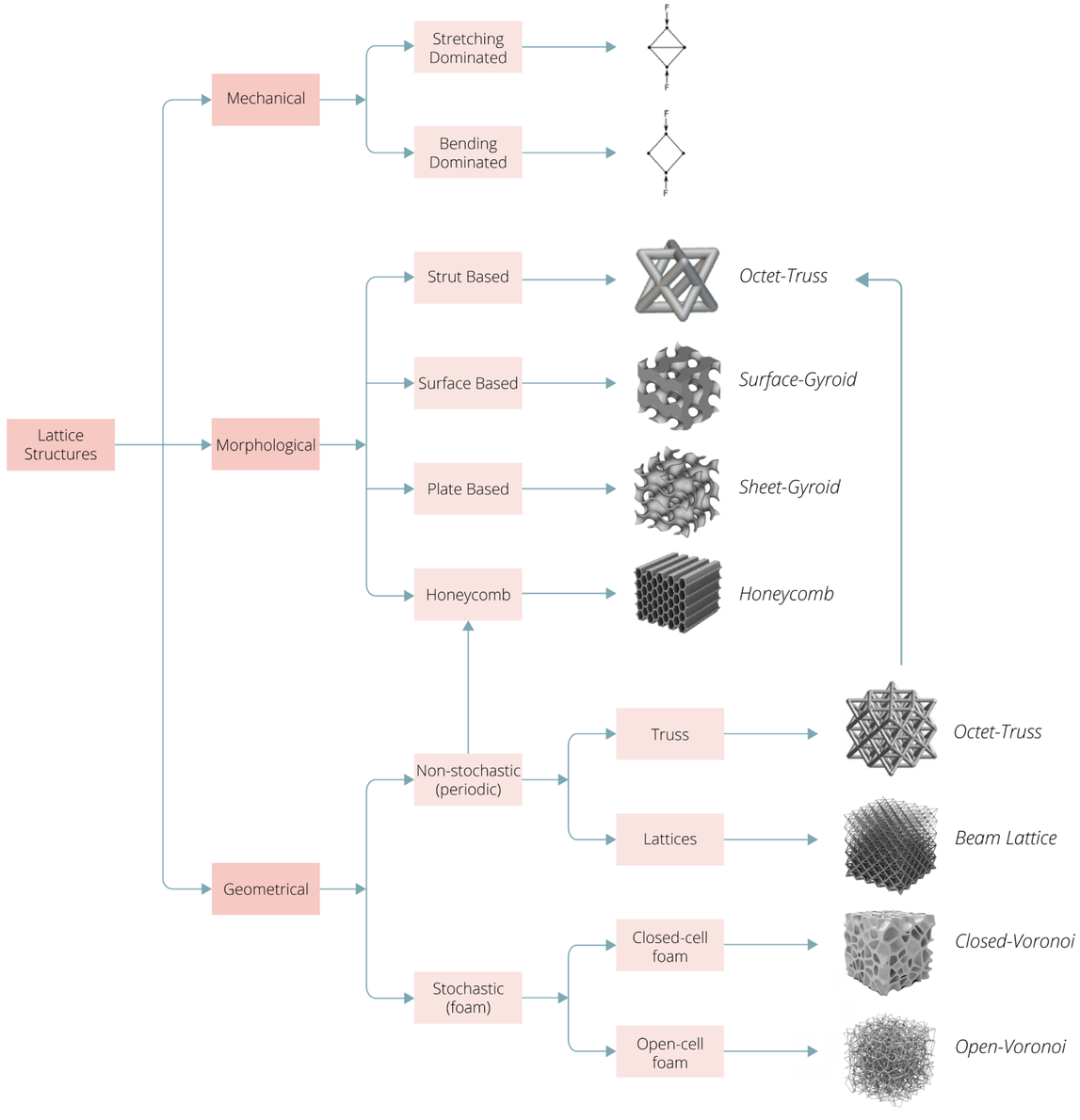


Figure 2.16 Lattice Structures Classification

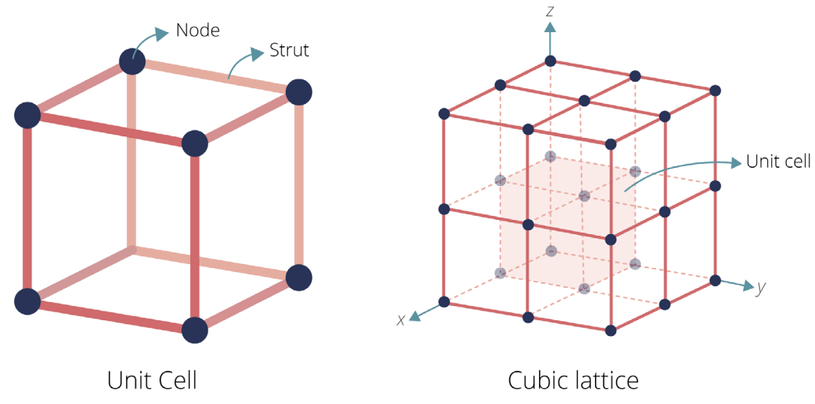


Figure 2.17 Strut-based lattice formed through a combination of unit cells

[68], [84]. Amongst the strut-based lattices, Vintiles stand out due to their unique geometry distinguishing them from traditional configurations such as cubic, tetrahedron, hexagon, octagon, and rhombic dodecahedron forms. Mekonen et al. [85] discussed the significance of the Vintile structures, stating that their optimized design enhances mechanical performance by reducing stress and deformation under load, making them advantageous in applications requiring high strength-to-weight ratios and efficient load distribution. They further performed comparative study involving various strut based cellular structures, from which the Vintile lattice demonstrated superior mechanical properties. Additionally, the optimized Vintile design in terms of unit size, lattice topology, and porosity further enhances its mechanical efficiency.

Amongst the geometrical lattices, non-stochastic lattices have a uniform cell configuration. From this, the octet truss is a prominent non-stochastic lattice with stretching-dominated properties, high stiffness, strength, and energy absorption efficiency [86]. It consists of interconnected struts arranged in a

pattern of regular tetrahedra and octahedra. This structure provides excellent strength-to-weight ratio and rigidity, making it ideal for applications where minimizing weight while maintaining structural integrity is crucial [87]. The octet truss design distributes loads efficiently throughout the structure. The geometric figures disperse load pressure equally along three sets of parallel planes. Pressure applied at any one point is instantly distributed throughout the entire structure, giving its great structural strength [87].

Further within the geometric category, stochastic lattices exhibit the structural characteristics of a sponge due to a randomized unit cell geometry, such as those based on Voronoi tessellations, whereas non-stochastic lattices are more regular structures, consisting of specific cell shapes such as honeycombs [78], [88]. This periodic arrangement of unit cells allows for a precise control over material properties by adjusting their cell geometry, supporting to achieve specific mechanical properties like stiffness, strength, and thermal conductivity [76]. The non-stochastic lattices overlap with the structural characteristics of morphological lattices in terms of the organization in the arrangement of unit cells [88].

From the geometric lattices, Voronoi has been mimicked in various architectural structures. Negm [89] provided detailed explanations of these Voronoi structures, stating that a Voronoi lattice divides spaces into regions based on a set of points, where each region is shaped so that any location inside it is closer to its assigned point than to any other point. Angelucci et al. [90] explained a simple method of creating Voronoi patterns (Figure 2.18), which starts by placing a set of seed points in the design area, which are then connected to their nearest neighbours, forming a set of triangles called Delaunay triangulation. To form the Voronoi diagram, the midpoints of Delaunay triangle edges are marked, and perpendicular bisectors are drawn. These bisectors form the edges of the Voronoi regions, resulting in polygonal cells. This natural pattern is commonly found in biological and physical systems, such as cellular structures, bones, blood vessels etc.

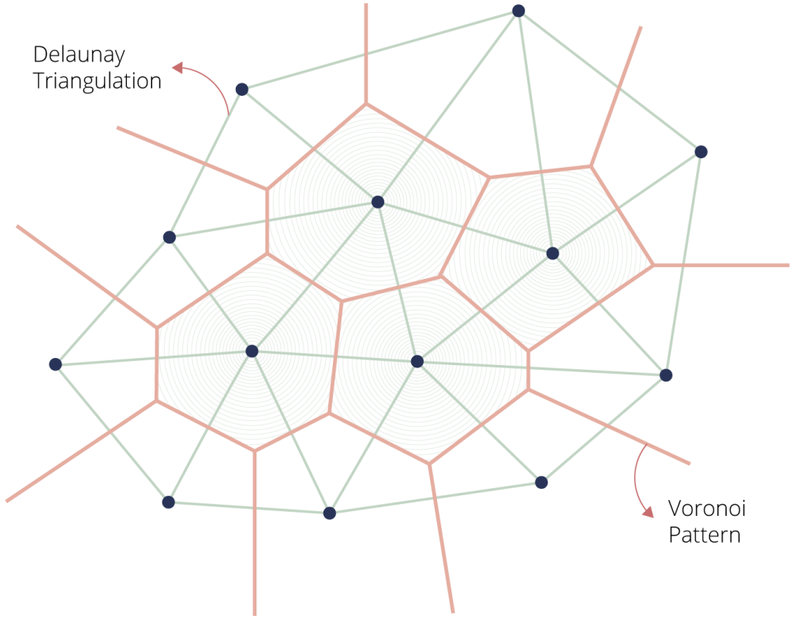


Figure 2.18 Voronoi pattern derived from Delaunay Triangulation

Voronoi-based lattice structures have been extensively studied for their unique mechanical properties. Research indicates that these structures can enhance energy absorption, increase stiffness, and reduce material consumption when compared to conventional grid-based systems [91]. For example, in tall buildings, Voronoi-like grids have been explored as an alternative to traditional hexagrid and diagrid systems, showing promise in improving lateral load resistance and seismic performance [90]. In dynamic applications, Voronoi-based closed-cell foams have been tested under impact loads, demonstrating superior energy absorption characteristics due to the irregularity of their cell structures [92]. They can be applied to both two-dimensional and three-dimensional configurations, allowing several applications in architecture

because of the unconventional patterns [89]. Studies have shown that Voronoi tessellations can be manipulated to control density variations, enhancing structural performance in both uniform and graded configurations [91].

Despite their advantages, Voronoi-based structures are not widely used in large-scale architecture and civil engineering. Unlike traditional grid systems, which have well-defined load paths, Voronoi structures require advanced computational methods for optimization [93]. The applications of the Voronoi latticing that does exist are confined largely to the overall structural forms, whereas their role in the inclusion of joinery systems is lacking [94]. Most building codes and structural design guidelines are based on traditional geometric systems such as rectangular grids and trusses. The introduction of Voronoi-based structures would require new validation methods and performance benchmarks, which adds an additional layer of complexity in their adoption [90]. Due to the conventional fabrication techniques, practical implementation of Voronoi often results in increased material waste from cutting and assembly inefficiencies [91].

Lattice-like configuration is frequently observed in large structures like bridges and tall building that integrate latticing in their structures to manage lateral loads in form of diagrid and hexagrid designs as a more regular form of structure [95] and Voronoi geometry as an irregular biomimetic pattern [90]. Friedman and Ibrahimbegovic [96] highlighted various lattice configurations and their innovative uses in structural design. An example of this is the Pantographic structures, like Hoberman's Iris Dome, that use a system of interlocking units, allowing for easy expansion and contraction. The Eiffel Tower serves as an early example of biomimicry in architecture, drawing inspiration from the latticing in the structure of bones, particularly the thigh bone (femur), that contains a trabecular lattice structure [97]. Gustave Eiffel mimicked the trabecular bone structure into the design of the Eiffel Tower, creating a lattice framework that. This approach allowed for a strong yet lightweight structure, reducing material use while enhancing stability and wind resistance.

In addition to their structural benefits, lattice structures can contribute to the sustainability of architectural projects. By optimizing material use and reducing the weight of joints, lattice designs can lower the overall material consumption and energy requirements [98]. It aligns with the growing emphasis on green building practices and reducing carbon footprints in the construction industry. Generally, applying lattice structures in architectural joints represents an amalgamation of structural innovation and aesthetic design, offering a pathway to more efficient, adaptable, and sustainable architectural solutions.

2.3 Digital tools

2.3.1 3D Modelling tools

The advancement of digital modelling tools in architecture has revolutionized the design and fabrication of biomimetic structures. Computational methods, particularly parametric and generative design, play a critical role in translating biological principles into architectural applications. Parametric modelling has enabled a shift from static typologies to dynamic, generative systems that respond to environmental and structural conditions [99]. Research shows a range of digital platforms that are used to digitally model such structures, a few from which have been more prevalent in architecture design. Tools such as Grasshopper, Rhinoceros 3D, Autodesk Revit, CATIA, SolidWorks, Fusion 360, Abaqus, and advanced finite element (FE) simulations have enabled architects to develop structures that exhibit organic adaptability, material efficiency, and structural resilience [81], [99], [100]. Grasshopper and Rhinoceros 3D are among the most widely used parametric modelling tools, offering architects the ability to create algorithmically generated designs that dynamically adapt to specific parameters [101].

Rhinoceros 3D, commonly known as Rhino, serves as a foundational platform for parametric modelling, providing powerful NURBS-based modelling tools that enable precise control over complex forms. One of the key advantages

of Rhino is its ability to handle freeform geometries, which are essential for replicating biological forms in architecture [99], [101].

Grasshopper is a visual programming language that functions as a plugin for Rhinoceros 3D, allowing to generate complex geometries through algorithmic design. Its node-based workflow enables users to create parametric models that can be easily adjusted in response to performance-based constraints and environmental factors. In biomimetic architecture, Grasshopper is widely used to translate natural growth patterns into digital models by leveraging computational algorithms such as reaction-diffusion patterns, and Voronoi tessellations. The integration of Grasshopper with Rhino allows for real-time parametric adjustments, making it particularly useful for designing biomimetic structures that require iterative refinements [99], [101].

Beyond Rhino and Grasshopper, Woodbury et al. [100] also delved into Autodesk Revit, a significant tool that integrates Building Information Modelling (BIM) with parametric data, streamlining material efficiency and structural optimization. Revit allows for the efficient coordination of complex biomimetic designs within broader architectural projects. Beyond this, Woodbury et al. [100] also analyzed the potential of CATIA (CAD, CAM, and CAE supporting software [102]) and SolidWorks (CAD software that provides both 2D and 3D design interfaces, with real-time collaboration, and cloud capabilities for seamless data sharing [103]) in modelling and analyzing complex geometries, however their architectural use is largely absent because of their engineering focused interface.

2.3.2 Structural optimization tools

Since Rhino/Grasshopper systems do not have any integrated stress analysis platforms, for performance analyses of designs, further external platforms and plugins are required to critically analyze the stability of the designed

structure. A dedicated program for this found in research was the Abaqus Finite Element Analysis software, that can perform digital stress simulations on models generated outside of its domain [81], [104], [105]. Abaqus has proven to be a versatile and powerful tool for stress analysis, offering the capability to model complex materials, intricate structural interactions, and diverse loading conditions [106].

Various studies were found that incorporated Abaqus to analyze the stress distribution and performance on a range of parts. Mohammed M. Eladly [107] performed stress analysis on a steel beam-to-column connection using simplified modelling techniques. The results of the simulation predicted the moment-rotation behaviour very precisely, providing significant insights into stress evolution, even under large deformations and complex contact interactions. From this study and from various others in literature, it was observed that Abaqus is flexible at handling diverse element types. Its solver capabilities, efficiently manage nonlinear behaviour, large deformations, and intricate contact interactions, ensuring robust and reliable simulations. Across all studies, results validated against experimental data exhibited precise information, emphasizing Abaqus's reliability in predicting stress distributions, deflection patterns, and failure modes [106], [107], [108].

As modern building designs become more complex, relying solely on an engineer's experience to create efficient joint configurations often results in the overuse of materials and less-than-ideal designs [109]. As discussed by Han et al. [109], in response to this, research into the optimization of structures has become prevalent. The topology optimization technique thus emerged as a method of designing components using computer algorithms to configure parts with an optimum material distribution based on a set of loads, conditions, and constraints defined by the user. Topology optimization uses a process of identifying and removing material from areas where it is not needed to support the structure, helping to reduce weight and creating an efficient design system [110].

The concept of topology optimization has actively been used by engineers to minimize a structure's strain energy while not compromising its strength [111]. It is a standard tool used in industry to produce lightweight parts [112]. Topology optimization also helps to create components with a unique design by creating voids in the initial solid geometry, with the resulting geometries often found to resemble natural structures [113]. Instead of starting with a preconceived design and adjusting, this method initiates with a solid block of material and removes unnecessary parts to find the most efficient shape. This can lead to innovative and unexpected designs that are not only structurally sound but also visually appealing [113].

By optimizing designs to be lighter, topology optimization also contributes to fuel savings, making it an environmentally friendly choice as demand for sustainable alternatives grows [114]. However, the applications of topology optimization are less evident in architectural and structural design than in other disciplines. The optimization of structural parts can greatly reduce the manufacturing cost since structural joints are the most expensive part of a structure [115], accounting for 15% to 45% of the total structural steel usage [116].

Various studies exist in the literature on the applications of topology optimization to customize structural joints. Li and Zhu [117] integrated structural topology optimization for designing revolute joints (hinge joints) based on a stiffness matrix to reduce the mass of the joint. Seifi et al. [115] studied topology optimization as a method of developing grid shell structural nodes under axial loading. Generating such joints in large numbers, with each node having a custom design, conventional manufacturing is a challenging. Zhu and Liu [116] applied multiobjective topology optimization on spatial structural joints to propose alternatives with equal strength and efficiency, while also improving their ability to resist vibrations. Further, according to the conclusions made Han et al. [109], joints designed with voids, such as those from topology optimization processes, demonstrate lighter weight and more

uniform stress distribution. They outperform joints with solid mass in terms of weight efficiency and stress distribution because the voids aid in effectively redirecting and distributing stress, minimizing stress concentrations, thereby enhancing mechanical performance [109].

One of the Stuttgart airport terminals consists of a tree-like structure [27], where each joint is crucial to hold the weight of the entire roof at one pivot point - the base trunk of the tree joint. The original joint design is cast to eliminate intersecting lines resulting from the welding of separate joint pieces [56]. While the cast joint is hollow from the inside, it still carries sufficient self-weight which can cause uneven distribution of stress. Thus, Wang et al. [56] utilized the principles of topology optimization to design tree-like joints (also known as three-branch joints) (Figure 2.19) with improved material distribution to properly manage stress and strain while also stepping away from the conventional method of designing, calculating, modifying, and redesigning. The optimized joint showed the same results as the original joint for maximum displacement, maximum equivalent stress, and maximum principal stress while reducing the weight of the joint by 48.57%, proving the benefit of utilizing topology optimization in structural design.

Similarly, Wang et al. [118] also conducted experiments on the same three-branch structure but took it a step further from basic topology optimization to a generative design process (Figure 2.20). Generative design advances the process of optimization to produce a set of designs to select as per the designer's liking [109]. Generative design builds from topology optimization, using the diverse boundary conditions applied to produce suitable results within those set conditions [119]. It is based on an artificial intelligence system to create comprehensive solutions [118], offering more effective solutions for the creation of novel designs.

Han et al. [109] carried out a similar process using a 2D cross-joint connection instead of a 3D joint, generating several node designs through a machine-

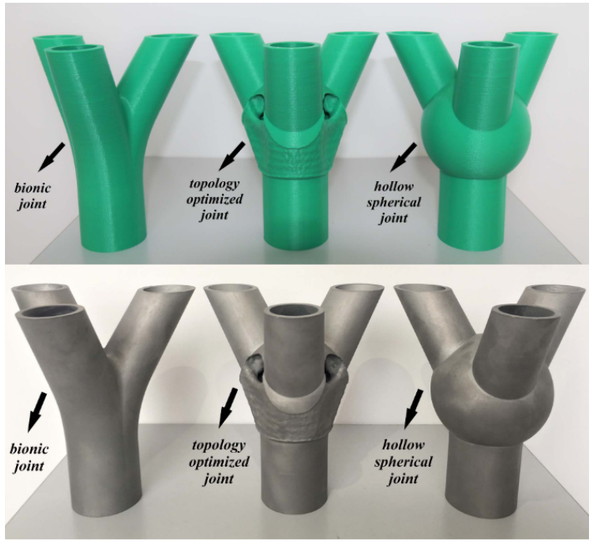


Figure 2.19 Above: plastic 3D printed joints; Below: SLM 3D printed joints [56]

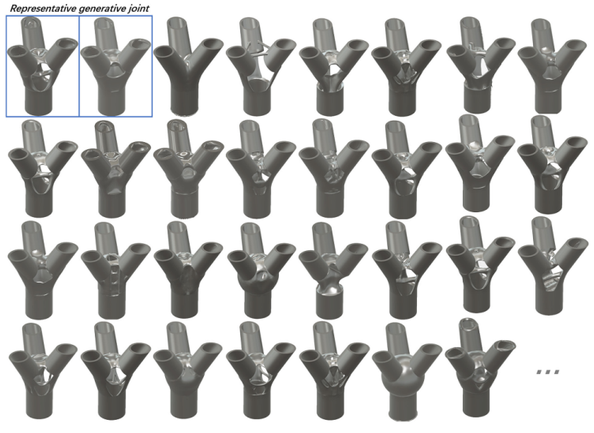


Figure 2.20 Generative design three-branch tree joints [118]

learning-based generative design algorithm (Figure 2.21). This process helped to isolate solutions based on the design objective and budget constraints. Han et al. [109] were able to achieve diverse creative configurations that also displayed superior static performance.

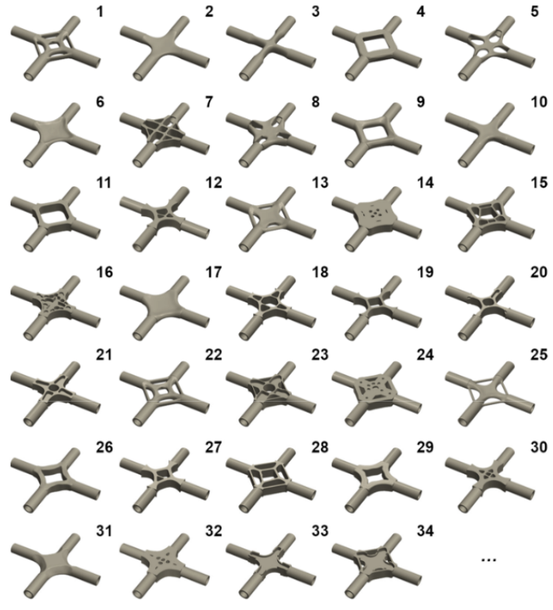


Figure 2.21 Cross-joint generative design based on machine-learning algorithm [109]

An example of topology optimization in architectural structures is the Bionic Tower, a high-rise building proposed for Abu Dhabi. Using topology optimization, engineers designed the tower's structural elements in a bracing design that keeps the building stable during high winds, matching both, the architectural vision and the need for structural efficiency (Figure 2.22). Another area where topology optimization has made a difference is the design of steel

beams. Traditionally, engineers would create beams with circular or rectangular openings to reduce weight. However, by applying topology optimization, they designed beams with custom-shaped openings that were even lighter and stronger (Figure 2.23). This technique not only improves performance but also allows for more creative design possibilities [113].

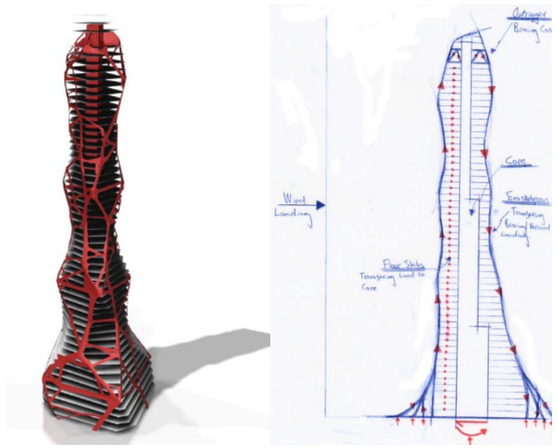


Figure 2.22 Bionic tower structural design based on topology optimization [120]

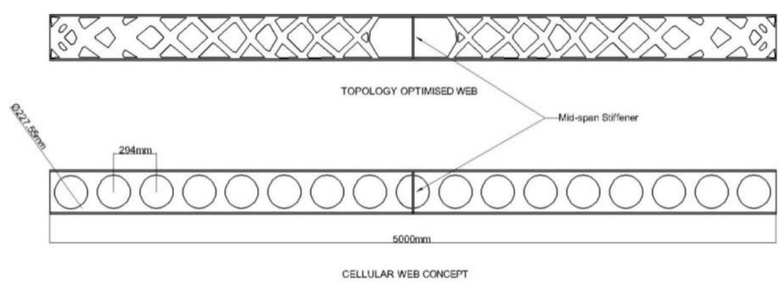


Figure 2.23 Top: Topology optimized beam, bottom: Cellular web beam [120]

In the literature, various software and plugins are found for performing topology optimization simulations. These programs are further categorized into two main mathematical methods of optimization that we commonly see in various studies – Solid Isotropic Material with Penalization (SIMP) and Bidirectional Evolutionary Structural Optimization (BESO) [116]. SIMP works by adjusting the material density within a design space to find the most efficient structure by reanalyzing material distribution until performance goals are reached [113]. BESO creates structures by selectively removing material where it is unwanted and adding it to regions with critical requirements [115].

Typically, generative iterations derive from evolutionary machine learning algorithms that require cloud computing for executing design exploration [109]. Further performance analyses of these algorithms were carried out using Altair HyperWorks 2021 stand-alone program by Han et al. [109]. Wang et al. [118] modelled the initial study geometry using SolidWorks 2019, importing it into a calculation program for generative design, and further analyzing through ANSYS 2020R1 software - a commercially available SIMP technique [121]. Both, Du et al. [122] and Wang et al. [56] modelled the initial design in SolidWorks as well, later importing it into Altair HyperMesh, a stand-alone program, based on the SIMP method, for topology optimization. HyperMesh has built-in postprocessing functions to analyze results. Jj et al. [113] used the SIMP technique for topology optimization on an I-section beam, further using ANSYS v.14 to refine the models. Seifi et al. [115], on the contrary, used the BESO methodology to obtain grid shell nodes with the stiffest structure within a given volume. The BESO code was further linked to ABAQUS as a structural analysis engine.

Syamsir et al. [123] explored Autodesk Fusion 360 (SIMP method) for the shape optimization of a gripper arm for PLA printing. It requires setting a parameter for target mass, that determines the result generated. The software also has built-in stress analysis simulation to analyze the performance of the optimized parts (Figure 2.24), although transition from optimization preface to stress

analysis preface is complicated because the optimization results are saved as a mesh while the stress analysis preface doesn't integrate well with meshes. Fusion 360 further allows setting up the model for 3D printing from within the software for efficient processing.

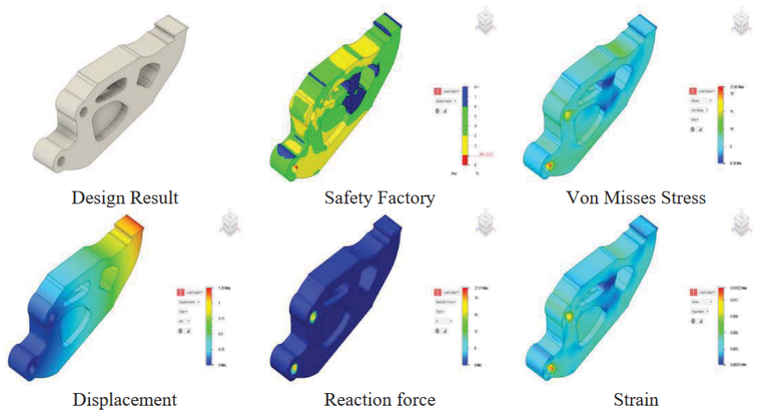


Figure 2.24 Shape optimization simulation results using static stress [123]

Curkovic [124] further explained the process of setting up a model for topology optimization in a CAD program, signifying the importance of applying constraints, defining preserving regions, and optimizing mesh settings. After designing the part, material properties are specified with a wide range of material selection. These materials are tailored to be compatible with 3D printing. The next steps include defining forces and constraints that calculate movements and strain in the part to help optimize it effectively. Lastly, it is crucial to define the contact points so that they remain unchanged in the optimization. After the process is completed, post-processing can be done to prepare the part for printing.

Selmi and İlerisoy [121] listed down and conducted experiments with various other programs for topology optimization, categorizing them according to the methods they utilize to perform the analysis. From this, we see additional options available for conducting the optimization than the literature has used, and some of these options are more suitable for users with experience in architectural programs. These include various Grasshopper plugins for Rhino, such as Millipede, TopOpt, Topos, Ameba, and Karamba3D. Of these, the former three are available for free use and based on the SIMP methodology, while the latter two rely on BESO and require commercial licensing. Selmi and İlerisoy [121] further state that Millipede is discontinued and may not comprehensively process the designs. Topos is comparative to Millipede in optimization, with faster processing time. Topos also displayed better Von Mises stress and displacement results when compared to Millipede and Ameba, calculated using SimScale. The results of optimizations in all three of them are shown in Figure 2.25.

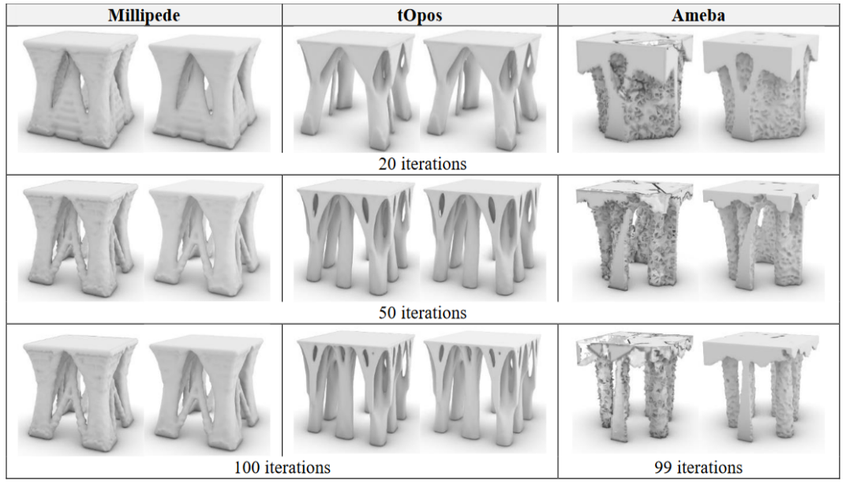


Figure 2.25 Comparison of topology optimization results generated by three Grasshopper plugins [121]

Topology optimization is significant for designing lightweight, high-performance structures, encouraging innovative designs. While topology optimization opens new possibilities, it also presents some challenges in fabrication because the optimized designs can be complex and difficult to manufacture using traditional methods and hence require advanced manufacturing methods [113].

2.4 Metal fabrication techniques

2.4.1 Conventional fabrication techniques

Steel fabrication is a critical process that involves cutting, bending, and assembling steel sheets and plates to build structures such as buildings, bridges, and machinery with high skill and precision. Typical conventional fabrication techniques involve computer numerical control (CNC) machines to produce accurate forms [6]. Traditional manufacturing techniques are mostly subtractive, involving cutting or removing material from a larger block to create products, typically for large-scale production due to the high costs associated with tooling and casting [125]. As per the Committee for International Development and Education on Construction of Tubular structures (CIDECT) [126] design guidelines, there are various procedures available to fabricate steel structures. The fabrication processes are typically divided into four categories, namely reduction, cutting, welding, and shaping [6].

The process of reduction typically involves altering the shape or size of a material, often by removing its sections or modifying the geometry. Reduction is focused on material deformation to achieve the desired form, without the removal of a significant amount of material. It consists various techniques including shearing, notching, punching, blanking, and slotting [6]. Shearing efficiently cuts metal sheets without generating waste, but it cannot handle complex shapes or thick materials, limiting its structural applications [6], [127], [128]. Notching, a variation of shearing, removes material from edges to prepare components for secondary processes, but its inability to make internal

cuts restricts its use in advanced fabrication [6], [129], [130]. Punching creates holes in metal sheets through high-pressure pressing, but the force applied can introduce errors, making it unsuitable for large-scale joint formation [6], [131]. Blanking, similar to punching, removes pre-cut sections for further use but remains confined to 2D designs, preventing its application in structural joints [6], [132]. Slotting, a CNC machining process, carves linear grooves with precision but is slow and limited to straight cuts, making it ineffective for multi-angled or large interlocking structures [133], [134], [135], [136].

Metal cutting processes typically involve laser cutting, plasma cutting, flame cutting, waterjet cutting, and band saw cutting that aim at separating steel into distinct pieces, using heavy and precise machinery [6]. Laser cutting, a high-precision CNC process, is effective for thin sheets but struggles with reflective metals and has material thickness limitations, restricting its application in heavy structural components [133], [137], [138]. Plasma cutting is a faster alternative for thicker metals, but it can lack precision and damage surfaces due to heat exposure, making it less viable for complex joints [6], [133], [139]. Flame cutting is cost-effective and capable of handling very thick metals up to 300 mm, but it is slow and not very precise without CNC assistance [6], [140], [141], [142]. Waterjet cutting offers versatility across different materials, including metals and composites, but its high cost, slow processing speed, and limited precision make it inefficient for mass structural fabrication [6], [143], [144], [145]. Band saw cutting, using a continuous rotating metal band, provides clean cuts but it is more commonly used for basic applications rather than intricate structural components [6].

Welding is a process of fusing metals by heating them to their melting point and then allowing them to cool to form a strong permanent bond. Common welding methods include (GMAW) – Gas Metal Arc Welding, TIG (GTAW) - Gas Tungsten Arc Welding, stick welding (SMAW) – Shielded Metal Arch Welding, and Arc Welding (FCAW) – Flux-Cored Arc Welding [6]. Further, tack welding is used to temporarily hold components in place but requires accuracy since

improper execution can compromise the final weld integrity. The welding process is also an integral part of managing stresses and deformations occurring due to material heating and cooling. Factors such as welding quality (including material thickness), welding order (impacts how material shrinks), and the type of welding used influence results [146]. When fabricating complex geometries with multiple pieces, traditional welding methods often lack the achievement of smooth transitions between components, leading to shrinkage due to residual stresses [56].

Metal shaping involves altering the workpiece by adding, subtracting and modifying the object using various techniques such as folding, bending, machining, flattening, and casting to mould, temper, and refine the steel into specific forms [6]. Folding and bending reshape flat sheets into desired forms without seams, adding strength, but material properties such as yield strength influence the bending process, requiring specific conditions for successful execution [6], [133], [147], [148]. Machining removes excess material to achieve precise shapes using tools like lathes, drills, and mills, although it is time-intensive and primarily applicable for small-scale components [6], [149]. Flattening is commonly performed on circular hollow sections (CHS) but improper flattening can cause cracking and weak points in structural components [133], [150].

Another shaping process is casting where molten metal is poured into a pre-designed mould and allowed to solidify into the desired shape, ideal for creating complex load-bearing joints due to their seamless nature and low residual stresses. However, custom casting is costly and time-consuming, especially for non-repetitive components, as it requires unique moulds and extensive finishing processes [11], [151]. Mecheter et al. [11] noted that fully customized parts demand high capital investment, increasing project budgets and environmental impact compared to newer methods like additive manufacturing. Casting also presents challenges such as excessive weight, stress concentrations, low precision, lengthy production cycles, and

environmental concerns [118]. Additionally, casting defects - categorized as pouring, inclusion, and cooling defects - can compromise structural integrity (Figure 2.26) [152]. Addressing these issues is essential for ensuring casting quality and structural performance.

While there are various ways of fabrication using conventional techniques, these methods pose several limitations, initiating from the idea that the development of a single part requires several different procedures to finish, which makes them unsuitable for low-volume, highly customized products [125].

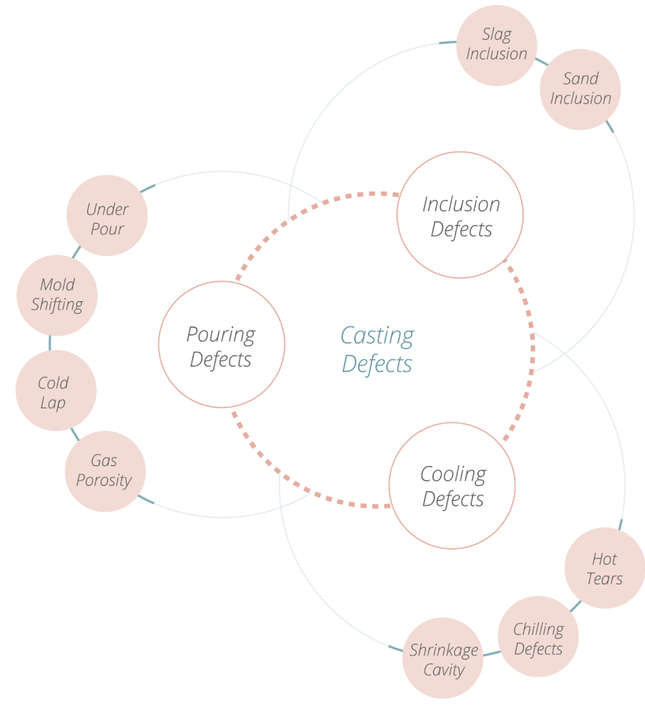


Figure 2.26 Casting defects

2.4.2 Additive Manufacturing process

The American Society for Testing and Materials (ASTM) [153], defined Additive Manufacturing (AM) as "the process of joining materials to make objects from 3D model data, usually layer upon layer". Additive manufacturing has enabled the fabrication of intricate structures that were previously difficult to achieve, with less post-processing and material wastage in comparison to conventional methods [154]. The advancements in AM opened the platform for various developments, particularly in employing lattice structures in various industries [155].

AM can enhance worker safety by reducing on-site labour in extreme environments and automating tasks. It also streamlines the supply chain by enabling on-demand production of customized components, cutting down lead times. As the industry struggles to find skilled workers, AM could lessen the demand for traditional trades while creating new jobs with different skill requirements. Additionally, AM can reduce the need for formwork in concrete construction, lowering costs, waste, and labour. It also allows for the creation of complex geometries that are difficult to achieve with traditional methods, offering new design possibilities without sacrificing efficiency. These potential benefits highlight the need for further exploration of AM technologies in construction [156].

AM integrates well with 3D models produced in Computer-aided Design (CAD) software, allowing for rapid prototyping of parts. A typical AM process includes a print file as a CAD model that is sliced into layers to be fed into the AM machine using a specific format of Standard Tessellation Language (STL) [157]. The STL format depicts the geometry of the model as a tessellation of triangles (also referred to as Standard Triangulation Language) to feed into the printing machine, communicating how the fabrication should physically take place [153]. This layering of the model defines the process from start to finish, culminating in the final product. Typical manufacturing methods involve

material deposition using a print head and a nozzle [153]. ffThe thickness and width of each layer depend on the type of AM process and material used, and the final product typically showcases the layer-by-layer build.

Today, a broad range of AM fabrication technologies and techniques are available that accommodate the fabrication of components from a micro-scale (parts that are a few centimeters in size) to large scale objects (parts that are several feet in length). A common aspect of all types is that they allow mass personalization, accommodating to various designs [158]. The processes that allow metal components to be additively made are discussed below.

Material extrusion (MEX)

Metal extrusion, also known as metal MEX, is defined by ISO/ASTM 52900: 2021 standard [159] as a process that uses a nozzle to selectively dispense material (Figure 2.27). It utilizes powdered metal and polymer binders to create a typical layer-by-layer print of a "green part". After printing completes, a de-binding process is performed to remove polymers from the green part to form a "brown part", followed by sintering to produce a unified metal product. MEX allows the use of various metals such as stainless steel, titanium alloys, nickel alloys, cobalt, and aluminium alloys [160], [161]. The advantage of using this method is that it is simple and cost-effective [162], allowing for the fabrication of multiple materials. However, it offers limited part resolution, poor surface finish [61] and a significant amount of the part shrinks in the furnace during sintering [163], leading to residual porosity [164]. Golab et al. [164] identified that the components produced by MEX have poor dimensional accuracy, which makes MEX unsuitable for structural applications as its limitations can impact the strength and precision of fabricated parts.

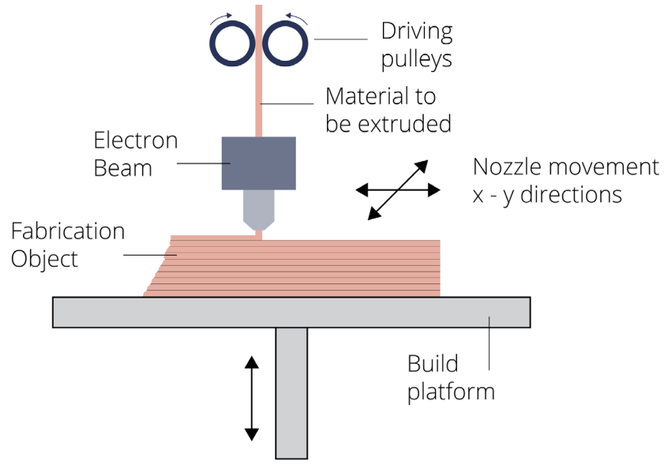


Figure 2.27 Material extrusion system (based on [165])

Binder Jetting (BJT)

ISO/ASTM 52900: 2021 [159] describes Binder Jetting (BJT) as a process that uses a liquid agent that is selectively deposited to join powder materials together. The binder must flow well, soak into the powder, hold parts together, and burn off cleanly [166]. The process employes a print head that selectively jets the liquid agent onto the powder material, adhering it according to the desired cross-section, and progressively builds the object layer-by-layer (Figure 2.28) [167]. The non bound powder provides support to the structure, allowing to fabricate complex geometries. BJT offers fast, low-cost production with full colour options with minimal oxidation and residual stresses, or phase changes due to room temperature fabrication, making the powder highly recyclable [166], [168]. However, achieving full density is challenging, with parts typically having 50–60% relative density and between 2.7–16.4% porosity, requiring post-processing like sintering or infiltration [169], [170]. Shrinkage during sintering can cause distortion due to uneven heating and

stress buildup [169]. High surface roughness and low dimensional accuracy further limit BJT's suitability for load-bearing structural components [61], [166], [169].

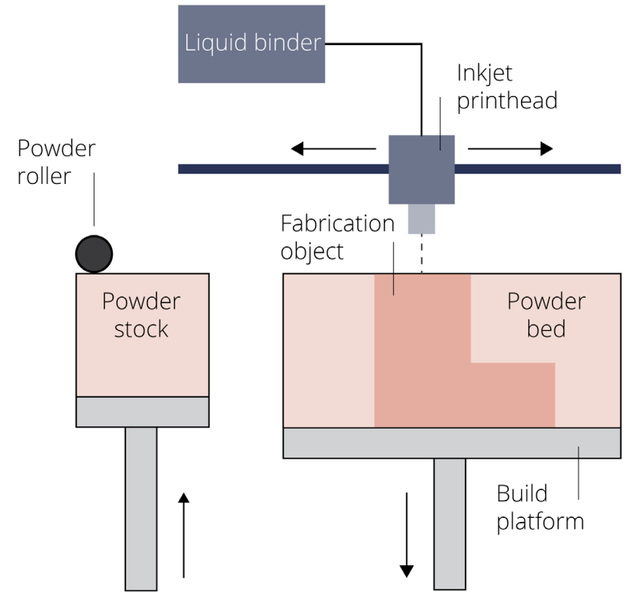


Figure 2.28 Binder jetting system (based on [171])

Powder Bed Fusion (PBF)

Powder bed fusion is a commonly utilized method of additive manufacturing for industrial purposes, that uses various sources of heat such as laser beam, electron beam, and infrared beam [172], [173]. As per the ISO/ASTM 52900: 2021 [159] standard, PBF is an additive manufacturing process that employs thermal energy to selectively fuse the regions in a powder bed (Figure 2.29).

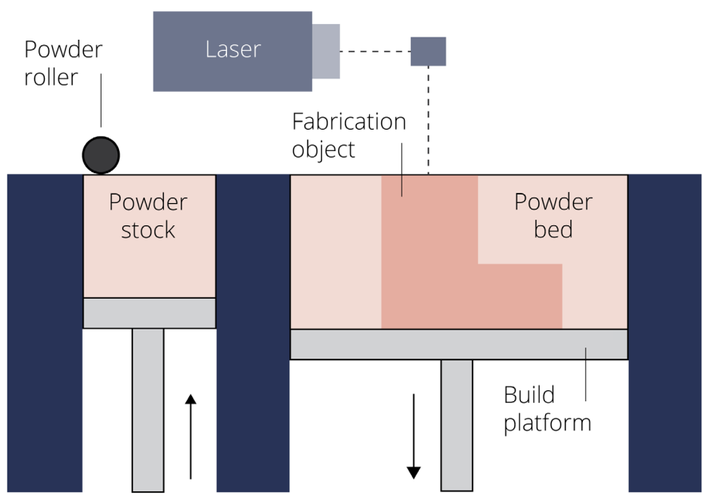


Figure 2.29 Powder bed fusion system (based on [171])

The process of Powder Bed Fusion is sub-divided into other processes based on the techniques employed. Selective Laser Sintering (SLS) uses lasers, commonly CO_2, to sinter powdered materials in an inert atmosphere. Surface finish and resolution depend on powder type and particle size [159], [173], [174]. Electron Beam Melting (EBM) has a tungsten filament electron beam in a vacuum, suitable for reactive materials like titanium. It offers high energy efficiency, minimal thermal deformation, and faster scanning speeds but cooling rates vary with layer deposition [173], [175]. Selective Laser Melting (SLM) fully melts metal powders (titanium, steel, aluminum) in an inert chamber with argon or nitrogen to reduce oxidation. The parts produced have a strong adhesion to the base to avoid any distortion due to stress while printing due to which parts with cantilevers are to be avoided [176]. Direct Metal Laser Sintering (DMLS) is similar to SLM but sinters rather than melts powder, enabling the use of metal alloys without binders. DMLS offers high accuracy

and strength but often requires post-processing due to surface roughness [173], [177], [178], [179].

While the PBF method allows for easy prototyping in a range of materials, it is a time-consuming process due to slow speed with limitations in sizing and structural properties of the materials [180]. The build volumes for PBF systems are typically limited to around 300 × 300 × 400 mm, with larger industrial machines reaching 500 × 500 × 500 mm. This restriction makes it challenging to fabricate large structural components in a single print, requiring part segmentation and assembly, which introduces weak points and compromises structural integrity [181].

Sheet Lamination (SL)

Sheet lamination is a process in which material sheets are bonded together to form parts (ISO/ASTM 52900: 2021) [159]. The process system is highlighted in Figure 2.30. It includes two categories: Ultrasonic Additive Manufacturing (UAM), which uses metal sheets and allows wire embedding but retains only 70% of the original material strength [174], [182], and Laminated Object Manufacturing (LOM), which uses paper or foils bonded with adhesives with no melting requirements [183]. SL can produce larger and curved parts using a curved mandrel, which helps reduce stress concentrations [182], [184]. However, SL has limited structural quality, with weak interlayer bonding often needing curing, heat treatment, or machining [189], [191]. The process also generates significant waste and is time-consuming. The bonding strength also varies by lamination technique, with adhesive-based bonds sometimes insufficient for long-term durability [183]. These challenges make SL less suitable for load-bearing and high-precision structural components.

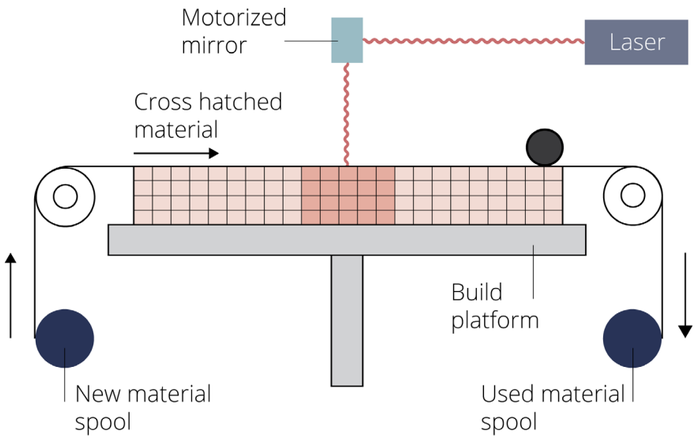


Figure 2.30 Sheet lamination system (based on [171])

Direct Energy Deposition (DED)

ISO/ASTM 52900: 2021 [159] defines DED as a process in which melted materials are fused together as they are being deposited, using a focused source of thermal energy such as a laser, an electron beam, or a plasma arc (Figure 2.31) [174]. DED machines are similar to a five-axis CNC milling machines, with the addition of an extrusion-like tool head [185]. The source material, in a powder or a wire form (0.25–0.5 mm), is deposited in a controlled chamber to reduce oxygen concentration or in a vacuum for electron beam [174], [186]. Multi-axis robotic arms enhance DED by enabling complex geometries and repairs [174].

Key DED types include Wire Arc Additive Manufacturing (WAAM) for large components with high deposition rates, Laser Metal Deposition (LMD) for precision applications, Electron Beam Additive Manufacturing (EBAM) for high deposition in vacuum environments (has high operational costs), and Wire

Laser Additive Manufacturing (WLAM) for balancing precision and efficiency. Its versatility in handling different materials and ability to produce mechanically strong components make it favoured heavy industry applications. While DED supports large parts and various materials, it also results in rough surface finishes and lower resolution compared to PBF, requiring precise control of energy input, feed rate, and head movement [187].

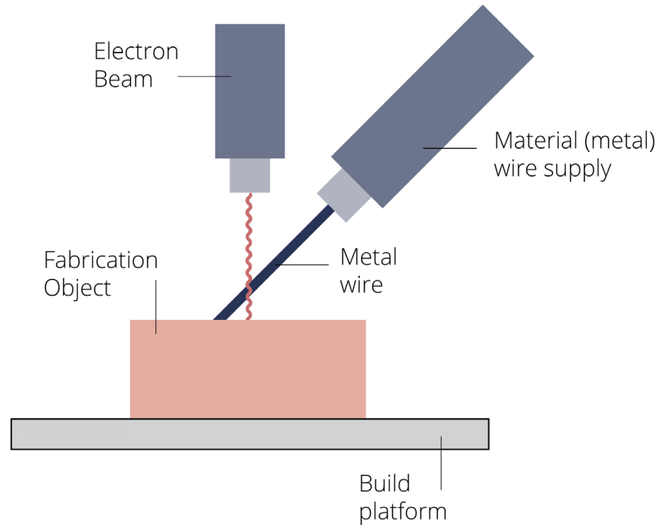


Figure 2.31 Direct energy deposition system (based on [171])

2.4.2.1 Role of Additive Manufacturing in prototyping

AM has significantly impacted prototyping by reducing development cycles, allowing for iterative design modifications, and facilitating the production of geometrically intricate structures that traditional manufacturing methods struggle to achieve [188]. While the above methods focused solely on

metal AM techniques, a commonly used AM technique is Fused Deposition Modelling (FDM), that uses plastic and polymer-based filaments to fabricate parts [189]. FDM is widely used due to its affordability, ease of operation, and ability to produce both functional and aesthetic prototypes with high dimensional accuracy [190]. The primary advantage of FDM is its ability to create customized, low-cost prototypes that aid in product development and testing [188], [190]. The technique is frequently used for rapid prototyping due to its capability to quickly iterate designs and manufacture functional parts before final production [190].

FDM builds objects layer by layer by extruding thermoplastic filaments through a heated nozzle [188], [191]. The filament is melted and deposited onto a build platform as thin strands following a digital model, creating a solid structure as it cools and solidifies [188], [192]. The printing process involves three primary stages: pre-processing, printing, and post-processing [193]. During pre-processing, a digital 3D model is sliced into layers, and the tool path is generated in form a G-code using slicer software [188], [194]. Slicer programs also offer features like custom supports, infill patterns, and print optimization settings [188], [194]. The printer then follows these instructions to deposit material layer by layer [195]. Post-processing may include support removal, surface finishing, or additional strengthening treatments [188], [194].

FDM printers support a variety of thermoplastic materials, including polylactic acid (PLA), acrylonitrile butadiene styrene (ABS), polyethylene terephthalate glycol (PETG), and thermoplastic polyurethane (TPU) [191], [193], [194]. ABS is preferred for applications requiring higher impact resistance and durability, while PETG offers a balance between PLA's ease of use and ABS's toughness [188], [194]. PLA is the most commonly used material due to its biodegradability, ease of printing, good surface finish, and high stiffness, making it suitable for visual and conceptual prototypes [188], [190], [193]. Additionally, PLA , which is made from fermented glucose, does not emit harmful fumes during printing, making it a safer option for indoor use [188], [194].

Optimizing FDM print parameters is crucial for achieving high-quality prints with PLA. Print speed, layer height, bed temperature, and nozzle temperature all influence the final print's strength and accuracy [192], [193], [195]. As per literature, a typical nozzle temperature range between 190-230 ^{o}C was observed [191], [193], [194], [195], with the print bed temperature ranging between 50-80 ^{o}C [188], [191], [193], [194]. Ideal print speeds were seen to between 30-90 mm/s, set as per the complexity of the print [191], [193], [194]. The typical layer height was set between 0.1-0.3 mm. Further, infill densities typically ranged between 10% –100% depending on the required part strength and weight [191], [193], [195]. Lower infill percentages reduce material use and print time, while higher infill improves structural integrity [190], [195].

Additionally, support structures play a critical role in FDM printing, especially for complex geometries with overhangs. The two main types of supports are breakaway supports, which can be manually removed, and dissolvable supports, which dissolve in a liquid solution [188], [190]. The supports can be configured in the slicer program, and printer builds them with weaker, which can be removed easily by breaking them away with hands in PLA printing [188].

2.4.2.2 Environmental and economic sustainability

When evaluating new technologies, particularly in the construction sector, the environmental impact and sustainability are critical considerations. The construction industry significantly contributes to global carbon emissions, with around 40% of the carbon footprint attributed to building activities [196], [197]. A substantial portion of this is due to the CO_2 embodied in construction materials and structural systems, with steel being a significant contributor [198].

While conventional steel fabrication is energy-intensive and generates significant waste, particularly due to complex joint fabrication, metal AM

presents an alternative by allowing the creation of complex geometries in a single process, potentially reducing material waste and energy consumption [199]. AM provides significant environmental and economic benefits, particularly for low-volume production. By creating parts layer-by-layer, AM minimizes material waste compared to traditional subtractive methods, which often involve substantial material loss. This reduction in waste leads to lower energy consumption and greenhouse gas emissions during production [200]. Additionally, AM benefits the environment by reducing pollutants, which are evident in a typical subtractive manufacturing process due to the use of harmful chemicals in casting release compounds, cutting fluids, and forging lubricants [201].

Additive Manufacturing has transformed recycling, reuse, remanufacturing, and repair, all key components of a sustainable circular economy. Unlike traditional recycling methods that require massive, centralized facilities, AM enables localized recycling, minimizing transportation costs and mitigating carbon emissions. Localized recycling in the context of AM is the ability to reuse and repurpose waste materials directly at or near the point of production, limiting the need for centralized recycling facilities. In metal AM over 95% of unused powder can be locally filtered and reused, while only a small fraction needs to be processed in centralized recycling plants [202]. For instance, AM effectively recycles materials like plastics and metals, allowing their reuse with minimal loss in quality. Additionally, AM facilitates the direct reuse of products at the end of their life without the need for recycling, which helps conserve resources and minimize waste. Prasad et al [203]. found that the transportation-related emissions for AM-produced parts are 55 tons of CO_2 per ton of material, compared to 1375 tons for conventional manufacturing (CM), leading to a 25-fold decrease in emissions due to shorter supply chains and decentralized production.

Studies have been conducted to comment on the environmental impact of AM. However, not having an extensive portfolio yet means that there is not

enough data on the Environmental performance of metal AM. There is little literary evidence currently available that has taken the initiative to gather data using Life Cycle Assessment (LCA) or through works conducted in other literature. Sice and Faludi [185] compared the environmental impacts of additive manufacturing and conventional manufacturing (CM), stating that AM presents both Environmental advantages and challenges compared to CM. Using LCA they found that AM typically consumes more energy, particularly with metals, due to the high energy demands of processes like SLM and EBM. However, AM can offset some of this energy consumption by eliminating intermediate production steps, thus reducing tooling impacts. AM also produces lightweight structures, which means that if required, they are easier to transport in a shorter time, contributing to lower environmental impacts [200].

Sice and Faludi [185] further elaborated on studies such as those by Priarone et al. [204] and Torres-Carrillo et al. [205], which demonstrated that while AM might have higher processing impacts, its benefits can become apparent when considering material savings and part design. For instance, the material impacts of metals like titanium can sometimes outweigh the processing energy. AM is advantageous with intricate or thin-walled designs, whereas CM is generally more efficient for manufacturing simple solid components. It causes the comparison between AM and CM to be a complex process, especially because one is an additive process and the other is subtractive, with each excelling in different contexts.

Sice and Faludi [185] concluded that to enhance the sustainability of AM, it is crucial to design parts that minimize print time and material usage, maximize printer utilization, and choose materials that reduce both embodied impacts and processing energy. Future improvements in AM could potentially surpass CM in sustainability, provided that standardized metrics for reference parts and system boundaries are established.

Further, AM presents significant economic impacts characterized by its cost structures and productivity. Key technologies such as EBM and DMLS demonstrate that machine productivity is crucial for controlling manufacturing costs. Economically, the Life Cycle Costing (LCC) analysis shows that DMLS is more cost-effective for parts with high geometric complexity, whereas conventional CNC is more economical for large-scale, simpler parts [11]. AM also introduces significant economic benefits by reducing idle time, minimizing material waste, and potential reductions in transportation energy costs [201].

However, the industry faces challenges in integrating design for AM, as many companies find it difficult to define cost-effective business cases and measure the value of AM compared to traditional methods. The global AM market is projected to grow substantially over the coming years. This growth reflects AM's increasing economic significance, fueled by its applications in consumer products [201]. As AM technology evolves, it is expected that improvements in system productivity and scaling up will reduce costs and enhance competitiveness [206].

2.5 Wire Arc Additive Manufacturing (WAAM)

Wire Arc Additive Manufacturing (WAAM) is a process that uses a wire feedstock to fabricate metal products through the Directed Energy Deposition (DED) method. This technique uses an arc to melt the metal wire (also known as DED-arc) [207], creating new layers on top of the previously formed ones [208], transforming the welding robot into a large-scale 3-D printer [209], The electric arc acts as a heat source to continuously melt the wire during the fabrication process. WAAM utilizes standard welding equipment rather than specialized additive manufacturing tools and materials, including a power source, welding torch, wire, and protective gas systems, integrating them with robotic or CNC systems for torch movement (Figure 2.32) [210].

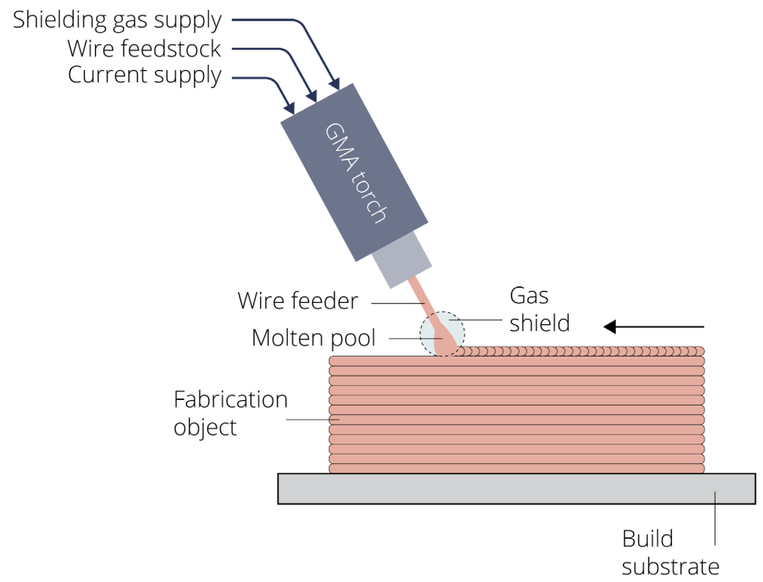


Figure 2.32 Wire Arc Additive Manufacturing system (based on [211])

WAAM systems are either machine tool-based or robotic arm-based with at least a 3-axis approach, with the availability of multiple power sources [207]. Additionally, WAAM supports a broad range of materials, including steel, aluminum, titanium, and nickel alloys, making it highly versatile. Unlike subtractive manufacturing methods, which generate substantial material waste, WAAM deposits only the required material, leading to improved resource efficiency [210].

Knezović and Topić [210] stated the WAAM process in detail, explaining that the WAAM process begins with designing a 3D CAD model using specialized software or reverse engineering methods like 3D scanning. This digital model

is then converted into a standard file format, typically .STL, and sliced into multiple 2D layers. These layers serve as the foundation for generating the toolpath, which dictates the movement of the welding torch during deposition. Once the toolpath is established, key welding parameters such as voltage, current, wire feed rate, travel speed, and shielding gas flow are carefully selected to ensure optimal material deposition. During the deposition phase, the first layer of material is applied to a baseplate, and subsequent layers are built up in a controlled manner, following the predefined toolpath.

Most materials use MIG (Metal Inert Gas)/ MAG (Metal Active Gas) equipment for deposition, since their low-heat-input system facilitates WAAM processes better. An inert shielding gas is used in MIG that does not interfere with the welding, whereas MAG, being the more common type of welding system, has an active shielding gas, such as carbon dioxide or oxygen, that contributes to the welding [212]. WAAM itself has different methods of fabrication, such as Gas Metal Arc Welding (GMAW), Gas Tungsten Arc Welding (GTAW), and Plasma Arc Welding (PAW). The latter two have a tungsten electrode for melting, while the former uses welding wire as the electrode [213]. WAAM has the advantage of having a higher deposition rate, ranging from 1-10 kg/hour or more [207], effectively utilizing materials, while being more cost-efficient compared to other DED processes [208]. Cost reductions come about more because the fabrication does not require enclosed inert chambers or a vacuum environment, nor are there safety concerns as with powder processes [213].

WAAM technology facilitates the production of large-scale parts, in comparison to other AM systems, hence allowing the fabrication of products for the structural and construction industry [207]. The cooling rate for WAAM is much less than those using an electron beam or a laser source [211]. The surface finish of the product generally has a waviness to it, that may require post-processing such as heat treatment or machining of the outer layer if a smoother finish is required [211]. The waviness retains to 1 mm thickness regardless of the part size, therefore, material efficiency is enhanced if the

part is enlarged [207].

From the WAAM processes available, Gas Metal Arc Welding-based Additive Manufacturing (GMAW-AM or GMAAM) is most suitable for creating larger geometries with some structural complexity [214]. The equipment used is comparatively lower cost and employs a direct current reverse polarity (DCRP) system in which the electrode is connected to the positive terminal, while the part under fabrication is connected to the negative terminal of the power being supplied. This generates higher heat at the electrode level and lower at the product level, creating a flow of charged ions from the electrode to the substrate. GMAW products also proved to have two to three times higher production rates in relation to their counterparts such as GTAW and PAW [214], whereas the energy efficiency of both GMAW and GTAW can be more than 90% [211].

WAAM also has a significantly lower Buy-to-Fly (BTF) ratio than traditional manufacturing methods. BTF ratio measures material utilization efficiency by comparing the initial mass of raw material used to the mass of the final component. Traditional manufacturing methods often have high BTF ratios, such as 10:1 or 20:1, meaning that for every 10 kg of raw material, only 1 kg is used in the final product, indicating significant material waste [215]. WAAM significantly lowers BTF ratios by depositing material only where needed, resulting in BTF ratios as low as 1.2:1 and 1.5:1 for certain components [215], [216]. A lower BTF ratios translate into reduced material waste and costs, making WAAM more suitable for high-performance applications.

2.5.1 WAAM layer building and parameters

A critical aspect of WAAM lies in the layer-by-layer deposition, where process parameters and path planning significantly influence the build quality. Various studies in literature studied the complexity of achieving defect-free layers,

laying emphasis on the importance of systematic parameter optimization. Wall et al. [217] studied the fabrication of a WAAM wall, highlighting that alternating deposition directions for each layer i.e. from right to left and then left to right, significantly improves the uniformity of the layers and minimizes distortions. This was compared to traditional unidirectional strategies that left behind residual stresses and surface irregularities. Similarly, Michel et al. [218] introduced modular path planning, which segmented layers into smaller sections to manage complex geometries. This approach ensured uniform deposition by tailoring paths for individual sections.

Song et al. [219] also studied WAAM layers, specifically at intersections. The study suggested that overlapping weld beads at intersections allows for better management of heat input and residual stresses, ensuring a uniform deposition through out. They also suggested reversing deposition directions layer-by-layer, similar to the findings of Wall et al. [217], because it enhanced structural stability, mitigating height discrepancies to as low as 0.8%. Furthermore, Adam et al. [220] found that maintaining adequate thickness for each layer was crucial, as thinner walls lacked the structural integrity to support consistent layer formation.

Since WAAM involves depositing layers of material onto a baseplate using an electric arc as the heat source, it can result in significant thermal expansion and contraction. With the material being deposited on one side of the baseplate only, these thermal effects can cause warping and deformation, leading to dimensional inaccuracies and mechanical instability [210], [221]. To counteract these issues, Mehnen et al. [214] tested the Balanced Building Strategy, which involves alternating material deposition on both sides of the baseplate. This ensures that thermal stresses are more evenly distributed, significantly reducing the risk of out-of-plane distortion. As each layer is added to one side, a corresponding layer is deposited on the opposite side, balancing the thermal expansion and contraction forces. This technique is particularly useful for producing large and structurally critical components. Mehnen et

al. [214] also experimentally and digitally validated these results using Finite Element (FE) models. In some cases, this strategy can also be leveraged to produce two identical or complementary components simultaneously, increasing production efficiency [210].

Further, these studies also highlighted the impact of varying parameters on the WAAM build. The most critical factors include wire feed rate WFR, travel speed, heat input, shielding gas, and wire selection—all of which directly impact how well the final part turns out [222]. Mohd Mansor et al. [222] delved deeper into the impacts of all the parameters. For the Wire feed rate, which controls how much material is deposited, too slow rate leads to poor bonding while too fast causes the risk of overheating and deforming layers. They further stated that for mild steel, specifically ER70S-6, an ideal Wire feed rate of 5.5 to 7.5 m/min helps achieve smoother, more consistent deposits. For the travel speed, since it impacts the bead shape and thermal cycles, higher speeds reduce defects like porosity, but going too fast can cause poor fusion. Heat Input also needs to be carefully balanced to avoid excessive re-melting or weak bonding [222]. Additionally, the selection of shielding gas also plays a role in in the final geometry of the weld beads. Wall et al. [217] identified that shielding gas composition (in this case a mix of Argon and Carbon dioxide) and wire feed speed directly affected bead geometry and deposition consistency. Whereas Michel et al. [218] laid emphasis on zoning, where parameters were dynamically adjusted within specific regions of a layer, such as thermal hotspots or intersections, allowing for greater control over bead height and width, ensuring uniformity across the build.

2.5.2 Geometric variability of WAAM deposited layers

While WAAM offers great capabilities for large scale fabrication, certain parameters need to be monitored to achieve the desired result. This includes an assessment of the weld pool and bead width to avoid rundown of

molten metal, placement accuracy, and maintaining interpass temperature between layers [223]. The weld pool is a critical factor in WAAM, influencing microstructure evolution and mechanical properties [222]. The size and stability of the weld pool are affected by earlier mentioned parameters such as wire feed rate, arc current, travel speed, and shielding gas composition [224]. Studies have demonstrated that excessive heat input results in wider beads, increased dilution, and potential defects like porosity and residual stress [225]. Advanced sensing techniques, such as optical pyrometry and infrared cameras, have been utilized for real-time weld pool monitoring to adjust heat input dynamically [224].

Weld pool dynamics play a crucial role in defining deposition quality. A larger weld pool leads to increased material fluidity, which can cause uneven solidification, whereas a smaller weld pool may result in insufficient fusion between layers, leading to weak interlayer bonding [224]. The interaction between the weld pool and cooling rates dictates grain structure formation, which subsequently impacts mechanical performance [226]. While FDM deposits softened filament with a predictable bead size and shape, WAAM fully melts metallic feedstock wire through a welding arc (Figure 2.33).

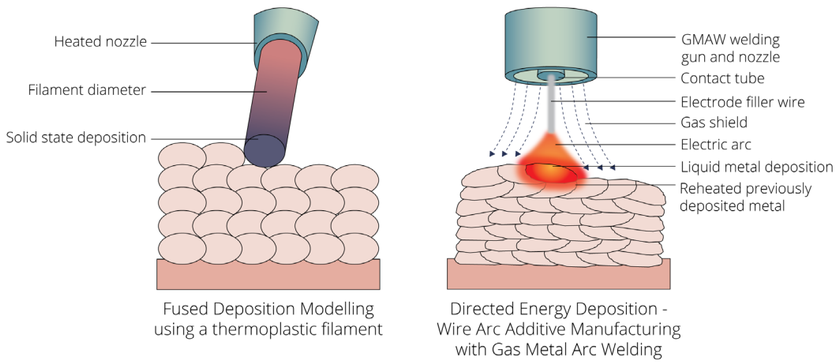


Figure 2.33 Comparison between FDM and GMAAM process (based on [209])

Huang et al. [227] described the character of the weld beads formed in the process. The weld beads are stacked to create the final workpiece, resulting in a surface with a distinct undulating pattern, resembling an ideal half-wave sinusoidal signal, accumulating weld bead layers with regular and periodic characteristics. This introduces much variability in the material's final form (Figure 2.34), influenced by factors like the type of metal alloy, the weld pool's behaviour, shielding gases, heat input, and how the molten metal moves and cools. Additionally, the local temperature, the shape of the surface it's being deposited onto, and gravity create an impact. Because of these variables, the transition from CAD design to printing with WAAM requires careful planning and precise control to ensure the process works as intended [209].

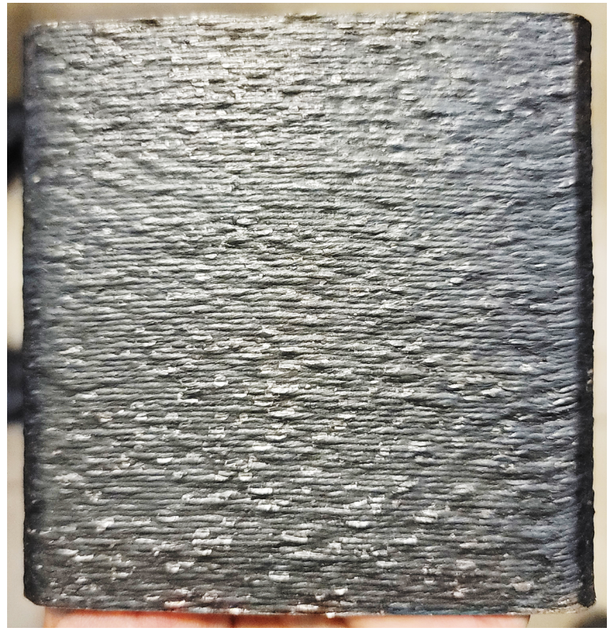


Figure 2.34 Geometric variability of the weld pool

Although there are studies and some advancements in maintaining the weld pool, challenges persist in sustaining consistency in multi-pass welding, especially for intricate geometries requiring variable energy input [228]. Existing monitoring systems need improved accuracy for predicting and compensating for thermal fluctuations [224].

In addition to the weld pool, weld path planning is also crucial in determining the structural integrity and geometric accuracy of WAAM components [228]. The choice of path directly influences layer height consistency and bead width. Advanced weld path planning methods incorporate adaptive toolpath generation, where algorithms dynamically adjust deposition trajectories based on real-time process parameters and component geometry [10]. One of the primary goals of such strategies is to optimize heat dissipation and reduce residual stresses, which directly influence material performance. Studies have shown that adaptive multi-directional toolpaths can significantly improve build efficiency and reduce thermal distortion [222]. In complex geometries, hybrid path planning approaches, such as combining linear and oscillatory paths, are being explored to enhance mechanical uniformity. These methods ensure that deposited layers achieve maximum adhesion with minimal internal defects [222].

All these investigations around weld paths proposed the use of effective path planning strategies to minimize heat accumulation and residual stresses. Each of these studies carried out various experiments to achieve the correct parameters that produced to achieve uniform deposition and structural stability. The parameters are material and robot specific and need various test runs to understand how changing the composition of shielding gas, wire feed speed, and travel speed impact the fabricated objects. However, challenges remain in achieving precise control over deposition paths for highly curved and intricate structures. Another major issue is the incomplete understanding of residual stresses, distortion, and material microstructure in WAAM studies, which limits its effectiveness [229]. Experimental setups often do not fully use

the technology's potential, with the machinery often lacking advanced features like multi-axis movement and sophisticated path planning capabilities [229].

In view of the weld pool and weld path management, various studies in literature were reviewed. Studies that conducted WAAM experiments showed that the majority of them have primarily focused on fabricating small-scaled and linear weld paths, straight walls, or cylindrical/arc type structures, including ring-shaped components [15], [215], [221], [225], [228], [230], [231], [232]. These geometries allow for relatively predictable thermal control. Walls have been extensively studied due to their direct application in structural elements, while cylindrical and ring-shaped components are common due to their symmetry, which allows uniform heat dissipation and stable deposition conditions [222].

However, research on more complex curvature conditions, such as path planning and weld pool adjustment in overhanging curved surfaces and freeform geometries is lacking. WAAM is inherently incompatible with support structures, making the impact of gravity on achieving thin-walled angled surfaces a crucial factor. Key challenges in such cases include the effects of gravity, material drooping, and insufficient interlayer bonding when printing fully curved surfaces and overhangs [232]. Therefore, gravity-induced distortions remain a significant obstacle when fabricating unsupported curvatures.

2.5.3 Mechanical anisotropy in WAAM

Anisotropy, as defined by Yusuf Khan [233], refers to a material property where its characteristics vary depending on the direction (x, y, or z axis). In terms of mechanical behaviour, this means that a material may respond differently to forces like compression or tension depending on the axis in which the force is applied. Unlike isotropic materials, which have uniform properties in all directions [234], anisotropic materials exhibit different strengths, ductility, and toughness along different orientations due to their

internal microstructural characteristics [235]. This behaviour arises from factors such as grain alignment, phase distribution, and defects introduced during manufacturing processes, particularly in metal AM, where layer-by-layer deposition significantly affects material behaviour [234], [235], [236]. In this case, anisotropy becomes a critical concern due to the inherent directional solidification and thermal gradients produced during deposition [237].

Considering anisotropy in WAAM fabricated parts is crucial for ensuring structural integrity and optimizing mechanical performance. Neglecting anisotropy can lead to premature failure in load-bearing applications, particularly when components experience multi-directional stresses [104], [238]. Various strategies have been employed in literature to mitigate anisotropic effects, including heat treatment, rolling, hybrid subtractive processing, and surface finishing techniques [238], [239], [240]. Computational modelling and optimization techniques have also been implemented to predict and control anisotropic mechanical responses in complex WAAM structures [104], [235], [237].

However, several gaps in the literature persist regarding its structural implications, particularly in how existing structural design codes fail to incorporate anisotropic material behaviour effectively. Laghi et al. [241] emphasized that the absence of standardized constitutive models for WAAM results in limited applicability in engineering designs, as current structural standards do not account for directional mechanical variations. Similarly, Mishra et al. [242] highlighted that while topology optimization strategies show promise for improving stiffness and mechanical performance, their integration into real-world structural design frameworks remains largely unvalidated due to the lack of experimental verification on large-scale WAAM structures. Hadjipantelis et al. [234] further noted that the absence of established mechanical property databases for WAAM materials complicates efforts to integrate anisotropy into engineering codes, making it difficult to predict structural behaviour with certainty. These gaps hinder the full adoption

of WAAM in critical structural applications.

WAAM components predominantly have orthotropic anisotropy, which means that they exhibit distinct mechanical properties in three principal directions: WAAM-L (longitudinal direction), WAAM-D (diagonal direction), and WAAM-T (transversal direction) [104]. These classifications are essential for understanding mechanical performance variations, as deposition direction often exhibits weaker mechanical properties due to incomplete fusion and interlayer defects [241], [242]. The directional impact on WAAM parts significantly influences their final mechanical properties and overall performance. Tensile strength and elongation are commonly superior in the longitudinal direction (WAAM-L) due to the columnar grain growth along the deposition path, while the diagonal direction (WAAM-D) often exhibits reduced strength and increased failure susceptibility along interlayer regions [234], [236], [241].

While existing studies provide insight into tensile and compressive performance along WAAM-L, WAAM-T, and WAAM-D directions, they do not sufficiently explore the combined effects of torsion, bending, and dynamic loads that are critical in real-world structures. Mishra et al. [242] highlighted that most experimental studies assess WAAM anisotropy under controlled laboratory conditions, whereas large-scale applications experience significantly more complex stress interactions. This gap in research limits the ability to accurately predict long-term mechanical behaviour, fatigue resistance, and failure mechanisms of WAAM components subjected to multi-directional forces [241].

Laghi et al. [241] introduced an orthotropic elastic model for WAAM stainless steel, showing that mechanical properties vary significantly between WAAM-L, WAAM-T, and WAAM-D. Their findings confirmed that Young's modulus in diagonal directions can be up to two times higher than in longitudinal or transversal orientations, indicating strong anisotropic elastic behaviour which

is significant for multi-axial loading due to higher stiffness. The Young Modulus is the measure of a material's stiffness, showing how easily it can be stretched or bent, making it crucial to predict the materials response to stress accurately. It is calculated by dividing the stress (force applied) by the strain (how much the material stretches compared to its original length). This property is important for designing structures to ensure that the part can handle stress without deforming. While Laghi et al.'s [241] findings state that this can be beneficial for improving stiffness in specific load-bearing applications, it also poses challenges due to uneven mechanical properties across different orientations. On one hand, a higher Young's modulus in WAAM-D enhances rigidity, reduces deformation, and can be strategically leveraged in topology optimization. However, it also creates structural weaknesses in WAAM-L and WAAM-T, increasing failure risks under multidirectional loading [104], [238]. Therefore, deposition path planning and post-processing treatments are crucial to mitigating these effects and ensuring optimal material performance.

Further, recent studies have highlighted that anisotropy in WAAM can be optimized using topology optimization techniques that simultaneously adjust the deposition path direction and structural layout [242]. Research by Mishra et al. [242] demonstrated that aligning deposition paths with the structural load directions significantly improves material stiffness, achieving up to 53% higher stiffness compared to traditional deposition strategies. This suggests that WAAM components should be designed with optimized print orientations to maximize mechanical performance. However, despite the advancements in topology optimization and predictive modelling, experimental studies validating these approaches under realistic structural load cases are insufficient, further complicating the integration of WAAM fabricated parts into high-performance structural applications [242], [243].

Moreover, Ma et al. [243] examined WAAM processed magnesium alloy and found that while tensile strength in WAAM-T was slightly higher than in

WAAM-L, there was no significant difference in hardness, elongation, or yield strength. This suggests that anisotropy in some WAAM fabricated materials can be relatively low, depending on microstructural evolution and process parameters. However, current computational models for WAAM anisotropy focus predominantly on simple geometries such as plates and single walls, failing to account for the complex geometries used in large-scale structures, such as trusses and multi-axial support systems.

In conclusion, mechanical anisotropy in WAAM is an inherent characteristic that significantly impacts material performance and structural reliability. The directional dependence of mechanical properties necessitates careful consideration in both design and manufacturing stages. By understanding and addressing anisotropic effects through process control, material selection, and post-processing strategies, WAAM can achieve higher structural reliability and performance in critical applications.

2.5.4 Current trends and applications

The construction industry is still new to the involvement of AM in its processes. Preliminary research indicates that employing AM in construction can significantly cut labour expenses, reduce material waste, and allow for the creation of intricate, customized designs that are difficult to achieve with conventional methods [156]. AM presents the possibility of designing structures with optimized loads [229]. The use of aggregate-based materials is the most common additive construction process. A noteworthy example of this is the Castilla-La Mancha 3D bridge in Madrid Spain, spanning 6.5m in length with a 3.5m width. Similarly, a Chinese company, Winson, developed a two storey (1,100m^2) 3D printed house, that took only a day to develop in the factory and two days to assemble on site [15]. There are also other works in this area of producing complex wall elements, components for a single-floor office building, and a curved bench in Loughborough University, etc. [244].

In contrast, the application of AM in metal construction is less widespread, though initiatives are underway by some companies for advancing this technology for structural design. In the Netherlands, Arup extended its streetlight design by creating nodes with unique geometries for an angled steel structure with tension cables (Figure 2.35). Due to the distinct design of each node, creating 1,200 nodes through manual cutting and welding would have been time-consuming. Instead, they employed AM technologies to 3D print the nodes, achieving faster production and higher quality. This approach also allowed the addition of intricate details through topology optimization that would be impossible to achieve through conventional means [245].

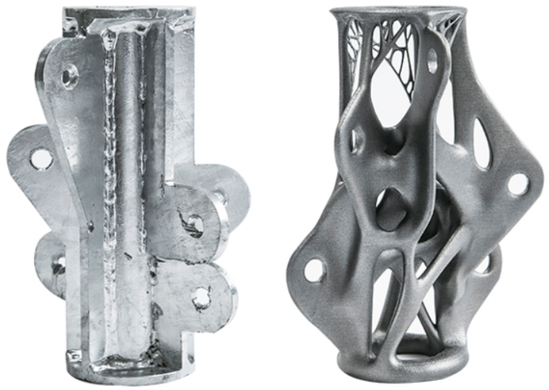


Figure 2.35 Steel node design by Arup – Left: Conventional design, Right: 3D printed design [245]

Perhaps the most notable works in progress are by MX3D, an Amsterdam-based AM company that has pioneered metal printing for structural developments. A prime example of their work is a 12 m long stainless-steel pedestrian bridge (Figure 2.36) completed offsite in Amsterdam in collaboration with Arup.

The bridge is designed to withstand up to 20 tons of weight without failure. 3D printing of the bridge also allowed the integration of a sensor network to collect structural data such as strain, displacement, and vibration, and environmental data such as air quality and temperature, aiding in monitoring bridge health in real time. This data is fed into a digital twin of the bridge to gain valuable insights for future metal AM structures. The use of AM allowed for a unique design and the incorporation of functionalities that would be otherwise impossible to achieve [246], [247].



Figure 2.36 3D printed pedestrian bridge by MX3D [246]

An additional advantage of AM in such a construction process is that it reduces the need for labour, thus lowering labour costs. The printing is carried out using a robot with no material waste and without the requirement of site clearing or cleaning. It also minimizes noise pollution in public spaces and avoids disrupting the public, a significant benefit compared to conventional construction methods, which would take much longer to complete.

MX3D has also worked on other architectural projects that demonstrate the use of AM to create distinctive structural forms. A notable project, done in collaboration with Takenaka, one of the largest architecture, engineering, and construction (AEC) firms in Japan, involved developing highly customized and engineered steel joints using the WAAM technology (Figure 2.37). The joint is topologically optimized to use less material while maintaining strength. It consists of a hollow pipelike structure that can provide extra reinforcement if filled with mortar. The connector is 4 mm thick with a mortar filling and achieves the same strength as an 8mm thick connector with 50% less material usage. The joint also successfully passed multiple destructive tests, demonstrating its effectiveness [248], [249].



Figure 2.37 Topology optimized joint concept by MX3D [249]

MX3D is involved in further developing metal AM structures, however, most of the construction industry still relies on conventional practices. If AM is adopted in the AEC sector, we will have a breakthrough in design that is both efficient and cost-effective.

Research presented by Carlos de Oliveira from Cast Conex, and Curt Decker, and Mark Douglass from Lincoln Electric, at the North American Steel Construction Conference (NASCC): The Steel Conference 2024 [250] elaborated on the advancements and versatility of GMAAM in connection design. They highlighted that the principles of GMAAM to deposit molten metal layer by layer produces highly precise, geometrically flexible components without the constraints of moulds used in casting. This process enables the direct reinforcement of connection regions and the elimination of complex welds like TYK joints (Figure 2.38), improving fatigue performance and reducing stress at critical points. Additionally, GMAAM allows for one-off, customized designs, making it ideal for projects with unique or non-repetitive connections. Its ability to produce parts quickly, with better internal quality and minimal voids compared to casting, positions it as a cost-effective and efficient solution for both structural and architectural applications [250].

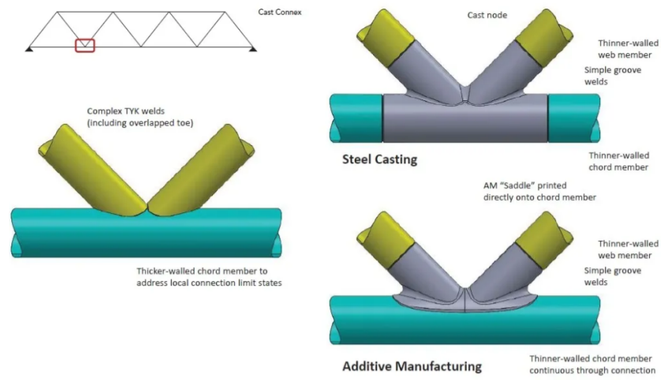


Figure 2.38 AM offers the advantage of cast nodes but with added benefit of eliminating the need to segment the chord [151]

Lincoln Electric further carried about the AM of a saddle connection (Figure 2.39) directly onto the Hollow Steel Section (HSS) chord, ensuring a seamless, highly integrated joint. This method improves structural rigidity while minimizing the need for additional welding or bolting, which are often sources of failure in traditional construction. AM allows for a smoother transition of stress flows within the connection, compared to the abrupt changes in geometry that occur with traditional welding or bolted gussets. As a result, fatigue resistance is significantly improved, making the connection ideal for high-performance applications where dynamic loading is a concern. Furthermore, this approach aligns with modern parametric and generative design workflows, allowing engineers to customize each connection to specific structural requirements without the constraints of standardization imposed by traditional fabrication methods [250].

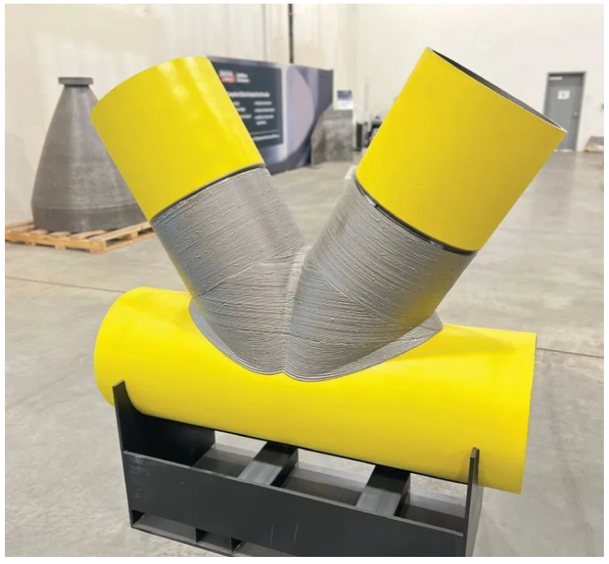


Figure 2.39 An AM saddle component printed directly onto a round HSS member [151]

Overall, AM fulfills the criterion of a fabrication-led design, that emphasizes on the importance of collaboration among architects, engineers, fabricators, and builders from the very beginning of a project. Instead of each professional working independently, this approach fosters a shared understanding of how design decisions impact the construction process, ensuring that the final structure is not only aesthetically pleasing and structurally sound but also practical and cost-effective to build [146]. Since cost is not dependent on the design complexity of the product, AM allows manufacturers to explore new realms of design to create unique products, while minimizing the number of components required [11].

Chapter 3

3. Methodology

This chapter examines the prototyping and manufacturing processes of joints designed specifically for Wire-Arc Additive Manufacturing (WAAM). The methodology includes four phases of study – the joint design (the processes involved in developing connection forms), joint topology optimization (the optimization of the developed forms using automated systems), PLA prototyping (physical study of joints), and establishing the GMAAM procedures based on the expert opinions (Figure 3.1). The research scope of these phases includes both, simulation-based approaches, such as topology optimization algorithms and stress analysis, and an experimental study, including FDM 3D printing and WAAM fabrication, to explore the feasibility and challenges of fabricating complex joint geometries. These methods aim to study how digital analysis and hands-on fabrication methods work together to refine the application of WAAM for complex architectural forms.

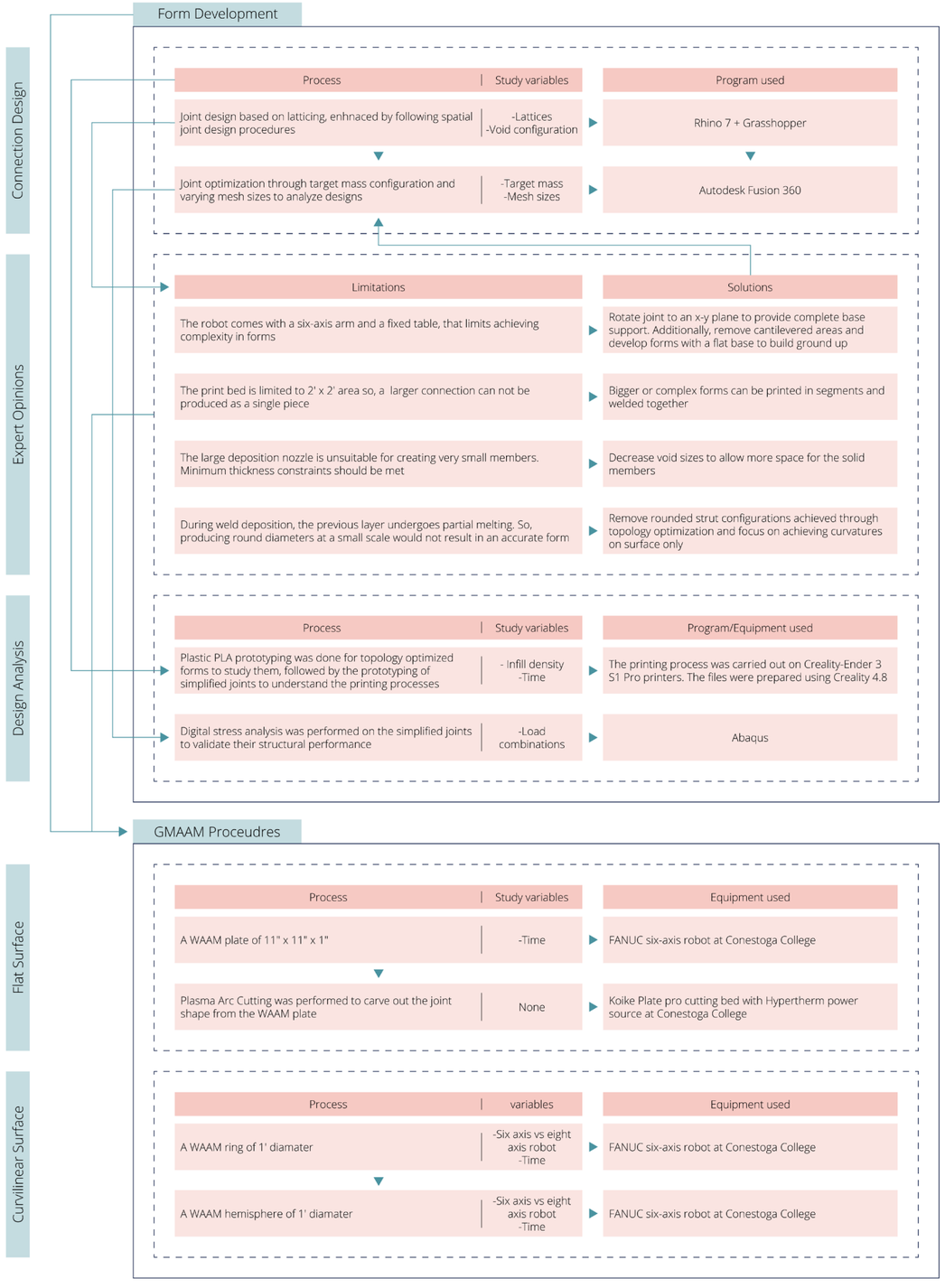


Figure 3.1 Schematic workflow of methodology

3.1 Joint design procedures

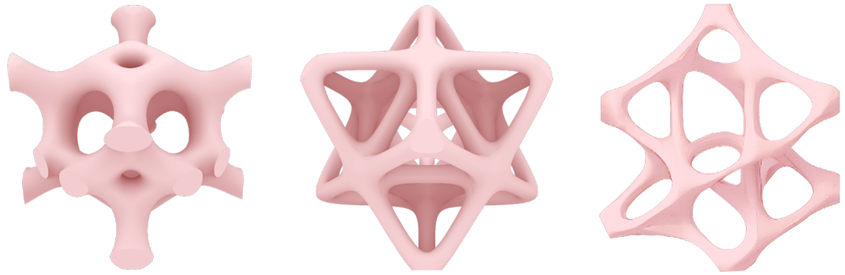
The research focused on configuring a three-way structural connection, intending to break the monotony of a typical structural member connector by introducing topology configuration while ensuring a lightweight design. This approach explored how latticing and optimization algorithms could redefine conventional connection geometries, balancing structural integrity, material efficiency, and aesthetic appeal. By leveraging computational design tools and finite element analysis (FEA), the study examined how material distribution could be optimized while maintaining load-bearing capacity.

3.1.1 Application of biomimicry in design

The inception of the base connection and its iterations lay in the exploration of biomimicry in structural design. From the previously stated studies in literature, one of the most remarkable structural systems found in nature is that of trees, that have evolved to distribute loads efficiently while maintaining structural integrity. Trees consist of a branching system to gradually distribute loads, reducing stress concentrations. Taking inspiration from a tree structure, this research delved into designing a branching joint connection that can be repeated and iterated multiple times along a structure to distribute loads efficiently. Branching connections are also a commonly occurring typology of joints found in various structural application, marking its significance.

The iterations focused on creating porous and lightweight configurations to reduce material use, based on the principles of naturally occurring Voronoi patterns and lattice structures. Various types of lattices generate a variety of designs and due to their repetitive nature, they naturally allow for multiple connection points to support the branching. For this study, a Vintile lattice [85] (Figure 3.2(a)), an Octet lattice [86] (Figure 3.2(b)), and a Voronoi lattice [91] (Figure 3.2 (c)) were used to explore joint options, proceeded by choosing the most suitable lattice in terms of its design functionality to be further

developed in this study. The choice of exploring these options are as follows: Vintile lattices are known to experience a lower deformation under stress and a higher stiffness to strength in comparison to other types of lattices, making it effective to bear mechanical loads. They also reduce stress concentrations that can result in structural failure, making them suitable for structural purposes [85].



(a) (b) (c)

Figure 3.2 Left: Vintile Latticing, Middle: Octet Latticing, Right: Voronoi Latticing – showing multi-branch connection points

Octet lattices are largely observed in the construction sector, predominantly as a truss system in the space frame structure [87]. This structure provides excellent strength-to-weight ratio and rigidity, distributing loads efficiently throughout the structure, making it ideal for applications where minimizing weight while maintaining structural integrity is crucial [251]. They also have a high stiffness and mechanical strength, with a high buckling resistance [252].

Voronoi patterns, a form of stochastic lattice, enhances global lateral stiffness, reducing displacement under wind and seismic loads. The lattices distribute forces more efficiently due to their irregularity [90]. Utilization of Voronoi patterns in structural design allow for efficient use of materials, helping to

identify optimal load bearing distribution network. They can also achieve higher porosity while maintaining strength, and a more uniform stress distribution, reducing the risk of premature failure, making them effective for applications where weight reduction and shock-resistance is required [91].

While latticing consists of various typologies, the study was limited to the choice of latticing to explore a range of designs while maintaining structural integrity. Vintiles consist of both vertical/ horizontal lines along with inclined struts creating an interwoven structure. Contrary to this, Octet only consists of angled struts with no pure vertical or horizontal elements, creating a triangular geometry. Voronoi, on the other hand, represents a completely different spectrum of latticing, with a more organic aesthetic and an irregular structure. Hence, each lattice is unique in their appearance, while also being structurally strong. However, the Voronoi was selected for further examination in this study.

With Voronoi lattice, the study was implemented to create a porous connection design. The organic nature of Voronoi was also more suitable to create varying void patterns. These patterns should work by creating cells around a set of points, that generate varying patterns and therefore, by fixing the number and location of points, the resultant geometry allowed for a more desirable outcome (Figure 3.3).

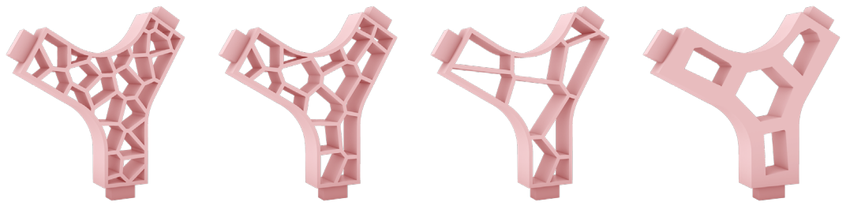


Figure 3.3 Voronoi latticing patterns – Left to right: Dense to light voids

In this application, the number of joint branches within the lattice was limited to three to iterate the joint at a preliminary level for reduced complexity of fabrication. Further, the connection was designed as a single-plane joint, limiting the latticing to a two-dimensional space. The area designated for joint was confined to a 2′ x 2′ perimeter in view of standard economic WAAM robot print bed sizes. Each branch featured a rectangular cross-section of 6″ x 4″ and was oriented at 0°, 135°, and 270° angles (Figure 3.4). The branch angles were based on a typical three-way Y shape connector, that are used for three branch connections.

The number of voids within the connection were also restricted to a total of four – one at each branch and one at the center. These void configurations correlate to the discussions from the literature, where Han et al. [109] applied topology optimization and generative design algorithms on a cross-joint (or four-branch joint). Most of the generated results consisted of a central void, while other iterations included voids at or around the branch that not only minimized material usage, but also ensured structural integrity, optimized stress distribution, and enhanced stiffness-to-weight ratio. Further analysis of their results showed that this placement of the voids aided in distributing loads more uniformly across the structure. The equivalent maximum stress on these joints was also comparatively much lower than those with solid configurations because the placement of voids balanced the load paths, optimizing the stress behaviour.

The central area between the branches, designated as a target mass, was drawn by joining the branches using 8-inch radius fillets to create a smooth transition between them (Figure 3.4). The fillets were necessary to avoid sharp angles at vertices that are more critical to failure – failing in a brittle manner at lower strain levels. Fillets at joints absorb more energy, proving to be more efficient [253]. This central joint piece was designed to be connected to the branches through a lock-and-key joint connection, reflecting how typically welding for connections is performed to ensure a secure attachment (Figure

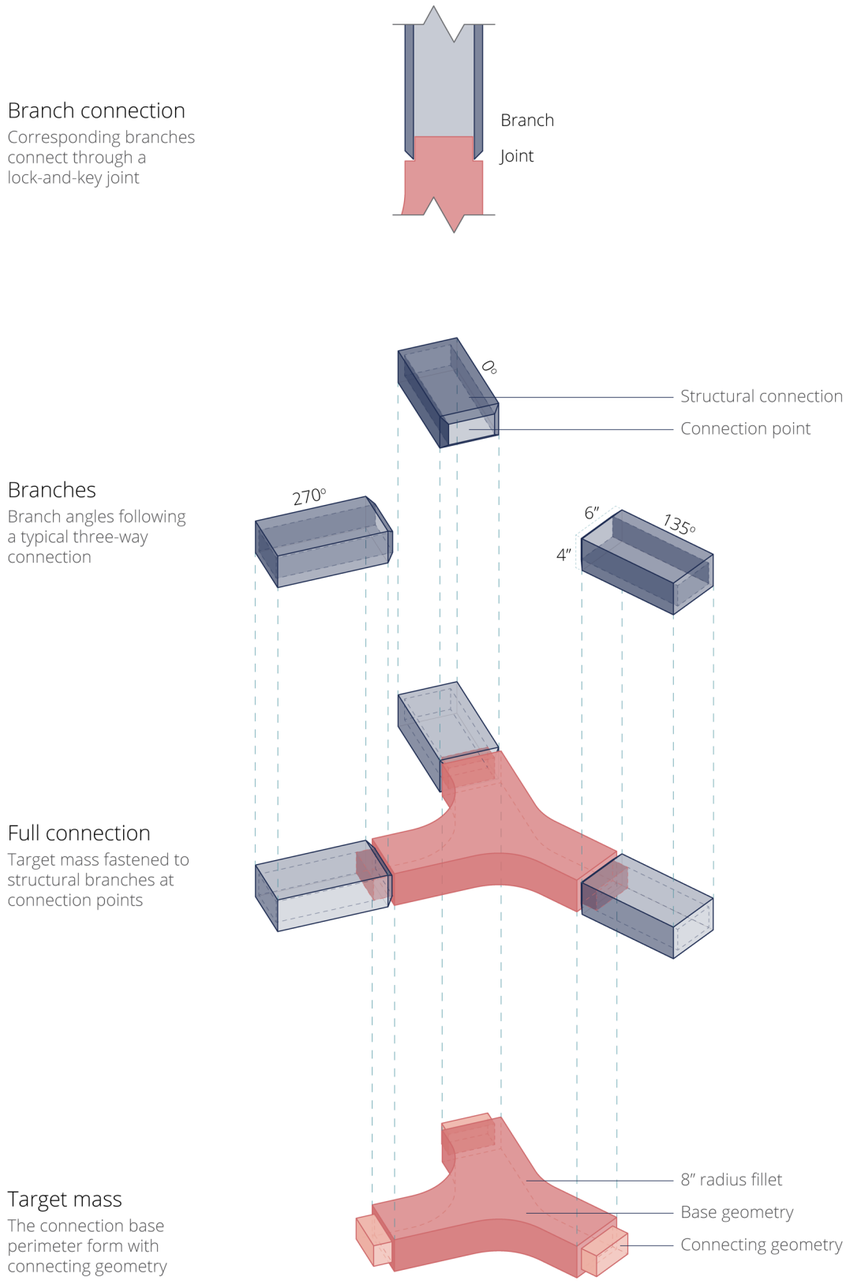


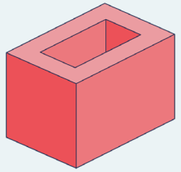
Figure 3.4 Base form - Study connection

3.4). Additionally, a rectangular cross-section was chosen over a circular one to facilitate joint stability for fabrication.

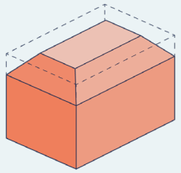
3.1.2 Operative design strategies

Operative design is a method that explores spatial formation through fundamental actions rather than predetermined forms. Operative design begins with spatial operations that serve as generative tools guiding the transformation of forms dynamically, rather than through rigid formal constraints [254]. The incorporation of this method into the design process allowed to enhance the joint form, paving a way for more design possibilities.

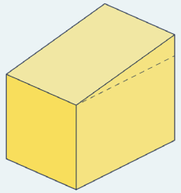
To achieve these dynamics in the form, the connections were further modified by implementing operative design strategies of subtractive and additive typologies (Figure 3.5). After carving out the target mass (Figure 3.6) with voids based on Voronoi patterns and preset ratios (discussed in section 3.4.3), methods like surface tapering (Figure 3.7), expanding (Figure 3.8), and shearing (Figure 3.9) were applied to enhance the top surface, while keeping the base flat. For further advancing the form, additional surface modifications were performed on both sides of the form to introduce curvatures. These design operations included inflating it to create a double-sided convex geometry (Figure 3.10) and pinching the form to create a double-sided concave joint and (Figure 3.11). These operations aided in adding dynamism to the form, enhancing void geometries, and introducing a variety of surface curvatures.



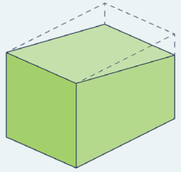
Subtraction - Carve:
Creating voids in the mass



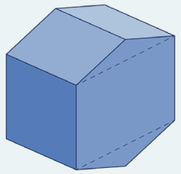
Subtraction - Taper:
Narrowing a side of the mass



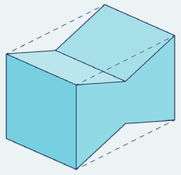
Addition - Expand:
Increasing one surface



Subtraction - Shear:
Decreasing one surface



Addition - Inflate:
Enlarging two sides



Subtraction - Pinch:
Compressing two sides

Figure 3.5 Subtractive and additive design operations

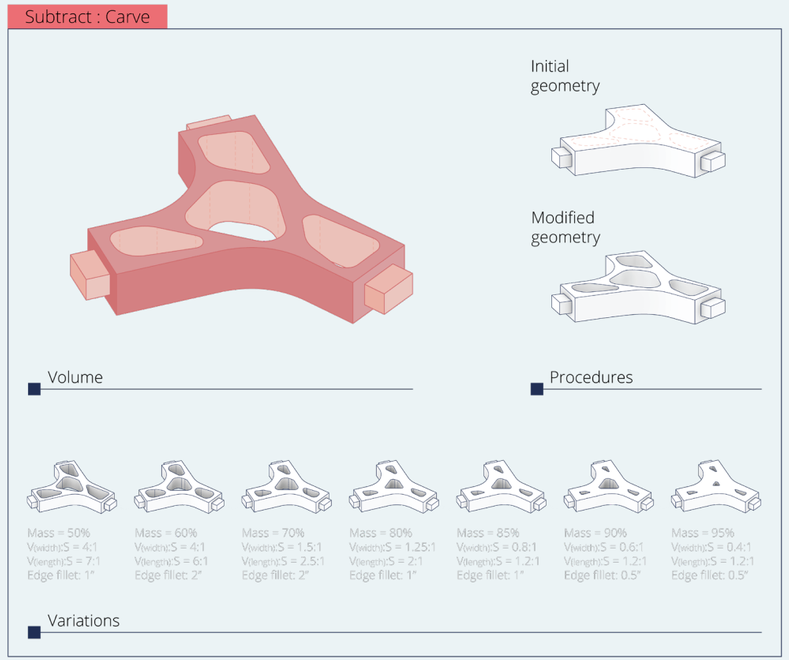


Figure 3.6 Subtraction – Carving: Create voids in the mass

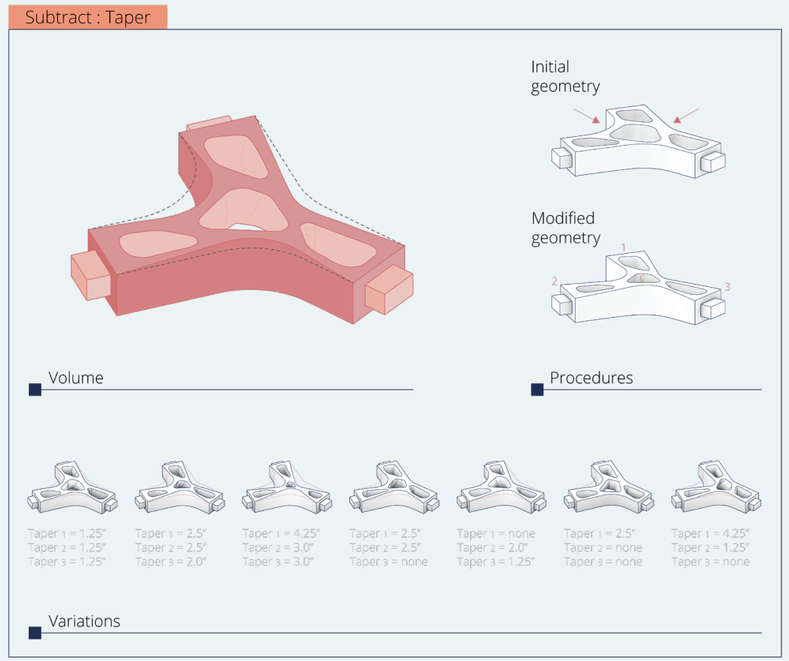


Figure 3.7 Subtraction – Taper: Gradual narrowing of the sides at the top

Add : Expand

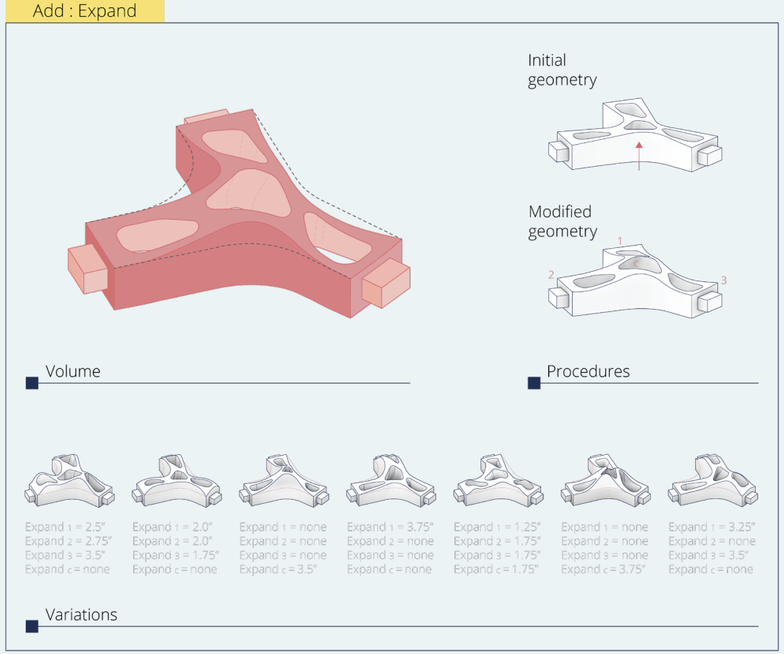


Figure 3.8 Addition – Expand: Stretch the top surface to create a convex surface topography

Subtract : Shear

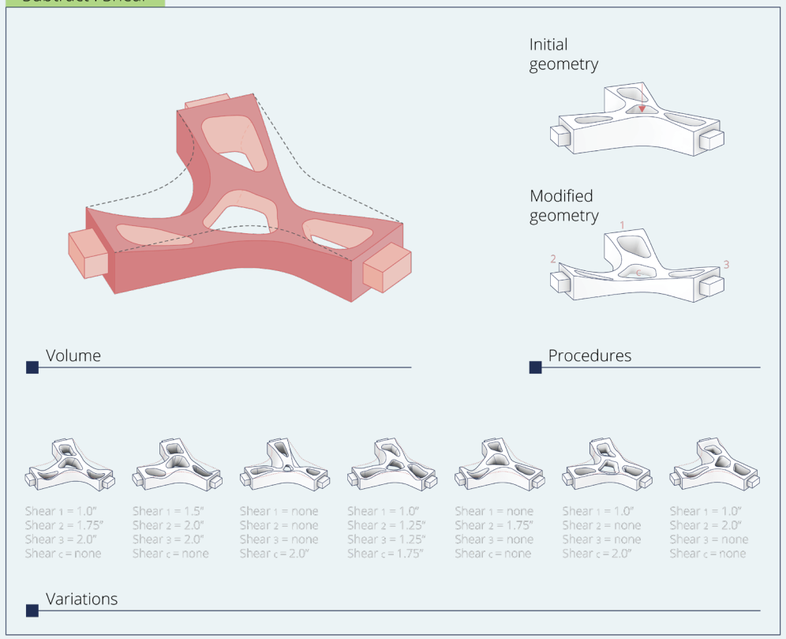


Figure 3.9 Subtraction – Shear: Push down the upper surface to create a concave topography

Add : Inflate

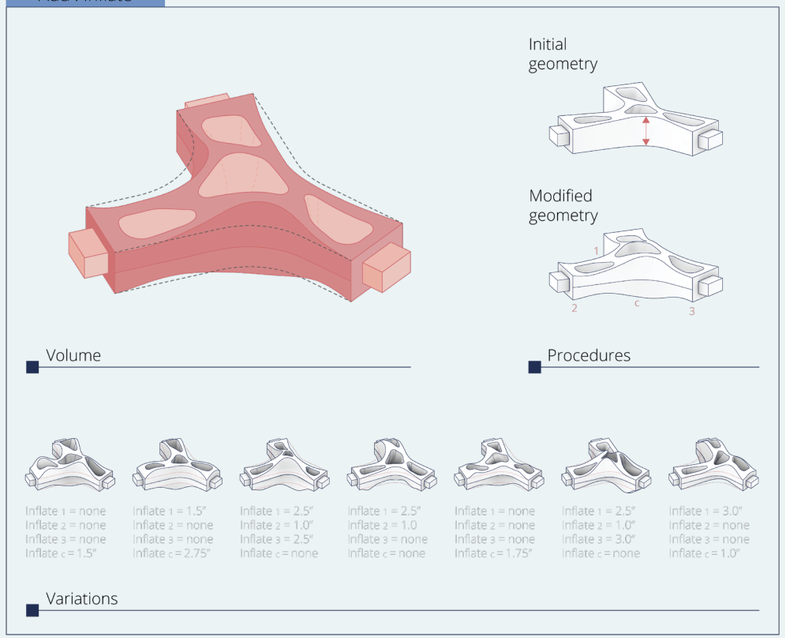


Figure 3.10 Addition – Inflate: Stretch both top and bottom surfaces outwards

Subtract : Pinch

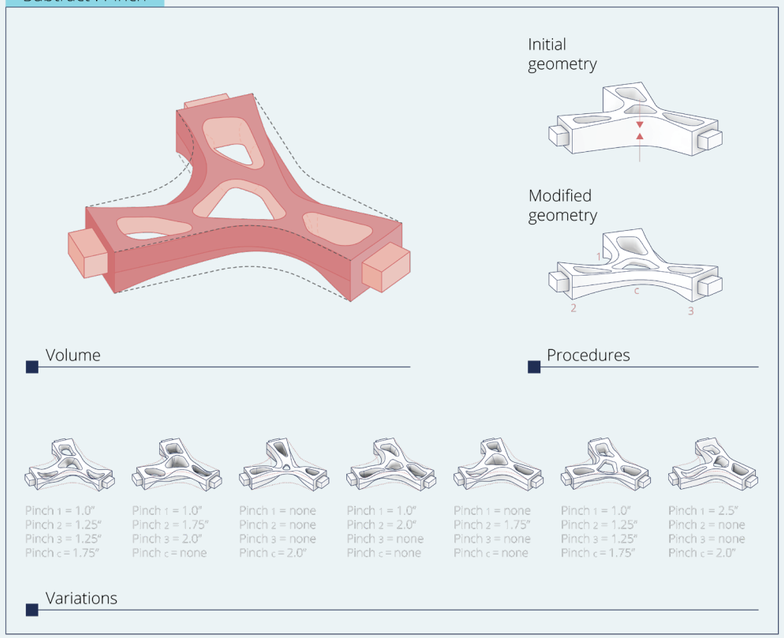


Figure 3.11 Subtraction – Pinch: Compress both the top and bottom surfaces inwards

3.1.3 Digital tools

The process of digital modelling and simulations consisted of a series of 3D software. The main program used, where the modelling was initiated and continuously iterated was the Rhino 7 environment. Rhinoceros is known for its versatility in computer-aided design software for free-form modelling and rapid prototyping [255]. It is versatile in handling complex geometries, allowing seamless integration with other software through efficient geometry exchange [256]. The initial branching structures were built and manipulated in Rhino to understand the branch connectivity and the regions that would undergo the connection redesign. Rhino remained the central program while going back and forth in finalizing the base connection and final joint designs.

Built into Rhino, Grasshopper is a visual algorithm editor that allows the creation of generative forms through programming without coding scripts [257]. The Intralattice [258] plugin in Grasshopper was utilized to generate various lattice structures and manipulate them to suit the desired outcome. Further, the built-in mesh and vector plugins were utilized to create Voronoi structures to develop an irregular lattice structure.

After obtaining an initial joint configuration, the connection was optimized using Fusion 360 and Abaqus FEA programs, validating the joint performance.

3.1.4 Final joint design

The initial joint configuration was optimized through shape optimization in Fusion 360 to understand the load paths and to ensure structural integrity of the initial design strategy. The optimization also contributed to the understanding of how automating the process reduces mass, what areas are the most critical, how to the optimization of parameters impact the resultant geometry, and how compatible are the automated geometries with WAAM. So, a study of various topology optimized forms contributed to further understanding ratios

and proportions, aiding to simplify the joint forms further in Rhino. After a series of processes consisting of digital design work in Rhino, to prototye with operative design, various factors shaped further modifications to create the final joint design.

3.2 Joint optimization

3.2.1 Digital stress analysis

After analyzing both pinched and inflated prototypes, the inflated form was selected for further study due to its ability to effectively test the limitations of curvature and demonstrate the impact of gravity in additive manufacturing. Preparing the simulation model involved a systematic process in Abaqus to conduct the stress analysis, accomplished by using the Abaqus user guide [259]. The initial iterations involved simpler models, such as cubes, to refine the setup and troubleshoot any issues with boundary conditions. The model, created in Rhino, was imported as a STEP (Standard for the Exchange of Product model data) file. During import, solid regions were merged to simplify geometry, and the connection points were isolated as separate parts to ensure accurate stress analysis of individual components. Any invalid geometry warnings were auto repaired and geometry editing tools were utilized to remove unwanted faces.

The material was set to WAAM steel, with a Young's Modulus of approximately 200 GPa, to mimic real-time conditions. The Young Modulus of a material is a fixed value, that measures its stiffness, showing how easily it can be stretched or bent, making it crucial to predict the materials response to stress accurately. It is calculated by dividing the stress (force applied) by the strain (how much the material stretches compared to its original length) in the elastic region of the stress-strain curve. This property is important for designing structures to ensure they can the part can handle stress without deforming.

Abaqus consists of various modules that allow the configuration of the model (Table 3.1). In the Property Module, sections were created and assigned to the model's parts, ensuring the accurate definition of material properties. Next, the Assembly Module was used to position and combine the components. The Step Module was then configured with refined increment sizes for computational efficiency and precision. The increment sizes refer to the time steps to solve the simulations. With that, the Field Output and History Output Requests were defined that allow to capture analysis data and configure them.

Parameters	Description	Module
Material Properties	Define material behavior for the analysis	Property Module
Sections	Assign sections to parts to define material application	Property Module
Step Increment Size	Controls the increment size for simulation steps	Step Module
Contact Pairs	Automatically selects interacting faces between parts	Interaction Module
Reference Points	Used to apply forces or constraints, located on datum midpoints	Interaction Module
Rigid Body Constraints	Makes ends behave as rigid bodies to simulate realistic motion	Interaction Module
Load Magnitude	Specifies the intensity of applied forces (1 kN)	Load Module
Boundary Conditions	Restrict movements at specific points to simulate fixed supports	Load Module
Mesh Technique	Determines meshing strategy, using Free technique with Tet Element Shape for complex parts	Mesh Module
Job Configuration	Settings for analysis submission and monitoring	Job Module

Table 3.1 Abaqus modules and parameters

Interactions between connection points and the connection geometry were defined in the Interaction Module, employing the "Find Contact Pairs" tool to automate the identification of contact regions, which is critical for simulating realistic load transfer. The Load module was used to specify load magnitudes and directions at the reference points, setting boundary conditions to simulate fixed supports by restricting movement in all directions. The reference points were created at the midpoints of the applied forces and constraints using datum tools.

Multiple loading configurations using 1 kN load were developed to replicate the realistic structural forces. 1 kN load is a unit load that serves as a standardized approach to evaluate loading conditions [260]. More complex scenarios involved combining point loads, moments, and opposing moments, simulating real-world conditions where multiple forces act simultaneously. The job for each configuration was then created and submitted in the Job Module, constantly monitored for a successful completion.

The model's complex geometry was handled effectively using the Abaqus free meshing technique with Tet elements, ensuring that the mesh captured the intricate details of the model. This systematic process provided valuable insights into the structural behaviour of the design under stress by highlighting zones that are critical under the different loading conditions, laying the groundwork for further refinement and testing. The obtained results are further discussed in Chapter 4.

3.2.2 Topology optimization studies

To iterate the connections and develop techniques for re-designing a three-way connection, an optimization algorithm was used in Fusion 360. The optimization was initiated by defining process parameters within the software that controlled the output geometry, following the guidelines provided by

Autodesk Fusion 360 product documentation [261]. Topology optimization plays a crucial role in optimizing structures for additive manufacturing, but the methodology applied for it must integrate considerations that impact surface roughness, mechanical anisotropy, and the influence of process parameters to ensure that the computationally generated designs are manufacturable and functionally reliable. This requires an iterative approach that bridges computational design strategies with process-aware constraints.

Surface roughness is a crucial consideration in topology optimization, particularly for AM processes such as WAAM. The layer-by-layer deposition technique in AM often results in irregular surface textures, especially when geometric transitions are abrupt or feature sharp edges [262]. This can negatively impact the functional performance of a component and increase post-processing requirements. To mitigate this, mesh refinement techniques were applied during topology optimization in Fusion 360. A fine mesh resolution was used to create a smoother geometry because a higher roughness would be amplified in WAAM finish. This was further supplemented by adjusting other mesh settings such as adjacent mesh size ratio (AMSR) that ensure smoother material transitions and prevent abrupt changes in mesh element size, and the maximum aspect ratio (MAR) to improve the overall shape quality of the mesh while maintaining manufacturability.

Mechanical anisotropy is a significant factor in the structural behaviour of AM components, as material properties vary depending on the direction of deposition [104]. To address this, Fusion 360 topology optimization ensured that material distribution was aligned with principal stress directions, reducing the risk of weak zones. Load-bearing regions were reinforced using stress-aware constraints, while stiffness was maximized to resist deformation under applied loads.

The manufacturability of topology optimized components is heavily dependent on process parameters that define the feature size, material distribution, and

load path efficiency. To ensure that the generated design remained within WAAM's resolution capabilities, minimum feature size constraints were implemented to eliminate thin, unprintable regions. To simulate real-world performance, unit load constraints per branch were introduced, ensuring the optimized joint could withstand expected forces without excessive deformation. Fusion already has pre-defined base settings for all the parameters that were refined to produce a smooth geometry based on multiple experiments to understand how changing the variables impacted the results. The concerning parameters are defined below, follow by the implemented values.

The model-based mesh size controls the surface finish of the resulting mesh. A lower value produces finer meshes that take longer computational time while higher values produce a coarse mesh that provides quick results but may result in inaccuracies [261].

- The adjacent mesh size ratio (AMSR) controls how smoothly the mesh transitions from smaller elements in detailed areas to larger elements elsewhere [263].

$$AMSR = (h_{i+1})/h_i$$

h_{i+1} = size of the larger adjacent element,
h_i = size of the smaller adjacent element.

- The maximum aspect ratio is the ratio of the longest dimension to the shortest dimension in an element. It sets an upper limit of the elongation of elements in a mesh [263].

$$MAR = h_{max}/h_{min}$$

h_{max} = longest edge of an element,
h_{min} = shortest edge of an element.

- The maximum turn angle on curves controls how many elements are generated along the curved edges and surfaces. A smaller angle increases the number of elements, providing greater precision [264].

- The minimum element size defines a lower limit for an element size in a mesh [264].

- Element order refers to the level of complexity and accuracy of the elements used in a finite element analysis (FEA) mesh. It determines how nodes are distributed within an element and how the shape of the element is interpolated by adjusting the criteria between linear or parabolic [263].

Table 3.2 lists all these parameters for the mesh settings with the values that were specified to generate the optimization results.

Property	Applied value	Pre-set value	Available range
Model-based mesh size (%)	1 - 2	5	1-10
Max. adjacent mesh size ratio	1.1	1.5	1-3 (small to large)
Max. aspect ratio	7	10	4-20 (small to large)
Max. turn angle on curves (Deg.)	60	60	10-60
Min. element size (%)	20	20	1-100
Element order	Linear	Linear	Linear or parabolic

Table 3.2 Topology optimization mesh parameters in Fusion 360

To produce a fine surface finish, the mesh size was kept at 1%. This was also compared to 2% mesh size to test how much the surface finish and in turn the resultant geometry varies by making the mesh slightly coarser. Hence, two sets of results were obtained for both mesh sizes. Adjacent mesh size ratio was set with a grading factor of 1.1 - a low value within the typical range of 1.0 to 3.0. The small grading factor limits the maximum edge length difference between

adjacent elements, ensuring a gradual transition between mesh elements and avoiding abrupt changes in the element size. The maximum aspect ratio was also reduced to a value of 7 from a standard 10. A lower value produces a more well-shaped result, making it more suitable for complex geometries. Other parameters like the turn angle, element size, and element order were kept at standard settings.

Further, the base connection form was set up using 3D modelling in fusion and prepared for the shape optimization. The connection points of the joint were designated as “preserved regions” to keep the connecting geometry unchanged. Next, the geometry was set to be optimized unit loads of 1 kN at each branch, representing the forces acting on the connection (Figure 3.12). The outer surface of each leg of the target mass was set as a constraint so that the simulation does not analyze them for free movement. The shape optimization criteria were then varied to guide the resulting design, including setting a desired limit on the resultant mass as a percentage of the initial target mass, achieving multiple outcomes by adjusting this criterion.

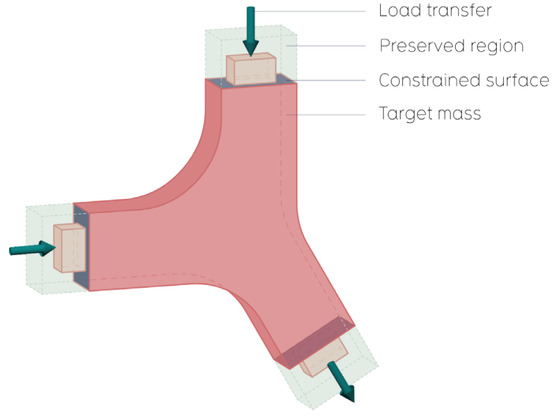


Figure 3.12 Model set-up in Fusion 360

As for the various shape optimization criteria in Fusion 360, there are two categories. One deals with the targeted output mass and the other manages the stiffness of the part. Stiffness is automatically set at maximum and cannot be changed because it ensures that part can resist deformation under applied loads, optimizing the stiffness-to-mass ratio by removing low-impact material to make the part lightweight yet strong. The target mass, however, can be adjusted based on the user requirements. For this study, a range of target masses were set to obtain multiple results, from 15% (low) to 65% (high), at 10% intervals to test how the set target mass percentage impacts the resulting geometry.

3.3 PLA prototyping

The AM processes played a pivotal role in the fabrication and validation of the design, enabling a direct transition from digital optimization to physical realization. Fused Deposition Modelling (FDM) based Polylactic acid (PLA) prototyping was performed to understand the designs better and identify potential issues that could arise in the actual metal print. PLA is a biodegradable plastic commonly used in extrusion-based FDM printing [265]. It is a quick and cost-effective method of fabricating prototypes with ease. PLA prototyping served as a gateway to understanding the behaviour of the forms during printing and how those results would translate to WAAM because of the similarity of both processes to fabricate by depositing material layer by layer.

For this, a set of the topology optimized forms were 3D printed to study aspects such as support structures, surface quality, impact of target masses and member thicknesses. Any issues they may arise during this stage were likely to be amplified during the WAAM process. An evaluation of these results further led to design modifications in the initial Voronoi joint, and the resulting geometries were also PLA printed for a physical analysis.

The topology-optimization results in Fusion 360 were converted to a mesh and then exported to Rhino 7 in an Object (.OBJ) format. In Rhino, the Grasshopper plugin was used for low level mesh smoothening to eliminate significant surface irregularities before 3D printing.

Printing of all the PLA prototypes was conducted at the MLab (Maker Lab) at the UWaterloo School of Architecture, Cambridge campus. The MLab hosts Creality Ender-3 S1 Pro 3D printers that follow a standard operating procedure. As per the lab usage manual, there are specific guidelines to follow to set up a print job. The printers have a print bed of 220 mm x 220 mm x 270 mm and are only compatible with PLA filaments of 1.75 mm thickness. Creality Ender-3 possesses a print setup program - Creality Slicer 4.8, which initiates the toolpaths for the printer to follow. The program also allows to set the infill density and pattern and creates automatic support structures for cantilevered regions. The lab guidelines also indicated setting the nozzle temperature to 210 ^{o}C. Once the print is initiated, the print bed temperature automatically rises to 60 ^{o}C as a default temperature. For a standard quality print, the layer height was set to the optimum default setting of 0.2 mm by the Creality Slicer, with a print speed of 50 mm/s for best results.

Following the guidelines of the MLab, the prototype prints were set up with same perimeters (Table 3.3) to ensure safety during printing and maintain quality outputs. To adjust the print size within the print bed limitations, the models were scaled down to a 1:6 scale (i.e., 1-inch in the printed model represents 6-inches in actuality). They were then exported in an STL (Stereolithography) format to Creality Slicer 4.8, that allowed to setup and visualize the print. The infill density varied from topology optimized joints to simplified joints according to the surface width for proper support. After several experiments with printing, a raft-type build plate adhesion was selected which builds a four-layered raft support underneath the actual print for a smooth printing process. Other types of adhesion methods resulted in messy print that did not stick to the print bed. The models were then exported as G-Code files for

Print Material	Nozzle temperature	Print bed temperature	Layer thickness	Print speed
1.75 mm PLA+ filament	210 °C	60 °C	0.2 mm	50 mm/s

Table 3.3 PLA process parameters



Figure 3.13 PLA prototyping - Work flow

printing. The G-code guides the printer about how the object layers would be deposited, defining tool paths for it to follow. The complete workflow from topology optimization to the printing of the prototypes is illustrated in Figure 3.13.

The PLA prototypes were divided into three categories. Firstly, the topology optimized joints were printed for geometries with a target mass of 25%, 45%, and 65% selected as the base cases for further analysis from both 1% and 2% mesh sizes. This resulted in a total of six prints from the topology optimized models. Various studies in literature, such as those by Wang et al. [56] and Wang et al. [118] took a similar approach, where they generated multiple joint designs through optimization algorithms and picked two to three representative joints to study further based on their weight reduction, aesthetic requirements, and manufacturability. This research followed a similar idea, selecting joints based on a 20% difference in their target mass, from both 1% and 2% mesh sizes. The selected joints resulted in a range of designs, from thin struts and large voids to thick struts with smaller voids. While the minimum target mass studied was 15%, the lowest prototyping mass selected was 25% in view of the discussion by Al-Tamimi [266], who highlighted that mass reductions below 75% risk compromising structural integrity, which was also visually evident in the results produced by the 15% target mass.

The second category included the operative designed joints that were achieved after multiple iterations as the finalized designs. For this, two prints were done - the inflated joint and the pinched joint, to physically analyze which of the two form is more suitable for testing WAAM criteria for curvatures better. Whereas the third category consisted of sectional prints which were done for understanding the behaviour of supports and what regions in the designed joints are capable of self supporting them selves. For this a longitudinal section through the entire inflated joint was printed at a 1:4 scale, while a zoomed in section was also fabricated at one of the branches at 1:3 scale for an enhanced analysis of the support structures.

3.4 WAAM application and learning techniques

3.4.1 Lab and equipment

After the completion of the digital work and the physical prototyping, the next phase of finalizing this research involved the WAAM process. The metalwork completed for this thesis was carried out in collaboration with the Conestoga College Cambridge – Fountain Street Campus, utilizing the Gas Metal Arc Additive Manufacturing (GMAAM) six-axis robot available at the Welding Technology Robotics Lab. The fabrication setup and procedures were carried out by the WAAM experts at the lab.

The WAAM prototyping was completed using an arc welding robot, FANUC ARC Mate® 100iD, with six-axis capabilities (Figure 3.14) [267]. The robot is paired with a Lincoln Powerwave® R450 power source and a wire feeder. With a payload capacity of 12 kg and a reach of 1441 mm across its six axes, including backflip movements, the robot allows the creation of compact welding cells. Its sleek design also optimizes workspace efficiency, while the fully integrated welding hose pack and utility cables further reduce clutter [267].

The ARC Mate® 100iD works up to a precision of ±0.02 mm. It has a mechanical weight of 145 kg that ensures stability during high-speed operations, and its hollow wrist design offers seamless tool integration for complex projects. The robot features a wide motion range and speed across all axes, allowing it to handle dynamic and varied tasks easily. To enhance durability, it comes with an IP54 dust and water protection rating as standard, with optional upgrades to IP55 or IP67 for environments that demand higher resistance to dust and moisture. This combination of advanced features ensures that the FANUC ARC Mate® 100iD delivers consistent, high-quality results for WAAM prototyping and other demanding applications [267].



Figure 3.14 FANUC ARC Mate 100iD Arc Welding Robot

The robot is equipped with a Fanuc standard Teach Pendant (TP) (Figure 3.15) [268], that allows for the manual programming of geometric objects and movements. The Teach Pendant is a robot controller, providing an easy way to program standard industrial robots, employing reference points, position registers, and offsets to guide the printing process without the need for external software programs. The Teach Pendant was used to setup and perform the WAAM processes for this research, handled by the welding team at Conestoga College.

However, due to its six-axis functionality, the robot arm restricts movement to fixed planes. It lacks the flexibility to reach certain angles or orientations required for more complex geometries, as seen in overhang experiments

done by Evjemo et al. [269], where the deposition angles beyond 43° are not attainable due to robot arm restrictions. This limitation is particularly problematic for intricate geometries with internal cavities or overhangs, as the robot cannot reposition the tool head without colliding with the workpiece [270]. To fabricate complex topology-optimized models, a robotic arm with at least eight axes and a rotating print table is necessary. This approach allows more flexibility in fabricating complex geometries without compromising structural integrity. Given access to only one WAAM robot, this thesis adopted form simplification based on latticing techniques and an analysis of topology optimization results to ensure compatibility with six-axis printing.



Figure 3.15 FANUC standard Teach Pendant

The WAAM procedures followed standard safety protocols for arc welding during fabrication to maintain a safe working environment. The robot used a default material - mild steel alloy feedstock wire, CSA W48/ISO 14341 - B-G 49A 3 C S6 (AWS A5.18 - ER70S-6) [271] as a standard for all of its processes.

The fabrication was conducted in a closed cell to shield against emitted sparks, heat, and intense light, safeguarding the people in the lab. A shielding gas was also utilized in the process to protect the weld pool from contamination by the surrounding air, which can affect the quality of the weld. As per the Canadian Welding Bureau [272] mixing carbon dioxide, a reactive gas, with Argon, an inert gas, helps to stabilize the arc and reduce spatter, improving the overall weld quality. Various studies in literature also used a combination of Carbon dioxide and Argon as shielding gases when working with ER70S-6 steel for optimal welding results [273], [274]. Changing the ratios of the gases produces welds of a different finish, which in this study was kept at 85% argon and 15% carbon dioxide, based on the previously conducted experiments by the welding lab team at Conestoga.

A fume ventilation system was also employed to manage welding fumes and maintain the air quality. Additionally, anyone on the site was required to adhere to the safety precautions, including wearing CSA-certified safety boots and safety goggles and dressing in 100% cotton long-sleeved shirt and pants. These measures ensured both the safety of the operators and the quality of the fabrication process.

3.4.2 Expert opinions

To understand how the WAAM process works with the available six-axis robot in relation to the optimized forms, multiple meetings were held with the arc welding experts from the partner lab at Conestoga. The meetings were a joint conversation with Professor Jim Galloway, and Professor C. Tam Nguyen, Ph.D., P.Eng., I.W.E. - the coordinators of welding program at Conestoga. Furthermore, Professor Tam was more involved with the production side of the prototypes, to set up and carry out the processes so, he had more expertise on the practical side of WAAM. Some of these conversations included Jackson Macor, an alumnus of Conestoga, who is currently working as a Manufacturing

Expert Reference	Discussion Criteria				
	Robot	Sizing	Design	Processes	Welding
Tam C. Nguyen	The robot comes equipped with a six-axis arm and a fixed table. An eight-axis robot with a rotating table is required to fabricate complex forms.	The printer allows a print area of 2'x2' but for material efficiency, the experimental setups can not exceed 1' limit.	Thin strut profiles that get generated due to topology optimization are not suitable for a large deposition nozzle. A minimum 4" thickness should be available.	As each WAAM layer deposits, the previous one undergoes partial melting, impacting the surface finish. Simple geometrical forms can be fabricated without the need of additional softwares to program the WAAM process.	When programming the robot manually through a teach pendant, the start and stop points of WAAM layers for a surface have to be randomized to prevent weakening of the structure.
Jim Galloway			The WAAM process is better suited for parts of a considerable size because printing thin profiles requires extended waiting times between each weld to accommodate heating and cooling buffers, leading to inefficiencies in production.	To solve fabrication issues or to form larger parts, forms can be divided into parts and fabricated individually. The pieces can then be field welded together manually with a heat input nine times greater than the WAAM welds to form a full connection.	Impact test results at -50°C showed WAAM material to have strong toughness properties, absorbing 120J energy, the welded region showed 40J, which is still considered a good toughness value, while the heat affected zone demonstrated 180J, making field welding a good alternative.
Jackson Macor	A base plate (substrate) is required for the WAAM process to build off from. The robot can not build additional supports, so the form always builds ground up without supports.		Occurrence of unsupported geometry requires another base plate to build off from, which is beyond the available robotic capabilities. Synthesizing the joints to a more 2D design that build vertically up from the surface, with a flat or self supported base is good for better printability aspects.	Plasma Arc cutting can be done to subtract simple forms from solid WAAM plates.	

Table 3.4 Expert opinions in relation to the optimized forms

and Welding Automations Technologist. Their input shaped the design work of this research as per the discussion points highlighted in Table 3.4.

Based on these discussion points, the following GMAAM constraints can be summarized. With the deposition of each weld pass the previous layer undergoes partial melting. With the presence of thin rounded geometry in the form, the profiles get a minimal base contact area, and the small radii form a flat block rather than maintaining their intended shape. Therefore, higher target masses that create thicker and flat surfaces are better supported in WAAM. However, as the target mass is reduced in optimization processes, a more defined strut form is generated, leading to printing challenges. This is the same with using latticing that have thin struts and larger voids because they present printing challenges with WAAM. In this case, according to the expertise of the robot operators at Conestoga College, cylindrical members that are oriented vertically should have a minimum of 4-inch diameter to facilitate the fabrication process. In case of the study joint, the branches of the joint have a width of 6 inches on all three sides. To have a 4-inch surface thicknesses plus a void at each branch is not dimensionally possible within overall study joint area. On the contrary, changing the direction of print for the same piece from vertical to horizontal increases print length and hence, allow for a smoother process.

Another major constraint of a six-axis robot is the inability to support the building of cantilevered structures. While the WAAM and typical PLA printing techniques are similar, plastic printing can build detachable supports for cantilevered regions due to the material's properties. In contrast, WAAM does not have the capability of building temporary supports that can be pulled apart. WAAM requires welding onto a base plate (a substrate), which is later removed by machining. In this scenario, the orientation of the part during print plays a significant role. With the targeted mass geometry in this study, at a vertical orientation the upper two branches are unsupported because they lack a base plate to build off from, making the fabrication impossible. In

this scenario, optimal printing orientation is to be considered and printing the form flat on its face removes this limitation, allowing to apply the WAAM procedure. This was also supported by Laghi et al. [104], who emphasized that WAAM prints should be printed in orientations that reduce unsupported overhangs to avoid excessive warping.

A significant information shared by the experts were the findings of the impact test for WAAM performance. According to the results, at -50 ºC, WAAM absorbed 120 J energy, the welded region absorbed 40 J, while the heat-affected zone demonstrated 180 J of absorbed energy. A higher absorbed energy value demonstrates better toughness properties and performance, and these results demonstrated that welding WAAM materials together can create strong structures and aid in developing complex forms, that are otherwise not facilitated in a singular piece print.

3.4.3 Form considerations in relation to WAAM

After discussions with the experts, the main aim of further form considerations was to address the WAAM application requirement. For this the first step was to eliminate the cantilevered branches and modify the form to make it compatible with a six-axis robot. For this purpose, the orientation of the connection was changed from x-z plane (vertical) to the x-y plane (horizontal) in view of the printing challenges that arise from unsupported regions in topology optimization as well as the branch connections that have no base support to build on (Figure 3.16). Changing the joint orientation, effectively laying it flat on its surface (Figure 3.17) provided a better understanding of how to manipulate the joint and explore design possibilities that are compatible with the WAAM robot. The change in joint print orientation also allows the fabrication of the thin members that occur with a lower target mass in the optimization or with closely spaced Voronoi cells because the robot toolpath can print in the longitudinal direction rather than at the thin transverse cross-section (Figure 3.18).

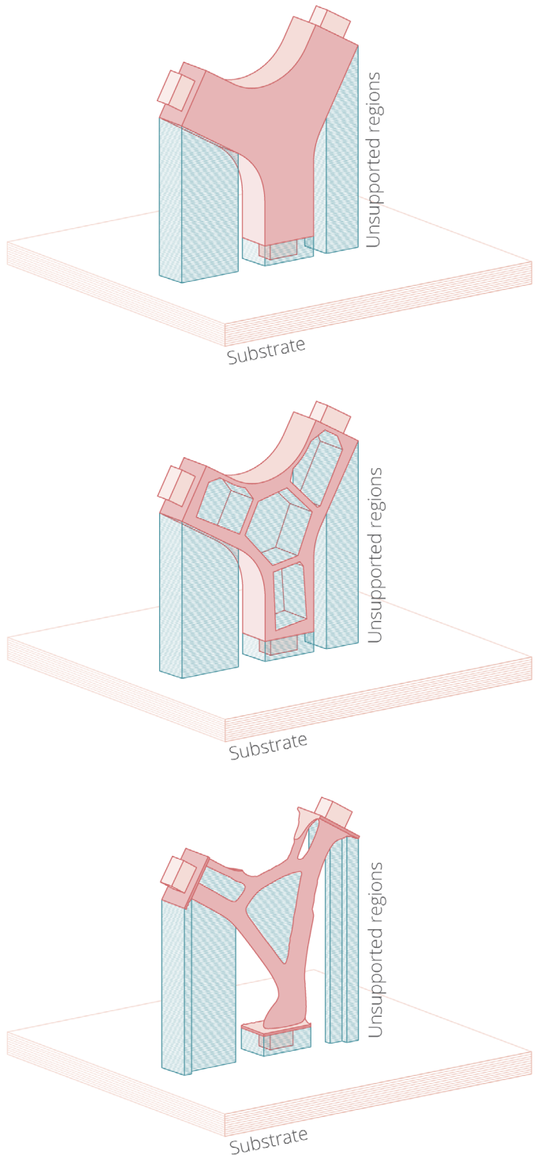


Figure 3.16 Unsupported (Cantilevered) regions occurring when printing the joints vertically on the substrate

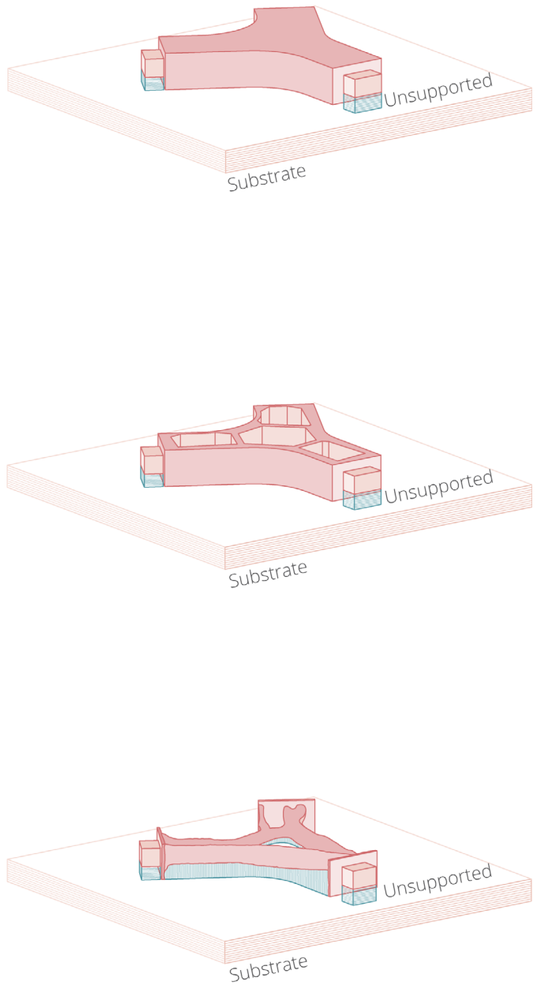


Figure 3.17 Horizontal print orientation creating minimal unsupported regions

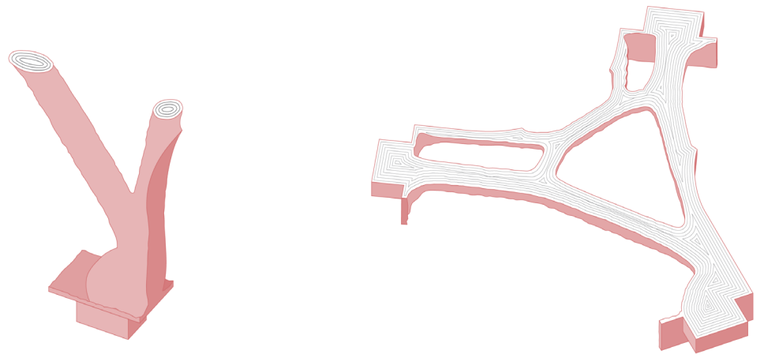


Figure 3.18 Left: Vertical print with thin cross-section; Right: horizontal print with wide cross-section

Further, a set of guiding parameters were defined to enhance form compatibility with WAAM procedures:

- The width of the opening at each branch can range between 1 inch and 4 inches - (Table 3.5). These limitations were set according to the structural performance and joint size. A void size less than 1 inch is very small, appearing as a puncture rather than a void (analyzed from the topology optimization results), losing its character and purpose of being a void.

- In view of the void width range, the subsequent surface width at each branch can range between 1 inch for a 4 inch-wide void (void to surface ratio 4:1) and 2.5 inches for a 1 inch wide void (void to surface ratio 0.4:1), as shown in Table 3.5. Surface width dimensions less than 1 inch result in very thin members, making the joint susceptible to failure [105], while a value above 4 inches would occupy any space available for a void within the 6 inch branch size, producing a solid block. Hence, the voids and surfaces follow these limits to produce balanced outcomes.

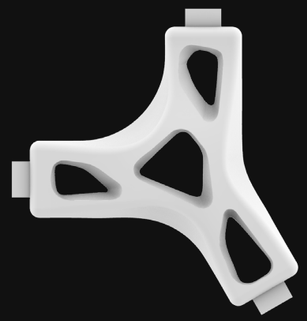
- Since the centre is wider than the branches, the surface width around the central void can range up to 4.5 inches for a 1 inch void (void to surface ratio 0.2:1) and 1 inch for a 4 inches void (void to surface ratio 4:1) - (Table 3.5). These ratios were calculated based on the minimum and maximum limits of the bounding surfaces, accounting for the space that is available to accommodate the void.

- A minimum of approximately 50% target mass can be achieved while staying in the pre-defined target mass boundary and adhering to the previously stated void to surface guides. This allows to have four larger voids with a 1 inch bounding surfaces, both at the centre and at the branches - (Table 3.5).

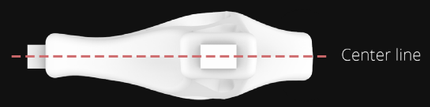
Target mass/%	Volume/cubic feet	Void width/inch	Void length/inch	Surface width at branch/inch	Surface width at centre/inch	Ratio - void width to surface	Ratio - void length to surface
50	0.27	4	7	1	1	4:1	7:1
60	0.32	4	6	1	2	4:1	6:1
70	0.38	3	5	2	2.5	1.5:1	2.5:1
80	0.44	2.5	4	2	3	1.25:1	2:1
85	0.46	2	3	2.5	3	0.8:1	1.2:1
95	0.51	1	3	2.5	4.5	0.4:1	1.2:1
100	0.54	0	0	0	0	0	0

Table 3.5 Void-to-Surface width ratios as per the target mass

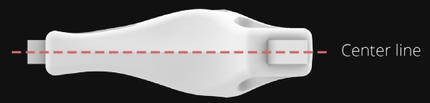
Table 3.5 outlines these numeric parameters, developed after digital testing of various void sizes within the available target mass space. For structural considerations, members less than 1 inch were eliminated to avoid weak joints. Likewise, a maximum strut size was set to maintain the desired number of voids within the available area. Further testing of different strut sizes in view of the targeted mass provided an estimate of a range of void sizes and void-to-surface ratios, which were used to guide void carving variations for joint operative design strategies stated earlier. Lower target masses can be achieved by manipulating the boundary of the target mass while retaining its branch connection point and maintaining the void-to-surface ratios.



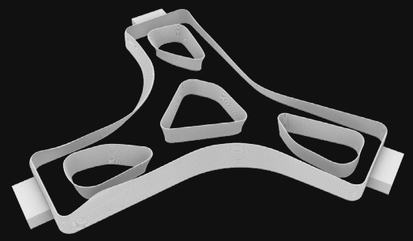
Joint - Plan View



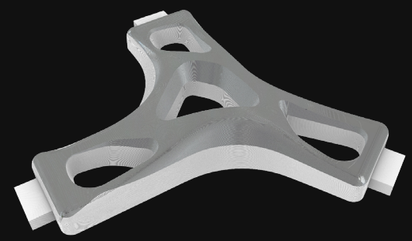
Joint - Top View



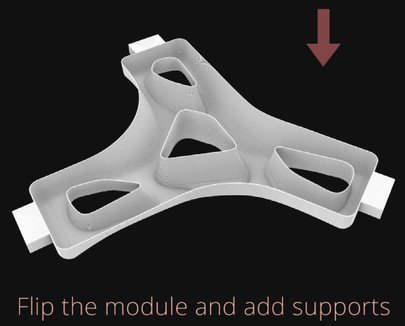
Joint - Side View



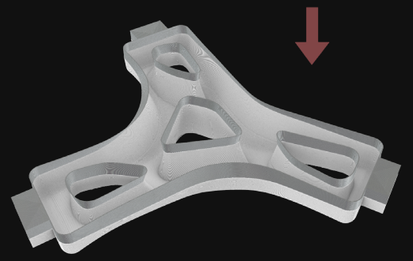
Print from center line above



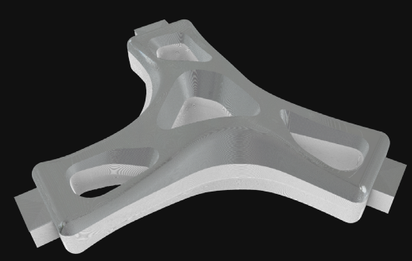
Complete print of module top



Flip the module and add supports



Continue printing the second half



Finalize the print

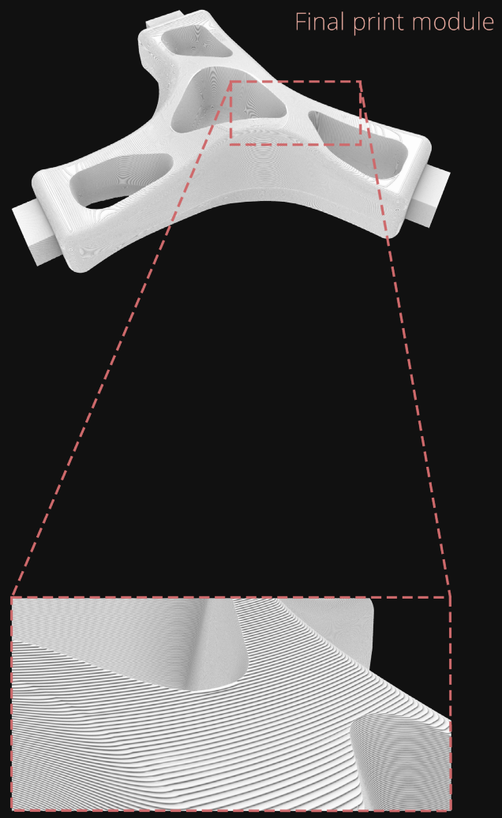


Figure 3.19 WAAM printing process for the inflated joint

To support the printing of the masses developed through design procedures that consist of double-sided curved surfaces, a printing procedure was developed. Taking into consideration the discussions with experts, the connection design was split into two parts horizontally across the center, to print the two pieces separately with a flat base, that can later be field welded together to form the whole connection. However, further discussions revealed that given the void sizes, welding on the interior side would be difficult.

For this, an alternate approach, based on the same idea of form splitting was developed that involved a flip-over printing method, where instead of printing the two pieces separately, the second one can be printed on top of the first one by flipping it over after cooling, as illustrated in Figure 3.19. This allows the manipulation of the form and achieving more complex geometries within WAAM limitations. Additionally, all the edges of the joint were filleted to create curved edge surfaces, allowing for a smoother print and an easy flow of movement for the robot. Curvatures also enhances structural performance because sharp corners introduce stress build up because of additional start and stop positions [275].

3.4.4 WAAM anisotropy and weld paths

The direction of welds in WAAM play a crucial role in determining the structural strength and performance of the fabricated joint, exhibiting anisotropic mechanical behaviour. The joint design corresponds to a vertical structural orientation, which allow for the loads to travel from the top branch to bottom branch. The longitudinal direction (WAAM-L) corresponds to the primary deposition path, exhibiting the highest tensile and compressive strength, as it aligns with the natural grain growth and solidification process of the weld pool.

For fabrication, the joint would be printed with weld layers parallel to the

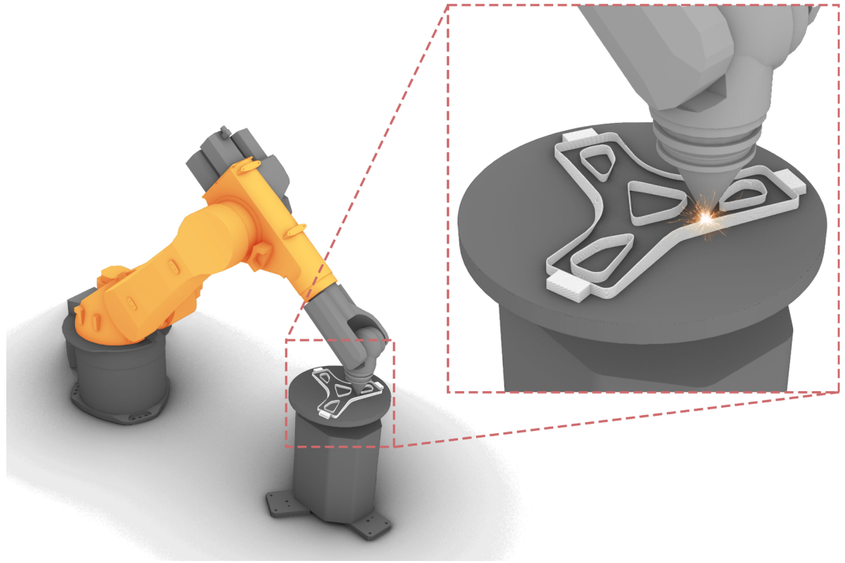


Figure 3.20 WAAM fabrication in x-y plane

horizontal plane, as illustrated in Figure 3.20. However, once rotated to its upright position, these weld layers would align with the direction of the applied loads ensuring that the top-to-bottom branch load transfer occurs along the strongest material direction. Lagi et al. [104] found that to maximize structural efficiency, the weld direction should be optimized based on the joint's expected loading conditions, following the natural force flow of the joint to improve load transfer efficiency. Aligning weld layers parallel to the main stress direction improves structural strength.

Further, printing the three-way joint in a horizontal orientation enhances the contribution of WAAM-D because the shear forces between branches are better distributed and heat is dispersed more evenly, reducing localized

stress concentrations at the intersections. This was also observed by Lagi et al. [104] who concluded that weld layers in diagonal direction (WAAM-D) can help balance stress distribution, particularly where load paths are non-linear. This is particularly beneficial in multi-directional load-bearing joints, where forces travel through different angles rather than purely vertical or horizontal planes.

However, while WAAM-L provides the highest strength, WAAM-T (transversal direction) remains the weakest due to layer-by-layer fusion boundaries, which can lead to premature failure under lateral shear forces. To mitigate these issues, crosshatch welding techniques, multi-pass welding, and post-processing treatments such as heat treatment can be applied to reinforce inter-layer adhesion and improve structural performance of the joint as implemented by Rodrigues et al. [276]. Given that the three-way branch connection experiences multi-directional forces, a graded material transition between WAAM-L and WAAM-D where the material is deposited in a controlled manner that blends both orientations smoothly, regions can further optimize load distribution.

3.4.5 Experiment 1 – WAAM plate

The additive manufacturing of a WAAM plate was the first piece fabricated to study the WAAM procedure. A simple plate was developed to get a basic understanding of the fabrication process and how the set parameters influence the fabrication process, how the weld layers interact with each other, what is the surface quality, and what deformations, if any, occur during metal deposition. Figure 3.21 shows the in-process plate printing by the WAAM robot. A rectangular plate measuring 280 mm x 260 mm with a thickness of 1 inch was selected for printing, representing half the original joint size. It was the maximum size feasible to print. This decision was informed by the expert opinions, who, based on prior WAAM experimentation, advised

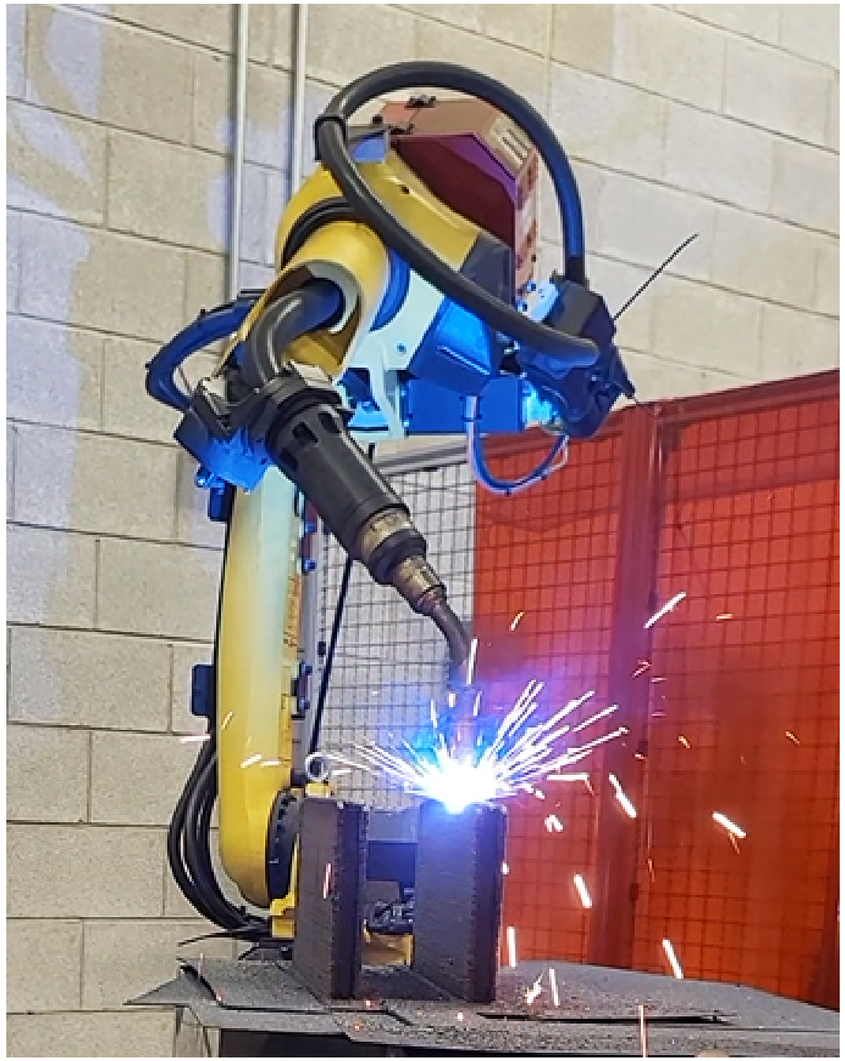


Figure 3.21 In process plate printing

against producing a full-scale steel block due to its impractical weight and material inefficiency. It allowed material conservation and optimized time while meeting experimental requirements. The 1 inch thickness was to accommodate the cutting capabilities of Plasma Arc equipment for the next step. After printing, the final length measured approximately 275 mm, with a 5 mm reduction (Figure 3.22), thickness of the plate was 27 mm, while the weight was approximately 15.2 kg.

The welding process was conducted for 4-5 hours daily. All the deposition parameters were based on previously optimized standards, reached through prior experimentations at the Conestoga Welding lab. Each deposited layer had a thickness of ~1.8 mm, achieved using eight beads per layer. The heat input for each weld pass was approximately 230 J/mm, with the robot operating at 26 inches per minute. A slower speed can cause the previous layer to solidify, and the next layer would not amalgamate with it properly. On the contrary, a faster speed does not allow enough time for the previously deposited layer to cool enough, where the hot new layer would not cause a meltdown of the form. Based on this speed, the deposition rate was ~1.9 kg/hr during arc-on time, resulting in an arc-on time of ~8.2 hours. The overall production time, including setup and cooling, was about 12.3 hours, yielding a deposition efficiency of approximately 67%.

As a standard WAAM procedure, water was pumped at the base during printing to cool the layers and manage the heat buildup. The substrate temperature during welding was maintained at approximately 200 °C. Before continuing the print the following day, the piece was preheated with a torch to 250 °C to ensure a uniform print quality.



Figure 3.22 WAAM plate

3.4.5.1 Plasma arc cutting

Following the fabrication and cooling of the plate, the next step was to cut out the joint shape from it. For this, the Plasma Arc Cutting method was employed (Figure 3.23), performed at the Conestoga welding lab, using the Koike Aronson PlatePro [277] cutting bed, with a Hypertherm [278] power source at the Welding Technology Robotics Lab at Conestoga College.

The workflow began with exporting the 2D silhouette lines of the extruded joint shape as a DXF file and then importing it into the SheetCAM program. In SheetCAM, lead-ins, lead-outs, and tool offsets were defined to ensure precision. The finalized cutting instructions were saved as an FGC file and uploaded to the CNC system to guide the cutting process.

The operation was conducted with specific parameters that were based on the technical recommendations provided by the manufacturer, further adjusted according to the thickness of the material: a travel speed of 15 inches per minute, a voltage of 83 V, a kerf width of 0.125 inches, and a torch height of 0.100 inch. This configuration ensured the precise shaping of the joint. Plasma arc cutting generates an electric arc through a welding power source, delivering 105 amps in this case. Compressed air was directed through the arc's path, where the intense heat ionized the gas to produce a focused plasma jet. This plasma, reaching temperatures of approximately 40,000 ^{o}F, melted or vaporized the metal to create clean and precise cuts. The plasma power source was a Hypertherm high-definition water-cooled torch, mounted on a CNC plasma table, ensuring accuracy and consistency in the cutting process.

The total arc cutting time was 1 minute and 53 seconds. After the completion of the cutting, a G-clamp was used to transfer the cut plate to a clean surface where it cooled down (Figure 3.24). Once cooled, the cut pieces were easily separated from the plate, leaving behind the joint form.

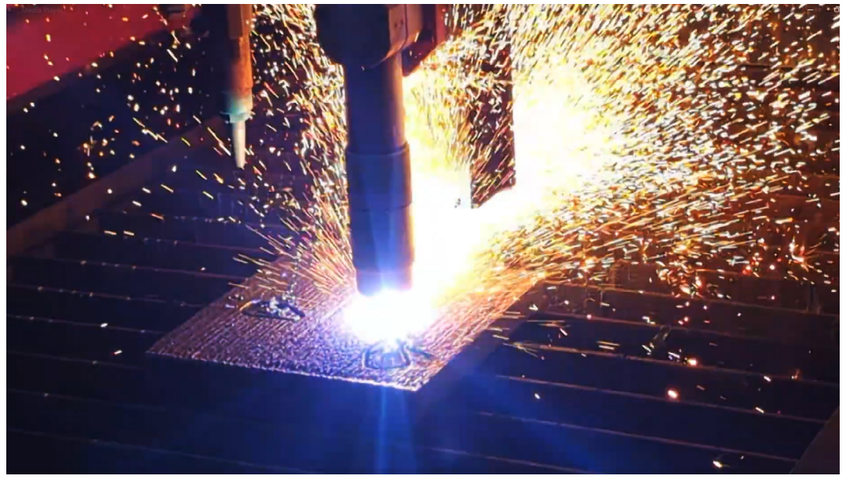


Figure 3.23 Plasma Arc Cutting



Figure 3.24 Plasma cut plate being transferred using a G-clamp

One of plasma cutting's key benefits is its ability to cut through all conductive metals, including aluminum, steel, and stainless steel, much faster than oxy-fuel methods for thinner materials. However, its limitations include reduced efficiency for thicker materials above 1-1/4-inch, due to which the WAAM plate was printed at a scale that produces a thickness of 1 inch.

3.4.6 Experiment 2 – WAAM hemisphere

The second WAAM fabrication involved a hollow hemisphere with a diameter of 300 mm. This print aimed to investigate the challenges of achieving curvature while accounting for the gravitational effects on the weld pool. A hemisphere, in particular, is significant in testing this because it introduces complex geometrical constraints that influence material deposition, cooling rates, and structural integrity. Unlike simpler curved surfaces, a hemisphere presents varying inclinations that challenge the consistency of the weld pool, making it an ideal form for assessing how gravitational forces impact layer adhesion, distortion, and overall print feasibility in WAAM processes.

The arc-on (printing) time was approximately four hours, but the entire process spanned several days. Initial setup and basic programming were first completed on a separate day, followed by the commencement of the printing process the following morning. The print continued for five days. During the first four days, the process was done from 8:00 AM to 8:00 PM daily, while on the last day, the print was completed around 1:00 PM.

The configuration of the print was done as per the manufacturer recommendations, setup using the Teach Pendant. The print consisted of layers deposited sequentially, with each layer starting and stopping at four seams located at the 12, 3, 6, and 9 O'clock positions. To prevent material weaknesses at repetitive start-stop points, the starting point and clockwise or counterclockwise deposition direction were randomized for each layer, in reference to the welding recommendations by Prof. Tam, stated in Table 3.4.

After each layer, the structure was allowed to cool to approximately 40–70 °C to enable cleaning, measuring the new height, and adjusting the robot's program to accommodate the updated circle radius, due to which the overall process was lengthy. This process was also necessary because the aim of this fabrication part was to carry out the study in two phases. First part consisted of studying the form in the ring form that required monitoring the process after the deposition of each weld layer. The second part was to study the form as a whole in terms of it surface curvature and finish. The progress made each day is shown in Figure 3.25.



Figure 3.25 Hemisphere print progress day 1 to day 5 - Above: Ring form, Below: Surface curvature

Supporting layers were built, when necessary, as the new circle was not always adequately supported by the preceding layer. These supports form a part of the final welded structure. Constructing these horizontal supporting layers presented a significant challenge, as the orientation of the part or the robot could not be altered.

The fabrication also utilized the ER70S-6 weld wire with a 0.035 inch diameter, with a wire feed speed of 200 inches per minute (ipm) and a linear travel speed of 20–22 ipm, interpolated into circular motion by the robot. The welding power setting was 900 W, yielding a measured voltage of 15–17 V and a current of 100–125 A. Deposition efficiency was approximately 90%, with minimal spatter. All these specs were maintained as per the manufacturer recommendations, with some modifications done in reference to the previous experiments carried out by the welding lab. The robot manipulated the welding gun to move in circular paths and was held perpendicular to the surface of the build. The final weighed 4.63 kg. The surface did not follow the hemisphere shape correctly at the top due to problems in execution, which could be eliminated if a proper slicing program is used to define the tool paths.

3.4.7 Limitations in WAAM procedures

The WAAM process posed several constraints that affected the design and production of the joint structures. In this study, the primary limitations encountered included the difficulty in printing cantilevers, thin struts, and complex curvatures. WAAM relies on self-supporting geometries, requiring careful deposition sequencing and angular orientation adjustments to mitigate deformation and ensure structural integrity. In fabricating intricate and complex geometries, one major limitation was the restricted degrees of freedom in standard six-axis robotic arms, which makes it difficult to access certain deposition angles. In complex multi-directional joints, certain areas become hard to reach, resulting in inconsistent weld fusion or poor material

deposition. Hence, this necessitated several design modifications to ensure the form's structural integrity and compatibility with the WAAM process. This limited the form exploration to cater to the capabilities of the available robot. If a more advanced robot, equipped with eight-axis robot arm was available, it would have allowed for additional range of motions, that could have made it possible to fabricate intricate forms without compromising the design. An 8-axis robot comes equipped with turn-able tables, allowing to fabricate forms that are much more advanced than those produced in this study [279].

Reliance on simulation tools, like digital stress analysis to assess the joints' performance was another limitation brought by the inability to fabricate the designed forms and test them physically. While digital analysis provides valuable insights into structural behaviour, they can't fully replicate how the joints would perform in real-world scenarios. Hands on physical testing in a civil lab could have provided a much deeper understanding of their behaviour under various conditions. For example, tensile strength tests would reveal the maximum force the joints can bear before failing, while compression tests could evaluate their performance under heavy loads. Fatigue tests, which simulate repeated loading, would help assess durability over time, and impact tests could show how well the joints withstand sudden shocks or extreme forces. Additionally, shear tests would measure the joints' stability against forces acting parallel to their surfaces. These physical tests would validate the structural connections and provide essential data to refine the designs further, ensuring they meet both practical and theoretical expectations.

The lab accessibility was also limiting, especially given that it is a central facility for welding and manufacturing research, creating a high demand and busy schedule for it. This limitation directly impacted the depth of the results presented in this study, as fewer iterations and comparative tests could be conducted than initially planned. With more time in the lab, additional prototypes could have been tested, providing a broader and more detailed analysis of the designs.

Chapter 4

Results and Discussion

This chapter outlines the findings from different research stages, concentrating on physical prototyping and digital analysis. By examining various aspects of additive manufacturing such as FDM PLA printing and Wire Arc Additive Manufacturing (WAAM) to digital stress simulations, the results provide valuable insights into the challenges and potential of creating complex joint geometries. The discussions focus on assessing the structural integrity, production viability, and material behaviour of the examined designs, emphasizing essential design factors and avenues for enhancement.

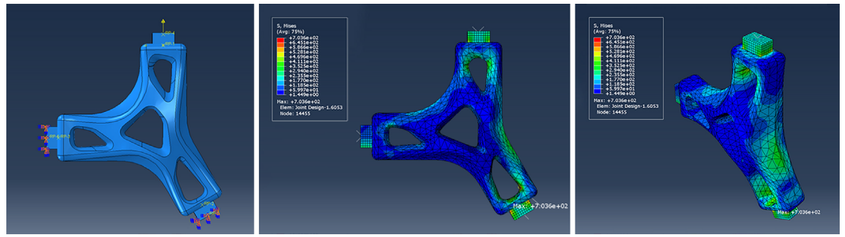
4.1 Digital stress analysis

The structural integrity of steel connections is critical in ensuring the safety and performance of architectural and industrial applications. For this, digital stress analyses of the inflated joint in Abaqus were performed under various loading configurations that provided comprehensive insights into its structural performance. Reference Points (RP) were assigned to each of the connection points where the load combinations were applied. The results highlighted distinct stress distribution patterns across various configurations involving moments and point loads applied to the connection points. The analysis generated a colour-coded gradient visualization of the stress distribution, highlighting specific areas of concern. Regions experiencing higher stress appeared in warmer tones, while the cooler tones of green and blue indicate low-stress areas. The following cases were performed to analyze the performance of the connection joint:

Case I: A single point load at the upper branch

The first study case (Figure 4.1) involved a 1 kN point load at the upper vertical connection branch at RP-4 while the other two branch connections at RP-5 and RP-6 were subjected to fixed supports. This setup resulted in a maximum stress of 703.6 Pa, which is only 0.00000036% of steel 200 GPa yield point,

with stress concentrated near the inner corner of the bottom branch near the RP5. This localized stress indicated the joint's ability to handle light point loads with minimal deformation, showcasing structural stability.

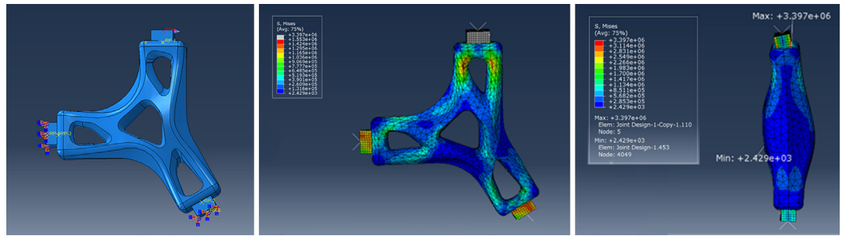


(a) (b) (c)

Figure 4.1 Case I: (a) Loading conditions, (b) and (c) Stress results

Case II: Moment Load at upper branch

In the second scenario (Figure 4.2), instead of a point load a moment load of 1 kN.m was applied at RP-4 in the clockwise direction while again the other two supports were fixed. This configuration produced the highest stress levels, with a maximum of 3.4 MPa (0.0017% of steel yield point) at the connection point and 1.55 MPa (0.00078% of steel yield point) within the connection. Stress was mainly concentrated at the corners close to the connection points, indicating that moments amplify stress more significantly than point loads. The form also experienced slight deformation, amplified by a large deformation scale factor.

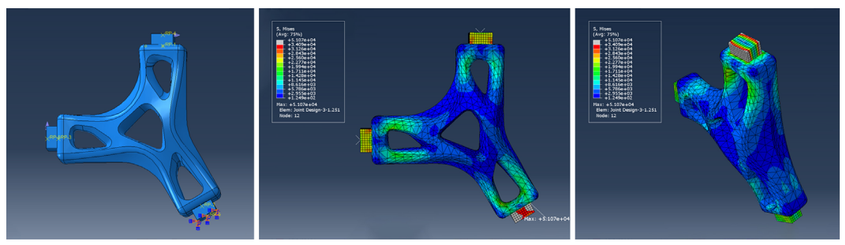


(a) (b) (c)

Figure 4.2 Case II: (a) Loading conditions, (b) and (c) Stress results

Case III: Dual Moments at upper and left branch

Figure 4.3 showcases case three, which also studied the impacts of clockwise moments, but applied at both RP-4 and RP-6, with RP-5 representing a fixed support. The maximum stress for this configuration was 51.07 kPa (0.000026% of steel yield point), concentrated near RP-5 and within the connection. Internal stresses peaked at 22.61 kPa (0.000011% of steel yield point), distributed more evenly due to the dual moment application. This configuration improved load distribution compared to a single moment load, although stress concentrations remained near RP-5.

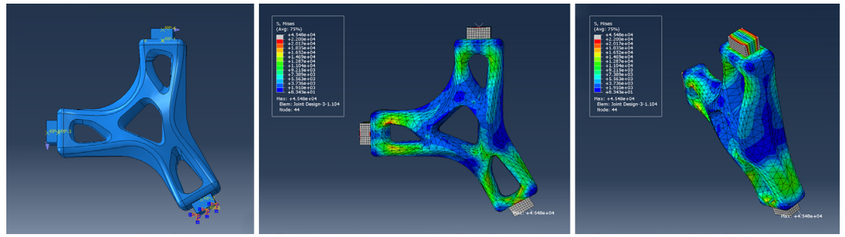


(a) (b) (c)

Figure 4.3 Case III: (a) Loading conditions, (b) and (c) Stress results

Case IV: Counteracting Moments at upper and left branch

The next configuration (Figure 4.4) applied a 1 kN.m clockwise moment at RP-4 and a 1 kN.m counterclockwise moment at RP-6, while RP-5 was fixed. This resulted in a maximum stress of 45.48 kPa (0.000023% of steel yield point), slightly lower than that produced in Case III. Stress concentrated near RP-5 and at the extrusion near RP-6, where the clockwise moment was applied. The maximum internal stress was approximately 22.0 kPa (0.000011% of steel yield point).

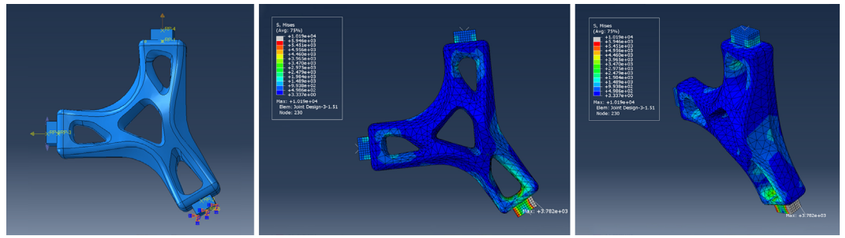


(a) (b) (c)

Figure 4.4 Case IV: (a) Loading conditions, (b) and (c) Stress results

Case V: Dual Point Loads at upper and left branch

The fifth case (Figure 4.5) featured two point loads of 1 kN applied at RP-4 and RP-6, with a fixed support at RP-5. This setup yielded the lowest stress, with a maximum of 3.78 kPa (0.0000019% of steel yield point) concentrated near RP-5. Internal stresses reached 1.65 kPa (0.000000825% of steel yield point), demonstrating a more evenly distributed load compared to moments.

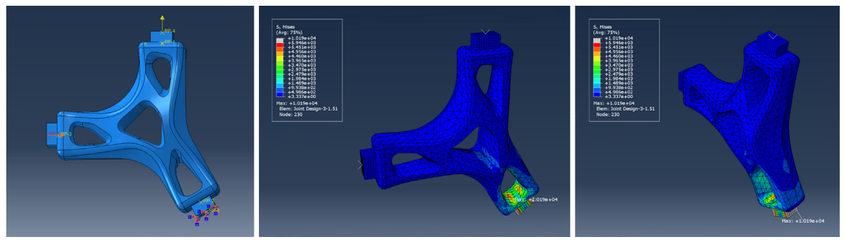


(a) (b) (c)

Figure 4.5 Case V: (a) Loading conditions, (b) and (c) Stress results

Case VI: Opposing Point Loads at upper and left branch

Similar to Case V, Case VI also studied two point loads of 1 kN at RP-4 and RP-6 but in opposite directions, with RP-5 having a fixed support (Figure 4.6). This resulted in a maximum stress of 10.19 kPa (0.0000051% of steel yield point), concentrated near RP-5. Internal stresses peaked at 5.95 kPa (0.000003% of steel yield point), with moderate stress levels distributed along the bottom branch.

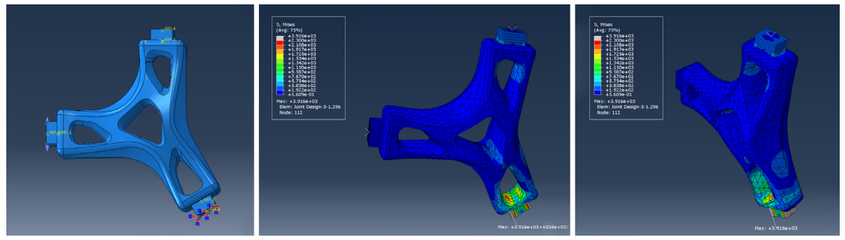


(a) (b) (c)

Figure 4.6 Case VI: (a) Loading conditions, (b) and (c) Stress results

Case VII: Opposing Moments at the left branch

The last configuration (Figure 4.7) introduced two opposing moments of 1 kN.m but at the same point – RP-6, with a fixed support at RP-5. This configuration produced a maximum stress of 3.92 kPa (0.000002% of steel yield point), with stress concentrated near RP-5. Internal stresses reached 2.3 kPa (0.0000012% of steel yield point), with reduced stress levels.



(a) (b) (c)

Figure 4.7 Case VII: (a) Loading conditions, (b) and (c) Stress results

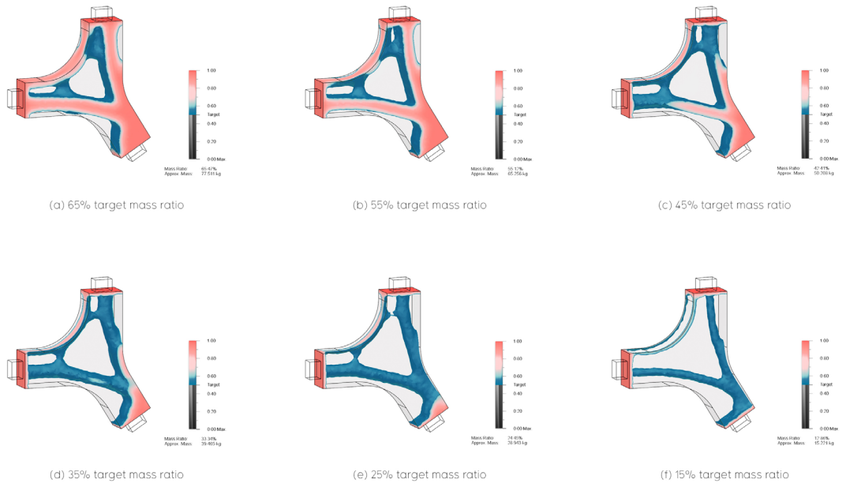
Overall, moments (Case II, Case III, and Case V) generated higher and more widespread stress distributions compared to the point loads (Case I, Case V, and Case VII), which resulted in localized stress near connection points. Stress concentrations were consistently observed at corners, protrusions, and intersections. These regions align with critical areas identified in stress concentration factors (SCF) studies by Schubnell et al. [280], where SCFs were highest near the weld toes of a T-welded joint, emphasizing the need for geometric refinements to reduce localized stress amplifications. Rotational forces, as seen in Cases II and III, produced the highest stress levels due to their amplifying effect on SCFs. Further, the stress results support the observations in WAAM processes by Zhang et al. [239], where anisotropy and stress concentration increased along fusion lines under directional loads (forces applied in specific directions).

To address these findings, potential design refinements could include reinforcing the thinnest sections of the joint by manipulating the void form to reduce stress concentrations [280]. Reducing abrupt changes in geometry can also improve the stress distribution in such cases [239]. Additionally, exploring alternative load scenarios and combinations in future iterations could provide further insights into the design's performance and optimization. These enhancements could contribute to greater structural resilience and improved functionality in the final implementation. Future analyses exploring additional load scenarios and geometric refinements can further enhance the connection's performance.

Despite these concentrations, all stress levels were well below the yielding stress of steel (200–400 MPa). This ensures the safety and reliability of the connections under typical loading conditions. These results emphasized the importance of understanding load distribution and optimizing designs to minimize stress concentrations in critical areas. Configurations with opposing forces or moments, such as in Cases IV, VI, and VII, demonstrated improved stress distribution and reduced peak stresses compared to unidirectional loads, suggesting that balancing loads can alleviate stress concentrations and enhance overall performance.

4.2 Topology optimization

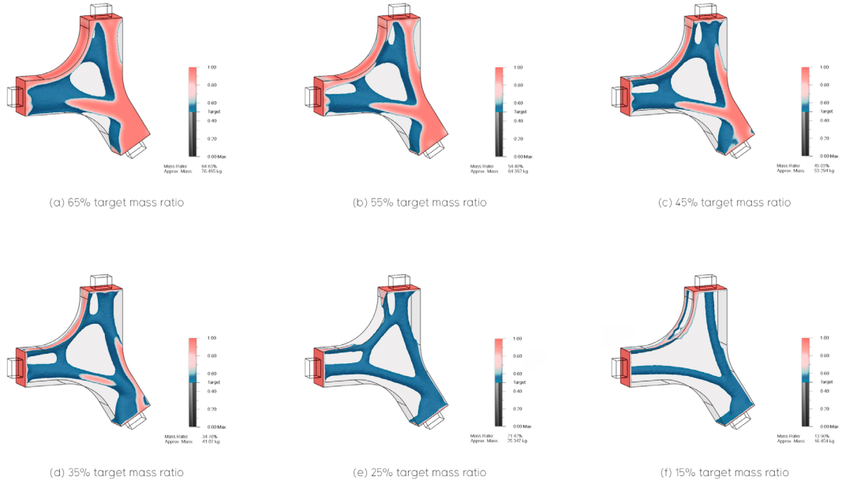
Topology optimization for a three-branch connection was done to generate forms that intelligently remove materials from unnecessary zones, focusing only on the critical areas. While keeping all the parameters same, two sets of results were obtained by adjusting the model-based mesh size between 2% (Figure 4.8) and 1% (Figure 4.9). Although the void to solid configurations is similar for both mesh sizes in each target mass, having a larger mesh size created a rough surface while a smaller mesh increased the surface quality, generating a smoother surface finish comparatively. A similar observation



(a) 65% target mass ratio (b) 55% target mass ratio (c) 45% target mass ratio

(d) 35% target mass ratio (e) 25% target mass ratio (f) 15% target mass ratio

Figure 4.8 Topology optimization results – 2% mesh size



(a) 65% target mass ratio (b) 55% target mass ratio (c) 45% target mass ratio

(d) 35% target mass ratio (e) 25% target mass ratio (f) 15% target mass ratio

Figure 4.9 Topology optimization results – 1% mesh size

is supported by A. A. Al-Tamimi [266], who investigated mesh dependency in orthopedic bone plates and concluded that finer meshes result in higher material removal, capturing more precise geometries, whereas coarser meshes reduce computational cost but sacrifice detail.

Setting the mesh size slightly higher, in this case at 2%, with a difference of 1%, the resulting outcomes produced more flat surfaces and less rounded struts, while having the mesh at 1% allowed the configurations to produce a more defined strut profile and less inconsistencies.

However, the overall form configurations for both mesh sizes were the same. This aligns with findings from Amir and Majdouba [281], where a finer mesh parameterization demonstrated a significant impact on optimization outcomes by achieving greater design accuracy. Thus, depending on the end use, adjusting the mesh value aids to generate significant difference in the overall object quality.

When comparing the form change between 15% target mass and 65% target mass (Figure 4.10), there are notable differences in the geometry. A lower target mass produced a very hollow form, with very thin strut members connecting the three nodes, focusing only on essential load-bearing paths while a high target mass produced bulkier forms with smaller voids. An analysis of the 15% target mass indicated that the thinnest strut profile was 0.25 inch thick while the thickest width was 2 inches. The majority of the mass was removed, creating a large triangular shaped central void. As the target mass increased from 15% to 25%, the void got sub-divided into three parts – a triangular void in the center while elliptical voids at the branches. While the thinnest strut profile was still 0.25 inch, present at only one location, the remaining strut thicknesses started increasing, with varying widths between 0.75 inches and 2.25 inches. With a continued increase in target mass, the voids became smaller while the struts became more defined and thicker, reaching up to 3.5 inches.

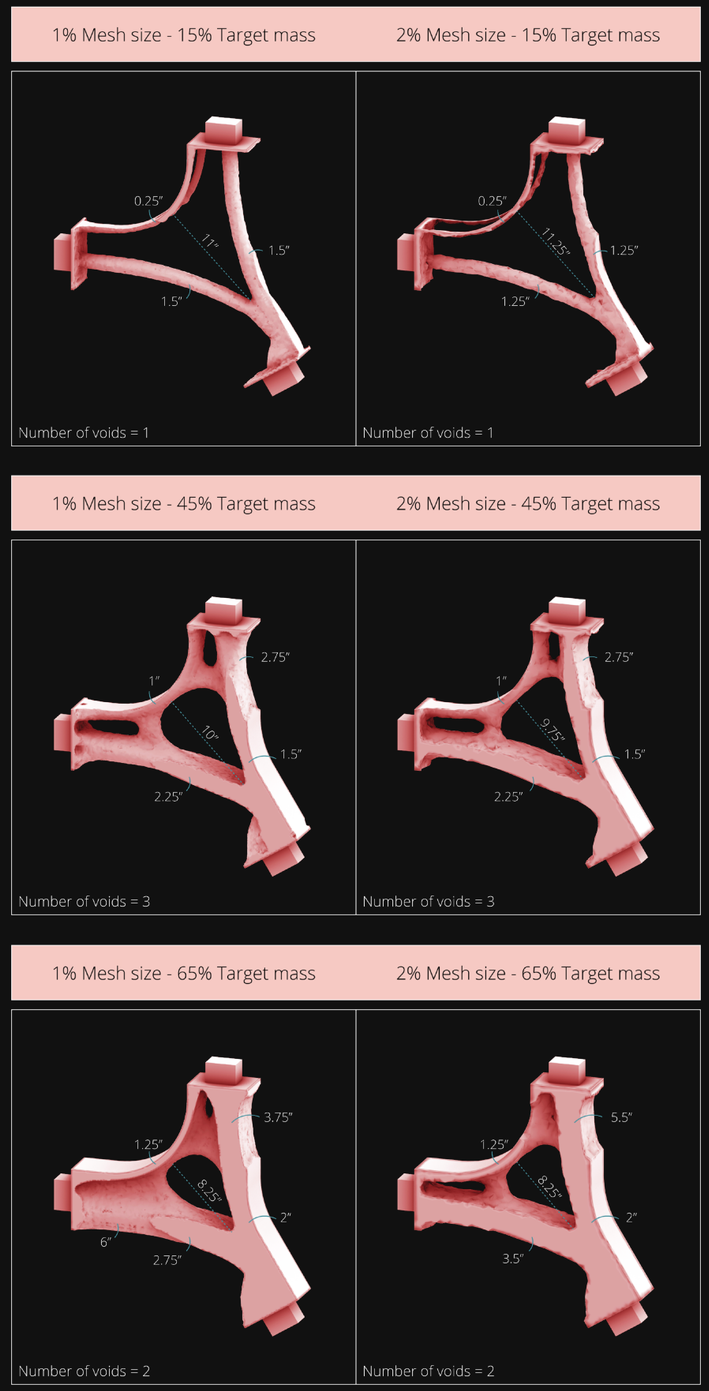


Figure 4.10 Progression of topology optimized joints as the target mass increased

This geometric variability between different target masses echoed topology optimization results in literature, such as in the study by Erőss and Markovits [282], who displayed results obtained for multiple target masses, ranging between 80% and 13%. With a decrease in the target mass, while the overall geometric configuration was similar, the thickness of the side walls greatly reduced, leaving behind thin connection members. Further, as elaborated by Mike Fiedler [283], a smaller target mass reveals the critical load path areas in a form, because mass reductions cater to both structural efficiency and material conservation.

The connection between the two upper perpendicular branches produced thinner struts while the connections of both with the third branch were wider due to the absence of a void at the branch. This was a consistent design feature throughout all the experiments and between both the target meshes. Even with the increase in the target mass, the thin strut maintained its sleek geometry and profile while the other sides started displaying flat edges and surfaces. These flat surfaces were more dominant in the 2% mesh size because the 1% mesh produced smaller grain and hence had the ability to remove material in a more refined manner. These impacts of mesh also corelate to teachings of Mike Fiedler from Autodesk [283], who indicated that a coarse mesh with fewer elements leads to larger, more obvious changes when elements are removed, while a finer mesh allows for more strategic and refined adjustments to the geometry.

Further, as seen in Figure 4.10, as the target mass reached 65%, the voids became significantly smaller. The central void reduced from an initial perpendicular height of 11.25 inches and side length of 18.25 inches in the 15% target mass to a height of 8.25 inches and side length of 7 inches in the 65% target mass. The voids in 65% target mass for both the mesh sizes got reduced to two, leaving behind a central void and one branch void to achieve the required mass.

The change in mesh size also impacted the geometry significantly, highlighting important considerations for joint design. The forms generated with 1% mesh exhibited smoother curves and refined voids, presenting a more polished and balanced geometry. In contrast, the 2% mesh stood out for its flat and rough surface finish, prioritizing durability and strength over refinement. These findings reaffirm that mesh size plays a pivotal role in topology optimization outcomes, particularly when aiming to balance computational efficiency with geometric precision. For applications requiring high accuracy and surface quality, finer meshes should be prioritized, while coarser meshes may suffice for early-stage conceptual designs or components where refinement is less critical.

4.3 PLA prototyping

The PLA prototyping phase served as a critical step in evaluating the feasibility of topology-optimized joint designs and their subsequent simplifications. By translating digital models into physical forms, this stage highlighted the practical implications of design decisions, material constraints, and manufacturing methods. The process provided tangible insights into how topology optimization influences joint geometry and print stability, paving the way for further refinements tailored to additive manufacturing techniques. All the prints were scaled down to meet the print bed limitations.

The initial PLA prototyping focused on topology-optimized joints, allowing for a physical study before making further design adjustments. The joints were printed in a horizontal orientation and analyzed on the creation of their support structures to understand if changing the orientation of the obtained forms would be favourable for WAAM for various target masses and what improvements can be made to the design to make it compatible with the available six-axis GMAAM robot. The optimized joints provided a base scenario to build further design decisions on, especially to understand the regions

where material can easily be reduced. They also provided a starting point to understand the possibilities and limitations of the WAAM process.

The comparison between the 2% and 1% mesh prototypes revealed significant information about their structural characteristics, print times, and surface qualities, offering valuable insights into joint design. Table 4.1 highlights the print times and the amount of filament used for all the joints. The increase in time is directly related to the mass of the filament used. A higher print time suggests that the product has a higher mass and hence a higher use of the filament. Further, the infill density for all the joints was kept at a low value of 8% because the struts were not wide or high enough to require a dense infill support (Figure 4.11).

Mesh 2%			
Target mass/%	Print time	Filament used	Infill density
65%	3 hrs 56 mins	30 g / 9.99 m	8%
45%	3 hrs 41 mins	27 g / 8.95 m	8%
25%	3 hrs 20 mins	24 g / 8.17 m	8%

Mesh 1%			
Target mass/%	Print time	Filament used	Infill density
65%	3 hrs 58 mins	31 g / 10.52 m	8%
45%	3 hrs 42 mins	28 g / 9.32 m	8%
25%	3 hrs 28 mins	22 g / 7.45 m	8%

Table 4.1 Results data of topology optimized PLA prototypes

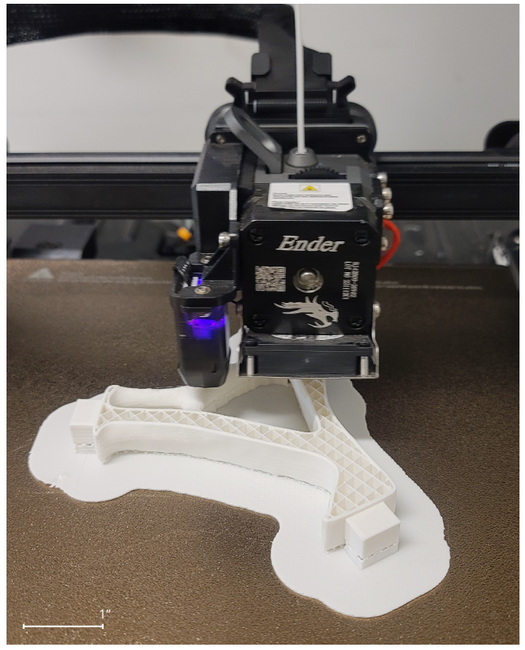


Figure 4.11 8% infill density in Topology Optimized joints

For the 65% target mass (Figure 4.12), the total print time for 2% mesh was 3 hours and 56 minutes, while for the 1% mesh took a total of 3 hours and 58 minutes – the longest time amongst all of them. Next, the 45% target mass (Figure 4.13), the 2% mesh prototype finished in 3 hours and 41 minutes whereas the 1% took 3 hours and 42 minutes, having a difference of only 1 minute. Lastly, for the 2% target mass category (Figure 4.14), the 2% reached a total time of 3 hours and 20 minutes while the 1% took 3 hours and 28 minutes to complete.

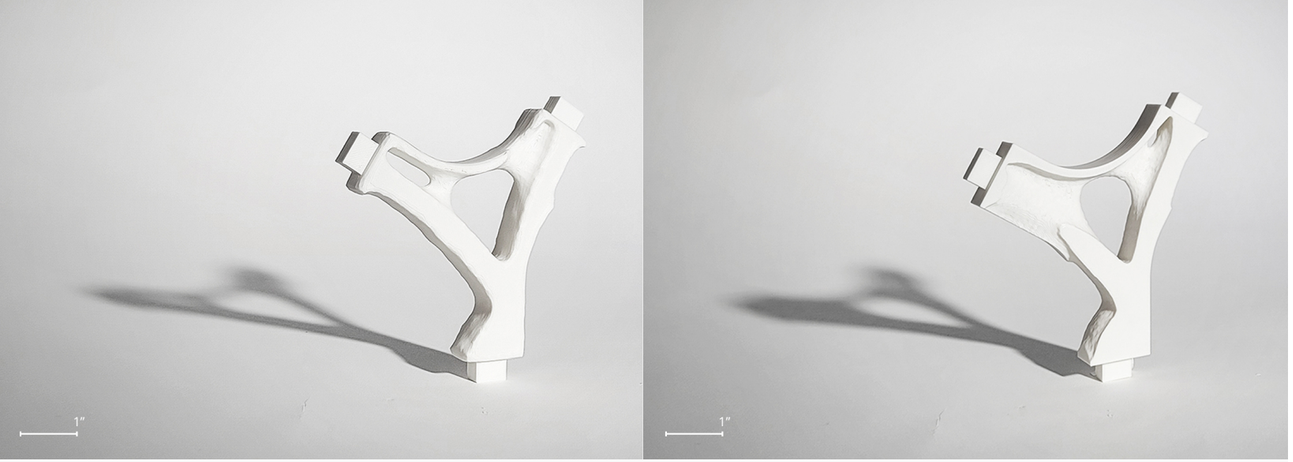


Figure 4.12 65% target mass prototypes at scale 1:6 - Left: 2% mass, Right: 1% mass

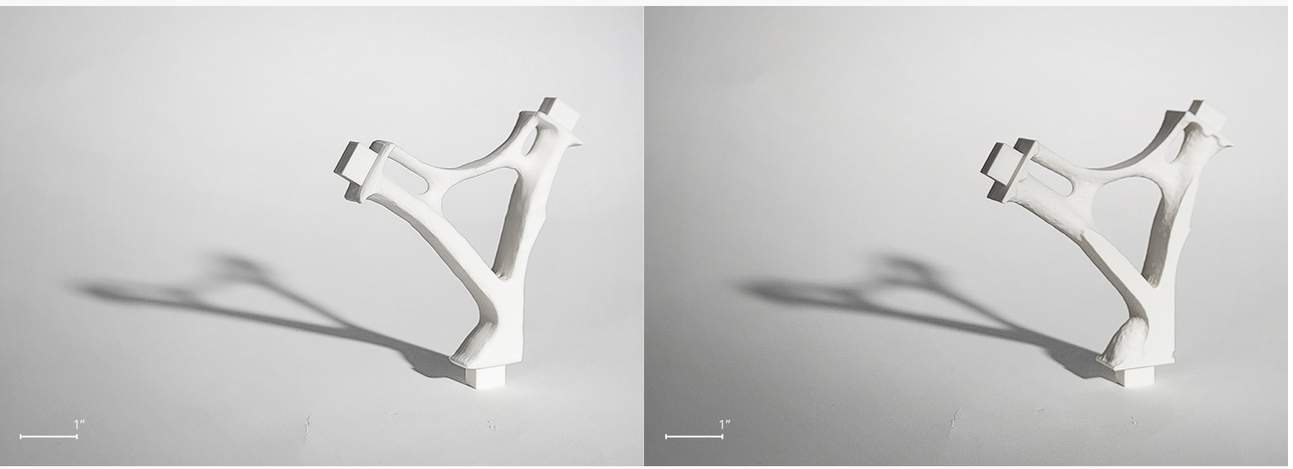


Figure 4.13 45% target mass prototypes at scale 1:6 - Left: 2% mass, Right: 1% mass

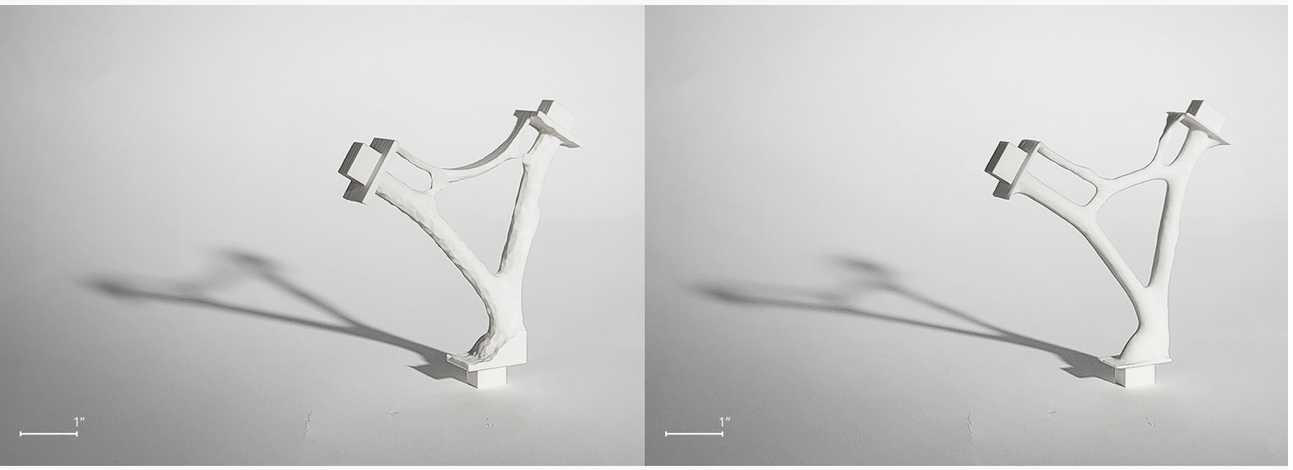


Figure 4.14 25% target mass prototypes at scale 1:6 - Left: 2% mass, Right: 1% mass

The print times for the same target mass joints for both mesh sizes were similar, with minor differences. As expected, the higher the target mass, the longer it took to print the joint. This is also evident from Syamsir et al.'s [123] results for PLA printed shape optimized parts, where they tested 40%, 50%, and 60% target masses. Each part showed a difference of a few minutes to print at the same infill density. Between 40 – 60%, a difference of 20% target mass, the print time difference varied from 15 mins to 23 minutes as per the infill density. This resonates with the current research results, where the print times for target masses at a 20% difference range between 14 to 21 minutes. Despite the significant difference in their mass, the print time for the 25% target masses was only marginally less than the 45% and 65% prints, attributed to a higher volume of built supports. This observation aligned with the findings of Fernandez-vicente et al. [195], where infill density variations impacted material efficiency but did not linearly correlate with reduced printing times due to geometric complexities.

Figure 4.15 displays the support structures for each of the joints, elaborating on the support forms and their density. Between 65% and 45% target masses, there is not much difference in the volume of support built because both these target masses resulted in somewhat flat surfaces. The major difference arises in the 25% target mass that required increased support structures to hold up the part compared to the other joints, especially because of the thinner struts and less flat surfaces. Further, there are also some notable differences between the supports of 1% mesh size and 2% mesh size. Since 2% mesh removes/adds larger chunks of material due to the mesh size, it made the form to be coarser compared to the 1%, impacting the volume of supports needed to retain that shape during printing. 1% mesh created a finer form due to more defined optimization surfaces, leading to better material distribution and void formation and hence, required more structural support during printing. Studying these prototypes revealed most of the material needs to be conserved at the side edges of the target mass connecting the branches with each other, while the central area can be reduced or increased as per the design and fabrication considerations.

2% Mesh Size, 65% Target Mass	2% Mesh Size, 45% Target Mass	2% Mesh Size, 25% Target Mass
		
A higher target mass produced less voids and more flat surfaces, requiring minimal support structures during printing.	As the target mass decreased, void sizes increased and struts became more thin. The joint still majorly consisted of flat regions and so, slightly higher amount of supports is required to print the structure.	At 25%, the joint became very light with thin struts. So, almost the entire base surface of the connection required supports to build it properly.

1% Mesh Size, 65% Target Mass	1% Mesh Size, 45% Target Mass	1% Mesh Size, 25% Target Mass
		
1% mesh produced more refined optimization, hence it required a slightly higher amount of supports than the 2% mesh.	The void size of 1% mesh is similar to the 2% mesh. The supports are concentrated in the same area but are in a higher amount because of the presence of less flat surfaces.	The supports have a more defined profile in compairson to the 2%, and reach the edge of all the three branches. Having a lower target mass, the supports are spread to the entire joint, and have more height in comparison to the 45% and 65%.

Figure 4.15 PLA prototypes print support structures of topology optimized joints

Additionally, the mesh settings and target mass variation impacted the surface quality of the print. Surface finish quality showed notable variation based on the configurations and the density of support structures required. All prints were printed with a 20% support density, a standard setting in Creality Slicer 4.8. A higher target mass produced flat surfaces with high-quality, smooth finishes due to minimal reliance on support structures. However, regions with thin curvatures or complex geometries such as those in 25% target mass required extensive supports, which often led to rougher texture and inconsistent surface quality (Figure 4.16). This occurs because the rounded profile of the struts has very minimal base contact, and this is where the roughness appears more obvious.

2% Mesh Size - 25% target mass	1% Mesh Size - 25% target mass
	
Higher mesh size produced a more coarse surface finish, with the addition to an increased roughness in regions with a support struture	Lower mesh size created less surface texture but display a high surface roughness in the regions attached to supports

Figure 4.16 Surface texture of 25% target mass prints - Left: 2% mesh size, Right: 1% mesh size

To improve the surface textures, mesh smoothing was applied based on Curkovic's [124] study that highlighted the importance of mesh smoothing as part of post-optimization. He emphasized it to be a critical factor in improving surface quality and manufacturability because it allows to remove any inconsistencies. To test this, one joint from each target mass was treated with mesh smoothening in Grasshopper while the other retained its original mesh surface. The results for both the original and treated meshes are shown in Figure 4.17. The 1% meshes with no smoothing showed very little surface texture because the mesh is already refined to some extent. The 2%, however, without smoothing had a very bumpy and rough finish quality, with visible polygonal mesh surfaces, that would be a lot more noticeable on a full scaled model. Both the 1% and 2% produced forms with crisp edges and more defined profiles without any mesh edits.

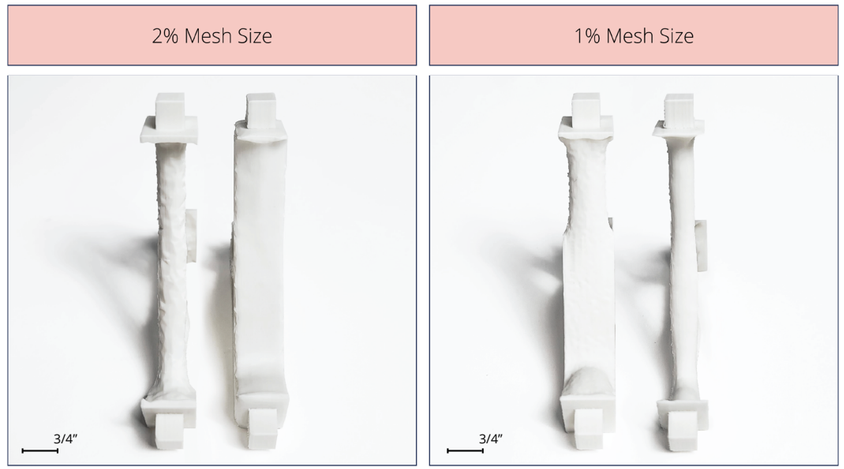


Figure 4.17 Comparison between unsmoothed and smoothed surface for 2% and 1% mesh sizes

For smoothening, the 2% mesh required a more intense mesh processing to significantly reduced the bumpy texture, but it also caused rounding of the edges, giving a more softened look. The 1% mesh, on the contrary, required minimal smoothening and retained its sharp and defined edges to some extent. Mesh finish influences the final form, especially with a process like WAAM that already produces surface irregularities, a coarse mesh may make it feel rough and less visually appealing.

These results are compatible to the observations made by Wang et al. [118], who tested PLA joint prints with different support densities. With a lower density, at 5% and 10%, the supported surfaces presented a very rough surface finish, but as the density was increased to 15%, the surface texture exhibited a smoother finish, improving the overall build quality, however, the impact of supports was still noticeable in curvilinear regions, both in PLA and metal print. Jiang et al. [284], in their review of support structures for additive manufacturing, also concluded that surface finishes can be heavily impacted by the support structures so, print directions, and designing optimized supports can be a way to enhance surface finish. Further, Syamsir et al. [123] also emphasized the significant influence of support placement and density on the final surface texture of the 3D-printed components, highlighting that regions demanding more supports are prone to imperfections caused by material overhangs and the removal process, reaffirming the importance of strategic support planning and surface postprocessing in achieving optimal finishes.

The study of topology-optimized joints using PLA prototyping highlighted critical considerations for integrating topology optimization with WAAM. The optimized joints produced during this research often included forms with complex geometries, thin curvatures, and voids that did not fully touch the base. These features required extensive support structures during printing, especially for reduced target masses (e.g., 25%), which resulted in more defined and intricate forms. However, WAAM inherently lacks the capability to

generate such support structures, limiting its compatibility with designs that rely on extensive supports for stability. This constraint necessitated focusing on joint configurations with flatter surfaces and higher target masses when using WAAM because they reduce the need for supports, as the larger, more continuous contact areas with the base ensure structural integrity during deposition.

However, the trade-off of using higher target masses is the reduced optimization of form. Larger target masses concentrate material across the geometry, leading to bulkier joints with fewer voids and limited material savings. This reduction in the design's structural efficiency and lightweight potential undermines the very principles of topology optimization. While WAAM excels at fabricating robust structures, its lack of support-building capability makes it better suited for simpler geometries with less refinement, thereby restricting its applicability to highly optimized and intricate joint designs.

Additionally, the surface quality resulting from WAAM's layer-by-layer deposition process poses further challenges. The coarse and irregular surface finish typical of WAAM may amplify the roughness observed in topology-optimized forms with complex geometries. As demonstrated in this study, mesh smoothing significantly enhances surface quality, especially for coarser meshes like the 2% size. However, WAAM's inherent limitations in achieving fine surface finishes suggest that designs for WAAM must prioritize configurations with minimal surface irregularities and simple load paths to reduce postprocessing requirements.

Lastly, the results also emphasized the importance of understanding material distribution and load path concentration. Designs with reduced target masses revealed critical areas where material must be preserved for structural stability. In WAAM, ensuring continuous deposition in these critical regions is essential to avoid structural weaknesses. This aligns with the principle that WAAM is better suited for fabricating structures that prioritize robustness over

intricate voids and lightweight design. To maximize the benefits of topology optimization for WAAM, future refinement of the connections focused on balancing form efficiency with manufacturability, to accommodate WAAM's capabilities based on the optimization outcomes.

To further investigate the implications of WAAM fabrication, two operative joints were printed (Figure 4.18). Both these prototypes showed their relationship to the connection branches as well. The first print performed for the pinched joint, having double-sided concave surfaces, took 6 hours and 18 minutes to complete. Conversely, the second print, was done for the inflated joint, consisting of double-sided convex surfaces, resulting in a total print time of 7 hours and 9 minutes. Both joints were fabricated as singular pieces using detachable support structures to study the external form of the joints.

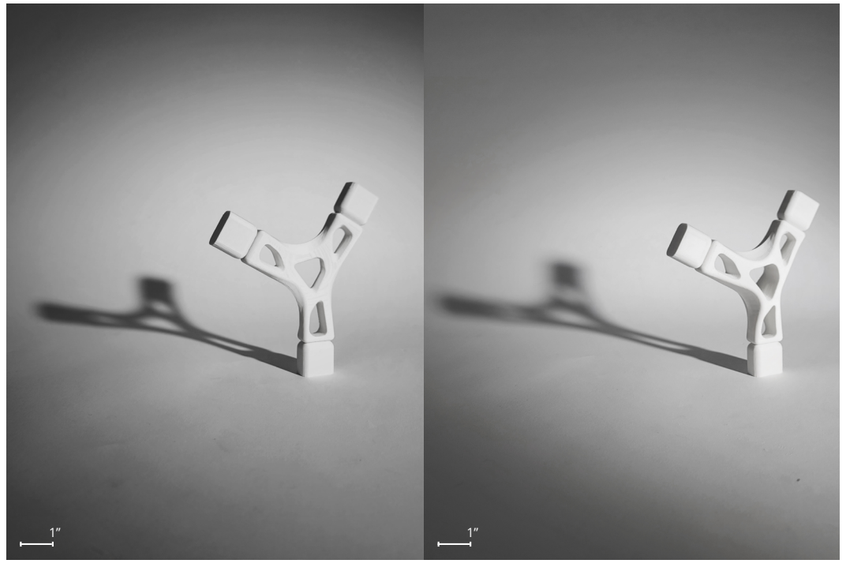


Figure 4.18 Operative design joints at scale 1:6 - Left: pinched joint, Right: inflated joint

Table 4.2 summarizes the print details of the two joint prints. Having wider surfaces, the joints necessitated a higher infill density to create a better support structure for the surfaces, keeping it at 25% (Figure 4.19). The pinched joint had double-sided concave surfaces, reducing its mass considerably compared to the inflated joint with double-sided convex surfaces. However, the print time and the mass of filament used for the pinched joint was still significantly high because of the increased volume of the support structure, similar to the results of the topology optimized joints. Likewise, the inflated joint also required considerable amount of support structure, especially at all three connection branches because the bulge raised the branches off the base.

Joint	Print time	Filament used	Infill density
Inflated	7hrs 9mins	57g / 19.09m	25%
Pinched	6hrs 18mins	52g / 17.56m	25%

Table 4.2 Results data of simplified joints PLA prototypes

The joint forms with their respective support structures are highlighted in Figure 4.20. An observation of these supports indicates that the WAAM process for such a joint in a singular piece is not possible and hence, the joint was designed to carry out the WAAM fabrication in two stages as discussed in Chapter 3 – Methodology. These findings align with Williams et al.'s [215] discussion of WAAM limitations, which emphasized that six-axis robots lack the flexibility for multidirectional welding, making supports essential for complex forms.

In fabricating the two prototypes, understanding their compatibility with WAAM was crucial. Since the research aimed to optimize connection designs through WAAM, focusing on the process's ability to achieve curvatures, both the pinched and inflated joints were analyzed based on their integration of

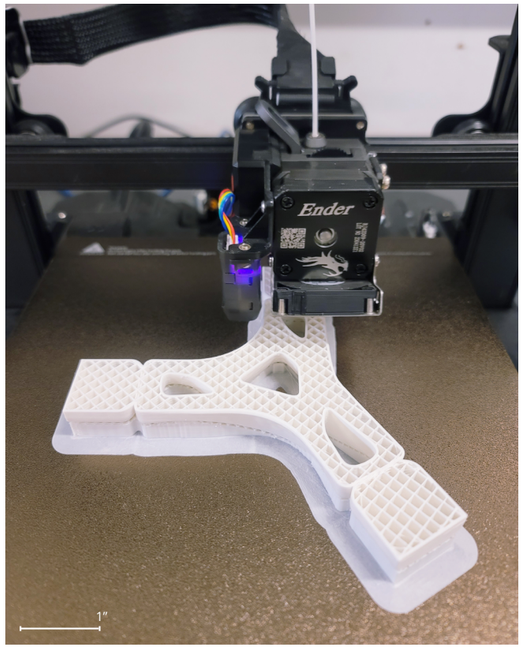


Figure 4.19 25% infill density in operative design joints



Figure 4.20 Left: Concave joint (top) with supports (bottom), Right: Convex joint (top) with supports (bottom)

curvatures. Further discussions and analysis were then centered around the inflated joint, due to the presence of more amplified curvilinear surfaces in it that challenge the WAAM fabrication.

As previously outlined, the WAAM fabrication process for these joints was set to be carried out in two steps in the flip-over printing. Therefore, the subsequent prototyping focused on studying one half of the inflated joint, analyzing it in sectional forms. For this, the form was bisected along the center and printed with a flat base to study the pattern of support structures. The support structures generated in PLA printing correlate to the supports that would be required in WAAM, thus, sectional prints helped to analyze the limitations of the WAAM robot to fabricate the given forms.

Figure 4.21 highlights the front view of a hollow part printed section with its support structure. An analysis of the support structure indicates that the tapered surfaces on the side can easily support themselves on the base layer but as the form transitions to the top surfaces, it necessitates the placement of supports during printing. As shown in Figure 4.22, the supports are only concentrated in the regions beneath the top surface because there is not enough curvature/arching to create self-supporting angles. Figure 4.23 further highlights a part of the structure, zoomed in at one end of the joint branch, for better understanding of the support proportions.

From here it was more noticeable that much of the region around the angled side walls were built without the need for reinforcement, but the entirety of the top surface could not be held up on its own during fabrication. The WAAM technique is comparable to the FDM process in the way that it builds the form layer by layer. A six-axis robot used in this study has a very similar deposition pattern that cannot support multidirectional welding, limiting its ability to fabricate complex hollow interiors without support structures. In that case, achieving complex top surfaces is feasible only if the form is solid or comprises self-supporting angles.

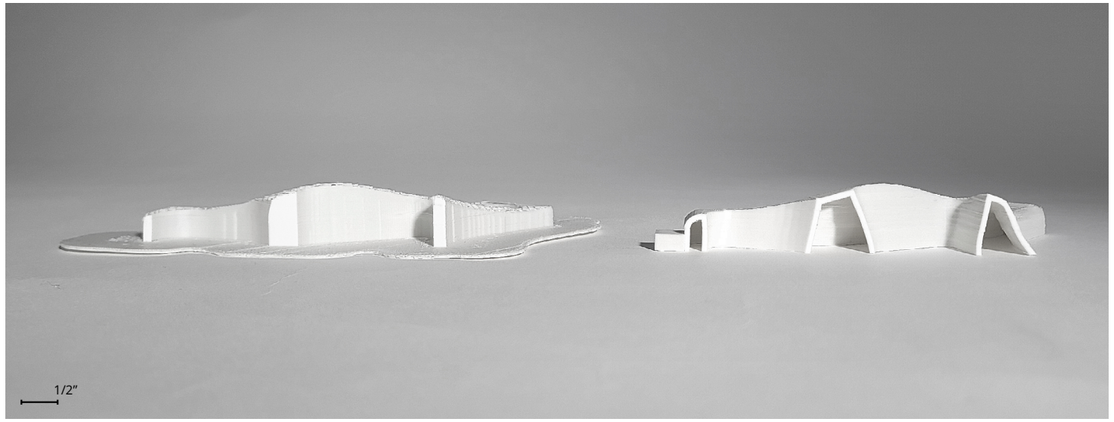


Figure 4.21 Front view of the hollow inflated joint section printed in PLA at a scale 1:4 – Left: support structure, Right: form

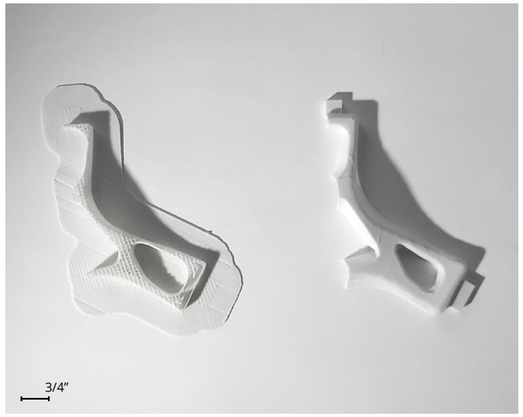


Figure 4.22 Top view of the hollow inflated joint section printed in PLA at a scale 1:4 – Left: support structure, Right: form

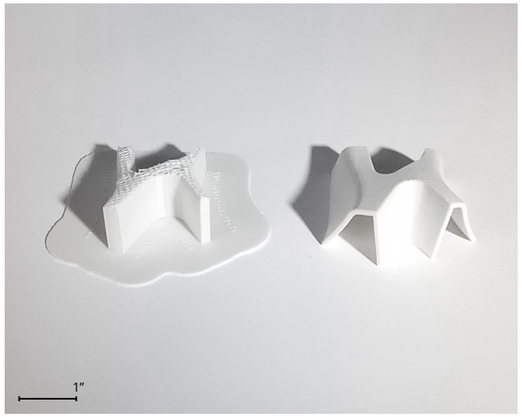


Figure 4.23 Double sided PLA printed section of an inflated joint branch at a scale 1:3 – Left: support structure, Right: form

Similar findings by Evjemo et al. [285] and Williams et al. [215] highlight the limitations of six-axis robots in depositing material for overhanging or hollow geometries. These systems are confined to predefined paths, unable to achieve complexity or weld in multi directions. Evjemo et al. [285] further demonstrated that non-vertical material deposition (depositing material at an angle, aligning it with the geometry) using six-axis robotic systems can mitigate some support needs but cannot fully address challenges posed by overhanging geometries.

Contrary to this, literature has developed methods that can create thin-walled curved overhangs using WAAM. An example of this is by Teng Foong et al. [232] who introduced an adaptive method using an overhang slicer algorithm and a biharmonic spline interpolation model that helps to dynamically adjust torch speed based on overhang angles, ensuring consistent layer height. They demonstrated that reducing torch speed for steeper overhangs of up to 37.5° effectively maintained layer height. Additional post-processing of toolpaths, such as reversing travel directions and adjusting start and end points, further improved layer uniformity, successfully producing high-quality overhangs with minimal distortions. So, advanced systems can support cantilevers in WAAM but it requires additional processing.

Figure 4.24 highlights the unsupported surfaces in the inflated joint, showcased at the sectional cuts through the central void, looking towards each branch. The sections show the void and solid geometry in relationship to each other. In view of this, Figure 4.25 shows the same sections, with alterations to form, making it internally solid. A solid interior is fully supported through the deposited mass and any surface curvature can be achieved. This change can retain the original geometry but at the expense of utilizing more time and resources in the fabrication process. Figure 4.26, on the other hand, shows the form without any changes, suggesting that an advanced WAAM robot, such as with eight-axes, can achieve a more complex form that is otherwise not attainable using a six-axis robot.

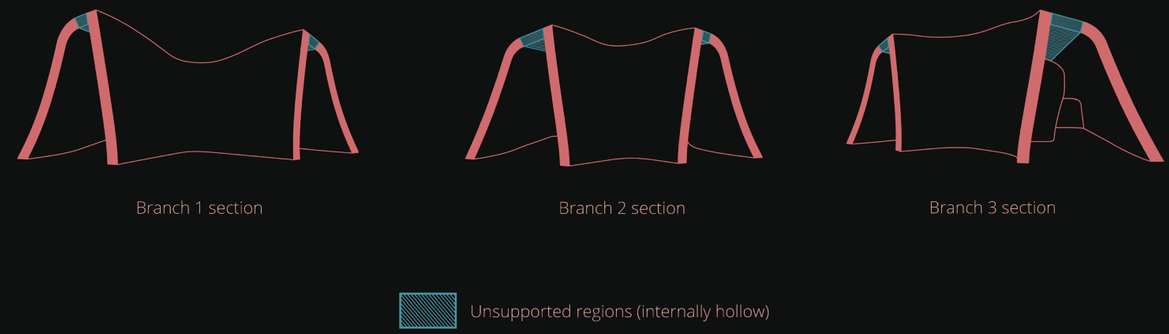


Figure 4.24 Inflated joint branch sections indicating the unbuildable regions for a six-axis robot

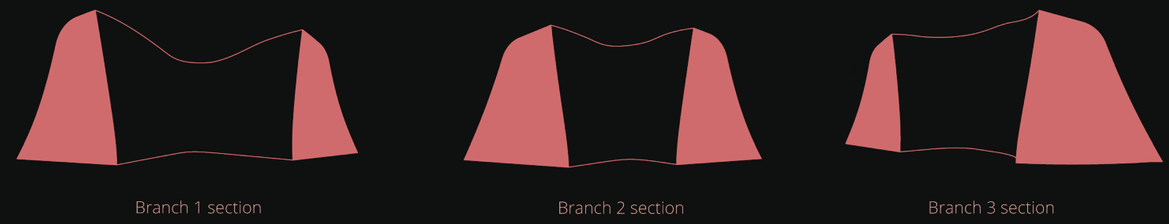


Figure 4.25 Inflated joint proposed branch sections to show how a six-axis robot can manufacture the form

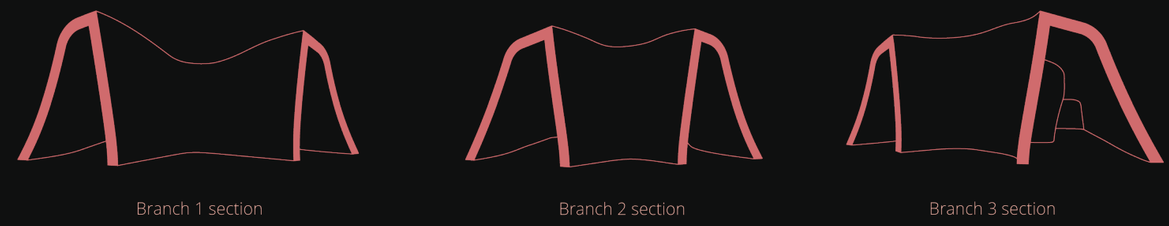


Figure 4.26 Inflated joint branch sections showcasing the joint form that can be fabricated using an eight-axis robot

Overall, a conclusion made by Evjemo et al. [285] and Williams et al. [215] on their results suggested that WAAM holds the ability to fabricate intricate designs but their dependency on support structures for cantilevered regions remains a critical limitation to explore its full potential. Since the need for supports can't be ignored in less advanced WAAM tools, methods such as topology-driven support optimizations and advanced tool path strategies can aid in producing forms with complex geometries.

4.4 WAAM procedures

The exploration WAAM prototypes was a pivotal step toward understanding the complexities and capabilities of this technique. In this section, three WAAM prototypes, were analyzed to identify and understand challenges associated with material deposition, thermal management, and structural stability. These experiments provide critical insights into optimizing parameters such as heat input, deposition rate, travel speed, and layer adhesion for diverse geometries.

4.4.1 WAAM plate

The fabrication of a WAAM plate served as the initial step in understanding the fundamental parameters and challenges associated with the WAAM process. The plate was set to a size of 280 mm in length, intended to be printed vertically at a suitable height as per the joint size of 260 mm, to assess the interlayer bonding. Being a flat geometry, the plate served as a baseline to evaluate the dimensional accuracy, observing any discrepancies between the assigned and the fabricated dimensions of the WAAM part. The goal was to establish a clear understanding of fundamental parameters, including weld paths, deposition rates, surface quality, and layer adhesion, before progressing to more complex geometries. This preliminary study was critical for identifying key variables and constraints that would influence subsequent fabrications of more complex geometries.

A notable observation of the WAAM plate was the variance in dimensions, where the length measured 275 mm rather than 280 mm, showing a minimal deviation from the original size, with a reduction of 5 mm due to edge curvatures and bending (Figure 4.27), resulting in a 1.8% decrease. Similar results were observed by Wall et al. [217], who experienced craters at the end of the bead path. Through further experiments they demonstrated that by enabling precise control over the start and stop current timing, these craters can be reduced because it allows the robot to pause effectively at the end of each layer.

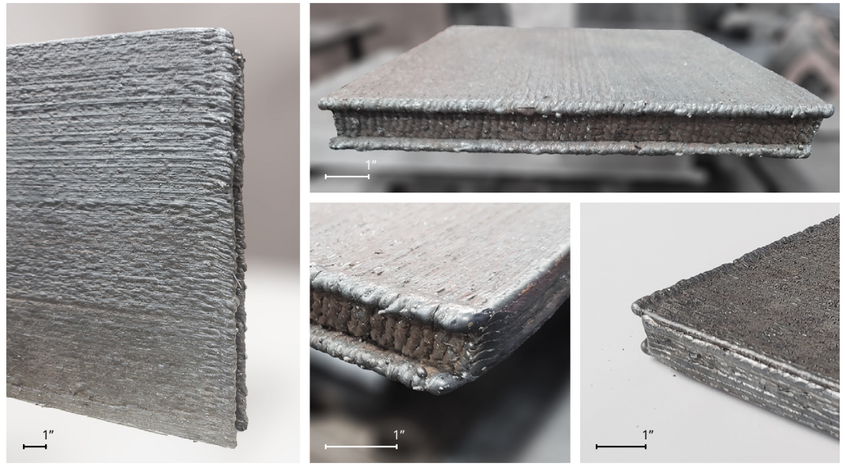


Figure 4.27 WAAM plate - Edge finishes

The height of the plate reached 260 mm where the print was stopped. Vertically, the correct dimensions were obtained by taking continuous measurements during the printing process. This is because vertical layers face dimensional discrepancy largely due to the partial melting of layers during deposition,

causing the weld height of each preceding layer to decrease as new layers are added. This behaviour highlighted the material anisotropy inherent in WAAM, where the WAAM-L direction showed superior stability and bonding due to grain alignment along the deposition path. In contrast, the WAAM-T direction exhibited weaker interlayer adhesion and greater susceptibility to height reductions caused by uneven thermal gradients. Adjustments to heat input and deposition parameters specific to WAAM-T can mitigate such discrepancies by enhancing the layer cohesion [104].

These findings also mirror observations in the WAAM literature, which point to heat input and thermal gradients as major factors affecting layer stability and dimensional precision [217], [286]. Rosli et al. [286] further demonstrated the correlation between the dimensional accuracy and the heat input by plotting results from different experiments that vary these perimeters showing that a lower heat input resulted in less dimensional change, providing a solution of maintaining dimensional precision. Laghi et al. [104] concluded that by carefully optimizing parameters such as heat input and deposition rate, the anisotropic effects in WAAM-T and WAAM-D directions can be minimized, ensuring uniform layer bonding across all orientations.

Although some dimensional discrepancies were observed in the plate, the deposition rate of 1.9 kg/hr ensured a good built quality. Williams et al. [215] found through various experiments that a range of 1-4 kg/hr produced efficient and reliable fabrication without compromising part fidelity. A lower deposition rate results in a better deposition of the weld beads, and a lower buy-to-fly (BTF) ratio, which is a measure of the amount of raw material acquired vs the material used in making a finished part [216], of less than 1.5. A lower ratio indicates low material wastage in the process.

The travel speed of 11 mm/s was slightly above the critical threshold of 8.33 mm/s as per literature, which can result in insufficient heat input causing risk of poor interlayer bonding, paired with surface irregularities [285]. However,

this combination of deposition rate and travel speed with the heat input of 230 J/mm improved the deposition uniformity, mitigating defects that occur due to high travel speeds. Therefore, the WAAM plate had good layer adhesion, producing a structurally upright wall.

A physical analysis of the plate build coupled with a comparison from literature provided insights that not only highlighted the critical role of parameter optimization in WAAM but also set a baseline for refining the process for more complex geometries. The plate was further treated with plasma arc cutting to extract a base form of the joint with 50% mass to study the void to surface relationship before further enhancing the joint form using design operations (Figure 4.28).

While the flat plate geometry offered a controlled and straightforward substrate for testing, it inherently limited the potential for producing diverse joint outcomes. Huang et al. [287] highlighted that flat geometries, such as plates, are primarily used for parameter testing and process optimization. While these configurations provide a straightforward platform for studying fundamental deposition behaviours, they lack the flexibility required for producing advanced joint designs.



Figure 4.28 Plasma cut joint form – 50% mass

4.4.2 WAAM hemisphere

The transition from the flat plate to a hollow hemisphere introduced a new dimension of complexity, requiring the WAAM process to accommodate geometric curvature, unsupported regions, and gravitational challenges. The hemisphere was fabricated to explore how the process performs under conditions that more closely mimic real-world applications of WAAM in curved or freeform structures.

This experiment was conducted in two distinct phases, focusing first on the base ring structure and then transitioning to the fabrication of the complete hemisphere, enabling a detailed analysis of the challenges and observations specific to each stage of the process.

4.4.2.1 Ring form

Fabricating the ring structure was the first step towards the understanding of challenges and opportunities in producing curved geometries using WAAM. Unlike the flat plate, the ring geometry introduced a circular path, offering insights into the influence of layer-by-layer deposition on curved surfaces. The ring structure served as a transitional form, bridging the gap between simple flat plates and more complex geometries like hemispheres.

Unlike the WAAM plate, where each layer was deposited over a flat surface, the internal structure for the ring was kept hollow, hence every new layer was directly supported on the preceding layer. The diameter of each deposited ring was minutely shorter than the preceding one, ensuring effective layer adhesion and structural support. A key difference between the plate and the ring were the deposition directions. While the plate experienced continuous linear horizontal welds, the ring was developed with concentric circular weld layers. These circular paths were not continuous but rather stopped after every quarter of a circle. As per the WAAM experts at the lab, the start and

stop positions were randomized for better heat management and control of material placement, helping to maintain dimensional precision. Wall et al. [217] and Michel et al. [218] also supported this configuration by laying emphasis on reversing the deposition direction and dividing longer weld layers into smaller segments to improve the build quality. This resulted in the ring to have four seam points, that blended with the overall surface finish.

The structure was developed with a single deposited weld layer for each ring, with resulting width of 4.8 mm and layer height of 1.6 mm. The advantage of having a single layer was that it reduced the discrepancies between inner and outer regions of the curved wall, resulting in a high-quality smooth print. This was synonymous to the findings in literature where Feng et al. [225] studied WAAM curvatures and noted variations in thermal gradients on both sides of the surfaces, specifically when the curvatures are tighter in smaller in radius. They further revealed that larger curvatures exhibited better material distribution and more consistent mechanical properties. The diameter of the ring was 300 mm and in view of the literature, the form had good heat distribution because the surfaces exhibited uniformity in the structure. The use of a thinner wire (0.035 inches) in comparison to the plate (0.045 inches) further controlled the heat input by producing a smaller molten pool, improving layer adhesion.

Table 4.3 summarizes the various perimeters set for the flat vs curved WAAM parts, highlighting the differences between the two. The wall was fabricated with a 200 J/mm heat input, which was lower than the plate, to prevent excessive melting and ensuring self-supporting deposition. While the plate used a high amount of heat input, having the same for the hollow ring would have caused unstable deposits and compromised structural integrity. These adjustments align with findings in the literature, which emphasize the need for lower heat input settings for thin-walled structures to maintain geometric fidelity and layer stability [225], [230]. Further, Treutler et al. [224] also experimented with a high and a low heat input to produce WAAM cylindrical forms and noted that a higher heat input created coarser microstructures

and a larger weld pool, while low heat can produce fine grain and enhance the surface textures. This also reflects the influence of material anisotropy, where the WAAM-L direction in circular paths contributed to better layer adhesion and surface uniformity, while WAAM-T regions required additional optimization to minimize irregularities caused by thermal gradients, as noted by Laghi et al. [104] as well.

Parameters	WAAM Plate	WAAM Hemisphere/Ring
Wire diameter	0.045”	0.035”
Shielding gas	85% Ar + 15% CO_2	85% Ar + 15% CO_2
Heat input	230 J/mm	200 J/mm
Layer height	1.8 mm	1.6 mm
Travel speed	11 mm/s	8.9 mm/s
Deposition rate	1.9 kg/hr or 527.8 mm^3/s	0.19 kg/hr or 53 mm^3/s
Deposition efficiency	67%	90%
Arc on time for printing	8.2 hrs	4 hrs

Table 4.3 WAAM Parameters comparison

4.4.2.2 Surface curvature

Building on the insights gained from the flat plate and the ring structure, the fabrication of the hemisphere represented a significant progression in the application of WAAM to complex three-dimensional geometries. The hemisphere posed unique challenges, including maintaining structural stability on a continuously curving surface and managing thermal effects that intensified with the geometry’s increasing height and curvature. The initial base ring provided a stable foundation, allowing for the evaluation of circumferential layer adhesion and thermal distribution. The transition to the complete hemisphere offered further insights into the layer-by-layer

deposition over unsupported regions and the interplay between deposition parameters and geometric accuracy.

The deposition rate for the hemisphere was the same as the ring form, set ten times lower than the plate, at 0.19 kg/hr (53 mm^3/s) to avoid sagging and structural instability. This tenfold reduction reflects the necessity of optimizing deposition rates for thin-walled or curved geometries to mitigate distortions caused by thermal gradients, as supported by existing WAAM studies [225]. Queguineur et al. [288] also stated that global deposition rates for a thick WAAM wall are higher because they allow better thermal conduction, reducing the waiting time between layers. In contrast, thinner walls face slower deposition rates due to reduced thermal efficiency. This was further supported by Laghi et al. [104] who discussed anisotropic weaknesses in WAAM-T, stating that lowering the deposition rate reduces stress accumulation and enhances uniformity. This approach helps to balance mechanical properties across all orientations.

Even with adjusted deposition rates, the hemisphere presented challenges due to its curvature, particularly in regions with tighter radii. As the surface approached the top, the layers were less supported on the base structure, facing gravitational pull and so, there were some distortions towards the top. Geng et al. [230] also noted that tighter curvatures in WAAM amplify distortions, underscoring the need for precise parameter control. They further commented that optimizing interlayer spacing and heat input is critical to achieving smoother textures and consistent dimensions in curvatures. Treutler et al. [224] incorporated a closed-loop system in his experiments, that continuously monitored the weld pool area and adjusted process parameters. This provides stable energy input, significantly improving geometric uniformity by reducing defects and surface waviness. Hence, constant evaluation of the object under fabrication could allow to reduce manufacturing problems.

Figure 4.29 shows the final form of the hemisphere, with its surface curvature

and the hollow interior. Figure 4.30 observes a surface study of hemisphere. The start and stop locations marked the four seams on the surface and were more profound on the surface curvature, depositing more amount of weld pool at those points. While the multiple seams disrupt the apparent surface texture, its importance was noted in literature where Feucht et al. [289] used WAAM to 3D print a bridge, whose cross sections started twisting due to induced thermal stresses as the fabrication progressed. To continue the process, the bridge was then divided into five strips so that it had enough cooling time to prevent deformation and maintain the form.

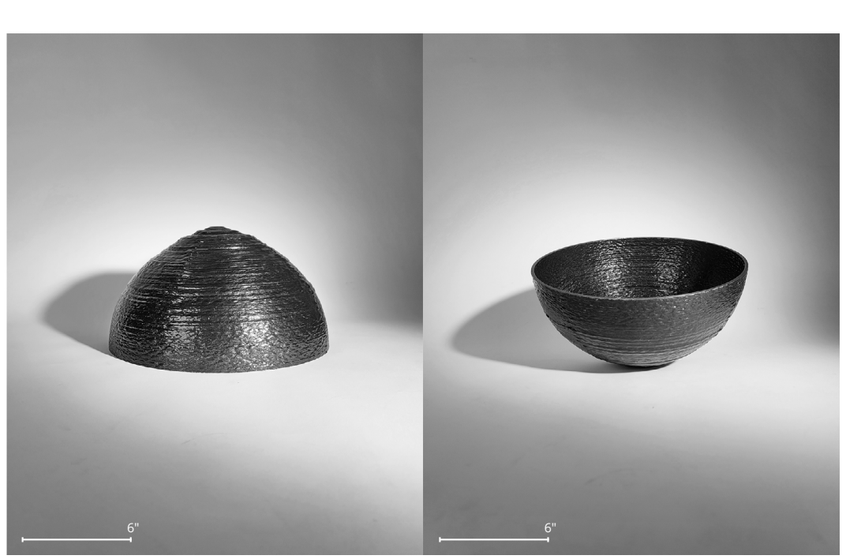


Figure 4.29 Hemisphere - Left: Surface curvature, Right: Hollow interior

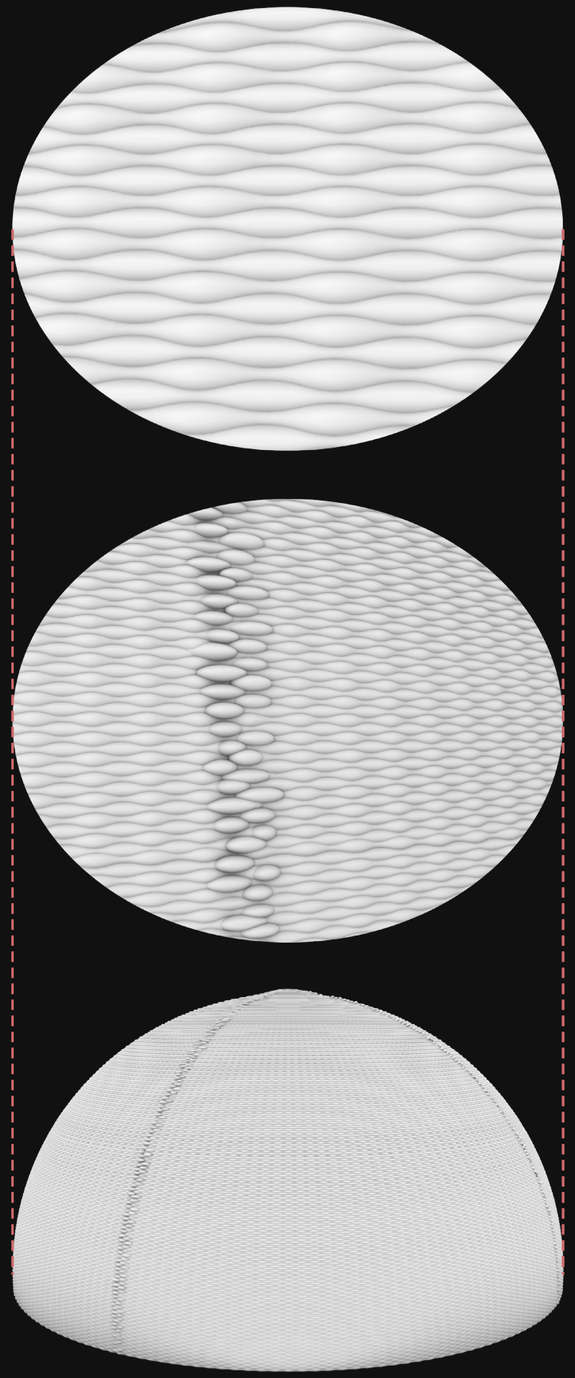


Figure 4.30 WAAM hemisphere - Surface study

The surface texture of the form was similar to the preceding two experiments where the new layer melted and amalgamated with the old one, creating an intertwined texture. These textures are typical in WAAM and depending upon the end use, may require post-processing to smoothen the surface [290].

Further, a digital sectional study of the hemisphere was done to understand the deposition patterns. Figure 4.31 shows the sectional profile and the curvature achieved, with a zoomed-in detail emphasizing the overlapping weld beads. These sectional profiles were developed by analyzing the base ring form during the fabrication process, supplemented by the study of various literature models that talked about weld beads such as those shown by Zhang et al. [239], Dinovitzer et al. [231], and Feucht et al. [289] These patterns, while controlled, show slight irregularities due to the melting and solidification process, affecting surface texture and uniformity. The surface waviness became lighter towards the top surface because the deposition paths were more spaced out due to the curvature as highlighted in Figure 4.32.

The hemisphere curvature provided a sense of what angles can be achieved by WAAM without the need for a support system. This was helpful in understanding the joint forms through a comparison of the surface curvatures. Figure 4.33 maps curvature angles ranging from shallow (near the base) to steep (at the top), achieved without support structures. Each angle is labeled, showcasing the progressive curvature built with layer consistency. This demonstrates WAAM's ability to produce varying inclinations, highlighting the importance of controlled weld pool dynamics and thermal management. The findings underscore the importance of controlled weld pool dynamics and thermal management in overcoming anisotropic challenges in WAAM and achieving smooth, precise curvatures for freeform designs, correlating to the findings by Laghi et al. [104].

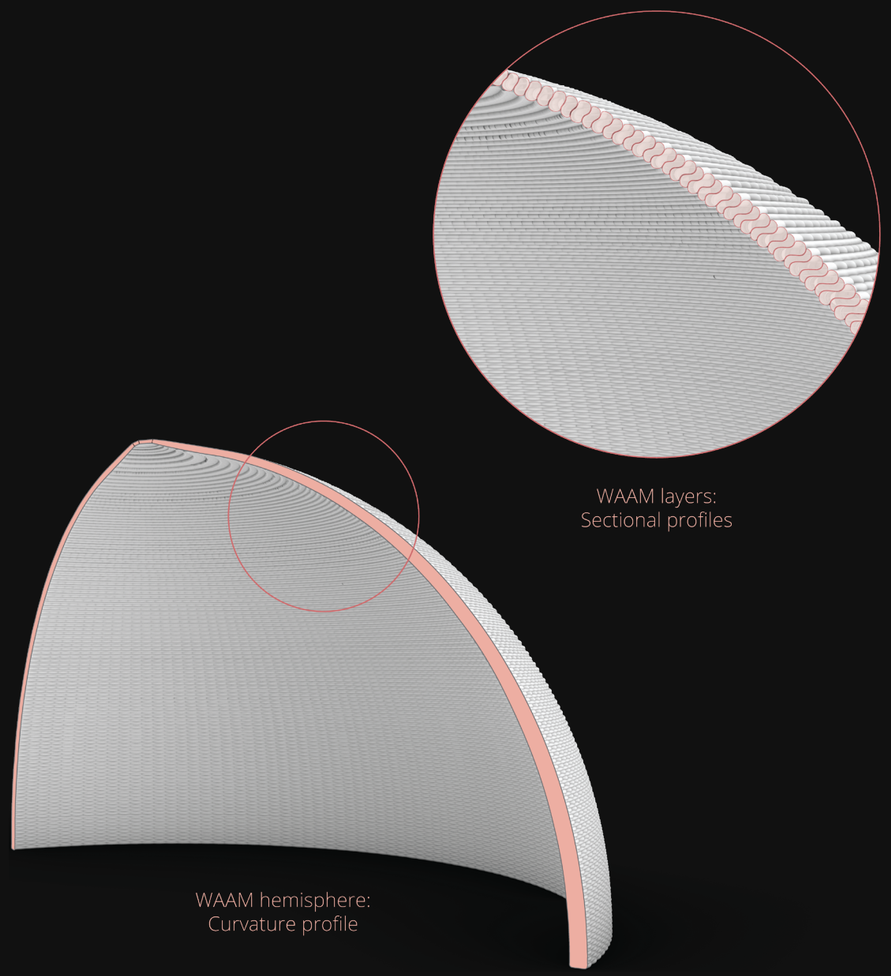


Figure 4.31 WAAM sectional profiles over a curvature – conceptual study

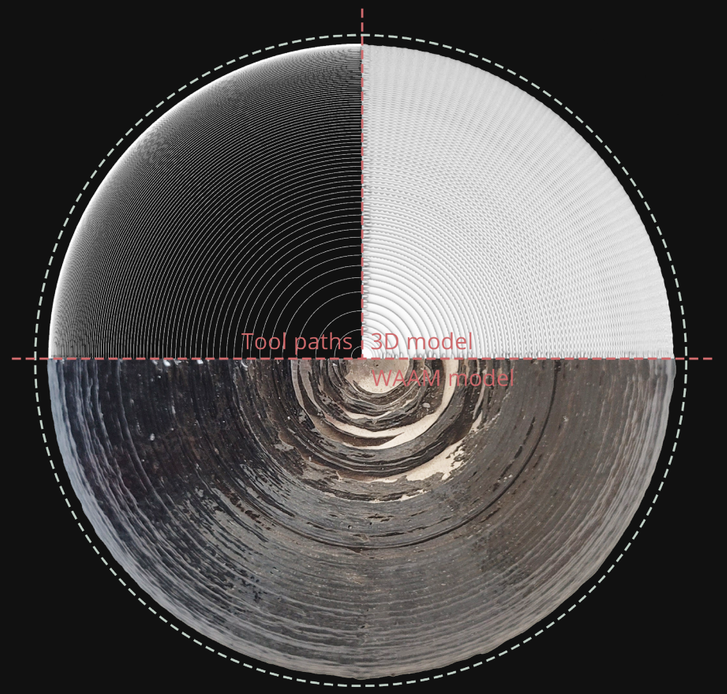


Figure 4.32 Hemisphere – Top view comparison between tool paths, 3D model, and WAAM fabrication

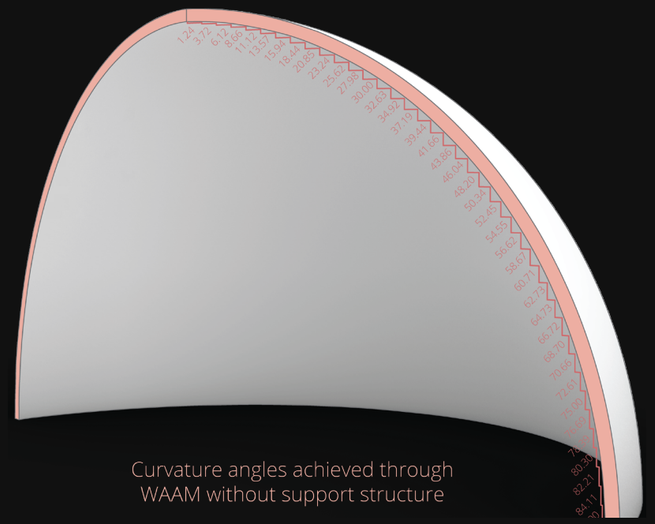


Figure 4.33 Possible curvature angles with WAAM without the need for a support structure

A comparative analysis of deposition times per layer was conducted across the three WAAM experiments: the flat plate, ring form, and hemisphere. Deposition time per layer was calculated by dividing the deposition distance of each weld layer by the deposition speed. The results are summarized in Table 4.4.

Parameters	WAAM Plate	WAAM Ring	WAAM Hemisphere						
Diameter	Not applicable	300 mm	250 mm	200 mm	150 mm	100 mm	50 mm	25 mm	5 mm
Layer distance	280 mm	1884.95 mm	1570.80 mm	1256.64 mm	942.47 mm	628.32 mm	314.16 mm	157.08 mm	31.42 mm
Travel speed	11 mm/s	8.9 mm/s	8.9 mm/s	8.9 mm/s	8.9 mm/s	8.9 mm/s	8.9 mm/s	8.9 mm/s	8.9 mm/s
Print time per layer	25.45 s	200 s	176.49 s	141.20 s	105.89 s	70.60 s	35.30 s	17.65 s	3.53 s

Table 4.4 Comparison of deposition time per layer

The WAAM plate, being a simple rectangular form, had a consistent length of 280 mm. With a deposition of 11 mm/s, the approximate deposition time per layer was 25.45 seconds. Comparatively, the travel speed for the ring and hemisphere was relatively slower, at 8.9 mm/s, resulting in a higher deposition time per layer, supplemented by a larger circumference value of the circular path.

The ring form was almost at a consistent diameter of 300 mm therefore, the per layer time calculation only accounted for a single diameter. The deposition time for the ring came around 200 seconds, which is eight times higher in comparison to the plate. This is also because the ring path covered approximately seven times the plate distance per layer. But when comparing the time taken for the ring layer to cover the same distance as the plate, there is an approximate difference of 6 seconds, with the ring around 31.5 seconds. This increase is attributed to both the larger circumference and the slower travel speed necessary for the ring's geometric configuration. Alternately, for the same per layer build time as the plate, the ring can only form up to 226.5 mm of its circumference – 53.5 mm less than the plate length. Such differences arise with an increase in geometry complexity, as supported from

literature stating that the time required to deposit each layer is influenced not only by factors such as deposition rate and process parameters but also the geometry of the part [207].

The hemisphere was a continuation of the ring form and hence, it followed the same travel speed but with varying diameters. Accounting for that, the Table 4.4 shows the time taken per deposited layer at different diameter intervals. There is a gradual reduction in time as the diameter decreased, with the time reducing below 4 seconds towards the end of the hemisphere due to a very minute radius. These calculations exclude pauses at each quadrant, including these would result in slightly longer actual print times.

4.4.3 Comparison of WAAM with PBF for joint fabrication

Digital comparisons for the fabrication of the inflated joint were made with alternative AM techniques to understand the effectiveness of the WAAM process, and comment on the suitability of the process in terms of time, budget, and design flexibility. Busachi et al. [291] highlighted through various studies that Powder Bed Fusion (PBF) and Directed Energy Deposition (DED) process such as WAAM are the most promising AM methodologies in the industry. Discussions with industry experts at the Multi-Scale Additive Manufacturing (MSAM) Lab at Waterloo (Figure 4.34) [292], explored PBF's suitability for fabricating the joint compared to WAAM. Francis Dibia, MSAM's Research Project Manager, provided insights into PBF processes and their implications for form printing.

Table 4.5 summarizes key discussion points with Francis Dibia. WAAM and PBF represent two distinct approaches to additive manufacturing, each with unique strengths and limitations. A fundamental print criterion highlighted by him was that the PBF has a limited size output, restricted by the size of its enclosed chamber and so, unlike WAAM, the other AM techniques produce



Figure 4.34 The MSAM Lab, UWaterloo - Kitchener, Ontario

Discussion Criteria					
AM Process	Sizing	Cantilevers	Solid/hollow form	Orientation	Cost
The form design is well suited for Laser Powder Bed Fusion (PBF).	The part can not be fabricated in full scale using any of the MSAM lab equipment. The maximum build plate size for PBF is 12" x 12" x 12". So, the piece needs to be scaled down to atleast half the size.	The part would require supports to build. PBF has the ability to construct supports of the same material with a weak build for easy removal afterwards.	PBF can manufacture both solid and hollow structures but in case of a hollow form, small sized holes would need to be embedded in the form at each branch to remove the powder that would get trapped inside the form during the build.	In a horizontal print the entire base surface would have a poor surface finish after the removal of the base support. so, it is recommended not to print horizontally. The form is better suited for a vertical print to achieve a maximum surface quality.	A horizontal print would be more cost efficient because it uses less amount of support material and has a low height. A vertical print would use a lot more volume of the supports with added height. A higher print is more costly.

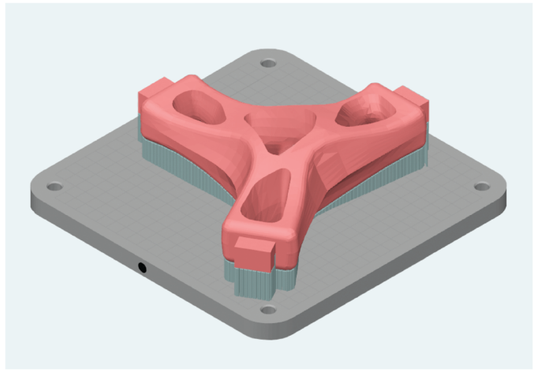
Table 4.5 MSAM Lab - Discussion overview with expert Francis Dibia

small-scale equipment. The critical features that were discussed in comparison to WAAM included the print orientation, fabrication of complex geometry, and the internal structure of the joint.

Powder Bed Fusion can create support structures from the same material, which are weak and removable, similar to PLA prototyping. WAAM, on the contrary, lacks this functionality so, achieving complex forms or cantilevers is challenging when using a robot with lower than eight axes or a rotatable print table.

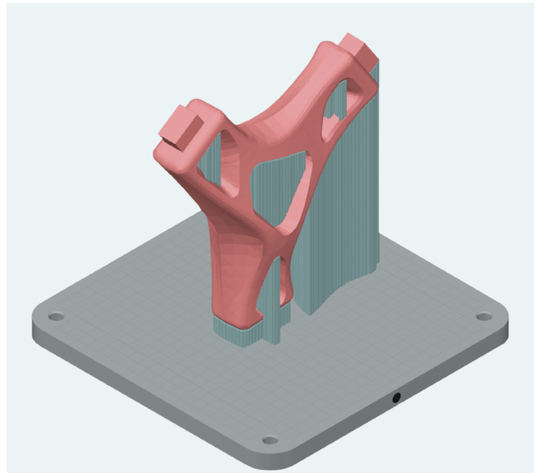
Another important aspect discussed was the print orientation. While WAAM optimized designs were focused to be horizontal, it was highlighted that a horizontal print in PBF would diminish the surface quality due to the supports contact (Figure 4.35). Where as in vertical orientation, the print would be supported on one of the connected branches and the remaining portion of the form is held up by support with minimal surface attachment (Figure 4.36).

Although vertical printing in PBF enhances quality it comes at a higher cost as well. PBF is already costly in comparison to WAAM, and support requirements further escalate expenses. WAAM remains cost-efficient for large-scale applications, requiring lower capital investment and feedstock costs [291]. A cost estimate was done for the WAAM process to compare its feasibility over PBF. Table 4.6 highlights costs for the joint at the same scale (1:3) as well as at the original size. The manufacturing costs were calculated using the cost of wire feedstock - $4/kg and robot operating cost of $150/hr. At 1:3 scale, with a deposition rate of 4 kg/hr, the joint estimated cost was approximately $160 and if the deposition rate is increased to 8 kg/hr, the cost would reduce to around $90. Looking at the production rates of a full-sized joint, at 4 kg/hr an estimated cost was $4,000 while at 8 kg/hr an estimated cost is $2,200. So, comparing WAAM to PBF, WAAM proved to be many times more cost-efficient, with the ability to create larger parts.



Build Information	Details
Build height	63.9 mm
Number of layers	2,129
Total part volume	4,86,051 mm^3
Total support volume	58,681 mm^3
Estimated build time	82 hours 18 min
MSAM research print cost	$4,300
Service bureau cost	$10,000

Figure 4.35 Powder Bed Fusion - Preview of horizontal print



Build Information	Details
Build height	215.04 mm
Number of layers	7,168
Total part volume	4,85,714 mm^3
Total support volume	1,64,481 mm^3
Estimated build time	134 hours 45 min
MSAM research print cost	$5,700
Service bureau cost	$14,000

Figure 4.36 Powder Bed Fusion - Preview of vertical print

Calculation Parameters
Cost of production robot = $150/hr
Cost of feedstock = $4/kg
Production cost = Consumable cost + (Machine rate x time)
= (Feedstock cost x Mass) +
(Machine rate x Mass/deposition rate)
Mass = Volume x Density of Steel
Density of steel = 0.284 lb/in^3

Joint @ Scale 1:1
Volume = 742.1 in^3
Mass = 742.1 in^3 x 0.284 lb/in^3
= 210.8 lbs (95.7 kg)
Production cost @ 4 kg/hr = (95.7 x $4) + ($150/hr x (95.7/4))
= 382.8 + 3588.75
= $3,971.55 (High range)
Production cost @ 8 kg/hr = (95.7 x $4) + ($150/hr x (95.7/8))
= 382.8 + 1794.375
= $2,177.175 (Low range)

Joint @ Scale 1:3
Volume = 29.58 in^3
Mass = 29.58 in^3 x 0.284 lb/in^3
= 8.4 lbs (3.81 kg)
Production cost @ 4 kg/hr = (3.81 x $4) + ($150/hr x (3.81/4))
= 15.24 + 142.875
= $158.12 (High range)
Production cost @ 8 kg/hr = (3.81 x $4) + ($150/hr x (3.81/8))
= 15.24 + 71.4375
= $86.68 (Low range)

Table 4.6 Inflated joint estimated print costs in WAAM

Additionally, PBF production time is higher although the part size is one-third of the actual dimensions. Contrary to this, WAAM offers a faster build because the deposition rate is significantly higher than that of PBF, leading to reduced production times. For example, WAAM deposition rates can reach up to 8 kg/hr [293], whereas PBF typically operates at a much slower rate due to the meticulous layer-by-layer sintering. The findings from Vartanian et al. [294] also demonstrated that PBF is about ten times slower and five times more expensive than DED. This makes WAAM particularly suitable for time sensitive projects, though additional post-processing may be required to achieve desired surface finishes [290].

Table 4.7 summarizes the aforementioned aspects of PBF and WAAM. PBF excels in fine details and high-resolution components, making it ideal for intricate designs but limited in scale. WAAM, on the other hand, often results in coarser surface finishes due to larger weld pools, but it benefits from post-processing techniques like robotic polishing to enhance surface quality [290]. WAAM offers a cost-effective and efficient solution for large-scale fabrication, with faster deposition rates and greater scalability than PBF. While PBF excels in fine details, WAAM remains the preferred choice for projects prioritizing speed, affordability, and industrial-scale production.

Aspects	Powder Bed Fusion (PBF)	Wire Arc Additive Manufacturing (WAAM)
Print size	Small-scale restricted to chamber size	Large-scale industrial pieces
Print orientation	Vertical for better surface quality	Horizontal design for efficiency
Complex geometry	Supports intricate geometries	Challenging for thin elements
Surface quality	High-resolution and superior finish	Coarser, may require post-processing
Cantilevers	Can create a removable support system for it	Can't create supports, requires multi-axis robot
Cost	Very high cost even for small parts	Significantly lower cost for large parts
Production time	Slower due to detailed sintering	Faster build with high deposition rates
Precision	Higher precision	Lower precision due to large weld pool
Material use	Powder material	Wire feedstock
Application	Small parts requiring fine details	Large-scale industrial applications

Table 4.7 Comparison between PBF and WAAM functionality

Chapter 5

5. Conclusion

This research on integrating Wire Arc Additive Manufacturing into structural steel fabrication has demonstrated both its potential and challenges in advancing the design and production of complex, lightweight, and topology-optimized joints. By leveraging computational optimization, digital simulations, and experimental fabrication, this study has explored how WAAM can supplement conventional fabrication methods, allowing for greater design flexibility, reduced material waste, and enhanced manufacturing efficiency. However, despite its advantages, the practical implementation of WAAM in construction remains limited due to technical constraints, fabrication inconsistencies, and post-processing requirements. This chapter summarizes the key findings, presents conclusions based on results, discusses limitations, and outlines future perspectives for further advancements in the field.

5.1 Summary

This research explored the amalgamation of Additive Manufacturing, specifically Wire Arc Additive Manufacturing in design and fabrication of structural steel joints. While conventional techniques have been widely adopted in the construction industry, they often impose geometric restrictions, material waste, lengthy production times, and significant labour costs. WAAM, by contrast, enables the layer-by-layer deposition of steel, allowing for material efficiency, geometric flexibility, and reduced reliance on moulds and labour. It offers an innovative alternative allowing for the customization of complex, lightweight, and structurally optimized steel connections. By leveraging topology optimization and biomimetic design principles, this research investigated how WAAM can be utilized to fabricate steel joints that are geometrically more complex than a typical connection, while retaining structural integrity and reduced material consumption, ultimately contributing to a more systematic and efficient fabrication system.

The study was conducted in multiple phases, beginning with digital modelling

and computational analysis to exploring the feasibility of topology-optimized joints. Digital tools such as Rhino, Grasshopper, Fusion 360, and Abaqus were used to design and analyze structural performance, material distribution, and load-bearing capacity of the joints. Prototyping was initially conducted using PLA (polylactic acid) filament 3D printing to test preliminary designs, assess fabrication challenges, and refine the forms before transitioning to WAAM fabrication.

WAAM fabrication experiments were carried out using a six-axis robotic arm, focusing on material deposition behaviour, curvature feasibility, and structural performance. The fabrication tests examined how WAAM printed steel parts respond to gravitational effects, and layer-wise anisotropies, which are crucial factors in determining their suitability for large-scale architectural applications. A key area of design investigation was the effectiveness of Voronoi latticing and topology optimization in improving load distribution, stress concentration, and material reduction without compromising structural integrity. This was supplemented by testing the feasibility of achieving curvatures and hollow forms with WAAM. Through iterative design modifications and fabrication trials, the study explored how deposition parameters, print orientation, and robotic toolpath planning influence the final quality of the printed joints.

However, while WAAM offers significant advantages, the study also identified challenges associated with WAAM fabrication. Factors such as surface roughness, heat-induced deformations, and anisotropic mechanical properties pose limitations on the precision and consistency of printed parts, requiring further refinements in deposition strategies and post-processing techniques. Additionally, unsupported geometries and overhanging structures also present fabrication challenges, requiring further design optimization to ensure successful printing.

While WAAM provides new possibilities for steel construction, its practical implementation in large-scale architectural projects remains an ongoing

challenge. The findings of this research indicate that process refinements, advanced simulation techniques, and hybrid fabrication approaches will be necessary to fully realize the potential of WAAM in steel joint manufacturing. Future research should focus on improving robotic automation, integrating multi-material printing, and enhancing real-time monitoring systems to address fabrication inconsistencies and ensure structural reliability. Additionally, full-scale load testing of WAAM-printed joints under real-world conditions will be crucial for validating their long-term durability and performance in dynamic environments. This study provides a strong foundation for future advancements, demonstrating that WAAM has the potential to revolutionize steel fabrication by offering new approaches to material efficiency, design customization, and sustainable construction methodologies.

5.2 Conclusion based on results

The findings of this research demonstrated that the application of material reduction through latticing and topology-optimization in joints can maintain significant structural integrity, but the process must be in consideration of the critical load paths. The integration of computational optimization, stress analysis, and experimental fabrication provided a clear validation of WAAM's potential to enhance steel joint manufacturing.

One of the conclusions of this study was that WAAM can successfully produce steel joints with complex geometries, offering significant advantages over traditional fabrication methods in terms of material efficiency, geometric flexibility, and production adaptability. The layer-by-layer additive process allows customization of structural components, offering new possibilities for architectural applications, enabling more efficient and aesthetically refined structural solutions. However, the research also highlights several critical challenges, including deposition anisotropy, heat-induced distortions, and surface irregularities, which may affect structural performance and fabrication

consistency. The anisotropic nature of WAAM-deposited steel presents a significant challenge, as the layer-wise build process introduces mechanical variations that must be accounted for in design and fabrication strategies. The findings suggest that further optimizations in robotic toolpath planning, deposition speed, and thermal regulation are necessary to enhance print consistency. Additionally, unsupported regions and overhanging geometries require further design modifications to ensure successful fabrication without excessive material buildup or print failures.

WAAM experiments showcased the feasibility of fabricating large-scale, robust structures while revealing inherent challenges, such as the inability to produce intricate supports, coarse surface finishes, and sensitivity to complex geometries. The exploration of flat plates, rings, and hemispheres demonstrated the process's capability to achieve geometric precision under controlled parameters, particularly with optimized heat input, deposition rates, and travel speeds.

However, challenges such as dimensional discrepancies, thermal gradients, and anisotropic effects persisted, particularly for thin-walled or highly curved geometries. To address these limitations, the study emphasized the need for tailored designs that prioritize:

- Simplified geometries with minimal surface irregularities to reduce reliance on extensive post-processing.
- Load paths and configurations optimized for WAAM's capabilities, focusing on self-supporting features.
- Advanced tool path strategies and parameter adjustments to improve layer adhesion and surface uniformity.

Comparative discussions with alternative additive manufacturing techniques, such as Powder Bed Fusion (PBF), further highlighted WAAM's advantages in cost efficiency and scalability for large-scale applications. While WAAM demonstrates significant potential for fabricating durable, large-scale

structures, its limitations necessitate a careful balance between topology optimization and manufacturability. Future studies can further explore advanced support strategies, multi-axis robotic systems, and hybrid manufacturing approaches to expand the design possibilities and enhance the performance of WAAM fabricated components. The findings from this chapter provide a solid foundation for the continued exploration of additive manufacturing technologies in architecture and industrial applications.

Overall, this research validates WAAM as an emerging technology with the potential to transform steel fabrication but also emphasizes the need for continued advancements in robotic automation and path planning. With further improvements in precision, mechanical consistency, and process automation, WAAM can become a mainstream solution for fabricating high-performance, customized steel joints. This study provides a strong foundation for future research, demonstrating that WAAM has the capacity to enhance architectural fabrication and structural engineering by offering more adaptable and efficient manufacturing methods.

5.3 Limitations

This study identified some limitations, primarily related to fabrication constraints, that affected the applicability, accuracy, and scalability of WAAM for structural steel joint fabrication. One of the key fabrication limitations stemmed from the six-axis robotic WAAM system used in this study. The print size and build orientation imposed restrictions on the complexity of geometries that could be fabricated, limiting the extent to which optimized joint designs could be realized. The deposition paths influenced by robotic motion constraints impacted the final design. Additionally, the study did not explore WAAM systems beyond the six-axis, which could potentially overcome some geometric constraints by enabling more intricate and multi-directional printing capabilities.

WAAM produced steel has anisotropic mechanical properties, that result in directional material variations. This hinders the prediction of the dimensional accuracy of the parts in comparison to the original joint design, necessitating advanced process control techniques, such as real-time temperature monitoring, adaptive deposition strategies, and post-processing heat treatments, to enhance the overall material reliability of WAAM fabricated components.

The study also considered only a single material composition, as it primarily focused on commonly used steel wire stock. WAAM has the capability to process various metal alloys, including stainless steel, titanium, and aluminum, which may exhibit different mechanical properties, printability challenges, and post-processing requirements. A broader study incorporating multiple material types and hybrid material strategies would provide a more comprehensive understanding how joinery connections are impacted by WAAM's fabrication.

Another methodological limitation was the reliance on digital stress simulations and PLA prototyping for preliminary design validation. While computational analysis in Abaqus provided useful insights into stress distribution, failure points, and load-bearing efficiency, these simulations do not fully capture real-world conditions, such as environmental exposure, cyclic loading, and long-term fatigue behaviour. Similarly, PLA prototyping, though valuable for early-stage form validation, does not replicate the mechanical and thermal behaviour of WAAM fabricated steel joints. This limitation highlights the need for experimental validation through full-scale physical testing, which would offer a more accurate assessment of joint performance under practical load conditions.

Furthermore, the study could benefit from comparative testing with traditionally fabricated steel joints, to quantify WAAM's performance relative to conventional manufacturing methods. A direct comparison between WAAM produced joints and conventionally welded or cast steel connections would

provide valuable insights into mechanical properties, cost-effectiveness, and production efficiency. Future research should focus on benchmarking WAAM fabricated joints against industry standard connections to determine how effectively WAAM can serve as a competitive alternative in real-world construction projects.

Overall, while this research demonstrated an understanding WAAM's potential in steel joinery fabrication, it also highlights areas that require further refinement. To make WAAM a reliable and scalable solution for structural joint manufacturing, improvements in robotic toolpath planning, material consistency, and the range of materials would be significant. Additionally, real-world validation through large-scale testing is essential to confirm practical applications. Future advancements in hybrid manufacturing, process automation, and real-time quality control will be useful to advance WAAM's potential for further architectural and engineering applications.

5.4 Future extension and application

The future of WAAM in architectural structures holds immense potential to transform the way we design, fabricate, and assemble steel components, integrating computational design with advanced fabrication. As illustrated in Figure 5.1, biomimetic-inspired structures can benefit significantly from WAAM's ability to create customized steel connections that balance structural efficiency with aesthetic expression. Unlike traditional steel fabrication methods, WAAM enables direct printing of complex, custom shaped connections, reducing material waste and production costs. As research in WAAM advances, improvements in scalability, precision, and structural performance could make WAAM a mainstream technique. Future advancements in path planning may further refine designs, anabling adaptive structural elements that respond dynamically to site-specific loading conditions. Integrating real-time sensor feedback and optimization could allow WAAM-fabricated joints to self-adjust

deposition parameters, enhancing precision, durability, and load distribution.

A key area of future development is the integration of advanced robotic systems in WAAM fabrication. Current WAAM processes are primarily limited to six-axis robotic arms, which impose geometric constraints on print orientation and structural complexity. Future research should explore the application of multi-axis robotic arms, and parallel robotic systems, enabling multi-directional deposition and continuous, large-scale additive manufacturing. Such advancements would allow for the seamless printing of doubly curved surfaces, overhanging structures, and integrated lattice systems, further expanding WAAM's applicability to complex, freeform architectural components.

Further, WAAM could also be enabled for on-site printing of steel structures, reducing the need for transportation. This capability would be particularly beneficial in remote locations, where transporting prefabricated materials is costly and impractical. Further research could also explore the use of multi-material printing, making use of material properties to enhance durability and performance. It can also be further advanced through post-processing techniques, such as laser smoothing and automated surface treatments to improve the quality and consistency of WAAM fabricated components, ensuring they meet architectural and structural performance standards.

Future research should focus on developing standardized testing methodologies and performance benchmarks to validate WAAM's structural reliability under real-world loading conditions. Comparative studies with traditionally fabricated steel connections will also be necessary to demonstrate WAAM's long-term durability and feasibility in mainstream construction. As advancements continue, WAAM will become an increasingly viable solution for creating complex architectural structures. By embracing this technology, the future of steel construction can shift toward a more flexible and precise paradigm, redefining the possibilities of parametric, high-performance architecture.

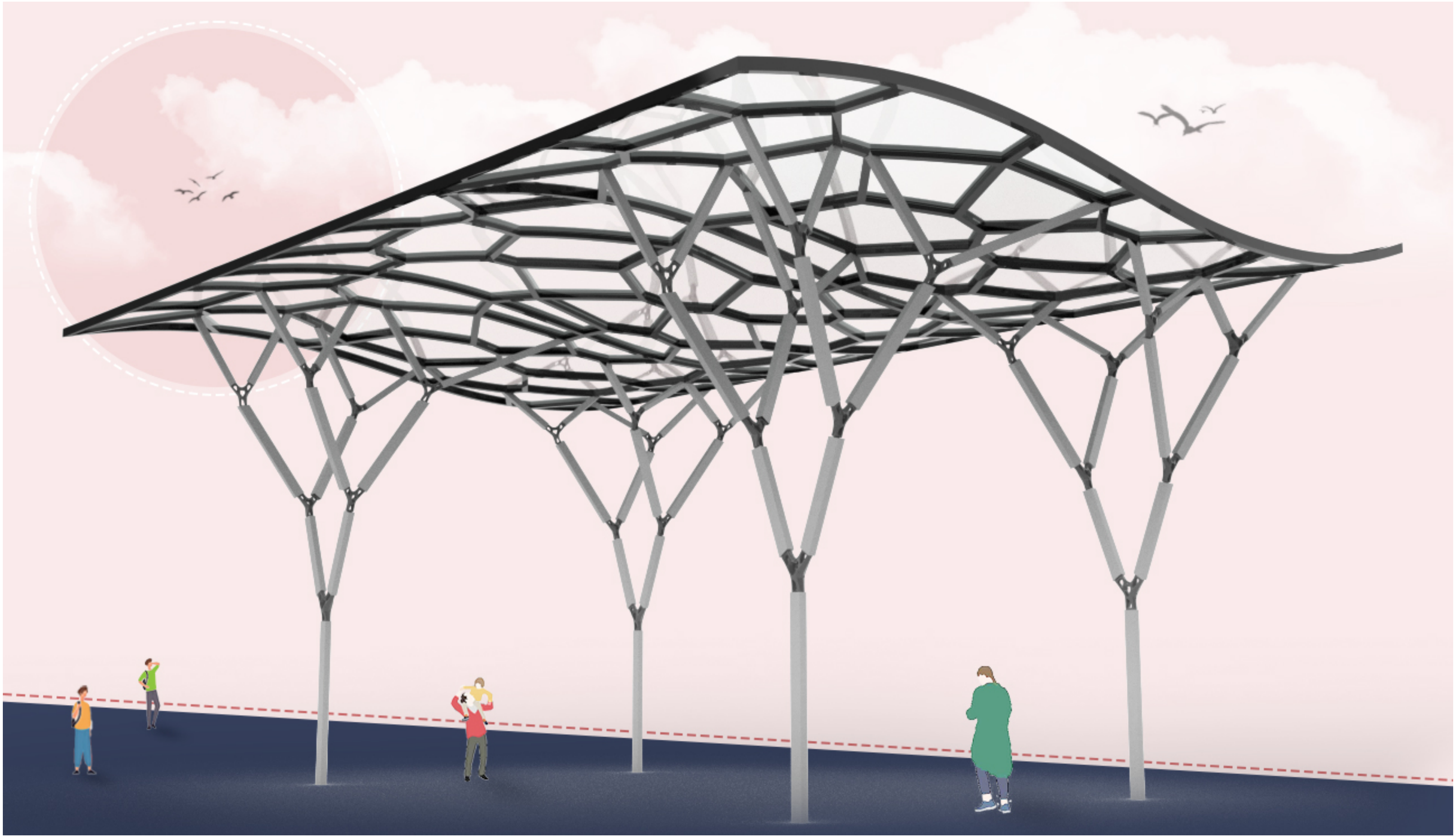


Figure 5.1 Application instance of the designed joint

Letters of Copyright Permission

Figure 2.6

CE

Clarissa Eyu
To You

Feb 17

Hi Mahirah,

Thanks for your email. You may use your images. Please attribute all images to NVIDIA.

Good luck with your thesis!

Clarissa Eyu
Corporate Communications
NVIDIA

Figure 2.9

MP

Matt Parkes
To You

Mar 11

Dear Mahirah,

Please feel free to use the images and reference the Nambian University Hydrology Center 'The Fogcatcher'.

Many thanks and best regards

Matt

Matt Parkes RIBA
Director of Architecture
atlas

Figure 2.11

SKIDMORE, OWINGS & MERRILL LLP
224 S. MICHIGAN AVENUE
CHICAGO, IL 60604

SOM

11 March 2025

Mahirah Rohail
University of Waterloo
200 University Ave W
Waterloo, ON N2L 3G1, Canada

Salutations,

We hereby grant permission to your request dated **02/28/2025** to publish **"NFN_001230_N304.tif" "NFN_001230_N2.tif" "NFN_001230_N59.png" and "NFN_001230_N56.png"** (the "SOM Material") in **Biomimicry Thesis by Mahirah Rohail** to be published by **University of Waterloo** upon the terms and conditions set forth herein.

Permission to use the SOM material is limited to the above and is non-transferable. The SOM material may only be reproduced for the express purpose described above and any inconsistent and/or subsequent use of the SOM Material constitutes reuse and requires written authorization from SOM. All displays of the SOM material must credit SOM as **Architect and Planner** and must display the copyright line: **© SOM.**

The SOM material are an instrument of services performed for a specific project at a specific point in time. It is mutually understood and agreed that the SOM material will be supplied "AS IS" and any re-use without specific verification or adaptation by Skidmore, Owings & Merrill LLP ("SOM") is at your sole risk, without liability to SOM. To the fullest extent permitted by law, you agree to defend, indemnify and hold SOM and its respective officers, partners, principals, directors, agents, employees, consultants, successors and assigns, harmless from and against all liability, loss, damages, costs and expenses, including attorneys' fees, which any of them may at any time sustain or incur by reason of any claim, cause of action or legal proceeding arising out of or in connection with any modification, misinterpretation, misuse or reuse by you or others of the SOM materials.
It is understood that the SOM material are not guaranteed or warranted, either express or implied, including but not limited to, warrant of merchantability, constructability or suitability for fitness or purpose.

Additionally, you agree to send a digital copy to my attention upon its release.

Please acknowledge your consent by returning a signed copy of this letter to my attention at Skidmore, Owings & Merrill LLP, 224 S. Michigan Avenue, Chicago IL, 60604. Thank you.

Yours truly,

Jade Leslie

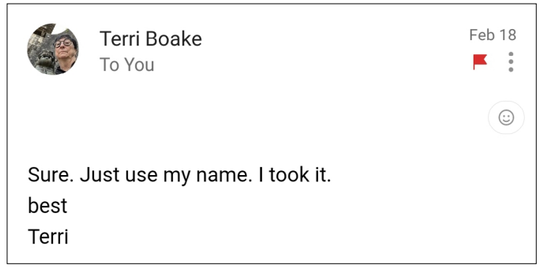
Jade Leslie

Chicago Communications

(312) 360-4096

jade.leslie@som.com

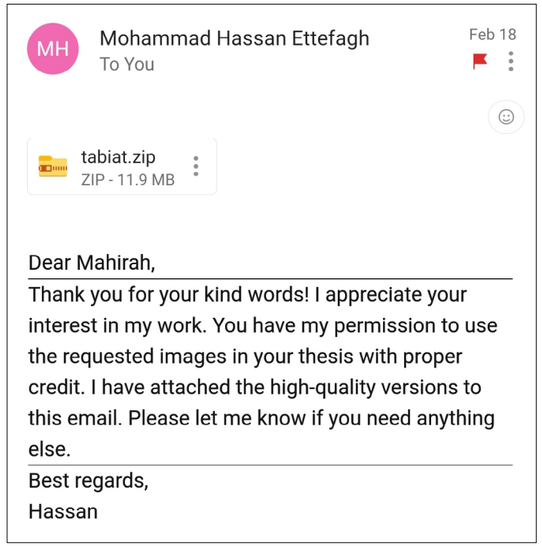
Figure 2.12



Terri Boake
To You
Feb 18

Sure. Just use my name. I took it.
best
Terri

Figure 2.13



MH
Mohammad Hassan Ettefagh
To You
Feb 18

tabiat.zip
ZIP - 11.9 MB

Dear Mahirah,

Thank you for your kind words! I appreciate your interest in my work. You have my permission to use the requested images in your thesis with proper credit. I have attached the high-quality versions to this email. Please let me know if you need anything else.

Best regards,
Hassan

Figure 2.19



CCC Marketplace

This is a License Agreement between Mahirah Rohail ("User") and Copyright Clearance Center, Inc. ("CCC") on behalf of the Rightsholder identified in the order details below. The license consists of the order details, the Marketplace Permissions General Terms and Conditions below, and any Rightsholder Terms and Conditions which are included below. All payments must be made in full to CCC in accordance with the Marketplace Permissions General Terms and Conditions below.

Order Date	30-Jan-2025	Type of Use	Republish in a thesis/dissertation
Order License ID	1573377-1	Publisher	American Society of Civil Engineers
ISSN	1943-541X	Portion	Chart/graph/table/figure

LICENSED CONTENT

Publication Title	Journal of Structural Engineering	Rightsholder	American Society of Civil Engineers
Article Title	Topology Optimization and 3D Printing of Three-Branch Joints in Treelike Structures	Publication Type	e-Journal
Author / Editor	American Society of Civil Engineers, American Society of Civil Engineers.Structural Division, Structural Engineering Institute.	Start Page	04019167
		Issue	1
		Volume	146
Date	01/01/1983	URL	http://ascelibrary.org/journal/jsendh
Language	English		
Country	United States of America		

REQUEST DETAILS

Portion Type	Chart/graph/table/figure	Distribution	Canada
Number of Charts / Graphs / Tables / Figures Requested	2	Translation	Original language of publication
Format (select all that apply)	Electronic	Copies for the Disabled?	No
Who Will Republish the Content?	Academic institution	Minor Editing Privileges?	Yes
Duration of Use	Life of current edition	Incidental Promotional Use?	No
Lifetime Unit Quantity	Up to 4,999	Currency	CAD
Rights Requested	Main product and any product related to main product		

NEW WORK DETAILS

Title	Additive Manufacturing: An adaptation of steel connections	Institution Name	University of Waterloo
		Expected Presentation Date	2025-04-01
Instructor Name	Dr. M.T.Araji		

ADDITIONAL DETAILS

Order Reference Number	Fig. 19 , Fig. 20	The Requesting Person / Organization to Appear on the License	Mahirah Rohail

REQUESTED CONTENT DETAILS

Title, Description or Numeric Reference of the Portion(s)	Fig. 19 , Fig. 20	Title of the Article / Chapter the Portion Is From	Topology Optimization and 3D Printing of Three-Branch Joints in Treelike Structures
Editor of Portion(s)	Wang, Longxuan; Du, Wenfeng; He, Pengfei; Yang, Mijia	Author of Portion(s)	Wang, Longxuan; Du, Wenfeng; He, Pengfei; Yang, Mijia
Volume / Edition	146	Issue, if Republishing an Article From a Serial	1
Page or Page Range of Portion	04019167	Publication Date of Portion	2020-01-01

Figure 2.20



CCC Marketplace

This is a License Agreement between Mahirah Rohail ("User") and Copyright Clearance Center, Inc. ("CCC") on behalf of the Rightsholder identified in the order details below. The license consists of the order details, the Marketplace Permissions General Terms and Conditions below, and any Rightsholder Terms and Conditions which are included below. All payments must be made in full to CCC in accordance with the Marketplace Permissions General Terms and Conditions below.

Order Date	25-Jan-2025	Type of Use	Republish in a thesis/dissertation
Order License ID	1571714-1	Publisher	ELSEVIER LTD.
ISSN	0143-974X	Portion	Image/photo/illustration

LICENSED CONTENT

Publication Title	Journal of constructional steel research : JCSR	Country	United Kingdom of Great Britain and Northern Ireland
Article Title	Joints for treelike column structures based on generative design and additive manufacturing	Rightsholder	Elsevier Science & Technology Journals
		Publication Type	Journal
Author / Editor	Steel Construction Institute (Great Britain)	Start Page	106794
Date	01/01/1981	Volume	184
Language	English		

REQUEST DETAILS

Portion Type	Image/photo/illustration	Distribution	Canada
Number of Images / Photos / Illustrations	1	Translation	Original language of publication
Format (select all that apply)	Electronic	Copies for the Disabled?	No
Who Will Republish the Content?	Academic institution	Minor Editing Privileges?	Yes
Duration of Use	Life of current edition	Incidental Promotional Use?	No
Lifetime Unit Quantity	Up to 4,999	Currency	CAD
Rights Requested	Main product, any product related to main product, and other compilations/derivative products		

NEW WORK DETAILS

Title	Additive Manufacturing: An adaptation of steel connections	Institution Name	University of Waterloo
Instructor Name	Dr. M.T.Araji	Expected Presentation Date	2025-04-01

ADDITIONAL DETAILS

Order Reference Number	N/A	The Requesting Person / Organization to Appear on the License	Mahirah Rohail

REQUESTED CONTENT DETAILS

Title, Description or Numeric Reference of the Portion(s)	fig 4. Generative design results: incomplete list.	Title of the Article / Chapter the Portion Is From	Joints for treelike column structures based on generative design and additive manufacturing
Editor of Portion(s)	Wang, Hui; Du, Wenfeng; Zhao, Yannan; Wang, Yingqi; Hao, Runqi; Yang, Mijia	Author of Portion(s)	Wang, Hui; Du, Wenfeng; Zhao, Yannan; Wang, Yingqi; Hao, Runqi; Yang, Mijia
Volume / Edition	184	Issue, if Republishing an Article From a Serial	N/A
Page or Page Range of Portion	5	Publication Date of Portion	2021-09-01

Figure 2.21



YM

Yang, Mijia
To You

Jan 25

Hi Mahirah,

You have my permission to reuse the image mentioned in your email.

Good luck,
M. Yang, Ph.D., P.E.
Professor and CE Program Coordinator,
Department of Civil, Construction and Environmental Engineering,
North Dakota State University
Tel: 701-231-5647
Office: CIE 201B

Figure 2.24

AIP PUBLISHING LICENSE
TERMS AND CONDITIONS

Mar 09, 2025

This Agreement between Mahirah Rohail ("You") and AIP Publishing ("AIP Publishing") consists of your license details and the terms and conditions provided by AIP Publishing and Copyright Clearance Center.

License Number	5958911419223
License date	Jan 30, 2025
Licensed Content Publisher	AIP Publishing
Licensed Content Publication	AIP Conference Proceedings
Licensed Content Title	Analyzing and modelling gripper arm using shape optimization of fusion 360 and 3D printing of polylactic acid
Licensed Content Author	Syamsir, Nurhidayat; Nur, Rusdi
Licensed Content Date	Nov 16, 2022
Licensed Content Volume	2543
Licensed Content Issue	1
Type of Use	Thesis/Dissertation
Requestor type	Student
Format	Print
Portion	Figure/Table
Number of figures/tables	2
Will you be translating?	No
Title of new work	Additive Manufacturing: An adaptation of steel connections
Institution name	University of Waterloo
Expected presentation date	Apr 2025
Portions	Figure 4, figure 6
The Requesting Person / Organization to Appear on the License	Mahirah Rohail

Figure 2.33

JG Jim Galloway
To You
Jan 27

Mahirah.pptx
PPTX - 666 KB

Mahirah: This document has been published publicly and is freely available online from the CWB-Association. You are welcome to reference it.

(I have attached original images and versions created by me that you are welcome to use.)

Jim Galloway, BASc, CET
Professor & Coordinator of Welding Programs
Conestoga College - Cambridge Campus
850 Fountain Street. South.,
Cambridge, ON N3H 0A8

Figure 2.36

Adriaan de Groot
adegfoto

Jan 24, 12:50 p.m.

Thank you for your message! of course, go ahead! thank you for asking :)

Double tap to ❤️

Figure 2.36
Figure 2.37

MX3D
Average response time: Within 1 hour

FEB 21

MX3D · 2:06 PM
Hi Mahirah, with proper credits to MX3D and if you send us a copy of your thesis to info@mx3d.com we allow you to use the images for your thesis. We look forward to receiving your thesis. Thanks for referencing MX3D. Kind regards, MX3D

Figure 2.37

LF **Leonard Faustle** Jan 17
To You

Hi Mahirah,

Thanks for reaching out. As far as I'm concerned you have my permission to use the images. Please do make sure that you check with MX3D as well, since the product is theirs.

Kind regards,

Leonard

Figure 2.38

CC **Cast ConneX - Info** Feb 3
To You

Hi Mahirah,

From what I remember about thesis-writing, image use, and "fair use" laws, if the information/images are publicly available, then for educational (non-commercial) publications likes your thesis, you may use the content so long as you provide the appropriate citation to the article and credit the creator.

So yes, you can use Cast Connex's image by citing the article and credited Cast Connex.

Good luck with your research!

Best,
Tarana

Tarana Haque, M.A.Sc., P.Eng.
Technical Sales Manager, North America

P: (416) 806-3521 x 1449
C: (647) 518-1257 **E:** t.haque@castconnex.com
CASTCONNEX
www.castconnex.com

Figure 2.39

DM

Douglass, Mark
To You

Feb 4

Rohail,

Yes, permission to use the image with citation. Appreciate you reaching out and asking for permission—I'm guessing most grad students wouldn't have done that!

If you think about it, send a PDF copy of your thesis if available.

Regards,
Mark

LINCOLN ELECTRIC | Additive Solutions

D Mark Douglass, PhD, CFA
Business Development Manager
+1 (216) 385-4496 (mobile)
+1 (216) 383-4221 (office)
26250 Bluestone Blvd, Euclid OH 44132
https://additive.lincolnelectric.com

Bibliography

[1] "Materials Science: Building the Tech Future | Stanford Emerging Technology Review." Accessed: Feb. 17, 2025. [Online]. Available: https://setr.stanford.edu/news/materials-science-building-tech-future

[2] T. D. Iluyomade, A. C. Okwandu, T. D. Iluyomade, and A. C. Okwandu, "Innovative materials in sustainable construction: A review," International Journal of Science and Research Archive, vol. 12, no. 1, Art. no. 1, 2024, doi: 10.30574/ijsra.2024.12.1.1048.

[3] S. Siengchin, "A review on lightweight materials for defence applications: Present and future developments," Defence Technology, vol. 24, pp. 1–17, Jun. 2023, doi: 10.1016/j.dt.2023.02.025.

[4] M. Jiang, "A Review of the Impacts of Industrial Revolutions in World History," Communications in Humanities Research, vol. 39, pp. 234–239, Aug. 2024, doi: 10.54254/2753-7064/39/20242245.

[5] L. Chen, "The Development of Steel Construction with the Innovation Brought by High-Tech Architecture," Lecture Notes in Education Psychology and Public Media, vol. 10, pp. 66–70, Sep. 2023, doi: 10.54254/2753-7048/10/20230057.

[6] G. Dawe, "The Ultimate Guide to Steel Fabrication: Benefits, Methods & Applications - Kanyana Engineering." Accessed: Apr. 05, 2024. [Online]. Available: https://kanyanaengineering.com.au/steel-fabrication-guide/

[7] L. Ahmad and M. Kasmuri, "The Effect of Steel Over Strength Ratio on Structure Behavior," Recent in Engineering Science and Technology, vol. 2, no. 04, Art. no. 04, Oct. 2024, doi: 10.59511/riestech.v2i04.79.

[8] L. Aly, A. M. El-Tair, and A. Nassar, "Life cycle cost analysis comparison between structural steel and light gauge steel structures," Innov. Infrastruct. Solut., vol. 9, no. 6, p. 197, May 2024, doi: 10.1007/s41062-024-01481-x.

[9] longsheng, "What is the Limitation of Conventional Machining Processes - LONGSHENG," https://www.longshengmfg.com/. Accessed: Sep. 02, 2024. [Online]. Available: https://www.longshengmfg.com/what-is-the-limitation-of-conventional-machining-processes/

[10] J. Jiang, X. Xu, and J. Stringer, "Optimization of Process Planning for Reducing Material Waste in Extrusion Based Additive Manufacturing," Robotics and Computer-Integrated Manufacturing, May 2019, doi: 10.1016/j.rcim.2019.05.007.

[11] A. Mecheter, F. Tarlochan, and M. Kucukvar, “A Review of Conventional versus Additive Manufacturing for Metals: Life-Cycle Environmental and Economic Analysis,” Sustainability, vol. 15, no. 16, Art. no. 16, Jan. 2023, doi: 10.3390/su151612299.

[12] G. Liu et al., “Additive manufacturing of structural materials,” Materials Science and Engineering: R: Reports, vol. 145, p. 100596, Jul. 2021, doi: 10.1016/j.mser.2020.100596.

[13] N. Haghdadi, M. Laleh, M. Moyle, and S. Primig, “Additive manufacturing of steels: a review of achievements and challenges,” J Mater Sci, vol. 56, no. 1, pp. 64–107, Jan. 2021, doi: 10.1007/s10853-020-05109-0.

[14] “Additive Manufacturing vs Traditional Manufacturing | MadeInAdd.” Accessed: Sep. 01, 2024. [Online]. Available: https://www.madeinadd.com/knowledge-hub/additive-manufacturing-vs-traditional-manufacturing

[15] C. Buchanan and L. Gardner, “Metal 3D printing in construction: A review of methods, research, applications, opportunities and challenges,” Engineering Structures, vol. 180, pp. 332–348, Feb. 2019, doi: 10.1016/j.engstruct.2018.11.045.

[16] J. W. Stamper, “The Galerie des Machines of the 1889 Paris World’s Fair,” Technology and Culture, vol. 30, no. 2, pp. 330–353, 1989, doi: 10.2307/3105107.

[17] “Ferdinand Dutert: Galérie des Machines (orthoslogos.fr).” Accessed: Sep. 04, 2024. [Online]. Available: https://orthoslogos.fr/architecture/galerie-des-machines/

[18] “The evolution of structural steel.” Accessed: Sep. 04, 2024. [Online]. Available: https://www.cgaeng.com.au/blog/the-evolution-of-structural-steel

[19] “BUILDING BIG: Databank: John Hancock Center.” Accessed: Sep. 05, 2024. [Online]. Available: https://www.pbs.org/wgbh/buildingbig/wonder/structure/john_hancock.html

[20] “John Hancock Center,” Architectuul. Accessed: Sep. 05, 2024. [Online]. Available: https://architectuul.com/architecture/john-hancock-center

[21] W. C. Agency, “John Hancock Center: History, Architecture, and Facts,” Buildings DB. Accessed: Sep. 05, 2024. [Online]. Available: https://buildingsdb.com/IL/chicago/john-hancock-center/

[22] “FARNSWORTH HOUSE.” Accessed: Sep. 08, 2024. [Online]. Available: http://

architecture-history.org/architects/architects/MIES%20VAN%20DER%20ROHE/objects/1945,%20farnsworth%20house.html

[23] “Our building - Centre Pompidou.” Accessed: Sep. 08, 2024. [Online]. Available: https://www.centrepompidou.fr/en/collection/our-building

[24] “Richard Rogers | Biography, Architecture, Buildings, & Facts | Britannica.” Accessed: Sep. 08, 2024. [Online]. Available: https://www.britannica.com/topic/Pompidou-Centre

[25] C. M. Highsmith, “View of architect Mies van der Rohe’s classic modernist Farnsworth House, Plano, Illinois.” Accessed: Dec. 06, 2024. [Online]. Available: https://www.loc.gov/pictures/item/2011633511/

[26] “Richard Rogers, One of the Leading Architects of the British High-Tech Movement,” ArchDaily. Accessed: Feb. 13, 2025. [Online]. Available: https://www.archdaily.com/405538/happy-birthday-richard-rogers

[27] “Stuttgart Airport Structural Case Study,” RikySongSu. Accessed: Feb. 05, 2024. [Online]. Available: https://www.rikysongsu.com/blog/2017/4/26/stuttgart-airport

[28] CatalpaSpirit, Deutsch: Terminal 1 am Stuttgarter Flughafen mit baumähnlichen Stützpfeilern. 2018. Accessed: Feb. 17, 2025. [Online]. Available: https://commons.wikimedia.org/w/index.php?curid=69170369

[29] “NVIDIA HQ: Voyager Building by Gensler,” Architizer. Accessed: Sep. 09, 2024. [Online]. Available: https://architizer.com/projects/nvidia-hq-voyager-building/

[30] “NVIDIA Voyager,” DBM Vircon. Accessed: Sep. 09, 2024. [Online]. Available: https://www.dbmvircon.com/projects/nvidia-phase-ii/

[31] “Behold Nvidia’s Giant New Voyager Building,” CNET. Accessed: Sep. 09, 2024. [Online]. Available: https://www.cnet.com/pictures/behold-nvidias-giant-new-voyager-building/

[32] S. Rabia, “Designing with Structural Steel - A Guide for Architects - 2nd Edition.pdf”, Accessed: Sep. 09, 2024. [Online]. Available: https://www.academia.edu/37471762/Designing_with_Structural_Steel_A_Guide_for_Architects_2nd_Edition_pdf

[33] “Elements of Aesthetics in Architecture: Concepts and Essential Tips.” Accessed: Sep. 09, 2024. [Online]. Available: https://janussteelopc.com/elements-of-aesthetics-in-

architecture/

[34] R. Ergün and F. Aykal, “The use of biomimicry in architecture for sustainable building design: a systematic review,” ALAM CIPTA International Journal Of Sustainable Tropical Design & Practice, vol. 15, pp. 24–37, Dec. 2022, doi: 10.47836/AC.15.2.PAPER03.

[35] J. M. Benyus, Biomimicry: innovation inspired by nature, 1st Quill ed. New York: Quill, 1998.

[36] “ISO 18458:2015(en), Biomimetics — Terminology, concepts and methodology.” Accessed: Feb. 11, 2025. [Online]. Available: https://www.iso.org/obp/ui/#iso:std:iso:18458:ed-1:v1:en

[37] E. Jamei and Z. Vrcelj, “Biomimicry and the Built Environment, Learning from Nature’s Solutions,” Applied Sciences, vol. 11, no. 16, Art. no. 16, Jan. 2021, doi: 10.3390/app11167514.

[38] N. Verbrugghe, E. Rubinacci, and A. Z. Khan, “Biomimicry in Architecture: A Review of Definitions, Case Studies, and Design Methods,” Biomimetics, vol. 8, no. 1, Art. no. 1, Mar. 2023, doi: 10.3390/biomimetics8010107.

[39] R. Rao, “Biomimicry in Architecture,” Apr. 2014, Accessed: Feb. 12, 2025. [Online]. Available: https://www.academia.edu/63197635/Biomimicry_in_Architecture

[40] M. Ahamed, H. Wang, and P. Hazell, “From biology to biomimicry: Using nature to build better structures – A review,” Construction and Building Materials, vol. 320, p. 126195, Feb. 2022, doi: 10.1016/j.conbuildmat.2021.126195.

[41] Yumpu.com, “nature structure - Skidmore, Owings & Merrill LLP,” yumpu.com. Accessed: Jan. 29, 2025. [Online]. Available: https://www.yumpu.com/en/document/view/6759084/nature-structure-skidmore-owings-merrill-llp

[42] O. A. Oguntona and C. O. Aigbavboa, “Nature inspiration, imitation, and emulation: Biomimicry thinking path to sustainability in the construction industry,” Front. Built Environ., vol. 9, Jan. 2023, doi: 10.3389/fbuil.2023.1085979.

[43] L. KAYA, C. Yücedağ, and H. Aşıkkutlu, REFLECTIONS OF BIOMIMICRY TO SPATIAL DESIGN. 2018.

[44] S. Sipahioğlu Kara and B. Gökmen, “Searching Biomimicry in the Vernacular Architecture,” 2022.

[45] M. hu, THE ART OF PERFORMANCE-DRIVEN STRUCTURE DESIGN – BIOMIMICRY APPROACH The Art of Performance-driven Design – Biomimicry and Structure. 2017.

[46] Ce. Aranas Uwe, English: Beijing, China: National Stadium, also known as “birds nest.” 2009. Accessed: Feb. 24, 2025. [Online]. Available: https://commons.wikimedia.org/wiki/File:Beijing_China_Beijing-National-Stadium-02.jpg

[47] N. Magdy and H. Abd, Biological modeling as a tool for promoting sustainable construction technologies and improving the energy efficiency. 2018.

[48] E. A. Hamdy, “Achieving Thermal Comfort by Simulating the Ecosystems of the Desert Environment,” in Advances in Architecture, Engineering and Technology, F. Rosso, C. Fabiani, H. Altan, and M. Amer, Eds., Cham: Springer International Publishing, 2022, pp. 227–242. doi: 10.1007/978-3-030-86913-7_15.

[49] H. and R. Kennedy, Namibian Desert Beetle Stenocara gracilipes. 2012. Accessed: Mar. 07, 2025. [Photo]. Available: https://www.flickr.com/photos/harryandrowena/8066930540/

[50] T. Saluja, “Understanding Biomimicry The three levels of Mimicry,” RTF | Rethinking The Future. Accessed: Feb. 13, 2025. [Online]. Available: https://www.re-thinkingthefuture.com/rtf-fresh-perspectives/a1285-understanding-biomimicry-the-three-levels-of-mimicry/

[51] WolfmanSF, English: The California Academy of Sciences, Golden Gate Park, San Francisco, California, as viewed from the tower of the de Young Museum (with the University of California, San Francisco Parnassus campus at the base of Mount Sutro in the distance). The building has a green roof. The three largest “hills” on the roof overlie the planetarium, swamp exhibit and rainforest exhibit (left to right). 2010. Accessed: Mar. 04, 2025. [Online]. Available: https://commons.wikimedia.org/wiki/File:California_Academy_of_Sciences_pano.jpg

[52] A. A. M. de Sá and D. M. Viana, “Design and Biomimicry: A Review of Interconnections and Creative Potentials,” Biomimetics, vol. 8, no. 1, Art. no. 1, Mar. 2023, doi: 10.3390/biomimetics8010061.

[53] T. Meyer Boake, “Poly Corporation Headquarters - The Skyscraper Center.” Accessed: Feb. 13, 2025. [Online]. Available: https://www.skyscrapercenter.com/building/poly-corporation-headquarters/15093

[54] M. Grigorian, “Biomimicry and Theory of Structures-Design Methodology Transfer from Trees to Moment Frames,” Journal of Bionic Engineering, vol. 11, no. 4, pp. 638–648, Oct. 2014, doi: 10.1016/S1672-6529(14)60075-5.

[55] I. Md Rian and M. Sassone, “Tree-inspired dendriforms and fractal-like branching structures in architecture: A brief historical overview,” Frontiers of Architectural Research, vol. 3, no. 3, pp. 298–323, Sep. 2014, doi: 10.1016/j.foar.2014.03.006.

[56] L. Wang, W. Du, P. He, and M. Yang, “Topology Optimization and 3D Printing of Three-Branch Joints in Treelike Structures,” Journal of Structural Engineering, vol. 146, p. 04019167, Jan. 2020, doi: 10.1061/(ASCE)ST.1943-541X.0002454.

[57] S. Majumder and P. Saha, Biomimicry and its adaptations to solve complex problems in civil engineering systems. 2014.

[58] A. Bucknell, “Building bridges: 7 designs that link cultures and communities,” The Spaces. Accessed: Feb. 13, 2025. [Online]. Available: https://thespaces.com/bridge-designs-across-the-world/

[59] “Tabiat Bridge,” Pixieset. Accessed: Feb. 13, 2025. [Online]. Available: https://ettefagh.pixieset.com/tabiat-bridge/

[60] S. Yiatros, A. Wadee, and G. Hunt, “The load-bearing duct: Biomimicry in structural design,” Engineering Sustainability, vol. 160, pp. 179–188, Jan. 2007, doi: 10.1680/ensu.2007.160.4.179.

[61] A. Nazir, K. M. Abate, A. Kumar, and J.-Y. Jeng, “A state-of-the-art review on types, design, optimization, and additive manufacturing of cellular structures,” Int J Adv Manuf Technol, vol. 104, no. 9, pp. 3489–3510, Oct. 2019, doi: 10.1007/s00170-019-04085-3.

[62] G. M. from S. M. Kingdom United, Honey Comb Structure. 2011. Accessed: Feb. 13, 2025. [Online]. Available: https://commons.wikimedia.org/wiki/File:Honeycomb_structure_(6248780733).jpg

[63] Ermell, English: Larvae of the house field wasp in the nest. 2023. Accessed: Feb. 19, 2025. [Online]. Available: https://commons.wikimedia.org/wiki/File:Haus-Feldwespe_(Polistes_dominula)_Nest-20230531-RM-171317.jpg

[64] “Photo by Valeria Danilova on Pexels,” Pexels. Accessed: Feb. 19, 2025. [Online]. Available: https://www.pexels.com/photo/clusters-of-blue-bubbles-in-close-up-shot-7011871/

[65] “Photo by ClickerHappy on Pexels,” Pexels. Accessed: Feb. 27, 2025. [Online]. Available: https://www.pexels.com/photo/green-leaf-2933378/

[66] L. Bryant, Giraffe Canvas. 2016. Accessed: Mar. 11, 2025. [Online]. Available: https://commons.wikimedia.org/wiki/File:Giraffe_Canvas_(177136325).jpeg

[67] H. Zhong, T. Song, C. Li, R. Das, J. Gu, and M. Qian, “The Gibson-Ashby model for additively manufactured metal lattice materials: Its theoretical basis, limitations and new insights from remedies,” Current Opinion in Solid State and Materials Science, vol. 27, no. 3, p. 101081, Jun. 2023, doi: 10.1016/j.cossms.2023.101081.

[68] C. Pan, Y. Han, and J. Lu, “Design and Optimization of Lattice Structures: A Review,” Applied Sciences, vol. 10, p. 6374, Sep. 2020, doi: 10.3390/app10186374.

[69] W. Tao and M. C. Leu, “Design of lattice structure for additive manufacturing,” in 2016 International Symposium on Flexible Automation (ISFA), Aug. 2016, pp. 325–332. doi: 10.1109/ISFA.2016.7790182.

[70] A. Ahmad, L. Belluomo, M. Bici, and F. Campana, “Bird’s Eye View on Lattice Structures: Design Issues and Applications for Best Practices in Mechanical Design,” Metals, vol. 13, no. 10, Art. no. 10, Oct. 2023, doi: 10.3390/met13101666.

[71] S. Ataollahi, “A review on additive manufacturing of lattice structures in tissue engineering,” Bioprinting, vol. 35, p. e00304, Nov. 2023, doi: 10.1016/j.bprint.2023.e00304.

[72] W. P. Syam, W. Jianwei, B. Zhao, I. Maskery, W. Elmadih, and R. Leach, “Design and analysis of strut-based lattice structures for vibration isolation,” Precision Engineering, vol. 52, pp. 494–506, Apr. 2018, doi: 10.1016/j.precisioneng.2017.09.010.

[73] S. A. Tyagi and M. M, “Additive manufacturing of titanium-based lattice structures for medical applications – A review,” Bioprinting, vol. 30, p. e00267, Apr. 2023, doi: 10.1016/j.bprint.2023.e00267.

[74] H. M. A. Ali, M. Abdi, and Y. Sun, “Insight into the mechanical properties of 3D printed strut-based lattice structures,” Prog Addit Manuf, vol. 8, no. 5, pp. 919–931, Oct. 2023, doi: 10.1007/s40964-022-00365-9.

[75] “Lattice Structures and their Applications – EDO Additive Solutions.” Accessed: Aug. 23, 2024. [Online]. Available: https://edo-additive.ch/blog/lattice-structures-and-their-applications/

[76] A. Changdar, S. S. Chakraborty, Y. Li, and C. Wen, “Laser additive manufacturing of aluminum-based stochastic and nonstochastic cellular materials,” Journal of Materials Science & Technology, vol. 183, pp. 89–119, Jun. 2024, doi: 10.1016/j.jmst.2023.09.045.

[77] K. Yeranee and Y. Rao, “A Review of Recent Investigations on Flow and Heat Transfer Enhancement in Cooling Channels Embedded with Triply Periodic Minimal Surfaces (TPMS),” Energies, vol. 15, no. 23, Art. no. 23, Jan. 2022, doi: 10.3390/en15238994.

[78] G. P. Borikar, A. R. Patil, and S. B. Kolekar, “Additively Manufactured Lattice Structures and Materials: Present Progress and Future Scope,” Int. J. Precis. Eng. Manuf., vol. 24, no. 11, pp. 2133–2180, Nov. 2023, doi: 10.1007/s12541-023-00848-x.

[79] Y. Liu, “Mechanical properties of a new type of plate–lattice structures,” International Journal of Mechanical Sciences, vol. 192, p. 106141, Feb. 2021, doi: 10.1016/j.ijmecsci.2020.106141.

[80] A. Nazir, A. B. Arshad, S.-C. Lin, and J.-Y. Jeng, “Mechanical Performance of Lightweight-Designed Honeycomb Structures Fabricated Using Multijet Fusion Additive Manufacturing Technology,” 3D Printing and Additive Manufacturing, vol. 9, no. 4, pp. 311–325, Aug. 2022, doi: 10.1089/3dp.2021.0004.

[81] C. Qi, F. Jiang, and S. Yang, “Advanced honeycomb designs for improving mechanical properties: A review,” Composites Part B: Engineering, vol. 227, p. 109393, Dec. 2021, doi: 10.1016/j.compositesb.2021.109393.

[82] R. Gorguluarslan, U. Gandhi, R. Mandapati, and S.-K. Choi, “Design and fabrication of periodic lattice-based cellular structures,” Computer-Aided Design and Applications, vol. 13, Aug. 2015, doi: 10.1080/16864360.2015.1059194.

[83] K.-M. Park, K.-S. Min, and Y.-S. Roh, “Design Optimization of Lattice Structures under Compression: Study of Unit Cell Types and Cell Arrangements,” Materials, vol. 15, no. 1, Art. no. 1, Jan. 2022, doi: 10.3390/ma15010097.

[84] T. Maconachie et al., “SLM lattice structures: Properties, performance, applications and challenges,” Materials & Design, vol. 183, p. 108137, Dec. 2019, doi: 10.1016/j.matdes.2019.108137.

[85] K. Mekonen, A. Nazir, Y. P. Yeh, J.-E. Chen, and J.-Y. Jeng, “Design, optimization, and validation of mechanical properties of different cellular structures for biomedical application,” The International Journal of Advanced Manufacturing Technology, vol. 106, Jan. 2020, doi: 10.1007/s00170-019-04671-5.

[86] P. Zhang, P. Yu, R. Zhang, X. Chen, and H. Tan, “Grid octet truss lattice materials for energy absorption,” International Journal of Mechanical Sciences, vol. 259, p. 108616, Dec. 2023, doi: 10.1016/j.ijmecsci.2023.108616.

[87] R. Chu, “Octet space frame structure and components for assembling such space frames,” US4869041A, Sep. 26, 1989 Accessed: Mar. 12, 2024. [Online]. Available: https://patents.google.com/patent/US4869041A/en

[88] J. Mueller, K. H. Matlack, K. Shea, and C. Daraio, “Energy Absorption Properties of Periodic and Stochastic 3D Lattice Materials,” Advanced Theory and Simulations, vol. 2, no. 10, p. 1900081, 2019, doi: 10.1002/adts.201900081.

[89] R. Negm, “The Concept of “ Voronoi Diagram”and its impact on the formation of Scenic Design,” International Design Journal, vol. 11, no. 2, pp. 185–199, Mar. 2021, doi: 10.21608/idj.2021.152352.

[90] G. Angelucci and F. Mollaioli, “Voronoi-Like Grid Systems for Tall Buildings,” Frontiers in Built Environment, vol. 4, 2018, Accessed: Feb. 10, 2024. [Online]. Available: https://www.frontiersin.org/articles/10.3389/fbuil.2018.00078

[91] H.-Y. Lei, J.-R. Li, Z.-J. Xu, and Q.-H. Wang, “Parametric design of Voronoi-based lattice porous structures,” Materials & Design, vol. 191, p. 108607, Jun. 2020, doi: 10.1016/j.matdes.2020.108607.

[92] Y. Song, Z. Wang, L. Zhao, and J. Luo, “Dynamic crushing behavior of 3D closed-cell foams based on Voronoi random model,” Materials & Design, vol. 31, no. 9, pp. 4281–4289, Oct. 2010, doi: 10.1016/j.matdes.2010.04.007.

[93] E. Mele, M. Fraldi, G. Montuori, G. Perrella, and vincenzo vista, “Hexagrid-Voronoi transition in structural patterns for tall buildings,” Frattura ed Integrità Strutturale, vol. 13, pp. 186–208, Dec. 2018, doi: 10.3221/IGF-ESIS.47.15.

[94] W. Rokicki and E. Gawell, “Voronoi diagrams – architectural and structural rod structure research model optimization,” MAZOWSZE Studia Regionalne, vol. 2016, pp. 155–164, Sep. 2016, doi: 10.21858/msr.19.10.

[95] M. Bruggi, “Conceptual Design of Diagrids and Hexagrids by Distribution of Lattice Structures,” Front. Built Environ., vol. 6, Jun. 2020, doi: 10.3389/fbuil.2020.00080.

[96] N. Friedman and A. Ibrahimbegovic, “Overview of Highly Flexible, Deployable Lattice Structures Used in Architecture and Civil Engineering Undergoing Large

Displacements," YBL Journal of Built Environment, vol. 1, no. 1, pp. 85–103, Jul. 2013, doi: 10.2478/jbe-2013-0006.

[97] N. Ramzy, "Sustainable spaces with psychological connotation: Historical architecture as reference book for biomimetic models with biophilic qualities," Archnet-IJAR, vol. 9, pp. 248–267, Jul. 2015, doi: 10.26687/archnet-ijar.v9i2.464.

[98] D. Rosen, S. Johnston, and M. Reed, "Design of General Lattice Structures for Lightweight and Compliance Applications".

[99] M. Waleed, A. Elmokadem, H. Hussein, and N. Badawy, "The Impact of Digital Tools on Parametric Architecture," Port-Said Engineering Research Journal, Feb. 2023, doi: 10.21608/pserj.2023.176865.1203.

[100] R. Woodbury, S. Williamson, and P. Beesley, "Parametric Modelling as a Design Representation in Architecture: A Process Account," Proceedings of the Canadian Engineering Education Association, vol. 0, Aug. 2011, doi: 10.24908/pceea.v0i0.3827.

[101] M. Stavric and O. Marina, "Parametric modeling for advanced architecture," International Journal of Applied Mathematics and Informatics, vol. 5, pp. 9–16, Jan. 2011.

[102] "CATIA," Dassault Systèmes. Accessed: Feb. 14, 2025. [Online]. Available: https://www.3ds.com/products/catia

[103] "The Proven Solution for 3D Design and Product Development | SOLIDWORKS." Accessed: Feb. 14, 2025. [Online]. Available: https://www.solidworks.com/proven-solution-3d-design-and-product-development

[104] V. Laghi, N. Babovic, E. Benvenuti, and H. Kloft, "Blended structural optimization of steel joints for Wire-and-Arc Additive Manufacturing," Engineering Structures, vol. 300, p. 117141, Feb. 2024, doi: 10.1016/j.engstruct.2023.117141.

[105] M. N. Bin Kamarudin, J. S. Mohamed Ali, A. Aabid, and Y. E. Ibrahim, "Buckling Analysis of a Thin-Walled Structure Using Finite Element Method and Design of Experiments," Aerospace, vol. 9, no. 10, Art. no. 10, Oct. 2022, doi: 10.3390/aerospace9100541.

[106] A. M. Gadade and M. Sutar, "Computationally Efficient Procedure for Stress Analysis of Laminated Composite Shell Subjected to Different Loading Using ABAQUS Software | IIETA." Accessed: Jan. 13, 2025. [Online]. Available: https://www.iieta.org/journals/rcma/paper/10.18280/rcma.300206

[107] M. M. Eladly, "Behaviour of stainless steel beam-to-column bolted connections–Part 1: Simplified FE model," Journal of Constructional Steel Research, vol. 164, p. 105784, Jan. 2020, doi: 10.1016/j.jcsr.2019.105784.

[108] J. Ye, G. Quan, X. Yun, X. Guo, and J. Chen, "An improved and robust finite element model for simulation of thin-walled steel bolted connections," Engineering Structures, vol. 250, p. 113368, Jan. 2022, doi: 10.1016/j.engstruct.2021.113368.

[109] L. Han, W. Du, Z. Xia, B. Gao, and M. Yang, "Generative Design and Integrated 3D Printing Manufacture of Cross Joints," Materials (Basel), vol. 15, no. 14, p. 4753, Jul. 2022, doi: 10.3390/ma15144753.

[110] "Topology Optimization 101: How to Use Algorithmic Models to Create Lightweight Design," Formlabs. Accessed: Aug. 24, 2024. [Online]. Available: https://formlabs.com/blog/topology-optimization/

[111] I. P. Rosinha, K. V. Gernaey, J. M. Woodley, and U. Krühne, "Topology optimization for biocatalytic microreactor configurations," in Computer Aided Chemical Engineering, vol. 37, K. V. Gernaey, J. K. Huusom, and R. Gani, Eds., in 12 International Symposium on Process Systems Engineering and 25 European Symposium on Computer Aided Process Engineering, vol. 37. , Elsevier, 2015, pp. 1463–1468. doi: 10.1016/B978-0-444-63577-8.50089-9.

[112] T. Sirola and I. Y. Kim, "Multi-joint topology optimization for stiffness constrained design problems," Struct Multidisc Optim, vol. 66, no. 6, p. 129, May 2023, doi: 10.1007/s00158-023-03581-1.

[113] K. Jj, K. Tsavdaridis, and V. Toropov, Applications of Topology Optimization in Structural Engineering. 2014.

[114] "Topology Optimisation | Benefits & Disadvantages | Software," Fractory. Accessed: Aug. 27, 2024. [Online]. Available: http://https%253A%252F%252Ffractory.com%252Ftopology-optimisation%252F

[115] H. Seifi, A. Rezaee Javan, S. Xu, Y. Zhao, and Y. M. Xie, "Design optimization and additive manufacturing of nodes in gridshell structures," Engineering Structures, vol. 160, pp. 161–170, Apr. 2018, doi: 10.1016/j.engstruct.2018.01.036.

[116] N. Zhu and J. Liu, "Multiobjective Topology Optimization of Spatial-Structure Joints," Advances in Civil Engineering, vol. 2021, no. 1, p. 5530644, 2021, doi: 10.1155/2021/5530644.

[117] L. Li and X. Zhu, “Design of compliant revolute joints based on mechanism stiffness matrix through topology optimization using a parameterization level set method,” Structural and Multidisciplinary Optimization, vol. 60, Oct. 2019, doi: 10.1007/s00158-019-02278-8.

[118] H. Wang, W. Du, Y. Zhao, Y. Wang, R. Hao, and M. Yang, “Joints for treelike column structures based on generative design and additive manufacturing,” Journal of Constructional Steel Research, vol. 184, p. 106794, Sep. 2021, doi: 10.1016/j.jcsr.2021.106794.

[119] S. Oh, Y. Jung, S. Kim, I. Lee, and N. Kang, “Deep Generative Design: Integration of Topology Optimization and Generative Models,” Journal of Mechanical Design, vol. 141, p. 1, Jul. 2019, doi: 10.1115/1.4044229.

[120] “Applications of Topology Optimization in Structural Engineering : High - Rise Buildings and Steel Components.” Accessed: Feb. 28, 2025. [Online]. Available: https://jjce.just.edu.jo/Home/ShowPaper.aspx?data=7%2fmElg3kzlRp5QrJUNibhfVwjeXJ0LMPttbhM4HocoM%3d

[121] M. Selmı and Z. Y. İlerisoy, “A Comparative Study of Different Grasshopper Plugins for Topology Optimization in Architectural Design,” GUJSPB, vol. 10, no. 3, Art. no. 3, Sep. 2022.

[122] W. Du, Z. Xia, L. Han, and B. Gao, “3D solid model generation method based on a generative adversarial network,” Applied Intelligence, vol. 53, Dec. 2022, doi: 10.1007/s10489-022-04381-8.

[123] N. Syamsir, R. Nur, A. Salam, and Y. Busrah, “Analyzing and modelling gripper arm using shape optimization of fusion 360 and 3D printing of polylactic acid,” AIP Conference Proceedings, vol. 2543, no. 1, p. 060012, Nov. 2022, doi: 10.1063/5.0094739.

[124] P. Curkovic, “Comparative Analysis of Topology Optimization Platforms for Additive Manufacturing of Robot Arms,” Designs, vol. 8, p. 98, Sep. 2024, doi: 10.3390/designs8050098.

[125] “3D Printing vs. Traditional Manufacturing: Differences and Comparison.” Accessed: Sep. 01, 2024. [Online]. Available: https://www.xometry.com/resources/3d-printing/3d-printing-vs-traditional-manufacturing/

[126] “CIDECT.” Accessed: Aug. 27, 2024. [Online]. Available: https://www.cidect.org/

[127] “What is Metal Shearing? - LWS Manufacturing & Welding,” LWS Manufacturing & Welding Ltd. Accessed: Aug. 28, 2024. [Online]. Available: https://www.lwsmetalfab.com/news/what-is-metal-shearing/

[128] admin, “Metal Shearing: Advantages and Disadvantages,” Cresco. Accessed: Feb. 16, 2025. [Online]. Available: https://crescocustommetals.com/metal-shearing-advantages-and-disadvantages/

[129] “Trimming & Notching - Industrial Press Applications,” Air-Hydraulics, Inc. Accessed: Aug. 28, 2024. [Online]. Available: https://www.airhydraulics.com/industrial-press-application/stamping-shearing-punching/trimming-notching/

[130] W. Hardware, “Sheet Metal Notching 101: Definition, Types, Working Process | CNC Precision Machining Service,” Worthy Hardware. Accessed: Feb. 16, 2025. [Online]. Available: https://www.worthyhardware.com/news/sheet-metal-notching/

[131] “Punching sheet metal - how does it work?,” CNC24. Accessed: Aug. 28, 2024. [Online]. Available: https://www.cnc24.com/resources/cnc/punching-sheet-metal-how-does-it-work/

[132] KDMFAB, “Sheet Metal Blanking: The Complete Guide,” KDM Fabrication. Accessed: Aug. 28, 2024. [Online]. Available: https://kdmfab.com/sheet-metal-blanking/

[133] “CIDECT.” Accessed: May 20, 2024. [Online]. Available: https://www.cidect.org/design-guides/

[134] W. Hardware, “What is Slot Milling? Definitions, Types, and Tips You Should Know,” Worthy Hardware. Accessed: Aug. 28, 2024. [Online]. Available: https://www.worthyhardware.com/news/what-is-slot-milling-definitions-types-and-tips-you-should-know/

[135] “CPC Scheme - B23D PLANING; SLOTTING; SHEARING; BROACHING; SAWING; FILING; SCRAPING; LIKE OPERATIONS FOR WORKING METAL BY REMOVING MATERIAL, NOT OTHERWISE PROVIDED FOR.” Accessed: Aug. 28, 2024. [Online]. Available: https://www.uspto.gov/web/patents/classification/cpc/html/cpc-B23D.html

[136] Akshay, “Metal Slotting.” Accessed: Feb. 16, 2025. [Online]. Available: http://www.vlsijunction.com/2019/11/metal-slotting.html

[137] “How Laser Cutting Is Used in Different Industries.” Accessed: Feb. 16, 2025. [Online]. Available: https://www.xometry.com/resources/sheet/how-is-laser-cutting-

used-in-industry/

[138] “What Are the Advantages & Disadvantages of Laser Cutting?,” Fractory. Accessed: Feb. 16, 2025. [Online]. Available: http://https%253A%252F%252Ffractory.com%252Flaser-cutting-advantages-disadvantages%252F

[139] “How Plasma Cutting Works? Advantages & Disadvantages,” Fractory. Accessed: Feb. 16, 2025. [Online]. Available: https://fractory.com/plasma-cutting/

[140] “Oxy Acetylene vs Plasma Cutting | UNIMIG Welding Guides & Tutorials,” UNIMIG. Accessed: Aug. 28, 2024. [Online]. Available: https://unimig.com.au/oxy-acetylene-vs-plasma-cutting/

[141] digitalmoves, “What are the advantages and disadvantages of flame cutting?,” flamekut. Accessed: Feb. 16, 2025. [Online]. Available: https://flamekutprofiles.co.uk/what-are-the-advantages-and-disadvantages-of-flame-cutting/

[142] “Plasma Cutting Vs Flame Cutting - R.M.P. Products.” Accessed: Feb. 16, 2025. [Online]. Available: https://rmpproducts.co.uk/plasma-cutting-vs-flame-cutting/

[143] “What Is Waterjet Cutting Technology and How Does It Work | TECHNI WATERJETTM,” TechniWaterjet. Accessed: Aug. 28, 2024. [Online]. Available: https://www.techniwaterjet.com/how-it-works/

[144] “Waterjet Cutting Pros & Cons,” Metal Cutting Corporation. Accessed: Feb. 16, 2025. [Online]. Available: https://metalcutting.com/knowledge-center/waterjet-cutting-pros-and-cons/

[145] Marketeer, “The Advantages and Disadvantages of Waterjet Cutting,” Ballard Machine Works. Accessed: Feb. 16, 2025. [Online]. Available: https://ballardmachineworks.com/2016/07/02/advantages-disadvantages-waterjet-cutting/

[146] “CIDECT.” Accessed: Aug. 27, 2024. [Online]. Available: https://www.cidect.org/design-guides/

[147] admin, “What is Sheet Metal Folding?,” ADS Laser. Accessed: Aug. 29, 2024. [Online]. Available: https://adslaser.co.uk/what-is-sheet-metal-bending/

[148] “What Is Sheet Metal Bending? - Find Out From Experts,” Salamander Fabrications. Accessed: Aug. 29, 2024. [Online]. Available: https://salamanderfabs.com/latest-news/what-is-sheet-metal-bending/

[149] “Metal machining – what is this process?” Accessed: Aug. 29, 2024. [Online]. Available: https://radmot.com/blog/metal-machining

[150] “Flattening and Punching,” Schmale Machinery USA LLC. Accessed: Aug. 29, 2024. [Online]. Available: https://schmale-machinery.com/flattening-and-punching/

[151] “Modern Steel Construction February 2024: Add to the Toolbox.” Accessed: Dec. 06, 2024. [Online]. Available: https://lsc-pagepro.mydigitalpublication.comhttps://lsc-pagepro.mydigitalpublication.com/article/Add+to+the+Toolbox/4706768/812610/article.html

[152] David, “Common Casting Defects and Discontinuities,” Reliance Foundry Co. Ltd. Accessed: Apr. 08, 2024. [Online]. Available: https://www.reliance-foundry.com/blog/casting-defects

[153] “ISO/ASTM 52900:2015(en), Additive manufacturing — General principles — Terminology.” Accessed: Jul. 18, 2024. [Online]. Available: https://www.iso.org/obp/ui#iso:std:iso-astm:52900:ed-1:v1:en

[154] S. Rouf et al., “Additive manufacturing technologies: Industrial and medical applications,” Sustainable Operations and Computers, vol. 3, pp. 258–274, Jan. 2022, doi: 10.1016/j.susoc.2022.05.001.

[155] “Classification of Cellular Solids (and why it matters) - PADT.” Accessed: Mar. 17, 2024. [Online]. Available: https://www.padtinc.com/2016/08/29/classification-of-cellular-solids-and-why-it-matters/

[156] D. Delgado Camacho et al., “Applications of additive manufacturing in the construction industry – A forward-looking review,” Automation in Construction, vol. 89, pp. 110–119, May 2018, doi: 10.1016/j.autcon.2017.12.031.

[157] M. Bhuvanesh Kumar and P. Sathiya, “Methods and materials for additive manufacturing: A critical review on advancements and challenges,” Thin-Walled Structures, vol. 159, p. 107228, Feb. 2021, doi: 10.1016/j.tws.2020.107228.

[158] S. Ford, L. Mortara, and T. Minshall, “The Emergence of Additive Manufacturing: Introduction to the Special Issue,” Technological Forecasting and Social Change, vol. 102, pp. 156–159, Jan. 2016, doi: 10.1016/j.techfore.2015.09.023.

[159] “ISO/ASTM 52900:2021(en), Additive manufacturing — General principles — Fundamentals and vocabulary.” Accessed: Jul. 20, 2024. [Online]. Available: https://www.

iso.org/obp/ui/#iso:std:iso-astm:52900:ed-2:v1:en

[160] C. Suwanpreecha and A. Manonukul, “A Review on Material Extrusion Additive Manufacturing of Metal and How It Compares with Metal Injection Moulding,” Metals, vol. 12, no. 3, Art. no. 3, Mar. 2022, doi: 10.3390/met12030429.

[161] H. Gong, D. Snelling, K. Kardel, and A. Carrano, “Comparison of Stainless Steel 316L Parts Made by FDM- and SLM-Based Additive Manufacturing Processes,” JOM, vol. 71, no. 3, pp. 880–885, Mar. 2019, doi: 10.1007/s11837-018-3207-3.

[162] O. Iyibilgin, C. Yigit, and M. Leu, “Experimental investigation of different cellular lattice structures manufactured by fused deposition modeling,” 24th International SFF Symposium - An Additive Manufacturing Conference, SFF 2013, pp. 895–907, Jan. 2013.

[163] 3DEO, “An Introductory Overview of Metal Extrusion 3D Printing,” 3DEO - Metal Additive Manufacturing. Accessed: Jul. 20, 2024. [Online]. Available: https://www.3deo.co/featured/metal-3d-printing-processes-metal-extrusion-3d-printing/

[164] M. Golab, S. Massey, and J. Moultrie, “How generalisable are material extrusion additive manufacturing parameter optimisation studies? A systematic review,” Heliyon, vol. 8, no. 11, p. e11592, Nov. 2022, doi: 10.1016/j.heliyon.2022.e11592.

[165] A. Patel and M. Taufik, “Extrusion-Based Technology in Additive Manufacturing: A Comprehensive Review,” Arabian Journal for Science and Engineering, vol. 49, Dec. 2022, doi: 10.1007/s13369-022-07539-1.

[166] A. Mostafaei et al., “Binder jet 3D printing—Process parameters, materials, properties, modeling, and challenges,” Progress in Materials Science, vol. 119, p. 100707, Jun. 2021, doi: 10.1016/j.pmatsci.2020.100707.

[167] P. Szymczyk-Ziółkowska, M. B. Łabowska, J. Detyna, I. Michalak, and P. Gruber, “A review of fabrication polymer scaffolds for biomedical applications using additive manufacturing techniques,” Biocybernetics and Biomedical Engineering, vol. 40, no. 2, pp. 624–638, Apr. 2020, doi: 10.1016/j.bbe.2020.01.015.

[168] T. Mateti, S. Jain, L. Ananda Shruthi, A. Laha, and G. Thakur, “Chapter 1 - An overview of the advances in the 3D printing technology,” in 3D Printing Technology for Water Treatment Applications, J. K. Pandey, S. Manna, R. K. Patel, and M. Qian, Eds., in Additive Manufacturing Materials and Technologies. , Elsevier, 2023, pp. 1–37. doi: 10.1016/B978-0-323-99861-1.00002-3.

[169] A. M. Elliott, C. L. Cramer, P. Nandwana, M. Chmielus, and A. Mostafaei, “Binder Jet-Metals,” in Encyclopedia of Materials: Metals and Alloys, F. G. Caballero, Ed., Oxford: Elsevier, 2022, pp. 120–133. doi: 10.1016/B978-0-12-819726-4.00144-7.

[170] K. Zhao et al., “Review of the types, formation mechanisms, effects, and elimination methods of binder jetting 3D-printing defects,” Journal of Materials Research and Technology, vol. 27, pp. 5449–5469, Nov. 2023, doi: 10.1016/j.jmrt.2023.11.045.

[171] J. Qin et al., “Research and application of machine learning for additive manufacturing,” Additive Manufacturing, vol. 52, p. 102691, Apr. 2022, doi: 10.1016/j.addma.2022.102691.

[172] “What is Powder Bed Fusion 3D Printing?” Accessed: Aug. 15, 2024. [Online]. Available: https://www.additivemanufacturing.media/articles/am-101-powder-bed-fusion-pbf

[173] R. Singh et al., “Powder bed fusion process in additive manufacturing: An overview,” Materials Today: Proceedings, vol. 26, pp. 3058–3070, Jan. 2020, doi: 10.1016/j.matpr.2020.02.635.

[174] N. Divakaran, J. P. Das, A. K. P v, S. Mohanty, A. Ramadoss, and S. K. Nayak, “Comprehensive review on various additive manufacturing techniques and its implementation in electronic devices,” Journal of Manufacturing Systems, vol. 62, pp. 477–502, Jan. 2022, doi: 10.1016/j.jmsy.2022.01.002.

[175] Y. Shi et al., “Electron beam metal additive manufacturing: Defects formation and in-process control,” Journal of Manufacturing Processes, vol. 101, pp. 386–431, Sep. 2023, doi: 10.1016/j.jmapro.2023.06.013.

[176] A. Álvarez-Trejo, E. Cuan-Urquizo, D. Bhate, and A. Roman-Flores, “Mechanical metamaterials with topologies based on curved elements: An overview of design, additive manufacturing and mechanical properties,” Materials & Design, vol. 233, p. 112190, Sep. 2023, doi: 10.1016/j.matdes.2023.112190.

[177] K. Ishfaq, M. Abdullah, and M. A. Mahmood, “A state-of-the-art direct metal laser sintering of Ti6Al4V and AlSi10Mg alloys: Surface roughness, tensile strength, fatigue strength and microstructure,” Optics & Laser Technology, vol. 143, p. 107366, Nov. 2021, doi: 10.1016/j.optlastec.2021.107366.

[178] “DMLS: Definition and Applications in 3D Printing,” Sculpteo. Accessed: Aug. 16, 2024. [Online]. Available: https://www.sculpteo.com/en/glossary/dmls-definition/

[179] M. Mishra, “Direct Metal Laser Sintering Advantages and Disadvantages,” HLH Prototypes Co Ltd. Accessed: Aug. 16, 2024. [Online]. Available: https://www.hlhprototypes.com/direct-metal-laser-sintering-advantages-and-disadvantages/

[180] “Powder Bed Fusion | Additive Manufacturing Research Group | Loughborough University.” Accessed: Aug. 15, 2024. [Online]. Available: https://www.lboro.ac.uk/research/amrg/about/the7categoriesofadditivemanufacturing/powderbedfusion/

[181] C. Berger, G. Schimo-Aichhorn, S. Gronau, F. Saft, S. Seiringer, and U. Scheithauer, “Potential and challenges for Powder Bed Fusion – Laser Beam (PBF-LB) in industrial ceramic additive manufacturing,” Open Ceramics, vol. 18, p. 100614, Jun. 2024, doi: 10.1016/j.oceram.2024.100614.

[182] J. Frketic, T. Dickens, and S. Ramakrishnan, “Automated manufacturing and processing of fiber-reinforced polymer (FRP) composites: An additive review of contemporary and modern techniques for advanced materials manufacturing,” Additive Manufacturing, vol. 14, pp. 69–86, Mar. 2017, doi: 10.1016/j.addma.2017.01.003.

[183] “Sheet Lamination | Additive Manufacturing Research Group | Loughborough University.” Accessed: Aug. 16, 2024. [Online]. Available: https://www.lboro.ac.uk/research/amrg/about/the7categoriesofadditivemanufacturing/sheetlamination/

[184] “Directed energy deposition | Additive Manufacturing and 3D Printing Class Notes | Fiveable.” Accessed: Feb. 16, 2025. [Online]. Available: https://library.fiveable.me/additive-manufacturing-and-3d-printing/unit-2/directed-energy-deposition/study-guide/MPdOviLtqLuwclPK

[185] C. V. Sice and J. Faludi, “Comparing environmental impacts of metal additive manufacturing to conventional manufacturing,” Proceedings of the Design Society, vol. 1, pp. 671–680, Aug. 2021, doi: 10.1017/pds.2021.67.

[186] “Directed Energy Deposition | Additive Manufacturing Research Group | Loughborough University.” Accessed: Aug. 16, 2024. [Online]. Available: https://www.lboro.ac.uk/research/amrg/about/the7categoriesofadditivemanufacturing/directedenergydeposition/

[187] “What is DED? - DED fully explained by the RAMLAB knowledge hub,” RAMLAB. Accessed: Feb. 16, 2025. [Online]. Available: https://www.ramlab.com/resources/ded-101/

[188] T. M. Joseph et al., “3D printing of polylactic acid: recent advances and opportunities,” Int J Adv Manuf Technol, vol. 125, no. 3, pp. 1015–1035, Mar. 2023, doi: 10.1007/s00170-022-10795-y.

[189] “The Ultimate 3D Printing Filament Guide for Your FDM Project | 3DSPRO.” Accessed: Feb. 17, 2025. [Online]. Available: https://3dspro.com/resources/blog/the-ultimate-3d-printing-filament-guide-for-your-fdm-project

[190] S. F. Iftekar, A. Aabid, A. Amir, and M. Baig, “Advancements and Limitations in 3D Printing Materials and Technologies: A Critical Review,” Polymers, vol. 15, no. 11, Art. no. 11, Jan. 2023, doi: 10.3390/polym15112519.

[191] D. Tomić, A. Fudurić, T. Mihalić, and N. Šimunić, “Dimensional Accuracy of Prototypes Made with Fdm Technology,” Journal of Energy Technology, vol. 10, no. 2, pp. 51–59, Jun. 2017.

[192] J. M. Chacón, M. A. Caminero, E. García-Plaza, and P. J. Núñez, “Additive manufacturing of PLA structures using fused deposition modelling: Effect of process parameters on mechanical properties and their optimal selection,” Materials & Design, vol. 124, pp. 143–157, Jun. 2017, doi: 10.1016/j.matdes.2017.03.065.

[193] X. Wang et al., “Research progress in polylactic acid processing for 3D printing,” Journal of Manufacturing Processes, vol. 112, pp. 161–178, Feb. 2024, doi: 10.1016/j.jmapro.2024.01.038.

[194] B. K. Park, D. J. Hwang, D. E. Kwon, T. J. Yoon, and Y.-W. Lee, “Fabrication and Characterization of Multiscale PLA Structures Using Integrated Rapid Prototyping and Gas Foaming Technologies,” Nanomaterials, vol. 8, no. 8, Art. no. 8, Aug. 2018, doi: 10.3390/nano8080575.

[195] M. Fernandez-vicente, W. Calle, S. Ferrándiz, and A. Conejero, “Effect of Infill Parameters on Tensile Mechanical Behavior in Desktop 3D Printing,” 3D Printing and Additive Manufacturing, vol. 3, pp. 183–192, Sep. 2016, doi: 10.1089/3dp.2015.0036.

[196] M. González-Torres, L. Pérez-Lombard, J. F. Coronel, I. R. Maestre, and D. Yan, “A review on buildings energy information: Trends, end-uses, fuels and drivers,” Energy Reports, vol. 8, pp. 626–637, Nov. 2022, doi: 10.1016/j.egyr.2021.11.280.

[197] T. Hong, J. Langevin, and K. Sun, “Building Simulation: Ten Challenges,” Building Simulation, vol. 11, Mar. 2018, doi: 10.1007/s12273-018-0444-x.

[198] J. Kim et al., “Decarbonizing the iron and steel industry: A systematic review of sociotechnical systems, technological innovations, and policy options,” Energy Research

& Social Science, vol. 89, p. 102565, Jul. 2022, doi: 10.1016/j.erss.2022.102565.

[199] A. Kanyilmaz et al., “Role of metal 3D printing to increase quality and resource-efficiency in the construction sector,” Additive Manufacturing, vol. 50, p. 102541, Feb. 2022, doi: 10.1016/j.addma.2021.102541.

[200] S. Jung, L. B. Kara, Z. Nie, T. W. Simpson, and K. S. Whitefoot, “Is Additive Manufacturing an Environmentally and Economically Preferred Alternative for Mass Production?,” Environ Sci Technol, vol. 57, no. 16, pp. 6373–6386, Apr. 2023, doi: 10.1021/acs.est.2c04927.

[201] M. Mehrpouya, A. Dehghanghadikolaei, B. Fotovvati, A. Vosooghnia, S. Emamian, and A. Gisario, “The Potential of Additive Manufacturing in the Smart Factory Industrial 4.0: A Review,” Applied Sciences, vol. 9, p. 3865, Sep. 2019, doi: 10.3390/app9183865.

[202] G. Prasad, H. Arunav, S. Dwight, M. B. Ghosh, A. Jayadev, and D. I. Nair, “Advancing Sustainable Practices in Additive Manufacturing: A Comprehensive Review on Material Waste Recyclability,” Sustainability, vol. 16, no. 23, Art. no. 23, Jan. 2024, doi: 10.3390/su162310246.

[203] G. Prasad, H. Arunav, S. Dwight, M. Ghosh, A. Jayadev, and D. Nair, “Advancing Sustainable Practices in Additive Manufacturing: A Comprehensive Review on Material Waste Recyclability,” Sustainability, vol. 16, p. 10246, Nov. 2024, doi: 10.3390/su162310246.

[204] P. Priarone, G. Ingarao, R. Lorenzo, and L. Settineri, “Influence of Material-Related Aspects of Additive and Subtractive Ti-6Al-4V Manufacturing on Energy Demand and Carbon Dioxide Emissions,” Journal of Industrial Ecology, vol. 21, Nov. 2017, doi: 10.1111/jiec.12523.

[205] S. Torres-Carrillo, H. Siller, C. Vila, C. López, and C. Rodriguez, “Environmental Analysis of Selective Laser Melting in the Manufacturing of Aeronautical Turbine Blades,” Journal of Cleaner Production, vol. 246, p. 119068, Oct. 2019, doi: 10.1016/j.jclepro.2019.119068.

[206] M. Baumers, P. Dickens, C. Tuck, and R. Hague, “The cost of additive manufacturing: machine productivity, economies of scale and technology-push,” Technological Forecasting and Social Change, vol. 102, pp. 193–201, Jan. 2016, doi: 10.1016/j.techfore.2015.02.015.

[207] “Wire Arc Additive Manufacturing (WAAM).” Accessed: Aug. 17, 2024. [Online]. Available: https://www.twi-global.com/technical-knowledge/job-knowledge/arc-based-additive-manufacturing-137.aspx

[208] P. Pesode and S. Barve, “Additive manufacturing of magnesium alloys and its biocompatibility,” Bioprinting, vol. 36, p. e00318, Dec. 2023, doi: 10.1016/j.bprint.2023.e00318.

[209] “WELD Magazine | SOUDURE Magazine - CAD-to-Print Integration for Wire Arc-Additive Manufacturing.” Accessed: Aug. 17, 2024. [Online]. Available: https://www.weldmagazine.com/weldmagazine/library/item/weld-spring2024/4177442/

[210] N. Knezović and A. Topić, “Wire and Arc Additive Manufacturing (WAAM) – A New Advance in Manufacturing,” in Lecture Notes in Networks and Systems, 2019, pp. 65–71. doi: 10.1007/978-3-319-90893-9_7.

[211] N. Kumar et al., “Wire Arc Additive Manufacturing – A revolutionary method in additive manufacturing,” Materials Chemistry and Physics, vol. 285, p. 126144, Jun. 2022, doi: 10.1016/j.matchemphys.2022.126144.

[212] “Learn the basis of MIG welding and MAG welding,” Kemppi. Accessed: Aug. 17, 2024. [Online]. Available: https://www.kemppi.com/en-US/support/welding-abc/mig-mag-welding/

[213] K. Li et al., “Additive manufacturing of ultra-high strength steels: A review,” Journal of Alloys and Compounds, vol. 965, p. 171390, Nov. 2023, doi: 10.1016/j.jallcom.2023.171390.

[214] S. Pattanayak and S. K. Sahoo, “Gas metal arc welding based additive manufacturing—a review,” CIRP Journal of Manufacturing Science and Technology, vol. 33, pp. 398–442, May 2021, doi: 10.1016/j.cirpj.2021.04.010.

[215] S. W. Williams, F. Martina, A. C. Addison, J. Ding, G. Pardal, and P. Colegrove, “Wire + Arc Additive Manufacturing,” Materials Science and Technology, vol. 32, no. 7, pp. 641–647, May 2016, doi: 10.1179/1743284715Y.0000000073.

[216] J. Barnes, A. Kingsbury, and E. Bono, Does “ Low Cost “ Titanium Powder Yield Low Cost Titanium Parts? 2016.

[217] E. Wall, G. Sharma, E. Freeman, W. Jarrell, and J. Austin, Evaluation of Single Wall Builds Using Wire Arc Additive Manufacturing. 2024. doi: 10.1115/MSEC2024-124101.

[218] F. Michel, H. Lockett, J. Ding, F. Martina, G. Marinelli, and S. Williams, “A modular

path planning solution for Wire + Arc Additive Manufacturing," Robotics and Computer-Integrated Manufacturing, vol. 60, pp. 1–11, May 2019, doi: 10.1016/j.rcim.2019.05.009.

[219] G.-H. Song, C.-M. Lee, and D.-H. Kim, "Investigation of Path Planning to Reduce Height Errors of Intersection Parts in Wire-Arc Additive Manufacturing," Materials, vol. 14, p. 6477, Oct. 2021, doi: 10.3390/ma14216477.

[220] G. Adam and D. Zimmer, "On design for additive manufacturing: Evaluating geometrical limitations," Rapid Prototyping Journal, vol. 21, pp. 662–670, Oct. 2015, doi: 10.1108/RPJ-06-2013-0060.

[221] J. Mehnen, J. Ding, H. Lockett, and P. Kazanas, "Design study for wire and arc additive manufacture," Int. J. of Product Development, vol. 19, pp. 2–20, Jan. 2014, doi: 10.1504/IJPD.2014.060028.

[222] M. S. Mohd Mansor et al., "Integrated approach to Wire Arc Additive Manufacturing (WAAM) optimization: Harnessing the synergy of process parameters and deposition strategies," Journal of Materials Research and Technology, vol. 30, pp. 2478–2499, May 2024, doi: 10.1016/j.jmrt.2024.03.170.

[223] P. Moore, A. Addison, and M. Nowak-Coventry, "Mechanical properties of wire plus arc additive manufactured steel and stainless steel structures," Weld World, vol. 63, no. 6, pp. 1521–1530, Nov. 2019, doi: 10.1007/s40194-019-00775-4.

[224] K. Treutler et al., "Properties oriented WAAM—microstructural and geometrical control in WAAM of low-alloy steel," Weld World, vol. 68, no. 2, pp. 247–257, Feb. 2024, doi: 10.1007/s40194-023-01666-5.

[225] T. Feng et al., "Effect of Trajectory Curvature on the Microstructure and Properties of Surfacing Wall Formed with the Process of Wire Arc Additive Manufacturing," Coatings, vol. 9, no. 12, Art. no. 12, Dec. 2019, doi: 10.3390/coatings9120848.

[226] A. Richter, T. Gehling, K. Treutler, V. Wesling, and C. Rembe, "Real-time measurement of temperature and volume of the weld pool in wire-arc additive manufacturing," Measurement: Sensors, vol. 17, p. 100060, Oct. 2021, doi: 10.1016/j.measen.2021.100060.

[227] Y. Huang, L. Yang, and Q. Xin, "Novel geometrical model and design mechanical parameters for CMT-WAAM stainless steel," Journal of Constructional Steel Research, vol. 210, p. 108071, Nov. 2023, doi: 10.1016/j.jcsr.2023.108071.

[228] D. Ding et al., "A shape control strategy for wire arc additive manufacturing of thin-walled aluminium structures with sharp corners," Journal of Manufacturing Processes, vol. 64, pp. 253–264, Apr. 2021, doi: 10.1016/j.jmapro.2021.01.029.

[229] K. Treutler and V. Wesling, "The Current State of Research of Wire Arc Additive Manufacturing (WAAM): A Review," Applied Sciences, vol. 11, no. 18, p. 8619, Sep. 2021, doi: 10.3390/app11188619.

[230] H. Geng, J. Li, J. Xiong, X. Lin, and F. Zhang, "Geometric Limitation and Tensile Properties of Wire and Arc Additive Manufacturing 5A06 Aluminum Alloy Parts," J. of Materi Eng and Perform, vol. 26, no. 2, pp. 621–629, Feb. 2017, doi: 10.1007/s11665-016-2480-y.

[231] M. Dinovitzer, X. Chen, J. Laliberte, X. Huang, and H. Frei, "Effect of Wire and Arc Additive Manufacturing (WAAM) Process Parameters on Bead Geometry and Microstructure," Additive Manufacturing, vol. 26, Feb. 2019, doi: 10.1016/j.addma.2018.12.013.

[232] L. Teng Foong, Y. Xiong, A. Dharmawan, S. Foong, and G. Soh, "Adaptive process control implementation of wire arc additive manufacturing for thin-walled components with overhang features," The International Journal of Advanced Manufacturing Technology, vol. 108, May 2020, doi: 10.1007/s00170-019-04737-4.

[233] Y. Khan, "Characterizing the Properties of Tissue Constructs for Regenerative Engineering." Accessed: Feb. 15, 2025. [Online]. Available: https://ocul-wtl.primo.exlibrisgroup.com

[234] N. Hadjipantelis, B. Weber, C. Buchanan, and L. Gardner, "Description of anisotropic material response of wire and arc additively manufactured thin-walled stainless steel elements," Thin-Walled Structures, vol. 171, p. 108634, Feb. 2022, doi: 10.1016/j.tws.2021.108634.

[235] B. Huangfu, Y. Liu, X. Liu, X. Wu, and H. Bai, "Anisotropy of Additively Manufactured Metallic Materials," Materials, vol. 17, p. 3653, Jul. 2024, doi: 10.3390/ma17153653.

[236] L. Sun, F. Jiang, R. Huang, D. Yuan, C. Guo, and J. Wang, "Anisotropic mechanical properties and deformation behavior of low-carbon high-strength steel component fabricated by wire and arc additive manufacturing," Materials Science and Engineering: A, vol. 787, p. 139514, Jun. 2020, doi: 10.1016/j.msea.2020.139514.

[237] L. Palmeira Belotti, T. van Nuland, M. Geers, J. Hoefnagels, and J. A. W.

Dommelen, “On the anisotropy of thick-walled wire arc additively manufactured stainless steel parts,” Materials Science and Engineering: A, vol. 863, p. 144538, Dec. 2022, doi: 10.1016/j.msea.2022.144538.

[238] L. Wang, J. Xue, and Q. Wang, “Correlation between arc mode, microstructure, and mechanical properties during wire arc additive manufacturing of 316L stainless steel,” Materials Science and Engineering: A, vol. 751, pp. 183–190, Mar. 2019, doi: 10.1016/j.msea.2019.02.078.

[239] S. Zhang, M. Gong, X. Zeng, and M. Gao, “Residual stress and tensile anisotropy of hybrid wire arc additive-milling subtractive manufacturing,” Journal of Materials Processing Technology, vol. 293, p. 117077, Jul. 2021, doi: 10.1016/j.jmatprotec.2021.117077.

[240] Y. NAKATA, T. Abe, and J. KANEKO, “Suppression of anisotropy by wire and arc additive manufacturing with finishing process,” Journal of Advanced Mechanical Design, Systems, and Manufacturing, vol. 15, pp. JAMDSM0066–JAMDSM0066, Oct. 2021, doi: 10.1299/jamdsm.2021jamdsm0066.

[241] V. Laghi et al., “Experimentally-validated orthotropic elastic model for Wire-and-Arc Additively Manufactured stainless steel,” Additive Manufacturing, vol. 42, p. 101999, Jun. 2021, doi: 10.1016/j.addma.2021.101999.

[242] V. Mishra, C. Ayas, M. Langelaar, and F. van Keulen, “Simultaneous topology and deposition direction optimization for Wire and Arc Additive Manufacturing,” Manufacturing Letters, vol. 31, pp. 45–51, Jan. 2022, doi: 10.1016/j.mfglet.2021.05.011.

[243] D. Ma et al., “Study on anisotropy of microstructure and mechanical properties of AZ31 magnesium alloy fabricated by wire arc additive manufacturing,” China Foundry, vol. 20, no. 4, pp. 280–288, Jul. 2023, doi: 10.1007/s41230-023-2187-2.

[244] A. Paolini, S. Kollmannsberger, and E. Rank, “Additive manufacturing in construction: A review on processes, applications, and digital planning methods,” Additive Manufacturing, vol. 30, p. 100894, Dec. 2019, doi: 10.1016/j.addma.2019.100894.

[245] “Arup pioneers 3D printed steel nodes,” Construction Management. Accessed: Aug. 18, 2024. [Online]. Available: https://constructionmanagement.co.uk/arup-pioneers-3d-printed-steel-nodes/

[246] “3D Printed Smart Bridge in Amsterdam,” MX3D. Accessed: Aug. 18, 2024. [Online]. Available: https://mx3d.com/industries/design/smart-bridge/

[247] “Long-awaited 3D-printed stainless steel bridge opens in Amsterdam,” Dezeen. Accessed: Apr. 08, 2024. [Online]. Available: https://www.dezeen.com/2021/07/19/mx3d-3d-printed-bridge-stainless-steel-amsterdam/

[248] “Use Case - Connector For Takenaka,” MX3D. Accessed: Aug. 19, 2024. [Online]. Available: https://mx3d.com/industries/construction/connector-for-takenaka/

[249] Backx, “MX3D + takenaka utilize robotic 3D printing to build a structural steel connector,” designboom | architecture & design magazine. Accessed: Feb. 05, 2024. [Online]. Available: https://www.designboom.com/architecture/mx3d-takenaka-3d-print-structural-steel-connector-12-12-2019/

[250] “NASCC: The Steel Conference,” NASCC: The Steel Conference. Accessed: Dec. 06, 2024. [Online]. Available: https://www.nascc.aisc.org

[251] M. Bolan, M. Dean, and A. Bardelcik, “The Energy Absorption Behavior of 3D-Printed Polymeric Octet-Truss Lattice Structures of Varying Strut Length and Radius,” Polymers, vol. 15, no. 3, Art. no. 3, Jan. 2023, doi: 10.3390/polym15030713.

[252] V. S. Deshpande, N. A. Fleck, and M. F. Ashby, “Effective properties of the octet-truss lattice material,” Journal of the Mechanics and Physics of Solids, vol. 49, no. 8, pp. 1747–1769, Aug. 2001, doi: 10.1016/S0022-5096(01)00010-2.

[253] A. Nazir, A. B. Arshad, S.-C. Lin, and J.-Y. Jeng, “Mechanical Performance of Lightweight-Designed Honeycomb Structures Fabricated Using Multijet Fusion Additive Manufacturing Technology,” 3D Printing and Additive Manufacturing, vol. 9, no. 4, pp. 311–325, Aug. 2022, doi: 10.1089/3dp.2021.0004.

[254] S. Shakti, “OPERATIVE DESIGN A Catalog of Spatial Verbs”, Accessed: Feb. 19, 2025. [Online]. Available: https://www.academia.edu/41882032/OPERATIVE_DESIGN_A_Catalog_of_Spatial_Verbs

[255] R. M. & Associates, “Features,” www.rhino3d.com. Accessed: Dec. 23, 2024. [Online]. Available: https://www.rhino3d.com/features/

[256] R. M. & Associates, “Rhino in Architecture, Engineering, and Construction,” www.rhino3d.com. Accessed: Jan. 31, 2025. [Online]. Available: https://www.rhino3d.com/for/architecture/

[257] S. D. created this N. Network, “Grasshopper.” Accessed: Dec. 21, 2024. [Online]. Available: https://www.grasshopper3d.com/

[258] "IntraLattice," Food4Rhino. Accessed: Jan. 31, 2025. [Online]. Available: https://www.food4rhino.com/en/app/intralattice

[259] "Abaqus Analysis User's Guide (2016)." Accessed: Dec. 22, 2024. [Online]. Available: http://130.149.89.49:2080/v2016/books/usb/default.htm

[260] V. Milosevic, B. Marković, and D. Stojić, "Effects of point loads on membrane structures," Građevinar, vol. 70, pp. 1033–1041, Dec. 2018, doi: 10.14256/JCE.1670.2016.

[261] "Fusion Help | Shape optimization study | Autodesk." Accessed: Jan. 28, 2025. [Online]. Available: https://help.autodesk.com/view/fusion360/ENU/?guid=SIM-SHAPE-OPTIMIZATION

[262] F. Kaji and A. Barari, "Evaluation of the Surface Roughness of Additive Manufacturing Parts Based on the Modelling of Cusp Geometry," IFAC-PapersOnLine, vol. 48, pp. 658–663, Dec. 2015, doi: 10.1016/j.ifacol.2015.06.157.

[263] "Fusion Help | Mesh quality | Autodesk." Accessed: Jan. 28, 2025. [Online]. Available: https://help.autodesk.com/view/fusion360/ENU/?guid=SIM-MESH-QUALITY

[264] "Fusion Help | Mesh Settings dialog | Autodesk." Accessed: Jan. 28, 2025. [Online]. Available: https://help.autodesk.com/view/fusion360/ENU/?guid=GUID-6DFF3995-E770-4ACD-AE93-B15BC96ABC7E

[265] "Ultimate Materials Guide - Tips for 3D Printing with PLA." Accessed: Nov. 19, 2024. [Online]. Available: https://www.simplify3d.com/resources/materials-guide/pla/

[266] A. A. Al-Tamimi, "3D Topology Optimization and Mesh Dependency for Redesigning Locking Compression Plates Aiming to Reduce Stress Shielding," International Journal of Bioprinting, vol. 7, no. 3, Art. no. 3, Invalid date, doi: 10.18063/ijb.v7i3.339.

[267] "ARC Mate 100*i*D." Accessed: Dec. 17, 2024. [Online]. Available: https://www.fanuc.eu/eu-en/product/robot/arc-mate-100id

[268] "Tablet Teach Pendant | FANUC America," fanucamerica. Accessed: Dec. 22, 2024. [Online]. Available: https://www.fanucamerica.com/products/robots/controllers/tablet-teach-pendant

[269] L. D. Evjemo, G. Langelandsvik, S. Moe, M. H. Danielsen, and J. T. Gravdahl, "Wire-arc additive manufacturing of structures with overhang: Experimental results depositing material onto fixed substrate," CIRP Journal of Manufacturing Science and Technology, vol. 38, pp. 186–203, Aug. 2022, doi: 10.1016/j.cirpj.2022.04.006.

[270] S. Radel, A. Diourte, F. Soulié, O. Company, and C. Bordreuil, "Skeleton arc additive manufacturing with closed loop control," Additive Manufacturing, vol. 26, pp. 106–116, Mar. 2019, doi: 10.1016/j.addma.2019.01.003.

[271] "ER70S-6 Carbon Steel MIG Welding Wire," Canada Welding Supply Inc. Accessed: Dec. 22, 2024. [Online]. Available: https://canadaweldingsupply.ca/products/er70s6-carbon-steel-mig-wire

[272] "What are some Shielding Gases that are used for Welding? | CWB Group." Accessed: Dec. 22, 2024. [Online]. Available: https://www.cwbgroup.org/association/how-it-works/what-are-some-shielding-gases-are-used-welding

[273] S. Liu et al., Mechanical Performance of ER70S-6 Low-Carbon Steel Fabricated by Wire Arc Additive Manufacturing. 2022, p. 85. doi: 10.3850/978-981-18-6021-8_OR-01-0075.html.

[274] A. Elsokaty, O. Oraby, S. Sadek, and H. Salem, "Influence of Wire Arc Additive Manufacturing Beads' Geometry and Building Strategy: Mechanical and Structural Behavior of ER70S-6 Prismatic Blocks," Journal of Manufacturing and Materials Processing, vol. 7, p. 3, Dec. 2022, doi: 10.3390/jmmp7010003.

[275] H. Lockett, J. Ding, S. Williams, and F. Martina, "Design for Wire + Arc Additive Manufacture: design rules and build orientation selection," Journal of Engineering Design, vol. 28, pp. 1–31, Aug. 2017, doi: 10.1080/09544828.2017.1365826.

[276] T. A. Rodrigues, V. Duarte, R. M. Miranda, T. G. Santos, and J. P. Oliveira, "Current Status and Perspectives on Wire and Arc Additive Manufacturing (WAAM)," Materials (Basel), vol. 12, no. 7, p. 1121, Apr. 2019, doi: 10.3390/ma12071121.

[277] "PlatePro," Koike Aronson, Inc. Accessed: Dec. 23, 2024. [Online]. Available: https://www.koike.com/platepro/

[278] "Explore Hypertherm's plasma cutting and gouging systems." Accessed: Dec. 23, 2024. [Online]. Available: https://www.hypertherm.com/en-US/products/plasma-cutting-and-gouging-systems/

[279] "Eight-Axis Robotic System Prints Composite Parts." Accessed: Feb. 07, 2025. [Online]. Available: https://www.additivemanufacturing.media/articles/eight-axis-robotic-

system-prints-composite-parts?utm

[280] J. Schubnell, O. Aydogan, and M. Jung, “Determination of stress concentration factors of welded joints from 3D-surface scans by artificial neural networks,” Procedia Structural Integrity, vol. 57, pp. 112–120, Jan. 2024, doi: 10.1016/j.prostr.2024.03.014.

[281] O. Amir and A. Majdouba, “Mesh-based topology, shape and sizing optimization of ribbed plates,” Struct Multidisc Optim, vol. 67, no. 6, p. 103, Jun. 2024, doi: 10.1007/s00158-024-03824-9.

[282] L. D. Erőss and T. Markovits, “Mass reduction method for topology optimisation of a Ti6Al4V part for additive manufacturing,” Production Engineering Archives, vol. 30, pp. 354–360, Sep. 2024, doi: 10.30657/pea.2024.30.35.

[283] M. Fiedler, “Understanding and Improving Your Results in Fusion 360 Simulation”.

[284] J. Jiang, X. Xu, and J. Stringer, “Support Structures for Additive Manufacturing: A Review,” Journal of Manufacturing and Materials Processing, vol. 2, no. 4, Art. no. 4, Dec. 2018, doi: 10.3390/jmmp2040064.

[285] L. D. Evjemo, G. Langelandsvik, S. Moe, M. H. Danielsen, and J. T. Gravdahl, “Wire-arc additive manufacturing of structures with overhang: Experimental results depositing material onto fixed substrate,” CIRP Journal of Manufacturing Science and Technology, vol. 38, pp. 186–203, Aug. 2022, doi: 10.1016/j.cirpj.2022.04.006.

[286] N. Rosli, M. R. Alkahari, and F. Ramli, Influence of process parameters on dimensional accuracy in GMAW based additive manufacturing. 2019.

[287] L. Huang et al., “A Review of Challenges for Wire and Arc Additive Manufacturing (WAAM),” Transactions of the Indian Institute of Metals, vol. 76, Jan. 2023, doi: 10.1007/s12666-022-02823-y.

[288] A. Queguineur et al., “Wire arc additive manufacturing of thin and thick walls made of duplex stainless steel,” Int J Adv Manuf Technol, vol. 127, no. 1, pp. 381–400, Jul. 2023, doi: 10.1007/s00170-023-11560-5.

[289] T. Feucht, J. Lange, M. Erven, C. Borg Costanzi, U. Knaack, and B. Waldschmitt, “Additive manufacturing by means of parametric robot programming,” Construction Robotics, Jun. 2020, doi: 10.1007/s41693-020-00033-w.

[290] N. Khanna, H. Salvi, B. Karaş, I. Fairoz, and A. Shokrani, “Cost Modelling for Powder Bed Fusion and Directed Energy Deposition Additive Manufacturing,” Journal of Manufacturing and Materials Processing, vol. 8, no. 4, Art. no. 4, Aug. 2024, doi: 10.3390/jmmp8040142.

[291] A. Busachi, J. Erkoyuncu, P. Colegrove, F. Martina, C. Watts, and R. Drake, “A review of Additive Manufacturing technology and Cost Estimation techniques for the defence sector,” CIRP Journal of Manufacturing Science and Technology, vol. 19, pp. 117–128, Nov. 2017, doi: 10.1016/j.cirpj.2017.07.001.

[292] “MSAM Lab - UWaterloo,” MSAM University of Waterloo. Accessed: Jan. 14, 2025. [Online]. Available: https://msam.uwaterloo.ca/

[293] W. Hackenhaar, J. A. E. Mazzaferro, C. C. P. Mazzaferro, N. Grossi, and G. Campatelli, “Effects of different WAAM current deposition modes on the mechanical properties of AISI H13 tool steel,” Weld World, vol. 66, no. 11, pp. 2259–2269, Nov. 2022, doi: 10.1007/s40194-022-01342-0.

[294] K. Vartanian, L. Brewer, K. Manley, and T. Cobbs, “POWDER BED FUSION vs. DIRECTED ENERGY DEPOSITION BENCHMARK STUDY:”.